



A. Yücel Odabaşı Colloquium Series

1st International Meeting

-

Propeller Noise & Vibration

6 - 7 NOVEMBER 2014

SDKM CULTURAL CENTRE, ISTANBUL TECHNICAL UNIVERSITY

www.ayocol.itu.edu.tr

Edited by

Emin Korkut

Onur Usta

M. Cansın Özden

Devrim B. Danışman



Faculty of Naval Architecture and Ocean Engineering



A Yücel Odabaşı Colloquium Series

1st International Meeting

-

Propeller Noise & Vibration

6 - 7 November 2014

SDKM CULTURAL CENTRE, ISTANBUL TECHNICAL UNIVERSITY

www.ayocol.itu.edu.tr

Edited by

Emin Korkut

Onur Usta

M. Cansın Özden

Devrim B. Danışman



Faculty of Naval Architecture and Ocean Engineering

TABLE OF CONTENTS

Keynote Addresses

Keynote Address 1: Propeller Noise in the Marine Environment

Patrick Fitzsimmons

Keynote Address 2: The Effects of Noise on the Marine Environment: Addressing the Shipping Footprint Issue

Michel André

SPONSORS	i
PREFACE	ii
COLLOQUIUM COMMITTEES	iii
PROF. A. YÜCEL ODABAŞI.....	iv

Papers

Vibration Control by Propeller Design	1
<i>Lyn Bodger, Stephan Helma, Noriyuki Sasaki</i>	
A Scaling Procedure for Modern Propeller Designs.....	7
<i>Stephan Helma</i>	
Experimental Determination of the Difference in Visual and Acoustic Cavitation Inception	19
<i>Christian Johannsen, Oliver Zarbock, Herbert Bretschneider</i>	
Systematic Cavitation Tunnel Tests of a Propeller in Uniform and Inclined Flow Conditions as Part of a Round Robin Test Campaign.....	25
<i>Batuhan Aktas, Serkan Turkmen, Emin Korkut, Patrick Fitzsimmons, Mehmet Atlar</i>	
Propeller Acoustic Measurements in Atmospheric Towing Tank	37
<i>Henri Haimov, Vicente Gallego, Enrique Molinelli, BorjaTrujillo</i>	
Measurement of Radiated Underwater Noise from a Small Research Vessel in Shallow Water	47
<i>Alex Brooker, Victor Humphrey</i>	
Propeller Cavitation Noise and Background Noise in the Sea.....	57
<i>Dietrich Wittekind, Max Schuster</i>	
Underwater Noise and Marine Wildlife: Current and Future Implication and Assessment	63
<i>Paula Kellett, Osman Turan, Atilla Incecik</i>	
Towards Human-Oriented Norms: Investigating the Effects of Noise Exposure on Board Ships	71
<i>Rafet Emek Kurt, Ismail Hakki Helvacioğlu, Osman Turan</i>	
Proven Benefits from Foul Release Coatings	79
<i>Trevor Solomon</i>	
Computational Fluid Dynamics Simulation of Cavitating Open Propeller and Azimuth Thruster with Nozzle in Open Water.....	85
<i>Tobias Huuva, Simon Törnros</i>	
Hydroacoustic Simulations Using OpenFOAM	91
<i>Fatih Ertunaz</i>	
Propeller Noise Investigations by Means of Middle Size Cavitation Tunnel Measurements	95
<i>Sebastian Kowalczyk, Pawel Hoffmann</i>	

Outlook on Marine Propeller Noise and Cavitation Modelling	101
<i>Artur K. Lidtke, Stephen R. Turnock, Victor F. Humphrey</i>	
The Usage of Propeller Tunnels for Higher Efficiency and Lower Vibration.....	109
<i>M. Burak Şamşul, Naz Görener</i>	
Underwater Radiated Noise Prediction for a Submarine Propeller in Different Flow Conditions..	113
<i>M. Cansın Özden, Ahmet Y. Gürkan, Yasemin Arıkan Özden, Talat G. Canyurt, Emin Korkut</i>	

SPONSORS



Istanbul Technical University



Turkish Shipbuilders'
Association



Turkish Lloyd



Turkish Chamber of Shipping



Çeksan Shipyard



Elkon Electrics



Gemak Shipyard



Gürdesan Ship
Machinery Corp.



Delta Marine Engineering &
Computer Trade Co.

PREFACE

As a tribute to the late Professor A. Yücel Odabaşı's (1945-2009) life-long endeavours in promoting the science of Naval Architecture and in particular Naval Hydrodynamics, his colleagues have organized various meetings since his passing. From 2014, these activities are to become a regular international colloquium aiming to focus on a different theme on each occasion, gathering specialists from around the world.

This is the first international meeting in the colloquium series with a special theme on "*Propeller Noise & Vibration*". Ambient noise levels at seas around the world have been increasing through different sources, propeller being the most dominant cause and this increase has negative effects on marine environment, particularly on marine mammals and fish varieties. International Maritime Organisation (IMO) and other bodies have been trying to set-up regulations to reduce/limit noise levels at seas. As much as the technical aspects the selected theme is aimed to generate some insight into the subject and highlight main concerns. We hope that this will be a biannual event in future.

The Proceedings contain the papers presented at A Yücel Odabaşı Colloquium Series; 1st International Meeting - Propeller Noise & Vibration, which took place at SDKM Cultural Centre of Istanbul Technical University, Turkey, on 6-7 November 2014. The Proceedings can be downloaded from the colloquium webpage at <http://www.ayocol.itu.edu.tr/>.

We wish to acknowledge the Sponsors of the Colloquium for their generosity. We would like to thank the authors and presenters for their valuable contributions. We would especially like to thank the keynote speakers of this year's event, Mr. Patrick Fitzsimmons and Dr. Michel André for sharing their knowledge and expertise in propeller noise and vibration and their effects on marine environment. We would also like to acknowledge the tremendous help and efforts of the members of the local organising committee in the preparation of the colloquium.

We hope that, while commemorating Prof. Odabaşı, this colloquium will offer a fruitful platform for domestic and international specialists together with the key-note lecturers on this thematic subject "*Propeller Noise & Vibration*".

Dr. Barbaros Okan

Dr. Emin Korkut

COLLOQUIUM COMMITTEES

Standing Committee

Dr. Sander Çalışal, *University of British Columbia, Canada / Piri Reis University, Turkey*

Dr. Ömer Gören, *Istanbul Technical University, Turkey*

Dr. Atilla İncecik, *Strathclyde University, Scotland*

Dr. Öner Şaylan, *Istanbul Technical University (Retired), Turkey*

Technical Committee

Dr. Mehmet Atlar, *Newcastle University, UK*

Mr. Patrick A. Fitzsimmons, *Lloyd's Register (Retired) / Newcastle University, UK*

Dr. Jürgen Friesch, *Hamburg Ship Model Basin (HSVA), Germany*

Dr. Emin Korkut, *Istanbul Technical University, Turkey*

Dr. Noriyuki Sasaki, *Newcastle University, UK*

Dr. Leszek Wilczynski, *Ship Design and Research Centre (CTO), Poland*

Local Organizing Committee

Dr. Devrim B. Danışman (Secretary), *Istanbul Technical University, Turkey*

Dr. İsmail H. Helvacıoğlu, *Istanbul Technical University, Turkey*

Dr. Şebnem Helvacıoğlu, *Istanbul Technical University, Turkey*

Mr. Şafak C. Karakaş, *Istanbul Technical University, Turkey*

Dr. Barbaros Okan (Chair), *Istanbul Technical University, Turkey*

Mr. M. Cansın Özden, *Istanbul Technical University, Turkey*

Mr. Onur Usta, *Istanbul Technical University, Turkey*

PROF. A. YÜCEL ODABAŞI



(1945 – 2009)

Professor Odabaşı, a graduate of ITU (1967), earned his Ph.D. degree from the same university in 1971. Following his Ph.D., he joined Strathclyde University where his work on the application of Lyapunov's theory to ship stability gained him a well deserved international reputation which was acknowledged by STAB Award in 2012 post mortem. In 1974 he joined BSRA where he worked on every field of ship hydrodynamics and made significant contributions, in particular in the field of wake scaling. In 1988 he moved to USA to set up BMT International as its first director and CEO. He returned to ITU-Turkey in 1991 where he inspired a generation of young academics while at the same time succeeding to lead Turkish Lloyd to worldwide recognition. He was awarded the gold medal of NECIES-UK and numerous awards from NAVSEA, SNAME, BSRA.

Vibration Control by Propeller Design

Lyn Bodger^{1*}, Stephan Helma¹, Noriyuki Sasaki²

¹Stone Marine Propulsion Ltd, Birkenhead, UK.

²Newcastle University, Newcastle Upon Tyne, UK

Abstract: Propeller research has generally been focussed on improving the open water efficiency, and by considering the various energy losses associated with the marine screw propeller, it can be seen that for a design brief with given main engine power and RPM input, plus a thrust requirement defined by the specified ship speed, the most fruitful area for improvement in efficiency by propeller design is a reduction in energy losses. The simple way to increase the efficiency is reduction of blade area, increase a load near the tip and larger diameter with low RPM. However, the vibration and noise will be the first obstacle thing when a designer tries to increase the efficiency of the propeller by these ways. This paper will present the simple prediction method of pressure fluctuations induced by thickness, propeller loading and unsteady cavitation taking not only propeller dimensions but also stern shape in the beginning of propeller design stage.

Keywords: Pressure fluctuations, prediction method, cavitation, wake distributions near propeller.

1 INTRODUCTION

Energy loss of propellers can be explained as follows;

The axial kinetic loss results from the acceleration of the fluid necessary to produce the propeller thrust and is fixed for a given propeller loading condition.

The rotational kinetic loss derives from the swirl induced in the fluid by the rotation of the propeller.

The viscous loss depends upon the profile drag originating from the viscous drag of wing sections.

Viscous losses are largely associated with the surface area of the blades which is in turn associated with the need to avoid the harmful effects of cavitation. The original NPT (New Profile Type) research led to the development of an aerofoil profile type with low drag characteristics coupled with excellent cavitation properties. The superior cavitation properties permitted the adoption of lower blade surface areas than those required by traditional designs and thus reduced the frictional losses of the propeller as a whole. NPT propellers designed according to this principle have proven to be very successful in delivering high propulsive efficiencies. In the last few years orders for over 150 NPT propellers have been secured by SMP, mainly for Far Eastern shipyards, with many vessels destined for Western owners.

One interesting characteristic of the NPT design was that the adoption of the new profile family reduced the optimum diameter below that of the optimum diameter of conventional propellers designed for the same installation.

This had a number of immediate benefits: reduced propeller weight and inertia; reduced propeller cost; improved shafting dynamics; improved clearances between the blade tips and the hull.

However, it became clear that the reduced diameter gave rise to other benefits in terms of the propeller hull

interaction factors, which along with the propeller open water efficiency make up the overall propulsive efficiency as in Equation 1.

$$\eta_D = \eta_O \frac{1-t}{1-w_T} \eta_R \quad (1)$$

where:

η_O = Propeller open water efficiency

η_R = Relative rotative efficiency

t = Thrust deduction factor

w_T = Mean wake fraction.

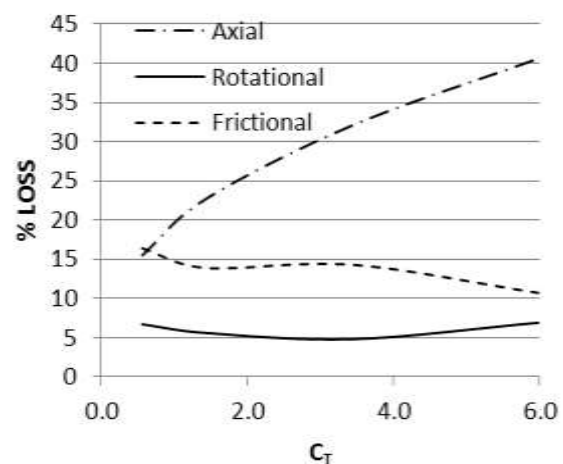


Figure 1 Energy losses from the propeller

Associated with the reduced propeller diameter is an increased propeller pitch necessary to ensure that the propeller absorbs the main engine power at the correct RPM. The increased pitch has the effect of reducing the thrust deduction factor.

Also, the reduced propeller diameter means that the blades are operating in a region of higher wake fraction which enables increased energy recovery from the vessel's boundary layer.

From equation 1 it is evident that these effects further increase the overall propulsive efficiency of the vessel.

It also became clear that in addition to improved overall efficiency the excellent cavitation performance and the reduced diameter of the NPT designs had further benefits in terms of a reduction in the excitation forces on the hull.

2 VIBRATION CONTROL BY PROPELLER DESIGN

In order to fully exploit the potential for improved overall efficiency and reduced excitation forces the NPT design method was expanded into a more holistic approach where interactions with the hull and effects on the hull were taken into account at an early stage in the propeller design process – see Figures 2 and 3.

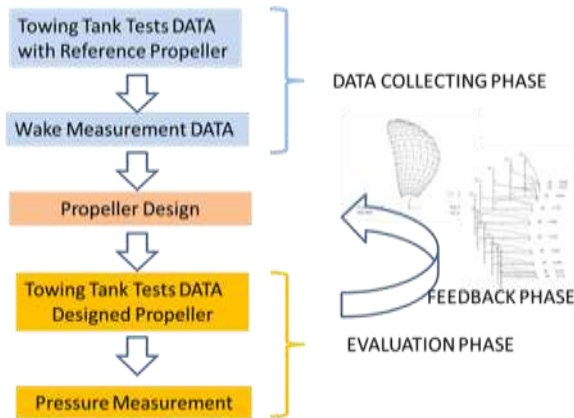


Figure2 Original design process for the NPT propeller

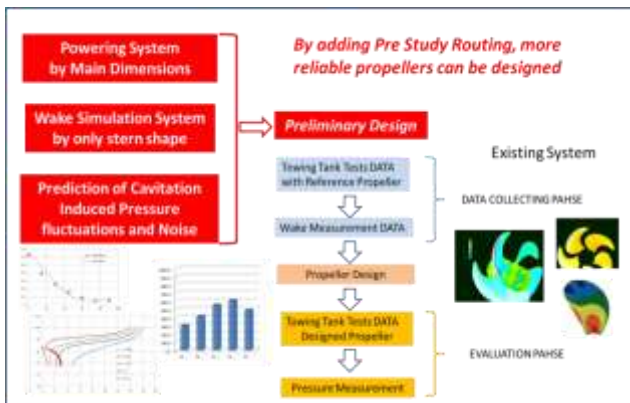


Figure3 Extended design process for the NPT propeller

Introducing the extended NPT propeller design process into the ship design process at an early stage enables the shipyard to take into account the enhanced overall propulsive efficiency in the selection of the main engine rating.

Furthermore, the ship designers will have a reasonable estimate of the cavitation performance of the propeller and estimates for excitation forces with their intended hull

form, thus allowing potential problems and possible solutions to be investigated at an early stage.. By this means the propeller design becomes fully integrated into the ship design and if necessary the propeller design may be adapted to control hull vibrations.

In this context, the characteristics of any particular NPT propeller can be exploited in a compromise manner along a continuum, with highest efficiency at one end and best cavitation performance at the other end, depending upon the particular demands of each ship design case. The enhanced efficiency of the NPT propeller means that even in those cases where some efficiency has to be sacrificed to achieve the required vibration levels, the overall propulsive efficiency will usually be better or at least no worse than with a conventional propeller optimised in terms of efficiency.

An important part of the extended NPT design process is the ability to estimate the level of pressure impulses on the hull before finalising the design and submitting it for evaluation by model testing.

Such a procedure has been developed and the results from its application have shown very good agreement with the predictions made from model experimentation.

Equation 2 gives an overview of the methodology.

$$K_{PZ} = \sqrt{K_{P0}^2 + K_{PC}^2 + 2K_{P0}K_{PC} \cos(\pi - \phi Z)} \quad (2)$$

$$K_{PC} = 0 \quad \text{if} \quad \sigma \geq \sigma_{CR}$$

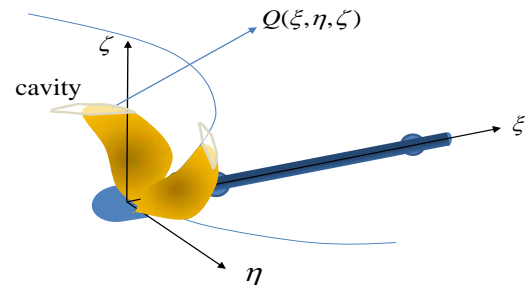


Figure 4 Coordinate system used in procedure for pressure impulse calculation

Where, K_{P0} is non-dimensional pressure fluctuations induced by blade thickness and blade lift force, K_{PC} is non-dimensional pressure fluctuations induced by cavitation occurrence. The angle ϕ is the phase difference between K_{P0} and K_{PC} , and Z is number of blades. σ_{CR} is the critical cavitation number for the cavitation inception. Full details of the calculation procedure have previously been presented by Sasaki while a brief review is given in the Appendix of this paper.

2.1 Example Case 1 (PCTC)

A good example of its utility was provided by the case of a series of PCTCs built in a Far Eastern shipyard. Preliminary model tests with a stock propeller revealed that the achievement of the contract speed presented a

significant challenge. The shipyard appreciated that the final design propeller would have to deliver a high efficiency whilst at the same time avoid exciting the aft end vibration to which this type of ship can be prone.

In order to satisfy the demanding specification the decision was made to fit an NPT propeller.

Leading particulars of the design specification are shown in Table 1.

Table 1 Leading dimensions of PCTC

Vessel Type	PCTC
Lpp (m)	190.00
Bm (m)	32.26
T (m)	9.00
Displacement Volume (m3)	30,267
MCR (kW)	12,200
MCR (RPM)	98.0
CSR (kW)	10,980

For comparison purposes the leading dimensions of the NPT propeller and an equivalent conventional design are shown in Table 2.

Table 2 Leading dimensions of NPT and conventional propeller designs

	NPT	Conventional
Blade No.	4	4
Diameter (mm)	6800	7000
P/D at 0.7R	0.902	0.849
BAR	0.460	0.512

Attention is drawn to the smaller diameter; the increased pitch ratio and the much reduced blade surface area.

The effectiveness of the NPT design can be seen in figure 5 which shows the predicted service speeds for the stock propeller and final NPT propeller.

The NPT design for the PCTC was also the subject of cavitation observations, a soft coating erosion test and pressure impulse measurements in a large cavitation tunnel. From the observations made the model basin concluded that there was very little risk of cavitation erosion occurring in service and this view was supported by the results of the erosion test. The pressure impulses were deemed to be moderate indicating that there was no expectation of problems arising from propeller induced pressure impulses.

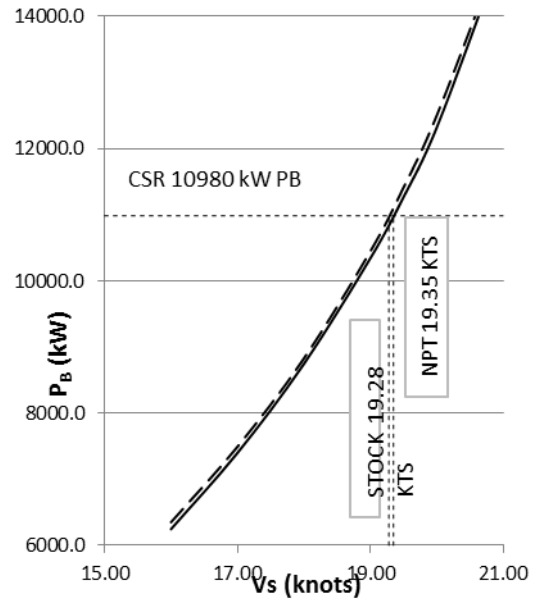


Figure 5 Predicted service speeds with NPT and stock propellers

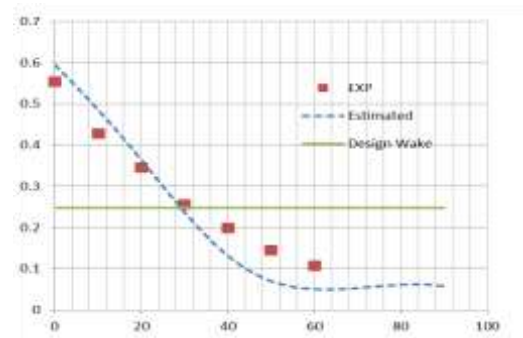


Figure 6 0.9R wake distribution as calculated and as measured

Figure 6 shows the comparison of predicted wake distributions at 0.9R radius and the experiment. The wake simulation is based the following equation.

$$w(0.9R, \theta) = A \cdot s_x(\theta)^2 + B \cdot s_x(\theta) + C \quad (3)$$

Where, s_x is non-dimensional distance between propeller position $(0.9R, \theta)$ and hull surface as shown in Figure 7.

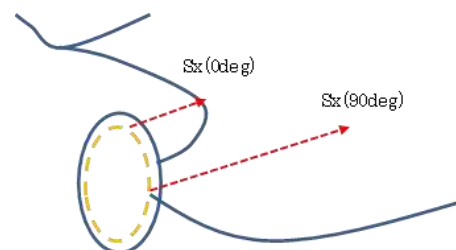


Figure7 Non-dimensional distance $s_x(=s_x/Lpp)$

The wake peak and slope of the wake toward top position ($\theta = 0$) are key for the prediction of pressure pulses and as shown have been accurately predicted.

CFD procedures may be used in the evaluation stage before moving on to model experimentation.

Figure 9 demonstrates the level of pressure impulses predicted by the model basin. The values calculated in the design stage prior to putting the propeller forward for verification by model testing are also shown. Attention is drawn to the good agreement between the values calculated and those derived from model experiments conducted by SSPA at a large cavitation tunnel as shown in Figure 8.

Table 3 Leading dimensions of RO/RO Ship (SR183)

Vessel Type	RO/RO
Lpp (m)	202
Bm (m)	45
T (m)	10.0
Prop Dia.(m)	6.6
MCR (kW)	14084
MCR (RPM)	126.5

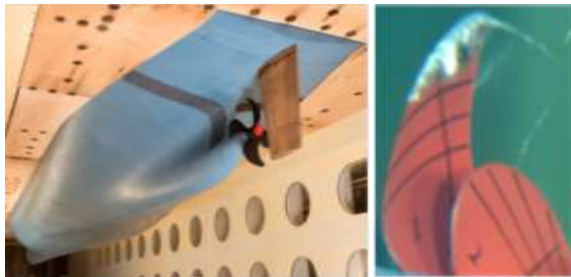


Figure 8 Cavitation test at SSPA large tunnel

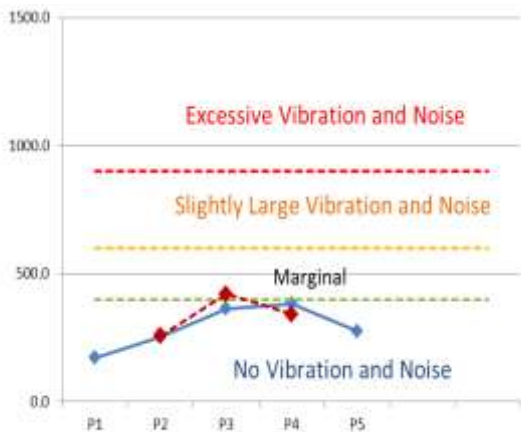


Figure 9 Pressure impulse levels

(Calculation: solid line, Experiment: dotted line)

2.2 Example Case 2 (RO/RO Skew Series)

If the predicted values for pressure impulses plot above the marginal line, the design will need to be changed. In order to reduce pressure fluctuations induced by a propeller, increased skew - which is a most effective countermeasure- will be considered. However, increased skew can have a negative influence on the propeller open water efficiency due to the heavier blade scantlings required to counteract the higher stresses incurred. Therefore it is very important to make an accurate prediction of the effects of changes in blade skew at early design stage. The preliminary design routine can predict this skew effect as shown in Figure 10.

In addition to the simple calculation method used to make preliminary estimates of the likely levels of pressure impulses, in more critical applications more sophisticated

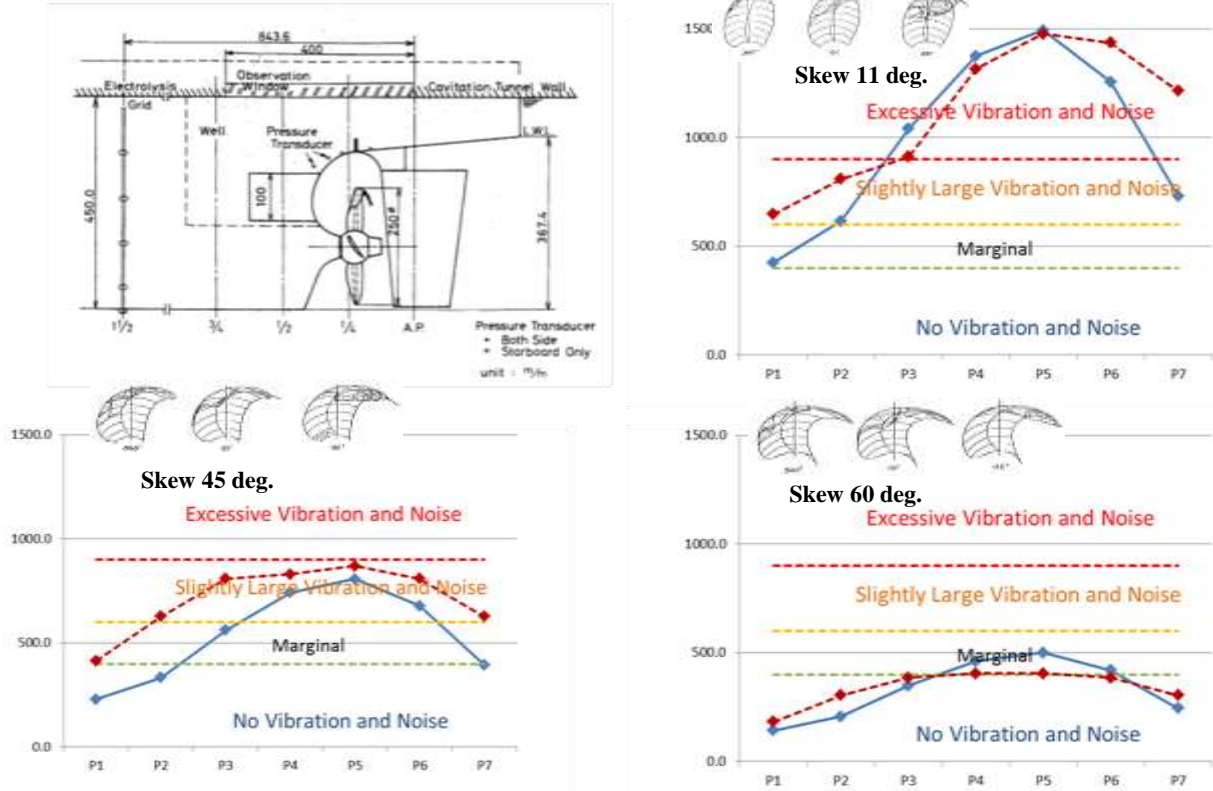


Figure 10 Effect of skew on the pressure fluctuations
(Calculation: solid line, Experiment: dotted line)

3 CONCLUSION

In conclusion it can be said that the NPT design procedure has been extended to take account of the interaction between the propeller and the hull.

Furthermore, as presented in Appendix a simple method has been developed which can reliably predict pressure impulse levels for different propeller geometries during the design process by introducing following design tools;

- (1) Simulation tool of wake distribution by after body shape based on S-X method.
- (2) Prediction tool of pressure fluctuations induced by propeller (blade thickness, blade lift and unsteady cavitation)

These two developments enable the designer to investigate confidently different design options adjusting the balance between the conflicting requirements of high efficiency and low excitation forces in order to deliver propellers fully compliant with the most demanding specification.

Appendix

Simple Calculation Method of Propeller Induced Pressure Fluctuations

Propeller induced pressure fluctuations ΔP_Z of point Q can be represented by equation (1).

$$\Delta p_Z = \sqrt{\Delta p_0^2 + \Delta p_C^2 + 2\Delta p_0\Delta p_C \cos(\pi - \varphi Z)}$$

$$\Delta p_C = 0 \quad \text{if} \quad \sigma > \sigma_{cr} \quad (1)$$

Where, ΔP_0 is the pressure fluctuation induced by blade thickness and blade lift force, ΔP_C is the pressure fluctuation induced by cavitation occurrence. The angle φ is the phase difference between ΔP_0 and ΔP_C and Z is the number of blades.

σ_{cr} is the critical cavitation number for cavitation inception.

Non-dimensionalising by dividing through by $\rho n^2 D^2$ (n and D is propeller rps and diameter respectively) the above expression can be written

$$K_{PZ} = \sqrt{K_{P0}^2 + K_{PC}^2 + 2K_{P0}K_{PC} \cos(\pi - \varphi Z)}$$

$$K_{PC} = 0 \quad \text{if} \quad \sigma > \sigma_{cr} \quad (2)$$

Pressure fluctuations induced by blade thickness and lift can be written in Equation (3).

$$K_{p0} = K_0 R_e^{-3} \quad (3)$$

Where, K_0 is magnitude of pressure fluctuations and R_e is a distance between calculation point and representative point for blade thickness and lift.

According to the experiment results obtained by Taniguchi (1928), K_0 and R_e can be represented by the following approximate expressions in the same definitions of Figure 4.;

$$K_0 = (0.0058Z^2 - 0.0972Z + 0.402) \frac{1}{2} K_Q \quad (4)$$

$$R_e = \sqrt{\frac{\xi^2 + \eta^2 + \zeta^2}{D}} - \frac{1}{2} (0.0117Z^2 - 0.0684Z + 0.72) \quad (5)$$

From Equation (1) to Equation (5), It is clear that the pressure fluctuations induced by blade thickness and lift is proportional to propeller torque coefficient K_Q and the distance between a representative point for blade thickness /lift and calculation point R_e^{-3} .

A larger number of the blades (Z) can reduce K_0 considerably. The ratio of 3 blades and 6 blades for K_0 is almost 1/5.

Pressure fluctuations induced by unsteady cavitation can be represented by introducing distance attenuation coefficient H , K_{PC} as follows;

$$K_{PC} = K_{C0} R_{ec}^{-H} \quad (6)$$

The amplitude of pressure fluctuation K_{C0} is a function of wake non-uniformity and 2nd derivative of cavitation volume and can be estimated based on full scale measurement data as follows;

$$K_{C0} = 0.0135(\sigma_{cr} - \sigma_n)^{1.525} \quad \sigma_n \leq \sigma_{cr}$$

$$K_{C0} = 0 \quad \sigma_n > \sigma_{cr} \quad (7)$$

The distance between a representative center of cavitation volume and calculation point R_{ec} can be represented by,

$$R_{ec} = \frac{d}{d_0} \quad (8)$$

Where,

$$d_0 = 0.377D \quad (9)$$

$$d = \sqrt{\xi^2 + (\eta - 0.201D)^2 + (\zeta - 0.430D)^2} \quad (10)$$

The attenuation factor H can be considered as a function of non-uniformity of wake and cavitation number.

According to the full scale measurements, H can be represented as follows;

$$H = 3 - 0.0866\Delta W(\sigma_{cr} - \sigma_n)^{5.287} \quad 1 \leq H \leq 3$$

$$\sigma_{cr} = 2.0 + 5.2\Delta W \quad (11)$$

REFERENCES

- Glover, E.J., (1987). Improving the Underwater Efficiency of Ships. I. Mar. E, London, UK.
- Huse E. (1972). Pressure Fluctuations on the Hull Induced by Cavitating Propellers. Norwegian Ship Model Experiment Tank Publication, No.111, March, Norway.
- Sasaki, N. and Nagamatsu S. (1984). Measurement of Surface Force on Ships and Quick Estimation Method. Sumitomo Technical Review, April, Japan.
- SR183 (1983) Research of Propeller and Stern Shape for the Purpose of Reduction of Stern Vibration and Noise. JSRA, 1981-1983, Japan.
- Takahashi H. (1977) Estimation of Surface Force Induced by Propeller, SNAJ, **141** (June).
- Taniguchi K.. (1928) On the Pressure Fluctuations in the Vicinity of Propellers. Journal of the Soc. of Nav. Arch. of West Japan.

A Scaling Procedure for Modern Propeller Designs

Stephan Helma^{1*}

¹Stone Marine Propulsion, Birkenhead, England, UK

Abstract: The extrapolation procedures currently used to scale propeller characteristics tested at model scale to their full scale performances are either based on a statistical, the Lerbs-Meyne or the recently developed strip method. With the emergence of so-called unconventional propellers and different design strategies associated with them, it has been questioned whether the assumptions used in these scaling methods are still universally valid. E.g. with tip and root unloading employed the circulation distribution deviates from the optimum, which is assumed by the Lerbs-Meyne method; more modern profiles show a different camber distribution and hence the drag coefficient must be aligned with the hydrodynamic inflow angle and not with the pitch to diameter ratio as assumed by the strip method (and implicitly by the ITTC 1978 method). The work presented still uses the assumption of the equivalent profile and will explain three possible modified scaling procedures ultimately resulting in a way to calculate the hydrodynamic inflow angle solely from one open-water test conducted at a constant Reynolds number. Finally exemplary results comparing a propeller of conventional type with a recent propeller designs will also be shown. The new proposed method shows a superior performance when compared to other scaling methods.

Keywords: Scale effects, ITTC 1978 power prediction, Lerbs-Meyne, strip method, open-water efficiency.

1 INTRODUCTION

In recent years new propeller design philosophies have emerged into the market. The NPT-, Kappel- and CLT-propellers are examples of these so-called unconventional designs. From the very beginning it was claimed by their designers that the existing scaling methods do not result in full scale predictions reflecting the actual performances observed. Based on the data available to the author this holds true for at least one of the above mentioned propeller types: The trial results regularly show a performance above the speeds predicted by different model basins. Generally speaking this behaviour never posed a problem in the past. With everybody now looking for the most efficient configuration more and more propellers are comparatively tested and the final design is decided on the outcome of the performance predictions. Some propeller manufactures even take the scaling procedure used at the model basin into their consideration when designing a propeller for a comparative test to gain a little advantage over competitors. These tests pose a complete new challenge to the model basins, since tiny differences – often as small as 0.01 kn – determine who wins the contract. This shows clearly that a more accurate scaling procedure is in high demand.

A “good” procedure to extrapolate open-water data measured in a towing tank to full scale data must satisfy the following criteria to be reliable and trustworthy:

1. Independence on the Reynolds number of the model test:

The extrapolated performance must be independent of the Reynolds number of the open-water data, which means, that regardless of the Reynolds number

experienced during the model test, the full scale prediction must be the same.

2. Independence of the propeller geometry:

The extrapolated performance must reproduce the relative merits of different propeller designs, that the same procedure can be used for any design and no design should be favoured.

3. Absolute accuracy:

The extrapolated performance must represent the actual performance figures of the propeller, although a predictable difference can be handled with an adjustment factor.

4. Reliability:

The analysis of the open-water data must give a criteria about the reliability of the test.

2 EXISTING SCALING PROCEDURES

Currently four main scaling procedures are used in model basins to scale the measured open-water data to full scale propeller performance:

1. No scaling
2. ITTC 1978 extrapolation method
3. Lerbs-Meyne method
4. Strip method

Independently of the scaling method applied, there are some local preferences in the implementation of the open-water tests, mainly concerning the Reynolds number used. Some model basins adheres strictly to the ITTC recommendation that the Reynolds number “must not be lower than $2 \cdot 10^5$ at the open-water test” (ITTC 1999) (some of them just fulfilling the recommendation running the open-water test at a Reynolds number of 2×10^5); some model basins conduct two tests (one at the Reynolds

number experienced during the self-propulsion test and one above 2×10^5 , using the lower to analyse the self-propulsion test, the other to scale to the full scale open-water curve); at least one model basin arranges for three open-water tests (one at the Reynolds number of the self-propulsion and two higher ones “to assess if the flow is fully turbulent”). If just one open-water test is conducted, it might or might not be scaled down to the Reynolds number experienced at the self-propulsion test.

2.1 No scaling

When predicting the full scale performance, the open-water test is not extrapolated to full scale, but a final correction factor is applied to the performance prediction.

2.2 ITTC 1978 Extrapolation Method

The ITTC 1978 extrapolation method assumes a linear correlation between the change in friction drag and change in thrust and torque coefficient (ITTC 1999). But “it should be kept in mind that both the relation between thrust/torque and drag coefficient and the relation between drag coefficient and Reynolds number are based on statistics and the basis for the statistical values is very small” (Kuiper 1992). This very clear warning should always be kept in mind when judging the accuracy of any results using this extrapolation method. With the emergence of new profile types this warning becomes more and more vehemently – especially when comparing propellers using different profile types.

The second problematic characteristics of this scaling method is the linear dependence of the change in the thrust coefficient on the pitch to diameter ratio P/D . To explain the impact of this assumption, let us consider a propeller with a flat camber line and compare it to one, where all the lift is generated by camber alone. The first propeller will have a higher pitch because the lift is only generated by the angle of incidence. Even if this propeller will perform worse than the cambered one, it will be favoured by the extrapolation method and might show a scaled performance superior to the second, cambered propeller.

The ITTC 1978 extrapolation method insists to test the propeller model at a Reynolds number “not [...] lower than 2×10^5 at the open-water test” (ITTC 1999). If you compared the performance extrapolated from open-water tests conducted at different Reynolds numbers you want to get the same values independently from the starting point. Figure 2 shows three full scale open-water curves of the same propeller but scaled up from different Reynolds numbers according to ITTC. Evidently the curve calculated from the lowest Reynolds number does not coincide with the other two curves despite the fact that the lowest Reynolds number of about $2.5 \cdot 10^5$ is well above the ITTC 1978 recommendation of $2 \cdot 10^5$. The propeller shown in Figure 7 exhibits an even worse behaviour: There is a big difference in the extrapolated performances depending on the starting point. The first propeller tested was of a Wageningen B type, the second was of the NPT type. Both propellers were tested at the same model basin.

2.3 Lerbs-Meyne Method

The Lerbs-Meyne method was published in 1968 (Meyne 1968) and derives a propeller with optimum distribution of circulation and no friction, that is the ideal propeller, from the open-water test at one Reynolds number. With an assumed drag ratio $\varepsilon_{0.7}$ of the so called equivalent profile at radius $0.7R$, the measured values η and c_{TH} , the open-water efficiency and the thrust coefficient, respectively, can be converted to η_i and c_{THi} of the ideal propeller. However there is only one valid combination of η_i and c_{THi} which can be read of the Kramer diagram (1939). Most likely the calculated $\eta_i(\varepsilon_{0.7})$ and $c_{THi}(\varepsilon_{0.7})$ do not coincide with the valid combination, so $\varepsilon_{0.7}$ has to be adjusted in an iterative process until the valid combination is met. The full scale values are calculated with a friction coefficient of 0.006.

The Lerbs-Meyne method seems to be the perfect scaling method, since the profile drag is calculated from the actually measured open-water values and it is aligned with the inflow. There are only two drawbacks. Firstly, it is based on an equivalent profile which represents the whole propeller blade. Secondly, it assumes that the propeller blade was designed with an optimum circulation distribution. This poses a problem with modern propellers which are almost always wake adapted designs. The designer also often unloads the tip or root region or the diameter is restricted, so the assumption of optimum circulation distribution does not hold for all designs.

The Figures 3 and 8 show the scaled open-water tests.

2.4 Strip Method

The strip method was developed by H. Streckwall of the HSVA model basin and published in 2013 (Streckwall et al 2013). When analysing an open-water test, the vector sum of the contributions of each radial section (strip) towards the friction resistance is calculated to get the friction resistance of the whole blade. When doing so, it takes into account the actual Reynolds number and the position of the transition point at the respective radial strip.

The strip method is certainly an advancement of the existing scale methods. The advantages are that it accounts for the actual turbulence in the inflow, e.g. in open-water and behind condition, by using two different friction lines. It also takes into account the actual distribution of chord length and pitch. The main potential problems are the alignment of the drag forces with the nose-tail pitch line instead of the actual inflow angle (see the respective note in section 2.2 about the ITTC 1978 extrapolation procedure) and the determination of the friction coefficients. As pointed out by Streckwall the calculation of the friction coefficient uses the local friction coefficients for laminar and turbulent flow as stated by Hoerner (1965) and the location of the transition point is derived from CFD calculations. These calculations were done for a set of propellers for two inflow conditions: One with low turbulence for the open-water curve, one with higher turbulence for the behind

condition as expected during self-propulsion tests. Final curve fittings result in the two friction resistance curves for the open-water and the behind condition. These derived curves are used for all propellers disregarding the actual profile used, whereas it is to be expected that the location of the transition point is strongly influenced by the section shape.

The scaled open-water tests can be found in Figures 4 and 9.

3 NEW SCALING METHODS, THREE OPTIONS

In the author's opinion the second goal of independence of the propeller geometry can only be realized if the drag coefficient is not parallel to the nose-tail pitch line but aligned with the hydrodynamic inflow as the theory of thin profiles suggests. Three ways to derive the hydrodynamic inflow angle from open-water tests will be shown in the following sections.

3.1 Equivalent Profile

Let us imagine that the propeller is built up of circumferential sections stacked on top of each other and each section experiences a lift and drag coefficient c_d and c_l . These coefficients are aligned with the hydrodynamic inflow angle β_i . Geometric considerations lead to the formulae (1a+b) for the thrust and torque coefficients K_T and K_Q :

$$K_T = \frac{\pi^2 Z}{4} \int_{x_h}^1 \frac{c_l(x) \cos \beta_i(x) - c_d(x) \sin \beta_i(x) c(x)}{\left[\frac{\cos \beta(x)}{\cos(\beta_i(x) - \beta(x))} \right]^2} \frac{c(x)}{D} x^2 dx \quad (1a)$$

$$K_Q = \frac{\pi^2 Z}{8} \int_{x_h}^1 \frac{c_l(x) \sin \beta_i(x) + c_d(x) \cos \beta_i(x) c(x)}{\left[\frac{\cos \beta(x)}{\cos(\beta_i(x) - \beta(x))} \right]^2} \frac{c(x)}{D} x^3 dx \quad (1b)$$

where

- Z = the number of propeller blades,
- x = the fractional radius r/R ,
- x_h = the fractional radius r_h/R of the propeller hub,
- $c(x)$ = the length of the section at fractional radius x ,
- $\beta(x)$ = the advance angle at fractional radius x ,
- $\beta_i(x)$ = the hydrodynamic inflow angle and
- D = the propeller diameter.

At this point we introduce the concept of the equivalent profile: We replace the whole propeller blade with one single section of length \bar{c} located at the fractional radius \bar{x} such that this profile shows the same characteristics as the original blade. Using this equivalent profile we can replace the chord distribution and all hydrodynamic values which depend on the fractional radius x in the integrand with constant values and extract these from the integral. We denote these values of the equivalent profile with the overbar $\bar{\quad}$:

$$K_T = \frac{\pi^2 Z \bar{c}_l \cos \bar{\beta}_i - \bar{c}_d \sin \bar{\beta}_i \bar{c}}{4 \left[\frac{\cos \bar{\beta}}{\cos(\bar{\beta}_i - \bar{\beta})} \right]^2} \frac{\bar{c}}{D} \int_{x_h}^1 x^2 dx \quad (2a)$$

$$K_Q = \frac{\pi^2 Z \bar{c}_l \cos \bar{\beta}_i + \bar{c}_d \sin \bar{\beta}_i \bar{c}}{8 \left[\frac{\cos \bar{\beta}}{\cos(\bar{\beta}_i - \bar{\beta})} \right]^2} \frac{\bar{c}}{D} \int_{x_h}^1 x^3 dx \quad (2b)$$

(For an alternative formulation of the equivalent profile, see appendix "A.1 Alternative Formulation of the Equivalent Profile".)

Note that for the equivalent profile the thrust and torque coefficients must remain the same as for the whole propeller blade, hence the $\bar{\quad}$ can be omitted.

After integration the equations (2a+b) become:

$$K_T = \frac{\pi^2 Z \bar{c}_l \cos \bar{\beta}_i - \bar{c}_d \sin \bar{\beta}_i \bar{c}}{4 \left[\frac{\cos \bar{\beta}}{\cos(\bar{\beta}_i - \bar{\beta})} \right]^2} \frac{\bar{c}}{D} \frac{1 - x_h^3}{3} \quad (3a)$$

$$K_Q = \frac{\pi^2 Z \bar{c}_l \sin \bar{\beta}_i + \bar{c}_d \cos \bar{\beta}_i \bar{c}}{8 \left[\frac{\cos \bar{\beta}}{\cos(\bar{\beta}_i - \bar{\beta})} \right]^2} \frac{\bar{c}}{D} \frac{1 - x_h^4}{4} \quad (3b)$$

And finally

$$K_T = \kappa_T B^2 (\bar{c}_l \cos \bar{\beta}_i - \bar{c}_d \sin \bar{\beta}_i) \quad (4a)$$

$$K_Q = \kappa_Q B^2 (\bar{c}_l \sin \bar{\beta}_i + \bar{c}_d \cos \bar{\beta}_i) \quad (4b)$$

using the following abbreviations for convenience:

$$\kappa_T = \frac{\pi^2 Z \bar{c}}{4 D} \frac{1 - x_h^3}{3} \quad (4c)$$

$$\kappa_Q = \frac{\pi^2 Z \bar{c}}{8 D} \frac{1 - x_h^4}{4} \quad (4d)$$

$$\kappa = \frac{\kappa_Q}{\kappa_T} = \frac{3}{8} \frac{1 - x_h^4}{1 - x_h^3} \quad (4e)$$

$$B = \frac{\cos(\bar{\beta}_i - \bar{\beta})}{\cos \bar{\beta}} \quad (4f)$$

Furthermore the advance angle $\bar{\beta}$ is known for a given advance coefficient J :

$$\tan \bar{\beta} = \frac{v_0}{\omega \bar{r}} = \frac{J}{\pi \bar{x}} \quad (4g)$$

Let us recapitulate the dependencies of each variable on the advance coefficient J , the fractional radius \bar{x} and the Reynolds number \overline{Rn} of the equivalent profile:

$$\begin{aligned} \bar{c} &= \bar{c}(\bar{x}) \\ K_T &= K_T(J, \overline{Rn}) \\ K_Q &= K_Q(J, \overline{Rn}) \\ \bar{c}_d &= \bar{c}_d(J, \overline{Rn}, \bar{x}) \\ \bar{c}_l &= \bar{c}_l(J, \bar{x}) \\ \bar{\beta} &= \bar{\beta}(J, \bar{x}) \\ \bar{\beta}_i &= \bar{\beta}_i(J, \bar{x}) \end{aligned}$$

$$\begin{aligned}\kappa_T &= \kappa_T(\bar{x}) \\ \kappa_Q &= \kappa_Q(\bar{x}) \\ \kappa &= \text{const} \\ B &= B(J, \bar{x})\end{aligned}$$

Strictly speaking the lift coefficient \bar{c}_l , the hydrodynamic inflow angle $\bar{\beta}_i$ and hence the factor B also depend on the Reynolds number, but this dependence is very weak as we will argue later.

3.2 Option 1 – Basic Profile Drag $\bar{c}_{d,0}$

For every propeller there is only one advance coefficient J_0 , where the equivalent profile does not generate any lift. This is similar to the zero-lift angle of attack of an aerofoil. It is worth noting that this operating point does neither occur at the J -value where K_T or K_Q becomes zero but its position will be between those two points. We reference all values corresponding to J_0 with the subscript 0.

3.2.1 Determination of the Basic Profile Drag $\bar{c}_{d,0}$

Starting with the equations (4a+b) we set the lift coefficient \bar{c}_l to 0:

$$K_{T,0} = \kappa_T B_0^2 \left(-\bar{c}_{d,0} \sin \bar{\beta}_{i,0} \right) \quad (5a)$$

$$K_{Q,0} = \kappa_Q B_0^2 \left(\bar{c}_{d,0} \cos \bar{\beta}_{i,0} \right) \quad (5b)$$

Isolating $\bar{c}_{d,0}$ from both equations and equalising them, results in an equation for $\bar{\beta}_{i,0}$

$$-\frac{K_{T,0}}{\kappa_T} \frac{1}{\sin \bar{\beta}_{i,0}} = \frac{K_{Q,0}}{\kappa_Q} \frac{1}{\cos \bar{\beta}_{i,0}} \quad (6)$$

Which can be solved for $\bar{\beta}_{i,0}$:

$$\tan \bar{\beta}_{i,0} = -\frac{K_{T,0}}{\kappa_T} \frac{\kappa_Q}{K_{Q,0}} = -\kappa \frac{K_{T,0}}{K_{Q,0}} \quad (7)$$

Unfortunately we still cannot determine $\bar{\beta}_{i,0}$ because we do not know at which value J_0 we have to evaluate the above equation. But if the equivalent profile does not produce any lift, it will not generate any induced velocities and hence the hydrodynamic inflow angle $\bar{\beta}_{i,0}$ becomes the advance angle $\bar{\beta}_i$ at J_0 :

$$\tan \bar{\beta}_{i,0} = \tan \bar{\beta}_0 \quad (8a)$$

$$-\kappa \frac{K_T(J_0)}{K_Q(J_0)} = \frac{J_0}{\pi \bar{x}} \quad (8b)$$

If we assume a value \bar{x} for the radial position of the equivalent profile, we can numerically solve any of the following conditional equations for J_0 .

$$\frac{J_0}{\pi \bar{x}} + \kappa \frac{K_T(J_0)}{K_Q(J_0)} = 0 \quad (9a)$$

$$\frac{J_0}{\pi \bar{x}} K_Q(J_0) + \kappa K_T(J_0) = 0 \quad (9b)$$

$$\frac{J_0^2}{2\pi^2 \bar{x}} + \kappa \eta_0(J_0) = 0 \quad (9c)$$

A good choice for \bar{x} might be either of the universally accepted values of 0.7 or 0.75.

With the value J_0 of the advance coefficient, where the lift coefficient \bar{c}_l becomes zero, known, the hydrodynamic inflow angle $\bar{\beta}_{i,0}$ can be calculated with the help of equations (8b) and (7) and finally the basic profile drag $\bar{c}_{d,0}$ is known from evaluating any of the equations (5a) or (5b) with $K_{T,0}$ or $K_{Q,0}$ from the measured open-water data:

$$\bar{\beta}_{i,0} = \bar{\beta}_0 = \arctan \frac{J_0}{\pi \bar{x}} \quad (10)$$

$$\bar{c}_{d,0} = -\frac{K_{T,0}}{\kappa_T B_0^2 \sin \bar{\beta}_{i,0}} = \frac{K_{Q,0}}{\kappa_Q B_0^2 \cos \bar{\beta}_{i,0}} \quad (11)$$

3.2.2 Determination of the Hydrodynamic Inflow Angle $\bar{\beta}_i(J)$

Starting again from the two equations (4a+b)

$$\bar{c}_l \cos \bar{\beta}_i - \bar{c}_d \sin \bar{\beta}_i = \frac{K_T}{\kappa_T B^2} \quad (12a)$$

$$\bar{c}_l \sin \bar{\beta}_i + \bar{c}_d \cos \bar{\beta}_i = \frac{K_Q}{\kappa_Q B^2} \quad (12b)$$

(rearranged here for clarity) the lift coefficient \bar{c}_l can be eliminated by multiplying (12a) with $\sin \bar{\beta}_i$ and (12b) with $\cos \bar{\beta}_i$ and subtracting the first from the second equation:

$$\bar{c}_d = \frac{1}{B^2} \left(\frac{K_Q}{\kappa_Q} \cos \bar{\beta}_i - \frac{K_T}{\kappa_T} \sin \bar{\beta}_i \right) \quad (13)$$

The linearised profile theory states that the drag coefficient remains constant for small angles of attack α and is equal to the minimum drag coefficient which occurs at the operating point where the profile does not generate any lift (Abbott & von Doenhoff 1959). In the case of the equivalent profile this corresponds to the statement that the drag coefficient $\bar{c}_d(J)$ remains constant for all values of J and is equal to the basic profile drag $\bar{c}_{d,0}$ – as long as the angle of attack α is small:

$$\bar{c}_d(J) = \bar{c}_{d,0} \quad (14)$$

With this assumption equation (13) becomes the conditional equation for $\bar{\beta}_i(J)$ which can be solved numerically for any given J :

$$\frac{1}{B^2|_J} \left(\frac{K_Q|_J}{\kappa_Q} \cos \bar{\beta}_i|_J - \frac{K_T|_J}{\kappa_T} \sin \bar{\beta}_i|_J \right) - \bar{c}_{d,0} = 0 \quad (15)$$

3.2.3 Determination of the Lift Coefficient $\bar{c}_l(J)$

Knowing the hydrodynamic inflow angle $\bar{\beta}_i$ from solving equation (15), the lift coefficient \bar{c}_l can be calculated from equations (12a+b):

$$\begin{aligned}\bar{c}_l &= \frac{1}{\cos \bar{\beta}_i} \left(\frac{K_T}{\kappa_T B^2} + \bar{c}_{d,0} \sin \bar{\beta}_i \right) \\ &= \frac{1}{\sin \bar{\beta}_i} \left(\frac{K_Q}{\kappa_Q B^2} - \bar{c}_{d,0} \cos \bar{\beta}_i \right)\end{aligned} \quad (15)$$

3.3 Option 2 – Two Open-water Tests at Two Reynolds Numbers

We can use two open-water tests conducted at two different Reynolds numbers Rn_1 and Rn_2 to calculate the

hydrodynamic inflow angle $\bar{\beta}_i(J)$, the lift and drag coefficients $\bar{c}_l(J)$ and $\bar{c}_d(J)$ and the added three-dimensional drag $\bar{c}_{d,3d}(J)$.

3.3.1 Determination of the Hydrodynamic Inflow Angle $\bar{\beta}_i(J)$

Starting with the equations (4a+b) we can eliminate the drag and lift coefficients $\bar{c}_d(J)$ and $\bar{c}_l(J)$ with the process described for the derivation of equation (13):

$$\bar{c}_l = \frac{1}{B^2} \left(\frac{K_Q}{\kappa_Q} \sin \bar{\beta}_i + \frac{K_T}{\kappa_T} \cos \bar{\beta}_i \right) \quad (17a)$$

$$\bar{c}_d = \frac{1}{B^2} \left(\frac{K_Q}{\kappa_Q} \cos \bar{\beta}_i - \frac{K_T}{\kappa_T} \sin \bar{\beta}_i \right) \quad (17b)$$

The theory of aerofoils states that the lift coefficient \bar{c}_l does not change with the Reynolds number (Abbott & von Doenhoff 1959). We can (reasonably) assume that if the lift does not change, the induced velocities will not change either, hence the hydrodynamic inflow angle $\bar{\beta}_i$ does not change with the Reynolds number for any given value of J :

$$\bar{c}_{l,1}(J) = \bar{c}_{l,2}(J) = \bar{c}_l(J) \quad (18a)$$

$$\bar{\beta}_{l,1}(J) = \bar{\beta}_{l,2}(J) = \bar{\beta}_i(J) \quad (18b)$$

where the subscript $_1$ and $_2$ denote the values corresponding to each of the two Reynolds numbers Rn_1 and Rn_2 .

By equalizing the equation (17a) evaluated at both Reynolds numbers, we get an analytical equation for the hydrodynamic inflow angle $\bar{\beta}_i(J)$:

$$\begin{aligned} \frac{1}{B^2} \left(\frac{K_{Q,1}}{\kappa_Q} \sin \bar{\beta}_i + \frac{K_{T,1}}{\kappa_T} \cos \bar{\beta}_i \right) \\ = \frac{1}{B^2} \left(\frac{K_{Q,2}}{\kappa_Q} \sin \bar{\beta}_i + \frac{K_{T,2}}{\kappa_T} \cos \bar{\beta}_i \right) \end{aligned} \quad (19a)$$

$$\tan \bar{\beta}_i = -\kappa \frac{K_{T,1} - K_{T,2}}{K_{Q,1} - K_{Q,2}} = -\kappa \frac{\Delta K_T}{\Delta K_Q} \quad (19b)$$

Substituting the now known value $\bar{\beta}_i$ into equations (17a+b) will yield the same lift coefficient for both Reynolds numbers but two different drag coefficients $\bar{c}_{d,1}(J)$ and $\bar{c}_{d,2}(J)$. An interesting observation is that both the hydrodynamic inflow angle and these coefficients are independent of the fractional radius \bar{x} of the equivalent profile.

3.4 Option 3 – Determination of the Hydrodynamic Inflow Angle $\bar{\beta}_i$ from Just One Open-Water Test

As seen above in equation (19b) the hydrodynamic inflow angle $\bar{\beta}_i$ over the range of the advance coefficient J can be calculated from the K_T and K_Q curves. In the following section a formal way do derive this hydrodynamic inflow angle from a single set of thrust and torque curves will be presented.

3.4.1 Determination of the Hydrodynamic Inflow Angle $\bar{\beta}_i(J)$

Starting with equation (17a), we reshape it to (and show their dependencies)

$$\begin{aligned} B^2(J, \overline{Rn}) \bar{c}_l(J, \overline{Rn}) \\ = \frac{K_Q(J, \overline{Rn})}{\kappa_Q} \sin \bar{\beta}_i(J, \overline{Rn}) \\ + \frac{K_T(J, \overline{Rn})}{\kappa_T} \cos \bar{\beta}_i(J, \overline{Rn}) \end{aligned} \quad (20a)$$

Usually this equation is looked at with the Reynolds number \overline{Rn} fixed resulting in the well-known open-water curves $K_T(J)|_{\overline{Rn}}$, $K_Q(J)|_{\overline{Rn}}$ and $\eta_o(J)|_{\overline{Rn}}$. If the same propeller were tested at different Reynolds numbers, the three-dimensional surfaces $K_T(J, \overline{Rn})$ and $K_Q(J, \overline{Rn})$ can be constructed. Cutting these surfaces at constant J -values results in the open-water curves $K_T(\overline{Rn})|_J$ and $K_Q(\overline{Rn})|_J$ depending on the Reynolds number. Omitting $|_J$, which indicates that the J -value is fixed, for clarity, equation (20a) is written for fixed values of J as

$$\begin{aligned} B^2(\overline{Rn}) \bar{c}_l(\overline{Rn}) = \frac{K_Q(\overline{Rn})}{\kappa_Q} \sin \bar{\beta}_i(\overline{Rn}) \\ + \frac{K_T(\overline{Rn})}{\kappa_T} \cos \bar{\beta}_i(\overline{Rn}) \end{aligned} \quad (20b)$$

We again assume that the hydrodynamic inflow angle $\bar{\beta}_i$ and the lift coefficient \bar{c}_l do not change with the Reynolds number, hence the coefficient B and the lift coefficient stay constant for a fixed J -value. This assumption will certainly hold true as long as no flow separation occurs.

With these assumptions made we develop the above equation (20b) for \bar{c}_l into a Taylor expansion series with respect to the Reynolds number \overline{Rn} :

$$\begin{aligned} B^2 \bar{c}_l = \left(K_Q + \Delta \overline{Rn} \frac{dK_Q}{d\overline{Rn}} \right) \frac{\sin \bar{\beta}_i}{\kappa_Q} \\ + \left(K_T + \Delta \overline{Rn} \frac{dK_T}{d\overline{Rn}} \right) \frac{\cos \bar{\beta}_i}{\kappa_T} \\ + \sigma(\Delta \overline{Rn}^2) \end{aligned} \quad (21a)$$

We subtract equation (20b)

$$0 = \Delta \overline{Rn} \frac{dK_Q}{d\overline{Rn}} \frac{\sin \bar{\beta}_i}{\kappa_Q} + \Delta \overline{Rn} \frac{dK_T}{d\overline{Rn}} \frac{\cos \bar{\beta}_i}{\kappa_T} + \sigma(\Delta \overline{Rn}^2) \quad (21b)$$

divide by $\Delta \overline{Rn}$

$$0 = \frac{dK_Q}{d\overline{Rn}} \frac{\sin \bar{\beta}_i}{\kappa_Q} + \frac{dK_T}{d\overline{Rn}} \frac{\cos \bar{\beta}_i}{\kappa_T} + \sigma(\Delta \overline{Rn}) \quad (21c)$$

apply the limiting process $\Delta \overline{Rn} \rightarrow 0$

$$0 = \frac{dK_Q}{d\overline{Rn}} \frac{\sin \bar{\beta}_i}{\kappa_Q} + \frac{dK_T}{d\overline{Rn}} \frac{\cos \bar{\beta}_i}{\kappa_T} \quad (21d)$$

and multiply by $d\overline{Rn}$

$$0 = dK_Q \frac{\sin \bar{\beta}_i}{\kappa_Q} + dK_T \frac{\cos \bar{\beta}_i}{\kappa_T} \quad (21d)$$

Now we can isolate the hydrodynamic inflow angle $\bar{\beta}_i$:

$$\tan \bar{\beta}_i = -\frac{\kappa_Q}{\kappa_T} \frac{dK_T}{dK_Q} = -\kappa \frac{dK_T}{dK_Q} \quad (22a)$$

or when using thrust and torque figures:

$$\tan \bar{\beta}_i = -\kappa \frac{DdT}{dQ} \quad (22b)$$

These equations determine the hydrodynamic inflow angle $\bar{\beta}_i$ over the whole range of the advance coefficient J just from the slope of the $K_T(K_Q)$ -curve. This relationship is strictly speaking only valid if the thrust and torque were measured at a constant Reynolds number (see appendix "A.2 Open-water Tests at Constant Reynolds number" how this can be achieved). Now the equation (22a) can be rewritten as

$$\tan \bar{\beta}_i = -\kappa \frac{\frac{\partial K_T}{\partial J}}{\frac{\partial K_Q}{\partial J}} \quad (23)$$

which facilitates the calculation, if the K_T and K_Q curves are given in their polynomial form.

The drag and lift coefficients can now be calculated from equations (17a+b). They do not depend on the location \bar{x} of the equivalent profile, neither does the hydrodynamic inflow angle $\bar{\beta}_i$.

4 FULL SCALE EXTRAPOLATION

Any of the three analysis presented above yields the values of the lift and drag coefficients \bar{c}_l and \bar{c}_d and the hydrodynamic inflow angle $\bar{\beta}_i$ for a particular open-water test (set of equations: [(17), (12), (16)], [(18b), (18a), (20b)], [(18b), (18a), (22a or b) (23)]). These values can be scaled separately using the theory of aerofoil sections and the corresponding experimental results.

4.1 Scaling the Lift Coefficient \bar{c}_l

Using results from the profile theory, it can be assumed that the lift coefficient \bar{c}_l remains constant when the Reynolds number changes.

Sometimes it is claimed that this assumption does not generally hold for all cases. There is no reason why the lift coefficient cannot be scaled with any appropriate method already existing or becoming available in the future.

4.2 Scaling the Hydrodynamic Inflow Angle $\bar{\beta}_i$

If the lift coefficient and hence the lift do not change, the induced velocities will not change either. That is equivalent to the statement that the hydrodynamic inflow angle $\bar{\beta}_i$ does not change with changes in the Reynolds number. If the lift coefficient \bar{c}_l were to be scaled, it is to be assumed that the influence on $\bar{\beta}_i$ is negligibly small and hence can be neglected.

That leaves us with the drag coefficient \bar{c}_d to be scaled.

4.3 Scaling the Drag Coefficient \bar{c}_d

The drag coefficient of a section can be split into a contribution of the friction \bar{c}_f and the section form drag $\bar{c}_{d,2d}$ (ITTC 1999)(Kuiper 1992)(Abbott & von Doenhoff 1959):

$$\bar{c}_d = 2\bar{c}_f \cdot \bar{c}_{d,2d} \quad (24)$$

Analysing the data available to the author using the empirical formulae for the section form drag (Abbott & von Doenhoff (1959) give the form drag as stated here,

but often the last term $60(\bar{t}/\bar{c})^4$ is not taken into account, because its contribution is very small (ITTC 1999)(Kuiper1992)

$$\bar{c}_{d,2d} = 1 + 2\frac{\bar{t}}{\bar{c}} + 60\left(\frac{\bar{t}}{\bar{c}}\right)^4 \quad (25)$$

and the ITTC 78 friction line (ITTC 1999)

$$\bar{c}_f = \frac{0.04}{\text{Rn}^{1/6}} - \frac{5}{\text{Rn}^{2/3}} \quad (25)$$

shows that the drag coefficients calculated with equations (17b) and (24) differ substantially. Kuiper (1992) mentions in his book that van Oossanens introduces a drag coefficient $\bar{c}_{d,3d}$ to account for "three-dimensional effects", which is added to the profile drag:

$$\bar{c}_d = 2\bar{c}_f \cdot \bar{c}_{d,2d} + \bar{c}_{d,3d} \quad (27)$$

According to these authors this three-dimensional added drag coefficient $\bar{c}_{d,3d}$ does not change with the Reynolds number.

In the author's opinion a proportional factor $\Pi_{\bar{c}_{d,3d}}$ is more suitable and would fit into the concept of the (two-dimensional) section form drag $\bar{c}_{d,2d}$:

$$\bar{c}_d = 2\bar{c}_f \cdot \bar{c}_{d,2d} \cdot \Pi_{\bar{c}_{d,3d}} \quad (28)$$

If no flow separation occurs, the section form drag $\bar{c}_{d,2d}$ only depends on geometrical features but neither on the Reynolds number nor on the advance coefficient, hence it is constant. The factor $\Pi_{\bar{c}_{d,3d}}$ accounts for the three-dimensional effects of the flow around the propeller and hence depends only on the advance coefficient. (Strictly speaking there will be an influence of the Reynolds number as well, since the thickness of the boundary layer changes and hence the three-dimensional flow around the propeller. For the moment we deliberately disregard this small effect.) The friction drag coefficient \bar{c}_f depends strongly on the Reynolds number:

$$\bar{c}_d(J, \text{Rn}) = 2\bar{c}_f(\text{Rn}) \cdot \bar{c}_{d,2d} \cdot \Pi_{\bar{c}_{d,3d}}(J) \quad (28)$$

If the friction coefficient \bar{c}_f were known, the three-dimensional drag $\bar{c}_{d,3d}$ can be calculated from the model test. Finally the drag coefficient \bar{c}_d for any scale can be reassembled with the friction coefficient \bar{c}_f for the selected Reynolds number, e.g. full scale propeller or self-propulsion test.

4.4 Scaling the Friction Drag Coefficient \bar{c}_f

The scaling of the friction drag with the Reynolds number is a matter of ongoing discussion. In the scope of this paper only some observations or suggestions should be made.

The difficulty of scaling propellers stems from the fact that the Reynolds numbers reached during open-water tests falls into the transitional region where the flow over the blades is not fully turbulent yet.

The traditional way to scale the friction drag coefficient \bar{c}_f is to use friction lines derived from experiments. One line which is universally used in the field of naval

architecture is the ITTC 1978 friction line (ITTC 1999). The note made in section 2.2 should always be kept in mind.

Another friction line often used in fluid dynamics is the Schlichting line (Schlichting & Gersten (2006)):

$$c_f = \frac{0.031}{\text{Rn}^{\frac{1}{7}}} - \frac{\gamma}{\text{Rn}} \quad (29)$$

where the value of the factor γ depends on the local Reynolds number where the transition from laminar to turbulent flow occurs.

These friction lines are applied to the equivalent profile.

A second approach is shown by Streckwall et al (2013). They integrate the local laminar and turbulent friction coefficients $c_{f,x,lam}$ and $c_{f,x,turb}$ along the section using two different formulations for the laminar and turbulent region (Hoerner 1965). The transition point is calculated by CFD methods.

$$c_{f,x,lam} = \frac{0.664}{\text{Rn}_x^{0.5}} \quad (30a)$$

$$c_{f,x,turb} = \frac{0.0592}{\text{Rn}_x^{0.2}} \quad (30b)$$

where Rn_x is the Reynolds number with respect to the distance from the leading edge of the profile.

Some suggestions to improve the calculation of the friction drag are:

- Using two open-water tests at different Reynolds numbers would result in two drag coefficients for the same J -value. If the friction line used has a second parameter beside the Reynolds number (like the Schlichting friction line), evaluating equation (28) for both Reynolds numbers results in two equations for the unknowns $\Pi_{d,3d}$ and this parameter, which can be readily solved.
- Instead of evaluating the friction line just for the equivalent profile, the friction drag can be integrated over the propeller blade as done by Streckwall et al (2013).
- If the location of the transition from laminar to turbulent flow were known, the local friction drag (30a+b) can be integrated over the blade using the actual transition point. This transition point could be established during the open-water test with a paint test. This approach would honour the actual section shapes.
- The friction drag can be calculated by solving the boundary layer equations for the actual section used with the help of computer programs such as XFOIL (Drela 2013) or JavaFoil (Hepperle 2006). This can be done for the equivalent section or – preferably – for each section with the subsequent integration over the blade.
- Since the laminar drag is well known, the propeller could be tested strictly with laminar flow over it. This removes the uncertainty of the transitional region. If

the flow remains attached over the whole bladed needs to be established.

5 EXEMPLARY RESULTS

A NPT propeller designed by Stone Marine Propulsion and a conventional propeller of the Wageningen B type were tested at three different Reynolds numbers at the model basin of SSPA in Gothenburg (Table 1 and Figures 1 and 6). All six open-water curves were scaled according to the ITTC 1978 (Figures 2 and 7), the Lerbs-Meyne (Figures 3 and 8), the strip method (Figures 4 and 9) and the proposed new method, option 3 (Figures 5 and 10). The new method uses the ITTC friction line to calculate \bar{c}_f .

Table 1 Main particulars of the propellers analysed

	Conventional	NPT	
D	7.3	6.8	m
P/D	0.673	0.902	–
$c_{0.7}$	1.9563	1.799	m
A_e/A_0	0.53	0.460	–
Z	4	4	–
λ	33.1818	27.143	–
Type	Wageningen B	New profile technology	

It is noticeable that the lowest Reynolds numbers of $2.5 \cdot 10^5$ and $3.5 \cdot 10^5$ is too low for all methods. The first three methods work reasonably well for the conventional propeller, whereas the scaled values for the NPT propeller shows a noticeable gap between the extrapolated efficiencies.

Applying the new method to the conventional propeller moves the efficiency curves scaled from the two higher Reynolds numbers on top of each other. For the NPT propeller the difference between these efficiency curves decreases noticeably.

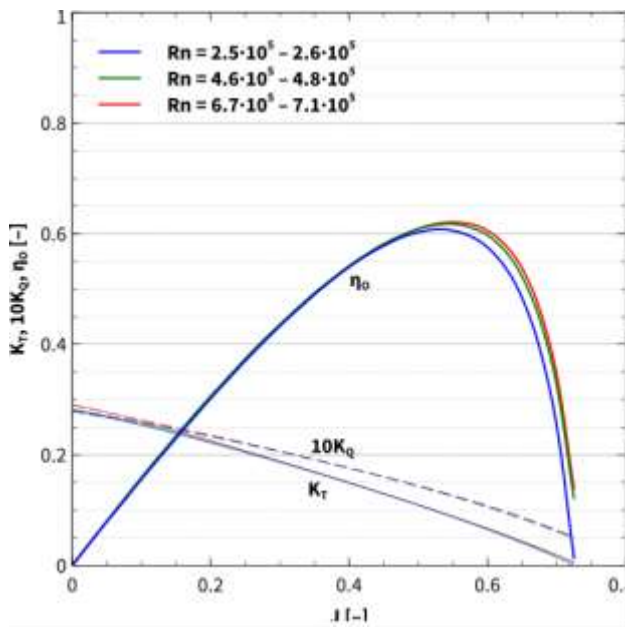


Figure 1 Open-water characteristics of the conventional propeller, measured values

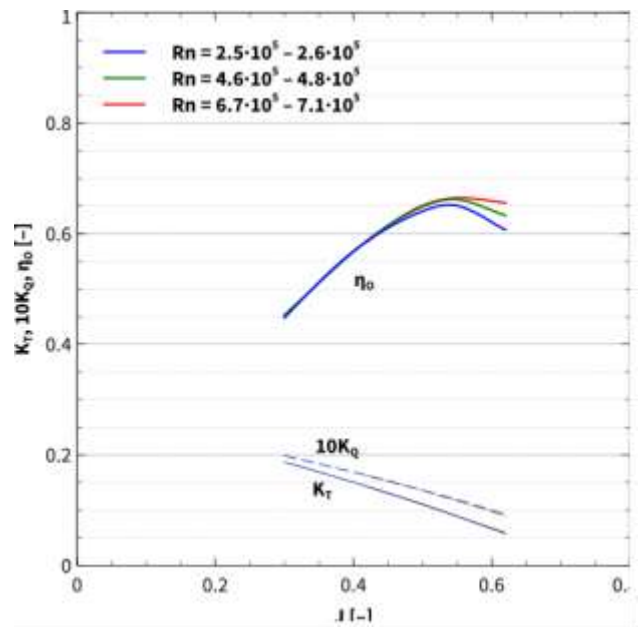


Figure 3 Open-water characteristics of the conventional propeller, scaled with the Lerbs-Meyne method. (Courtesy of H. Streckwall.)

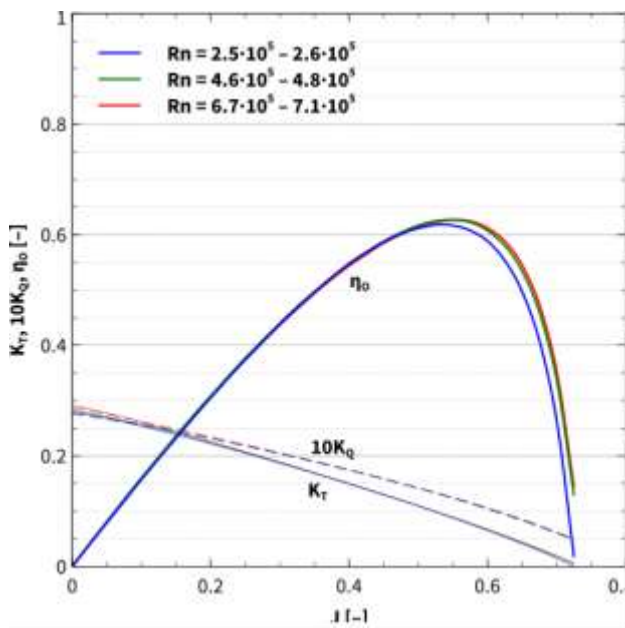


Figure 2 Open-water characteristics of the conventional propeller, scaled according to the ITTC 1978 method

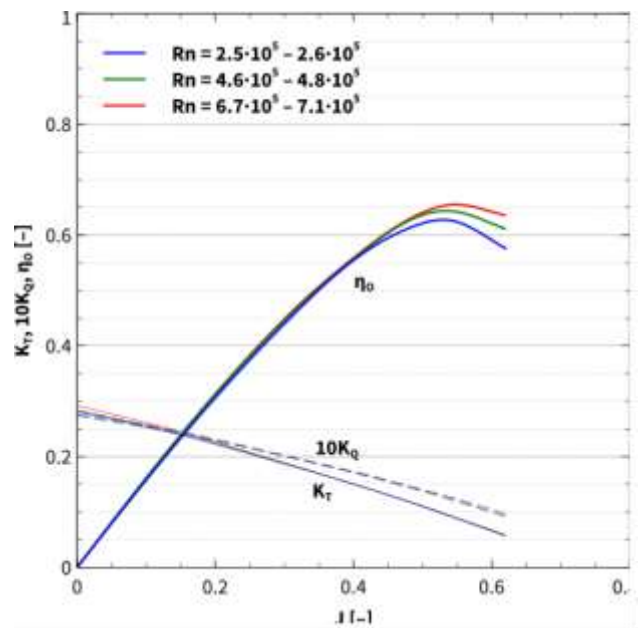


Figure 4 Open-water characteristics of the conventional propeller, scaled with the strip method. (Courtesy of H. Streckwall.)

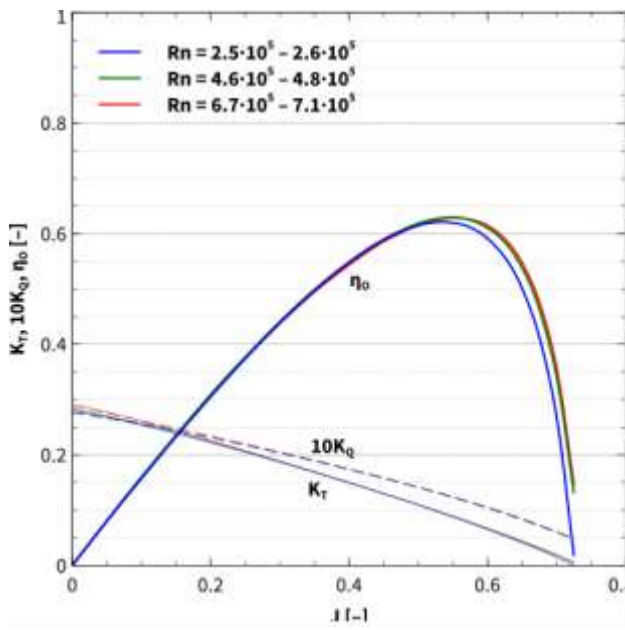


Figure 5 Open-water characteristics of the conventional propeller, scaled with the new method, option 3

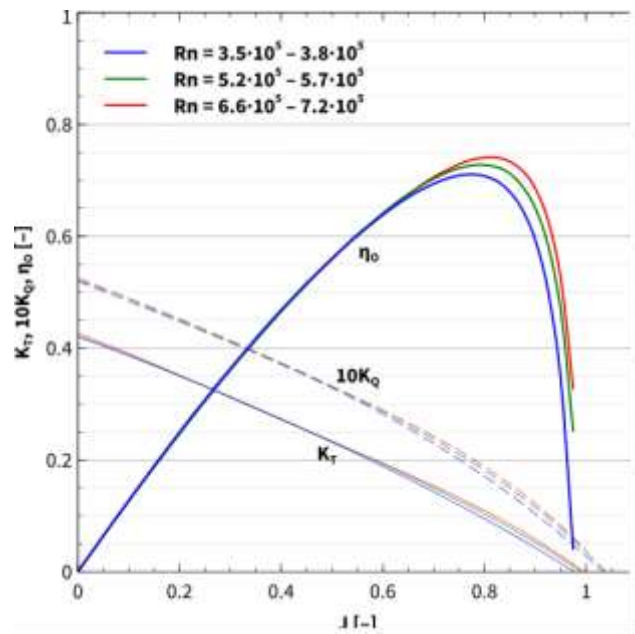


Figure 7 Open-water characteristics of the NPT propeller, scaled according to the ITTC 1978 method

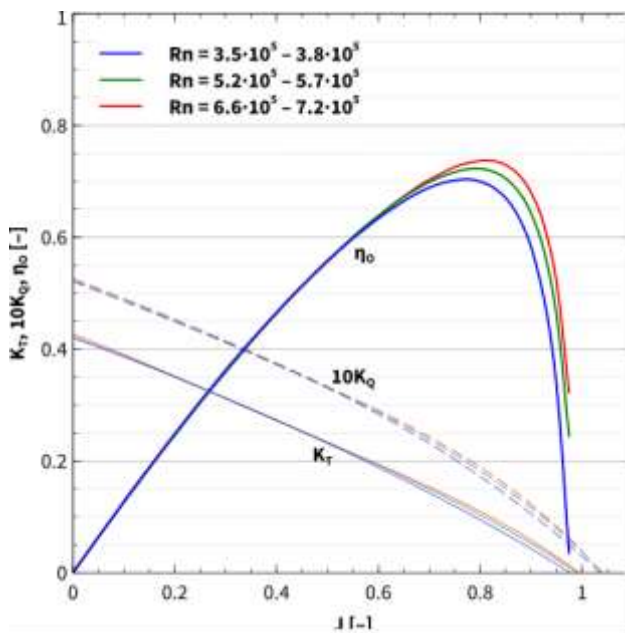


Figure 6 Open-water characteristics of the NPT propeller, measured values.

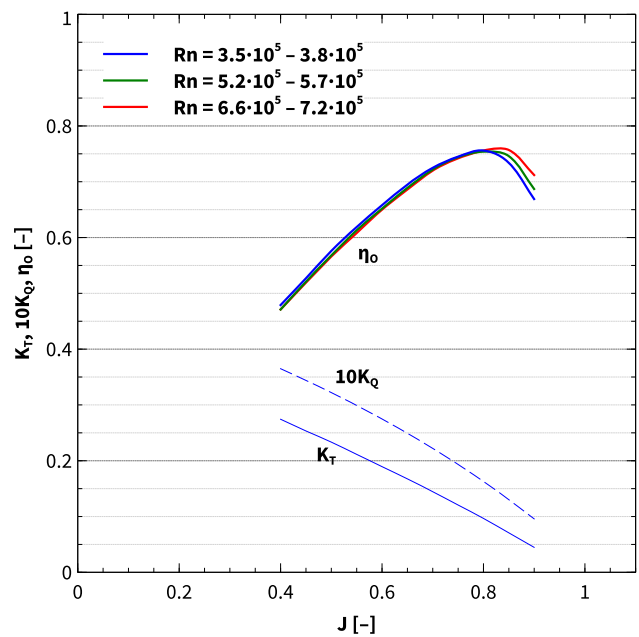


Figure 8 Open-water characteristics of the NPT propeller, scaled with the Lerbs-Meyne method. (Courtesy of H. Streckwall.)

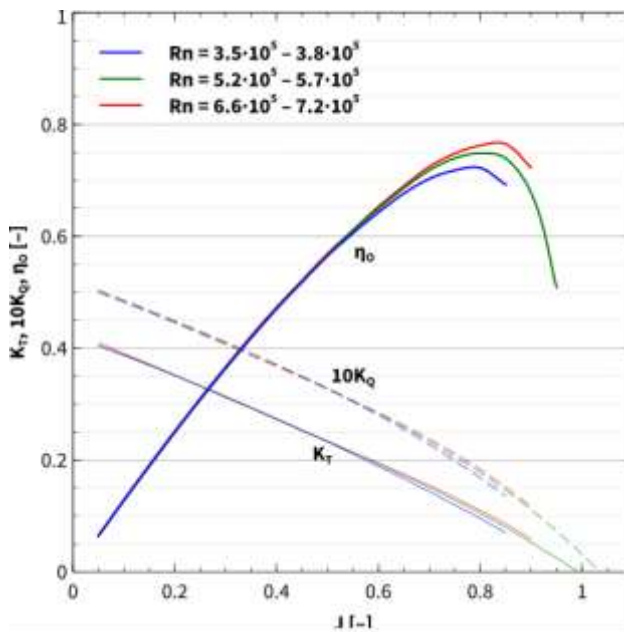


Figure 9 Open-water characteristics of the NPT propeller, scaled with the strip method. (Courtesy of H. Streckwall.)

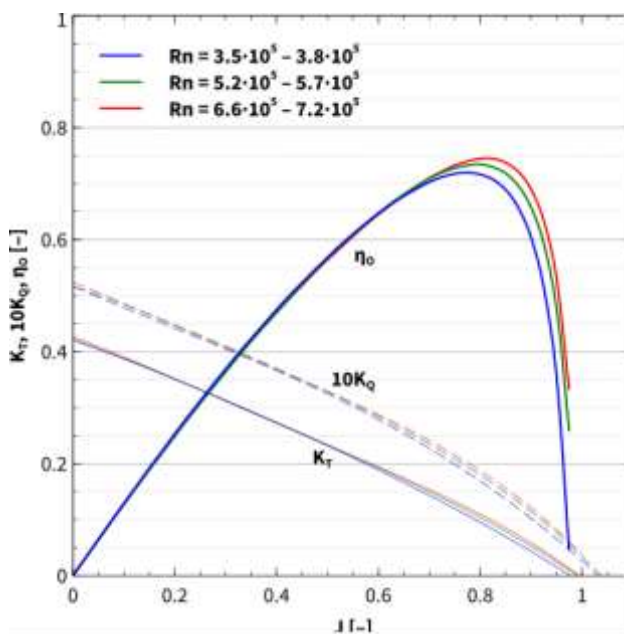


Figure 10 Open-water characteristics of the NPT propeller, scaled with the new method, option 3

6 CONCLUSIONS

A new method to extrapolate open-water performance data was presented. It makes use of the concept of the equivalent profile. It is entirely independent of the propeller geometry or the blade loading and works for all propellers which do not experience flow separation. By calculating the hydrodynamic inflow angle from just one set of open-water curves, it is able to align the drag and friction forces to the actual inflow as the theory of wings suggests.

This new method has the potential to replace the existing methods as shown in the exemplary results.

This new method should be applied to as many performance predictions as possible and compared with the trials data to validate its suitability. This can only be done by a model basin which has the extensive data base to make this comparison reliable.

It was also shown that the ITTC 1978 recommendation for a minimum Reynolds number of $2 \cdot 10^5$ might be too low and it should be considered to be raised.

REFERENCES

- Abbott, I. H. & von Doenhoff, A. E. (1959). 'Theory of Wing Sections'. Dover Publications, Inc., New York, USA.
- Drela, M (2013). 'XFOIL. Subsonic Airfoil Development System'. <http://web.mit.edu/drela/Public/web/xfoil/>.
- Hepperle, M (2006). 'JavaFoil – Analysis of Airfoils'. <http://www.mh-aerotoools.de/airfoils/javafoil.htm>.
- Hoerner, S (1965). 'Fluid Dynamic Drag: Practical Information on Aerodynamic Drag and Hydrodynamic Resistance'. Hoerner Fluid Dynamics.
- ITTC (1999). '1978 ITTC Performance Prediction Method'. ITTC – Recommended Procedures and Guidelines, 7.5 – 02 – 03 – 01.4.
- Kramer, K. N. (1939). 'The Induced Efficiency of Optimum Propellers Having a Finite Number of Blades', NACA TM 884.
- Kuiper, G. (1992). 'The Wageningen Propeller Series'. MARIN Publication 92-001, Wageningen, The Netherlands.
- Meyne, K. (1968). 'Experimentelle und theoretische Betrachtungen zum Maßstabseffekt bei Modellpropeller-Untersuchungen'. Schiffstechnik, Vol 15.
- Schlichting, H. & Gersten, K (2006). 'Grenzschicht-Theorie'. Springer, Berlin, Heidelberg, New York.
- Streckwall, H., Greitsch, L., Müller, J., Scharf, M. & Bugalski, T. (2013). 'Development of a Strip Method Proposed to Serve as a New Standard for Propeller Performance Scaling', Ship Technology Research **60**, No. 2, p. 58-60.

APPENDIX

A.1 Alternative Formulation of the Equivalent Profile

In section "3.1 Equivalent Profile" the blade was replaced by a single profile where all variables depending on the fractional radius x were considered constant. Alternatively only unknown values could be replaced by their constant counterpart from the equivalent profile.

It can be noticed that the difference $\beta_i - \beta$ is small, hence $\cos(\beta_i - \beta)$ is approximately 1. The equations (1a+b) become

$$K_T = \frac{\pi^2 Z}{4} \int_{x_h}^1 \frac{c_l(x) \cos \beta_i(x) - c_d(x) \sin \beta_i(x) c(x)}{\cos^2 \beta(x)} \frac{c(x)}{D} x^2 dx \quad (\text{A1a})$$

$$K_Q = \frac{\pi^2 Z}{8} \int_{x_h}^1 \frac{c_l(x) \sin \beta_i(x) + c_d(x) \cos \beta_i(x) c(x)}{\cos^2 \beta(x)} \frac{c(x)}{D} x^3 dx \quad (\text{A1a})$$

Here the lift and drag coefficients c_l and c_d and the hydrodynamic inflow angle β_i are unknown and will be replaced by the values of the equivalent profile such that the K_T and K_Q values do not change. Now these values can be written outside the integral:

$$K_T = \frac{\pi^2 Z}{4} (\bar{c}_l \cos \bar{\beta}_i - \bar{c}_d \sin \bar{\beta}_i) \int_{x_h}^1 \frac{1}{\cos^2 \beta(x)} \frac{c(x)}{D} x^2 dx \quad (\text{A2a})$$

$$K_Q = \frac{\pi^2 Z}{8} (\bar{c}_l \sin \bar{\beta}_i + \bar{c}_d \cos \bar{\beta}_i) \int_{x_h}^1 \frac{1}{\cos^2 \beta(x)} \frac{c(x)}{D} x^3 dx \quad (\text{A2b})$$

Introducing abbreviations as before:

$$K_T = \gamma_T (\bar{c}_l \cos \bar{\beta}_i - \bar{c}_d \sin \bar{\beta}_i) \quad (\text{A3a})$$

$$K_Q = \gamma_Q (\bar{c}_l \sin \bar{\beta}_i + \bar{c}_d \cos \bar{\beta}_i) \quad (\text{A3b})$$

with

$$\gamma_T = \frac{\pi^2 Z}{4} \int_{x_h}^1 \frac{1}{\cos^2 \beta(x)} \frac{c(x)}{D} x^2 dx \quad (\text{A4a})$$

$$\gamma_Q = \frac{\pi^2 Z}{8} \int_{x_h}^1 \frac{1}{\cos^2 \beta(x)} \frac{c(x)}{D} x^3 dx \quad (\text{A4b})$$

$$\gamma = \frac{\gamma_Q}{\gamma_T} = \frac{1 \int_{x_h}^1 \frac{1}{\cos^2 \beta(x)} \frac{c(x)}{D} x^3 dx}{2 \int_{x_h}^1 \frac{1}{\cos^2 \beta(x)} \frac{c(x)}{D} x^2 dx} \quad (\text{A4c})$$

All equations developed for the equivalent profile can be used by replacing $\kappa_T B^2$, $\kappa_Q B^2$ and κ with γ_T , γ_Q and γ , respectively.

A.2 Open-Water Tests at Constant Reynolds Number

Traditionally the model basins keep the propeller revolutions constant and change the carriage speed when conducting open-water tests. This results in a range of Reynolds numbers. It would be perfectly feasible to reduce the shaft revolutions whenever the carriage speed increases to keep the Reynolds number constant.

For any given change ΔJ of the advance coefficient J , the changes Δn and Δv_0 in propeller revolutions and carriage speed, respectively, are:

$$n + \Delta n = n \frac{\sqrt{J^2 + (\pi \bar{x})^2}}{\sqrt{(J + \Delta J)^2 + (\pi \bar{x})^2}} \quad (\text{A5a})$$

$$v_0 + \Delta v_0 = v_0 \frac{\sqrt{1 + \left(\frac{\pi \bar{x}}{J}\right)^2}}{\sqrt{1 + \left(\frac{\pi \bar{x}}{J + \Delta J}\right)^2}} \quad (\text{A5b})$$

Experimental Determination of the Difference in Visual and Acoustic Cavitation Inception

Christian Johannsen^{1*}, Oliver Zarbock², Herbert Bretschneider¹

¹Hamburg Ship Model Basin (HSVA), D-22305 Hamburg, Germany

²Andritz Hydro GmbH, D-88212 Ravensburg, Germany

Abstract: For navy ships, research or passenger vessels as well as high comfort class mega yachts the noise generating effect of propeller cavitation can be a problem. The ship speed up to which the propeller operates free of cavitation is a quality feature here. Cavitation inception tests with complete ship models carried out in large testing facilities are a standard to predict cavitation inception for those ships. Purely visual cavitation investigations, however, suffer from the fact that cavitation might be hearable already before it can be detected by eye. On the other hand, scaling effects involved in vortex cavitation inception can spoil the result of a purely acoustic inception test at model scale. To overcome these problems, Andritz Hydro and the HSVA performed an experimental study to determine the gap between acoustic and visual tip vortex cavitation inception for a full scale propeller blade tip of 1.8 m characteristic chord length in HSVA's HYKAT tunnel. In a large range of Reynolds numbers up to almost full scale values and at different angles of attack acoustic and visual cavitation inception points were determined separately. As a result it can be stated that the difference between visual and acoustic propeller cavitation inception speed is much smaller than two knots as commonly assumed.

Keywords: Tip vortex cavitation, acoustic cavitation inception, visual cavitation inception, scale effects.

1 INTRODUCTION

Besides erosion damages in the material of ship propellers as well as vibrations excited in the structure of ships, propeller cavitation can have a third disadvantageous effect: Cavitation makes noise. For navy propellers, but not only for navy propellers, the ship speed up to which the propeller operates free of cavitation is therefore an important quality feature.



Figure 1 Test section of HSVA's HYKAT

It is well known that cavitation on a ship propeller can be acoustically detected at significantly other ship speeds than those, where the cavitation becomes visible. This is a nasty phenomenon because cavitation inception predictions – as they are a standard investigation before a navy propeller is built in full scale – are normally based on model tests, where cavitation inception is determined visually. The detectability of a navy vessel due to

propeller cavitation noise, or the acoustic annoyance of the sensitive owner of a luxurious mega yacht usually start earlier than would be derived simply from such a visual cavitation inception test.

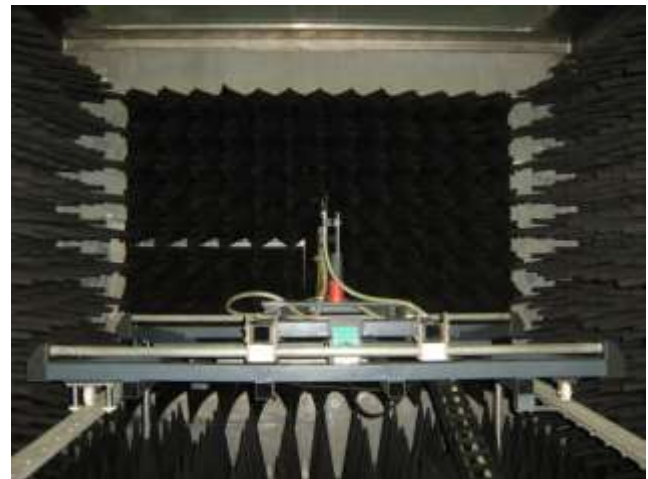


Figure 2 Anechoic measuring chamber of HYKAT

2 STATE-OF-THE-ART CAVITATION INCEPTION EXPERIMENTS

State-of-the art cavitation testing facilities, such as HSVA's Hydrodynamics and Cavitation Tunnel (HYKAT) allow precise determination of visual and acoustic cavitation inception at model scale with the propeller acting behind the complete ship model. The huge test section dimensions of such a tunnel allow installation of the whole ship model (Figure 1), which ensures that the model propeller operates in the realistic,

three-dimensional wake field generated by the model itself. No insufficient wake simulation by wire screens or dummies is required. The extremely low background noise level of this tunnel allows detection of the very first propeller cavitation noise – sometimes even before one can see it. Therefore the tunnel is equipped with an anechoic hydro-acoustic measuring chamber below the test section, where sensitive hydrophones are placed, as shown in Figure 2 (Friesch 1991).

Observation of all kinds of developed cavitation and prediction of sheet cavitation inception are straight forward in such a facility and are based on the common assumption of cavitation number identity between model and full scale. Those tests in HYKAT give reliable full scale predictions as can be seen exemplarily in Figure 3 for the cavitation behavior of a Frigate at maximum speed (Johannsen 2006).

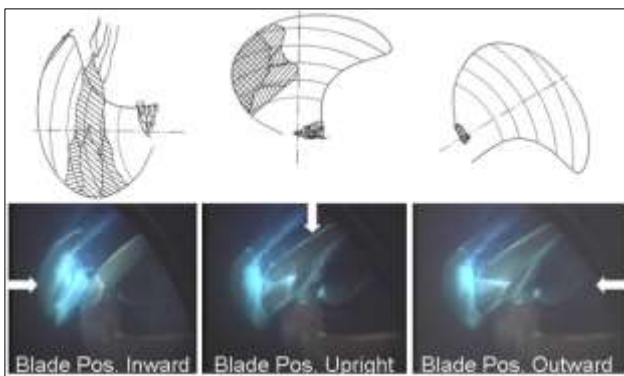


Figure 3 Model - full scale correlation for a frigate

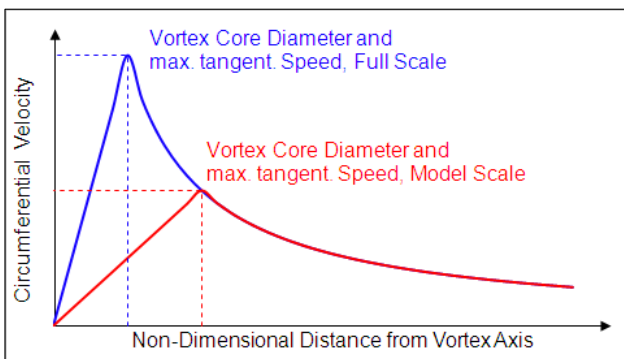


Figure 4 Rankine vortex model

With respect to vortex cavitation inception behind the hub of the propeller or at its tip, one has to deal with the fact that this kind of cavitation is considerably delayed at model scale due to the much smaller Reynolds number. The – relatively speaking – too high viscosity at model scale causes a larger vortex core and consequently a lower rotational speed close to the vortex axis, followed by higher pressure there (Figure 4).

This cavitation inception delay is well-known at least since McCormick's semi-empirical investigations performed on delta wings (McCormick 1962), which led to the commonly applied McCormick correction of vortex cavitation inception obtained at model Reynolds numbers:

$$\frac{\sigma_{incept, Full Scale}}{\sigma_{incept, Model Scale}} = \left(\frac{Re_{Full Scale}}{Re_{Model Scale}} \right)^m \quad (1)$$

Here is $\sigma_{incept.}$ = cavitation number at the inception point of vortex cavitation; Re = Reynolds number; and m = so-called McCormick exponent. McCormick derived a value of $m \approx 0.35..0.4$ from his investigations. This value, however, has meanwhile been modified by the model basins according to their own correlation studies. HSVA uses a value of $m = 0.3$ as a result of extensive studies undertaken onboard of German frigates (Friesch & Johannsen 1995).

Even if originally meant as a pure viscosity correction, McCormick's formula is nowadays rather used as a general correlation tool that also considers gas content and wake scaling effects.

The consequence of Equation (1) is a considerable scale correction as can be seen in the tip vortex cavitation inception diagram shown exemplarily in Figure 5, where cavitation numbers σ_n are plotted versus thrust coefficients K_T . The intersection points between model and full scale vortex inception curves on one hand and ship operating curve on the other can be several knots of ship speed apart from each other.

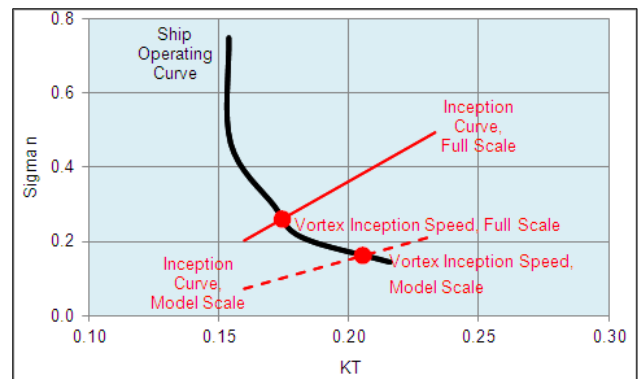


Figure 5 Suction side tip vortex cavitation inception

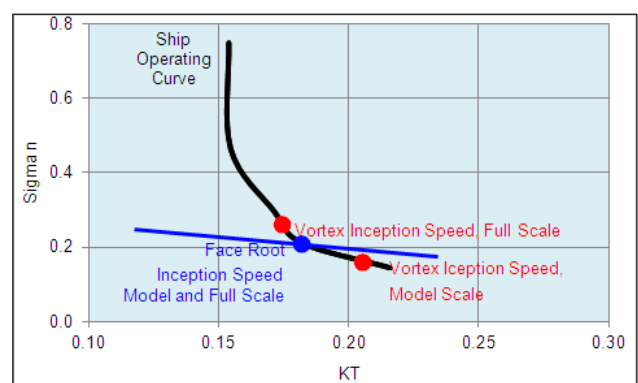


Figure 6 Tip vortex and root cavitation inception

For *visual* cavitation inception this up scaling is not a problem as long as the correlation exponent m is sufficiently approved for the testing facility, as it is the case for HYKAT (Johannsen 2006). Table 1 shows the very good full scale agreement of cavitation inception predictions obtained from visual inception tests in

HYKAT, applying the above scaling procedure with $m=0.3$.

For *acoustic* cavitation inception the up scaling is a problem indeed, as will be explained in the next section.

Table 1 Accuracy of cavitation inception predictions obtained in HYKAT

	$\frac{\text{Predicted Vortex Cav. Inception Speed}}{\text{Full Scale Vortex Cav. Inception Speed}}$
Ship 1, Prop. 1	1.02
Ship 1, Prop. 2	0.98
Ship 2	1.02
Ship 3	0.99

3 THE ACOUSTIC CAVITATION INCEPTION PROBLEM

The problem with model tests for acoustic cavitation inception becomes obvious as soon as we include, e.g., the inception curve for face root cavitation in the inception diagram in Figure 5. The result is shown in Figure 6.

This kind of cavitation is known to follow the "normal" scaling assumption

$$\sigma_{incept,Full\ Scale} = \sigma_{incept,Model\ Scale} \cdot \quad (2)$$

As a result of that, root cavitation starts *earlier* than tip vortex cavitation at model scale (i.e. at higher cavitation number), but *later* in full scale. This behavior is not a "manufactured" outlier but is the normal case for a low noise navy or a high comfort class mega yacht propeller. The same typically happens to suction side sheet cavitation.

When performing a visual cavitation inception test the engineer in front of the test section window can easily concentrate on tip vortex cavitation inception, mentally simply blinding out the already existing root and/or sheet cavitation.

In an acoustic cavitation inception test such a cavitation behavior would be fatal. Weak acoustic tip vortex inception would not be hearable anymore because of the developed noise generated by the root cavitation at the same time already. Subsequent application of Equation (1) to acoustic tip vortex cavitation inception would be impossible, because its inception point σ_{incept} at model scale could not be detected.

So what is the way out? Water speed and model size and consequently the Reynolds number are limited in a cavitation tunnel – even if it is as big as HYKAT.

Increasing the Reynolds number by heating the water as Charles Parsons did in his first cavitation tunnel? Raising the tunnel water temperature to, e.g., 50° C would indeed nearly halve the ratio $Re_{Full\ Scale}/Re_{Model\ Scale}$. Nevertheless, the technical problems involved would be immense.

Using a different liquid with less viscosity? Pentane (C₅H₁₂) would reduce the above Reynolds number ratio to almost one third without any heating. But filling the

HYKAT with 1.5 million liters of highly explosive Pentane is not an option at all. Mercury would work even better, but visibility in a cavitation test in mercury would be rather poor.

4 CAVITATION INCEPTION STUDY WITH A FULL SCALE PROPELLER TIP

To overcome the problem, Andritz Hydro, the home of the well-known "Escher Wyss Propellers" for Navy and Mega-Yacht applications, and the HSVA performed an experimental study to determine the gap between acoustic and visual tip vortex cavitation inception for a full scale propeller blade tip of 1.8 m characteristic chord length in HSVA's HYKAT. The idea behind that was to enable continuation with visual tip vortex cavitation tests at model scale in future, and to deduce the acoustic inception point from these tests by application of the gap between visual and acoustic vortex cavitation inception as found in the present study.

Vague estimates for this gap have been mentioned here and there in the past. Values up to two knots difference are known to the authors, but are based on doubtful comparisons between full scale acoustic measurements on one hand and model test based visual inception predictions on the other.

5 THE TEST SET-UP

The tests were carried out in HYKAT, having test section dimensions of 11 m x 2.8 m x 1.6 m (L x B x H), see Figure 1.

The propeller blade tip and the very rigid device for its angular adjustment were designed and delivered by Andritz Hydro. The blade tip made of brass represented the radial range from 0.8 R to 1.0 R of a roughly 4 meters diameter controllable pitch navy propeller at scale 1, including the anti-singing trailing edge on suction side. The chord length of the tip at 0.8 R was 1.8 m and it penetrated roughly 0.4 m into the test section (Figure 7). The radial pitch of the original tip had been modified to meet in the uniform flow conditions in HYKAT the same angle of attack, as occurs in average over one revolution in behind conditions under the ship. Mechanically, this pitch setting ($\Delta\Phi = 0$) could be varied from $\Delta\Phi = -22^\circ$ to $+22^\circ$ by means of the angular adjustment device in order to change the blade load. During the tests the pitch was varied from -10° to $+10^\circ$, which is much more already than the variation that the propeller tip of a twin screw navy vessel typically experiences in reality due to the inhomogeneity of the wake field as well as due to ship maneuvering. The inflow velocity was varied in HYKAT between 5 m/s and 10 m/s. This is indeed less than the typical circumferential speed of a propeller tip of a navy vessel (somewhat like 25 m/s), but higher speeds were not possible in this testing campaign. The blade tip was mounted on starboard side of the test section while visual observation and documentation was done from portside (Figure 7).

Hydro-acoustic noise measurements were performed by means of a hydrophone (RESON TC 4032) located in the

anechoic chamber below the test section. The noise excited in the test section propagated through the Perspex windows at the bottom into the acoustic chamber equipped with anechoic cladding to minimize sound reflections. The distance from the center of the blade tip to the hydrophone was 2.04 m.



Figure 7 Test set-up in HYKAT

A commercial signal analyzer (ONO SOKKI CF 5210) was used to record the signals, to perform frequency analysis (FFT) and to calculate and store the 1/3 octave bandwidth spectra. The center frequency range amounted from 1.6 to 100 kHz with averaging over roughly 30 seconds.

Supplementary online hydrophone signal control was enabled by an audio amplifier with variable amplification

and appropriate earphones to determine the "subjective" cavitation inception.

The oxygen saturation index (OSI) of the tunnel water – the ratio of dissolved oxygen concentration and the saturation concentration – was continuously measured and recorded by an optical device (VISIWATER DO ARC 120).

6 TEST RESULTS

Inception speeds and noise levels were measured in 67 different combinations of pitch and inflow speed.

At zero pitch setting the blade tip was free of cavitation at any tunnel pressure. At pitch settings $\Delta\Phi$ up to $\pm 5^\circ$ it was still not possible to determine acoustic cavitation inception, because it occurred at tunnel pressures being so low, that increasing flow noise due to air bubble growth predominated the low noise of beginning cavitation. At pitch settings above $\pm 5^\circ$ it was possible to determine visual and acoustic cavitation inception separately.

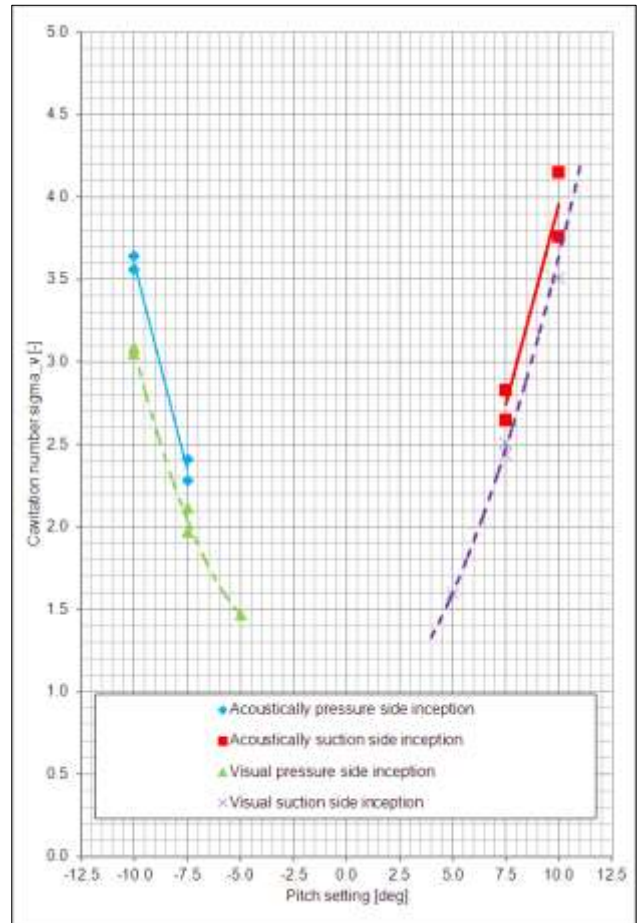


Figure 8 Cavitation inception diagram

Figure 8 shows the results. The cavitation numbers

$$\sigma_V = \frac{P_{incept} - P_{vapor}}{\frac{1}{2} \rho v^2} \quad (3)$$

of desinent tip vortex cavitation are given versus the pitch setting $\Delta\Phi$ of the blade tip. Here is P_{incept} the tunnel pressure at visual and acoustic tip vortex cavitation inception (desinent cavitation) respectively. P_{vapor} and ρ

are the vapor pressure and the density of the tunnel water and V is the inflow speed.

A gap between visual and acoustic cavitation inception can be recognized in Figure 8 indeed, which seems to slightly increase with larger pitch settings. The cavitation numbers for acoustic cavitation inception are higher than those for visual inception. Simply speaking, cavitation could be heard before it could be seen.

The cavitation numbers obtained at cavitation inception were then transformed into ship speeds using the operating data of the vessel that the propeller tip was taken from. It was found, that the $\Delta\sigma_V$ -values between acoustic and visual inception correspond to ship speed differences of $\Delta V \leq 1.5$ knots. This value can be used in future for a conservative estimate of acoustic cavitation inception from a visual cavitation inception test carried out at model scale in a state-of-the-art cavitation tunnel. This overcomes the deficiencies described in Sec. 3 of this paper for a hydro-acoustic cavitation inception test.

This result qualitatively confirms the well-known fact that usually the noise of cavitation is perceptible before (i.e. at a lower ship speed) it can be seen. In numbers, however, the difference is much smaller than usually expected. At small pitch angles, representing propellers acting in quite a homogeneous wake field, acoustic cavitation could not even be provoked at all with this blade tip under laboratory conditions in HYKAT.

For the practice of full scale sea trials on the hydro-acoustic test range this means that a sudden noise increase at ship speeds much lower than visual cavitation inception speed can most probably not be attributed to a malfunction of the propeller with respect to its noise behavior. Other reasons for such a noise increase should be taken into account in such a case. The next paragraph gives examples for that.

7 DETERMINATION OF CAVITATION INCEPTION AT SEA

Whenever an acoustic survey during the sea trials reveals the typical characteristic of cavitation noise, this noise is immediately attributed to the inception of propeller cavitation. This is understandable to some extent, since at the propeller, in particular at its tip, highest velocities are obtained.

In many cases, however, this conclusion could be discovered as premature by subsequent careful investigations. In one case for example, the propeller was blamed for its bad acoustic behavior, while at the end cavitation emanating from an unfavorable fairing of a shaft supporting A-bracket turned out to be the noise source. In another case it was the cavitation noise of a rotary fresh water pump that misled people to blame the propeller.

On the other hand, confusion can also result from the fact that propeller cavitation is hearable and would also be visible indeed, but cannot be detected by eye because of the adverse location of its occurrence. Full scale propeller

cavitation observation is normally performed using windows in the shell above the propeller or by means of a boroscope. It is a matter of fact that not all parts of the propeller can be properly examined this way. Vortex cavitation emanating from the blade overhang at the root of a controllable pitch propeller is an example for such a case.

This section of the paper should not be misunderstood as a guideline how to excuse a badly performing navy propeller. But it is a plea to perform full scale cavitation investigations with much care and with a highly experienced staff.

8 SUMMARY

Visual and acoustic cavitation inception tests have been performed in HYKAT, HSVAs large Hydrodynamics and Cavitation Tunnel with a full scale propeller blade tip at high Reynolds numbers in homogeneous inflow.

The tests revealed that tip vortex cavitation is hearable earlier than visible indeed, but the difference is much less than two knots in ship speed. This finding can be used to estimate acoustic cavitation inception from a visual cavitation inception test carried out at model scale in a state-of-the-art cavitation tunnel.

Whenever cavitation noise can be detected in full scale much earlier than cavitation can be seen at the propeller, other noise sources should therefore be carefully considered before the propeller is blamed.

REFERENCES

- Friesch, J. (1991). 'HYKAT – The New Cavitation Test Facility of Hamburg Ship Model Basin'. Int. Symp. on Hydro- and Aerodynamics in Marine Engineering, Varna, Bulgaria.
- Friesch, J., Johannsen, C. (1995). 'Study on Tip Vortex Cavitation Inception for Navy Propellers'. Int. Symp. on Cavitation, Deauville, France.
- Johannsen, C. (2006). 'Model - Full Scale Correlation of Propeller Cavitation for MEKO® Vessels', MECON 2006, Hamburg, Germany.
- McCormick, B.W. (1962). 'On Cavitation Produced by a Vortex Trailing from a Lifting Surface', Journal of Basic Engineering.

Systematic Cavitation Tunnel Tests of a Propeller in Uniform and Inclined Flow Conditions as Part of a Round Robin Test Campaign

Batuhan Aktas^{1*}, Serkan Turkmen¹, Emin Korkut², Patrick Fitzsimmons¹, Mehmet Atlar¹

¹School of Marine Science and Technology, Newcastle University, Newcastle upon Tyne NE1 7RU, UK

²Istanbul Technical University, Faculty of Naval Architecture and Ocean Engineering, 34469 Maslak-Istanbul, Turkey

Abstract: This paper presents a systematic cavitation tunnel tests with a 214mm diameter model propeller of a catamaran research vessel, which is subjected to uniform and inclined flow conditions, to investigate its efficiency, cavitation and underwater radiated noise characteristics. The experiments were conducted in the Emerson Cavitation Tunnel of Newcastle University based on the starboard side of the 5-blades and right-handed propeller of the University's research vessel, *The Princess Royal*. In the paper the details of the tests and results of the significant findings for the effect of the shaft inclination on the propeller efficiency, cavitation and underwater radiated noise characteristics are discussed. A better understanding is sought in relation to the noise signatures of different types of cavitation. The systematic tests presented in the paper also have a long term objective, which will be achieved in due course, as being the first experiment of an organized round robin test campaign that is being currently undertaken by the 7 members of the Underwater Noise Community of Practice (CoP) of Hydro-Testing Forum (HTF) for which the University of Newcastle is a member. This long term objective is to repeat similar tests in the different facilities of all CoP members to reveal the relative merits of their testing facilities for underwater noise investigations, hence to learn more from their practices and experiences.

Keywords: Cavitation, underwater radiated noise, inclined shaft effect, systematic propeller tests, round robin noise tests

1 INTRODUCTION

The ambient noise levels of the world seas have been increasing. Amongst various sources contributing to this trend the low frequency contributions due to increasing shipping noise have been a recent concern since the low frequency range of the underwater noise spectrum is also used by marine mammals for their communications (IMO, 2011; MEPC, 2010). This fact has been expected to harm the survivability of marine mammals in the long term (Hildebrand, 2005).

As far as shipping noise is concerned, there are various sources on board of a ship. Amongst these sources propeller cavitation is considered to be the dominating one in contributing to the overall radiated noise spectrum above the cavitation inception threshold. This overshadows the other sources and dominates the overall spectrum resulting in a significant rise in the sound levels over the noise spectrum (Abrahamsen, 2012; Arveson & Vendittis, 2000).

Some recent noise measurement campaigns have used opportunistic approaches to compile a full-scale noise database for commercial shipping. This has been achieved by deploying a hydrophone close to a marine traffic way and combining the noise data recorded with data from the ship's Automatic Identification Systems (AIS) (McKenna et al, 2012; MCR, 2011). The results of such campaigns have indicated a difference of 20-40 dB within the same type of commercial vessels indicating that ship noise levels are not readily associated with AIS-type data.

More detailed knowledge is required of the flow environment for which each propeller has been designed such that in the design stage, information can be gained which then can be used to control the propeller performance in terms of unwanted levels of cavitation and noise.

Increasing environmental concerns for potential harm, which may adversely affect the marine biodiversity, have recently targeted propeller cavitation noise from commercial shipping. As a result there has been a concentration of attention in the field of underwater radiated noise and mitigation measures through co-operative research and workshop activities at local, European and international levels. These include organisational bodies such as International Maritime Organisation (IMO) (IMO, 2011), Marine Environmental Protection Committee (MEPC) (MEPC, 2010), European Marine Strategy Framework Directive (MSFD), 27th International Towing Tank Conference (ITTC) (ITTC 2014), Hydro-Testing Alliance Network of Excellence (HTA-NoE) (AMT 2011), Hydro-Testing Forum (HTF) (AMT 2013) etc.

In complementing the above activities Joint Research Programme (JRP)10, which was called "Noise Measurements", was established within the Hydro Testing Alliance Network of Excellence (HTA-NoE) and which successfully completed its mission in 2011 (AMT 2011). The members of JRP10 decided to form a working group to further investigate underwater radiated noise issues.

* Corresponding author e-mail: b.aktas@ncl.ac.uk

This working group, which was initially named “Noise Working Group” (NWG), later became “Noise Community of Practice (Noise CoP)” of Hydro Testing Forum (HTF) as a longer continuation of the HTA-NoE, which was phased out by then (AMT 2013). The first important task of the Noise CoP has been to undertake a round robin test campaign to investigate the cavitation and noise characteristics of the model propeller of Newcastle University (UNEW)’s Deep-V type catamaran research vessel, *The Princess Royal*. The main stimulus for such task was that the Noise CoP members have diverse testing facilities; and *The Princess Royal* and its associated data are easily accessible. Moreover *The Princess Royal* has been providing a focus to be a benchmark vessel through various collaborative research activities e.g. the Cooperative Research Ships (CRS) consortium and the EC-FP7 SONIC project consortium (SONIC, 2012), in which some of the Noise CoP members are also participants, and hence this could provide further complementary exploitation opportunities within the CoP.

The above status and readily available scaled propeller model of *The Princess Royal* made it beneficial to conduct a systematic round robin cavitation test campaign. In order to investigate unsteady flow effects the CoP decided to test the model propeller in uniform but systematically varied inclined shaft (or flow) conditions. This would provide the CoP members with an opportunity to test the same propeller in different facilities and hence to compare its efficiency performance, cavitation and noise characteristics. Furthermore the results of the entire test campaign will enable the members to quantify the basic differences in the measurements and hence to investigate the relative merits of their facilities.

The initial experiments of this round robin model test campaign were conducted in the Emerson Cavitation Tunnel of Newcastle University based on modelling the starboard hull of *The Princess Royal* with its 5-bladed right-handed model propeller. Seven different shaft inclination angles (θ) were systematically varied in uniform flow ranging from $+9^\circ$ to -9° over 3 different cavitation numbers ($\sigma_V = 13.9, 8.1, 4.5$) and 8 different advance coefficients (J) ranging from 0.4 to 0.75 .

This paper presents the details and results of the first test campaign conducted by Newcastle University. Section 2 gives a short literature review of research work on inclined shaft effects on propellers. Section 2 gives a description of the experimental set-up and test conditions. Section 4 presents open water propeller performance results, while Section 5 gives cavitation observations. Section 6 gives noise measurements, Section 7 presents a discussion of results and finally Section 8 gives conclusions.

2 INCLINED SHAFT EFFECT ON PROPELLERS

The inclined shaft (or flow) effect on a propeller is a well-known unsteady flow phenomenon that can occur either

due to structural reasons or motions of the vessels whilst underway. The structural reasons may be imposed by the engine arrangements, ensuring sufficient shaft submergence, or vertical propeller tip clearance with the hull and improving wake flow to the propeller. On the other hand the motions of the vessel can be caused due to the stern wave and hence resulting dynamic trim, pitching and heaving in heavy seas, yawing and drifting of the vessel during manoeuvring. Figure 1 shows a representative sketch to describe some fundamentals of the inclined flow phenomenon.

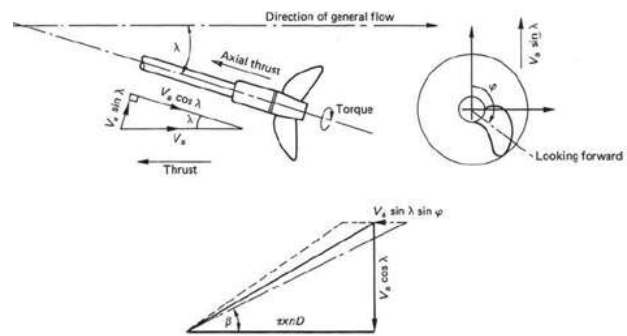


Figure 1 Inclined flow effect (Carlton 2012)

As shown in Figure 1 the effect of inclined flow manifests itself as a cyclic variation of the inflow angle to the propeller. This effect is more severe at the inner radii since the tangential velocity variation there becomes a greater percentage of the shaft rotational vector, compared to the blade tips. The oblique flow increases the angle of attack variation and hence the detrimental effects of inclined flow to the propeller sections will generate different kinds of cavitation phenomena leading to a range of cavitation and radiated noise.

The literature on shaft inclination has generally explored this effect in terms of the cavitation extent and overall performance (thrust, torque) of a marine propeller. The related studies mainly concentrated on the validation of the inclined flow theory proposed by (Gutsche, 1964). The investigations reported in e.g. (Hadler 1966, Kozhukharov & Sadovnikov 1983) are typical examples of these studies. The investigations conducted by (Taniguchi et al. 1969) and Kozhukharov & Sadovnikov (1983) also involved extensive experiments in validating Gutsche’s quasi-steady flow theory.

In his pioneering work Gutsche conducted a combination of theoretical and experimental research work involving six model propellers. The propellers selected were varied in terms of the blade area ratio (BAR), pitch to diameter ratio (P/D) and all had a 200 mm diameter. The simulated shaft inclination angles were chosen as 0° , 20° and 30° . By utilizing the experimental data a quasi-steady flow analysis method was developed. The explanatory English description of Gutsche’s study can be found in (Hadler, 1966). Taniguchi et. al’s experimental investigation was conducted in the Mitsubishi Experimental Tank using 5 super cavitating propellers with different P/D and EAR ratios. The propellers were subjected to relatively smaller

shaft inclination angles of 0° , 4° and 8° (Taniguchi et al. 1969).

Even though one may find further examples of other experimental studies, as reported e.g. in (Carlton, 2012), the study conducted by (Kozhukharov & Sadovnikov, 1983) carries greater importance due to the detailed cavitation sketches included for the conditions tested. The results obtained from the selected systematic series of cavitating screw propellers, that were developed using a lifting surface code, were used for populating the data and a validation study was conducted using the quasi-steady Gutsche method.

Even though the inclined flow effects can cause serious performance problems for a propeller such as: loss of thrust; erosion; intensified cavitation; and thrust and torque fluctuations, a comprehensive experimental investigation on the inclined phenomenon in a systematic manner, so far, has been rather scarce. Underwater radiated noise data is even more scarce. The present assessment of propeller cavitation and noise characteristics at different flow inclinations provides an essential body of such missing data.

3 EXPERIMENTAL SET UP & TEST CONDITIONS

Experiments were carried out in three groups of tests at the Emerson Cavitation Tunnel (ECT) of Newcastle University (UNEW), which has a large test section with a cross-sectional area of 1.22 m by 0.81 m ($B \times H$) as shown in Figure 2. Further details of the tunnel including the recent enhancements are given in Atlar (2011).

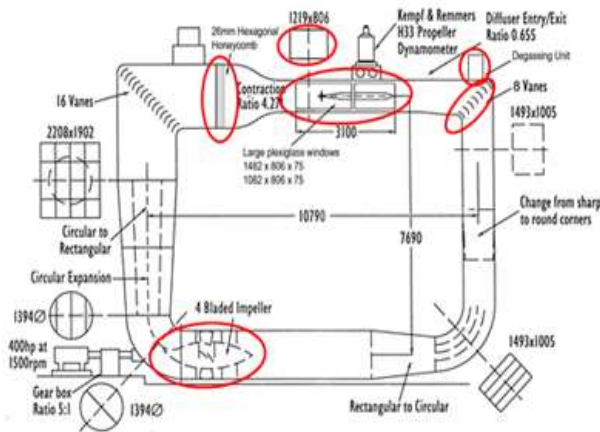


Figure 2 Emerson Cavitation Tunnel and recently improved zones (Atlar, 2011)

The first group of these tests was to obtain the open water efficiency performance of the model propeller in systematically varied shaft inclination angles at 3 different vacuum levels (cavitation numbers) and hence to investigate the effect of the flow inclination and cavitation on the propeller performance. The second group of tests involved cavitation inception measurements with the model propeller under the same inclination and vacuum conditions. The third group of tests comprised the

underwater noise measurements with the model propeller, once again, under the same flow and vacuum conditions. All of the tests were conducted at a 4 m/s tunnel inflow speed recorded at the measuring section and for advance coefficients (J) ranging from 0.4 to 0.75 . Table 1 gives an overall summary of the test conditions. The cavitation number (σ_V) given in Table 1 is defined as follows:

$$\sigma_V = \frac{P_a + \rho g h_s - P_v}{0.5 \rho V^2} \quad (1)$$

Where P_a is the Atmospheric pressure; ρ is the density of water, g is the gravitational acceleration, h_s is the shaft immersion of the propeller, P_v is the vapour pressure, V is the tunnel inflow velocity.

As shown in Table 1 the angle convention for the shaft inclination during the tests was such: a positive angle indicated that the dynamometer shaft was inclined in upward direction with the tip at the 12 o'clock position moving towards the incoming flow whilst a negative angle indicated the opposite (downward) direction. The experimental procedure was repeated for both negative and positive angles in order to account for the tunnel's speed profile at the propeller plane as shown in **Figure 3**.

Table 1 A summary of test conditions

	Test Type		
	Open water performance tests	Cavitation inception tests and observations	Noise measurements
Shaft Incl. Angle ($^\circ$)	0, 3, 6, 9, -3, -6 and -9		
Cavitation Condition	i. Atmospheric condition ($\sigma_V=13.9$)	ii. Medium vacuum condition ($\sigma_V=8.1$)	iii. High vacuum condition corresponding to vessel's fully loaded condition ($\sigma_V=4.5$)
J Range Tested	0.75, 0.70, 0.65, 0.60, 0.55, 0.50, 0.45, 0.40		

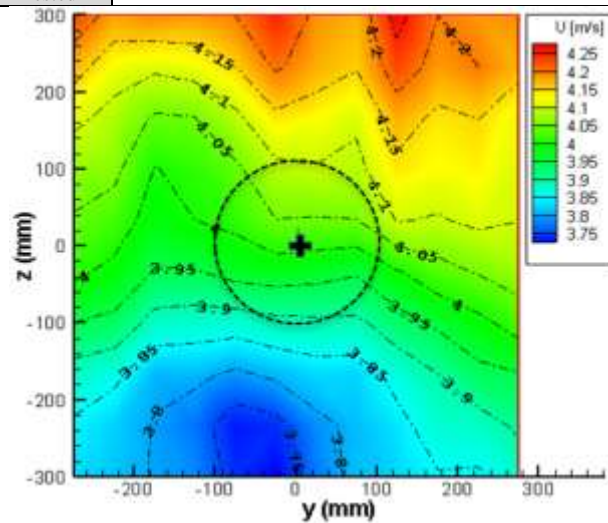


Figure 3 The axial speed profile of the Emerson Cavitation Tunnel for 4m/s inflow velocity measured at the propeller plane where the origin is the shaft centerline

3.1 Propeller Design and Model Propeller

The propeller model used for the cavitation tunnel tests represented the starboard side propeller of *The Princess Royal* with a scale ratio of 3.5 that gives a 214mm model propeller diameter. This model was manufactured with a high accuracy for cavitation testing as shown in Figure 4 alongside the full-scale port side propeller. The principal dimensions of the propeller and the vessel are given in Table 2 and Table 3, respectively, (Atlas et al., 2013). The loading condition in Table 3 corresponds to the light load departure condition of the vessel.

Table 2 Main particulars of the propellers of *The Princess Royal*

Propeller	
Diameter, D	0.75 m
Pitch Ratio at 0.7R, P/D	0.8475
Expanded Blade Area Ratio, A_E/A_0	1.057
Number of Blades, Z	5
Rake angle	0°
Skew angle	19°
Direction of rotation	Right handed
Scale ratio, λ	3.5
Design Advance Coefficient, J	0.5
Material	NiAlBr

Table 3 Main particulars of *The Princess Royal*

Vessel	
Ship type	Catamaran
Length between perpendiculars, L_{PP}	16.45 m
Length on water line, L_{WL}	16.523 m
Breadth, B	7.03 m
Draught at mid-ship, T	1.748 m
Draught at aft perpendicular, T_{AP}	1.763 m
Draught at forward perpendicular, T_{FP}	1.732 m
Block Coefficient, C_B	0.362
Service speed, V_S	15 knots
Material	Aluminium



Figure 4 Views of full-scale (port) and model-scale (starboard) propellers of *The Princess Royal*

4 OPEN WATER PERFORMANCE TESTS

Open water (thrust, torque and hence efficiency) performance tests with the model propeller were carried out according to the ITTC procedures for the open water tests (ITTC, 2011), using a K&R H33 dynamometer and Cussons Type H101-27 shaft height and angle adjustment system of the Emerson Cavitation Tunnel. The tests were performed to cover the whole advance coefficient (J) range of the tunnel and systematic shaft angle combination under the Atmospheric and 2 additional different vacuum conditions as specified in Table 1. The tunnel inflow speed (V) was kept at 4 m/s and the advance coefficients (J) were varied systematically by changing the rotational speed of the propeller (n).

In order to achieve accurate results in the open water tests, the sampling rate for the measurements was 1000 Hz. The tests were repeated 6 times for the level shaft under Atmospheric conditions, and 3 times for the other conditions, as stated in Table 1. The thrust and torque values were then averaged and presented in non-dimensional coefficients: K_T for thrust, K_Q for torque and η_0 for propeller efficiency defined as:

$$J = \frac{V}{nD} \quad K_T = \frac{T}{\rho n^2 D^4} \quad K_Q = \frac{Q}{\rho n^2 D^5} \quad \eta_0 = \frac{J}{2\pi} \frac{K_T}{K_Q} \quad (2)$$

Where T is thrust, ρ is the density of water, Q is the torque and D is the diameter of the propeller.

For the plotted advance coefficients a simple cosine correction was applied to the advance coefficients as $J_{corrected} = J \cos\theta$, where θ is the shaft inclination angle. A typical representation of the open water performance curves for the high vacuum condition, whilst varying the shaft inclination angle, is shown in **Figure 5**. The full representation of the entire open water performance curves can be found in Aktas et al. (2014)

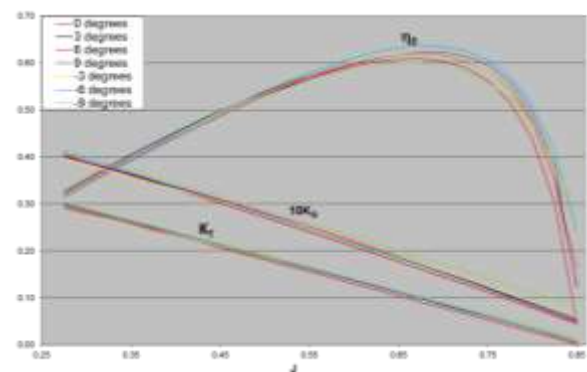


Figure 5 Open water performance of model propeller, for various inclination angles at high vacuum condition

During the tests the propeller Reynolds number (R_e) range varied from 4.03×10^6 to 8.22×10^6 . Here R_e is defined based on the propeller chord length at 0.7R as follows:

$$R_e = \frac{C_{0.7R} \sqrt{V^2 + (0.7\pi n D)^2}}{\nu} \quad (3)$$

Where $c_{0.7R}$ is the chord length at $0.7R$ and ν is being the kinematic viscosity of tunnel water.

5 CAVITATION OBSERVATIONS

The cavitation observation recordings were made during the experiments both for cavitation inception/desinence detection and for well-developed cavitation. Two different configurations for the recordings were used: one using a strobe with a high-speed video camera; and the other using a continuous light source with the high-speed video camera. In the former configuration the cavitation images were captured using the TTL signal from the electric motor driving the shaft to trigger both the strobe and the high-speed video. In the latter a powerful continuous light was used with the high-speed video to obtain a better understanding of the cavitation dynamics. **Figure 6** shows typical frames from the recordings made with Dantec Dynamics Nanosense Mk II high-speed video camera (running at 2000 frames per second) for the cavitation developments at -9° inclination angle under the high vacuum condition for varying advance coefficients. A full set of such images, covering the entire test range, can be found in Aktas et al. (2014)

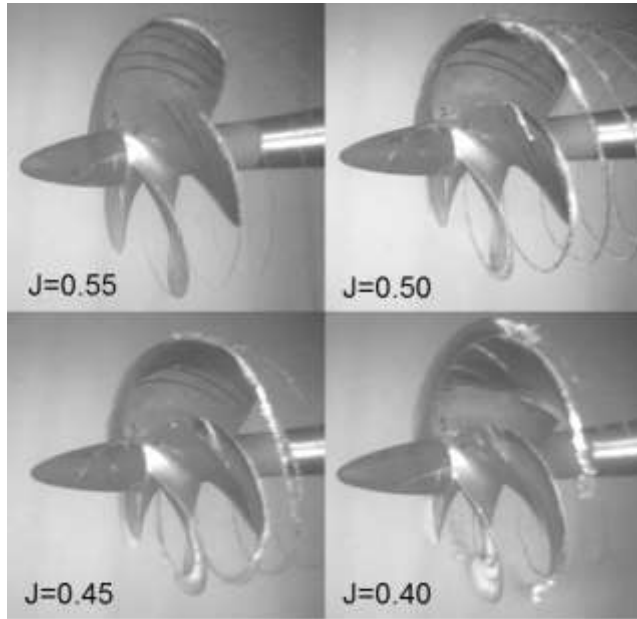


Figure 6 Cavitation developments at -9° inclination angle under high vacuum condition

5.1 Cavitation Inception

Inception and desinence points for respective cavitation events were recorded on video as well as by eye. The procedure for the inception measurements was performed such that the tunnel flow velocity was kept constant at 4 m/s . The tunnel static pressure was also set to a constant value and the rotational speed of the propeller was initially increased until a visual appearance of an unattached cavitating tip vortex cavitation was observed. This was recorded as the inception point of the respective cavitation. The rotational speed was then increased up to the point that the tip vortex attached to the blades and

then was decreased until the vortex disappeared from the tip of the propeller. This was accepted as the desinence point of the cavitation. Typical images of the inception and desinence point are shown in **Figure 7** for the propeller model at 0° inclination angle under the high vacuum condition. The inception/desinence points all the tested conditions are presented in **Table 4**.

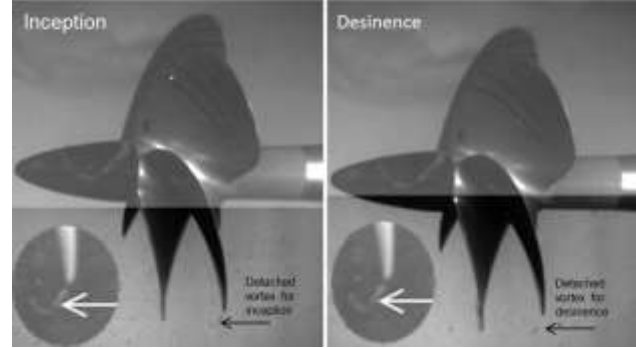


Figure 7 Images of the cavitation inception and desinence points for propeller model at 0° inclination angle under high vacuum condition

Table 4 Cavitation inception and desinence points of propeller model at varying inclination angles and cavitation

Atmospheric condition							
Inclination angle	0°	3°	6°	9°	-3°	-6°	-9°
Cavitation Type	TV	TV	TV	TV	TV	TV	TV
Inception (RPM)	2128	2102	2047	2003	2138	2165	2095
Desinence (RPM)	2188	2126	2076	2093	2165	2186	2110
$J_{\text{Inception}}$	0.527	0.534	0.548	0.56	0.525	0.518	0.535
σ_i	0.758	0.772	0.811	0.845	0.748	0.737	0.782
Medium Vacuum Condition							
Inclination angle	0°	3°	6°	9°	-3°	-6°	-9°
Cavitation Type	TV	TV	TV	TV	TV	TV	TV
Inception (RPM)	2013	1916	1900	1860	2004	2013	1921
Desinence (RPM)	2030	1946	1930	1938	2002	2030	1962
$J_{\text{Inception}}$	0.557	0.585	0.59	0.603	0.56	0.557	0.584
σ_i	0.489	0.537	0.541	0.566	0.492	0.498	0.542
High Vacuum Condition							
Inclination angle	0°	3°	6°	9°	-3°	-6°	-9°
Cavitation Type	TV	TV	TV	TV	TV	TV	TV
Inception (RPM)	1903	1856	1828	1793	1875	1860	1803
Desinence (RPM)	1914	1860	1832	1797	1879	1870	1807
$J_{\text{Inception}}$	0.589	0.604	0.614	0.625	0.598	0.603	0.622
σ_i	0.303	0.316	0.325	0.337	0.31	0.314	0.332

In **Table 4** the inception cavitation number (σ_i) is defined based on the resultant velocity as follows:

$$\sigma_i = \frac{P_{st} - P_v}{0.5\rho V_R^2} \quad (4)$$

Where the resultant velocity (V_R) is defined by

$$V_R = \sqrt{V^2 + (0.7\pi nD)^2} \quad (5)$$

In addition to the RPM values corresponding to the cavitation inception and desinence points, **Table 4** also

includes the corresponding advance coefficients ($J_{inception}$) for these points to be able to relate them to the radiated noise levels. Table 4 illustrates the effect of the varying shaft inclinations on the inception/desinence points

Figure 8 shows trends in the effect of the shaft inclination as the angle was increased in an upward (positive) and a downward (negative) direction from the level shaft condition. Inception occurred earliest at the higher inclination angles. While this effect was not symmetrical with angle at the Atmospheric condition, it became more so with the increasing vacuum in the case of the medium and high level of vacuum conditions.

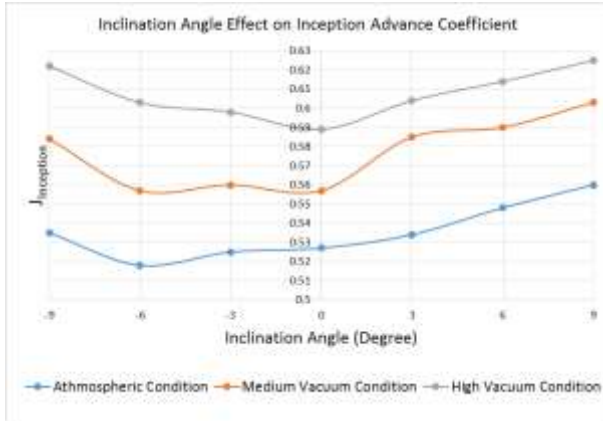


Figure 8 Variation of cavitation inception J number (Advance Coefficient) with respect to inclination angles

6 NOISE MEASUREMENTS

Noise measurements were also carried out at the 7 different shaft inclination angles and 3 different cavitation conditions. The measurements were recorded using a Bruel and Kjaer type 8103 miniature hydrophone mounted in a water filled, thick walled steel cylinder placed on the outside of the tunnel's plexiglas window. This cylinder was glued onto the starboard window level with the center of the propeller boss when the shaft inclination is zero and at a horizontal distance of 0.61 m from the shaft centerline, as shown in Figure 9 (top picture). The hydrophone signals were collected by further Bruel and Kjaer hardware and software; in this case a PC based "PULSE" digital acquisition and analysis software system up to a frequency of 25 kHz, was used.



Figure 9 A view of hydrophone glued on the side window (top photo); An overall view of the dynamometer with inclined shaft arrangement in test section of tunnel (bottom photo)

6.1 Analysis and Presentation of the Noise Results

A common practice in the analysis and presentation of the noise levels is to reduce the measured values of Sound Pressure Levels (SPL) in each 1/3 octave band to an equivalent 1 Hz bandwidth by means of the correction formula recommended by (ITTC 1987) as follows.

$$SPL_1 = SPL_m - 10 \log \Delta f \quad (6)$$

where SPL_1 is the reduced sound pressure level to 1 Hz bandwidth in dB; re 1 μPa , SPL_m is the measured sound pressure level at each centre frequency in dB; re 1 μPa and Δf is the bandwidth for each 1/3 Octave band filter in Hz.

The ITTC also required that the sound pressure levels be corrected to a standard measuring distance of 1 m using the following relationship.

$$SPL = SPL_1 + 20 \log(r) \quad (7)$$

Where SPL is the equivalent 1 Hz at 1 m distance sound pressure level in dB; re 1 μPa and r is the reference distance for which the noise level was measured.

The PULSE settings for 1/3 octave band analysis, are shown in Table 5. The data presentation was preferred in a waterfall format in order to eliminate the influence of any instantaneous disturbance. This was achieved by using the multi-buffer option of the PULSE software and by triggering the system for every 0.25s.

Table 5 Noise Data Acquisition System Settings in PULSE system

Bandwidth	<i>1/3 octave</i>
Lower center frequency	<i>20 Hz</i>
Upper center frequency	<i>20 kHz</i>
Acoustic weighting	<i>as signal</i>
Reference Pressure	<i>1 μPa</i>
Overall bands - weighting	<i>none</i>
Average update overload	<i>accept</i>
Average mode	<i>exponential</i>
Averaging time	<i>1s</i>
Tau	<i>1/2s</i>

The total noise spectra data (i.e. the propeller plus the tunnel background noise) in the form of [SPL vs Frequency] plots can be found in (Aktas et al. 2014) for all the measured conditions. The data show the effects of the varying advance coefficients, inclination angles and cavitation numbers as stated in Table 1. **Figure 10** is a typical presentation of the noise spectra over a *20 kHz* frequency range displaying the effect of varying shaft inclinations at a fixed *J* and high vacuum condition (low cavitation number).

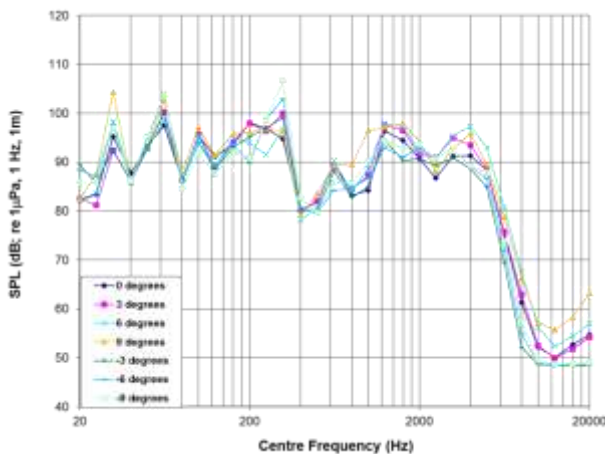


Figure 10 Comparison of noise levels at varying inclination angles at advance coefficient of $J=0.60$ under high cavitation condition

Figure 11 gives qualitative information on the background noise level of the Emerson Cavitation Tunnel. The figure also presents SPL spectra of the propeller corresponding to the $+6^\circ$ inclination angle at advance coefficient *0.4* for the three cavitation conditions as given in Table 1.

In order to have a better understanding of trends in the noise spectra at various conditions, the measured noise data were extracted and presented at three fixed frequencies: namely *630 Hz*, *6.3 kHz* and *20 kHz*. These correspond to frequency ranges where the SPL amplitudes were significantly distinct from the background noise and showed strong variations with the advance coefficient and shaft inclination angle.

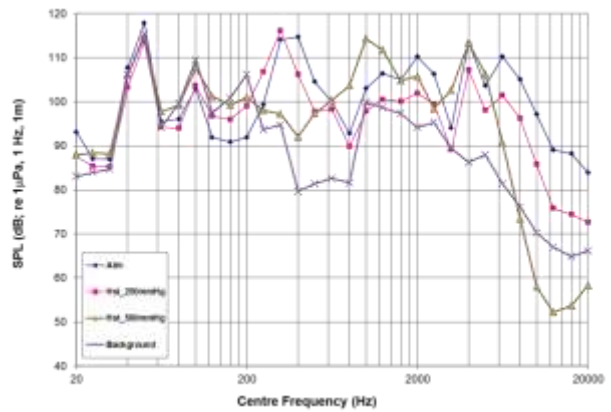


Figure 11 Background noise level spectrum (at Atmospheric cond.) and SPL for 6° inclination at $J 0.4$ (at various cavitation cond.)

In Figure 12 the effect of varying advance coefficients on the SPL are shown for systematically varied shaft angles and for three cavitation conditions at *630 Hz*. The SPLs show relatively less sensitivity to the variations in *J* except for three distinct *J*'s, where the peak SPL values were recorded, due to the strong tip vortices as supported by the selected cavitation images on the right row of Figure 12. This frequency was also close to the 4th blade harmonic. In order to illustrate the effect of the shaft inclination further three cross-plot curves were extracted and shown in Figure 13 for systematically varied advance coefficients and for three cavitation conditions at *630 Hz*. These cross plots do not show any significant asymmetry for the positive and negative angles of the shaft inclination across the three cavitation conditions imposed. Similar plots for the SPLs are also shown in Figure 14 and Figure 15 for *6.3 kHz*. In the first group of these plots, Figure 14, the noise levels appear to increase in a near monotonic manner from high to low *J*-values at each of the three-cavitation conditions whilst in the second group of the plots, Figure 15, a little asymmetry with the angle of inclination can be observed, although there is a weak tendency towards higher levels for the positive inclination angles.

During the tests tip vortex and sheet cavitation were the main types observed together with their complex interaction at the blade trailing edge. This interaction was also reflected in the noise levels for certain operating conditions. This was particularly strong with the trailing edge vortex breakdown due to interaction with the sheet cavity extending downstream at $J=0.4$. This effect was independent of the flow inclination angles. This phenomenon is illustrated in **Figure 16** for the zero and 6° shaft inclination together with its consequent effect on the SPL's as shown in **Figure 14** which displays a distinctive hump at $J=0.4$ for the high vacuum condition (i.e. bottom graph). Similar observations were also given in e.g. (Bark 1986; Bark 1988; Konno et al. 2002)

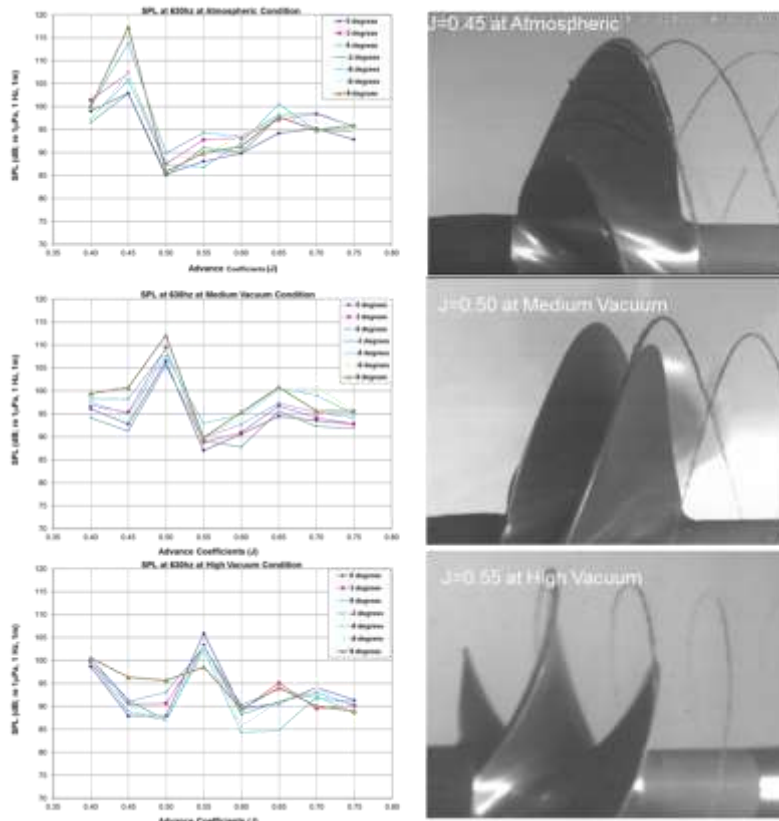


Figure 12 The left row: Comparison of noise levels for varying shaft inclination angles on advance coefficients under different cavitation conditions at 630 Hz. The right row: Images of the cavitation patterns at respected J's

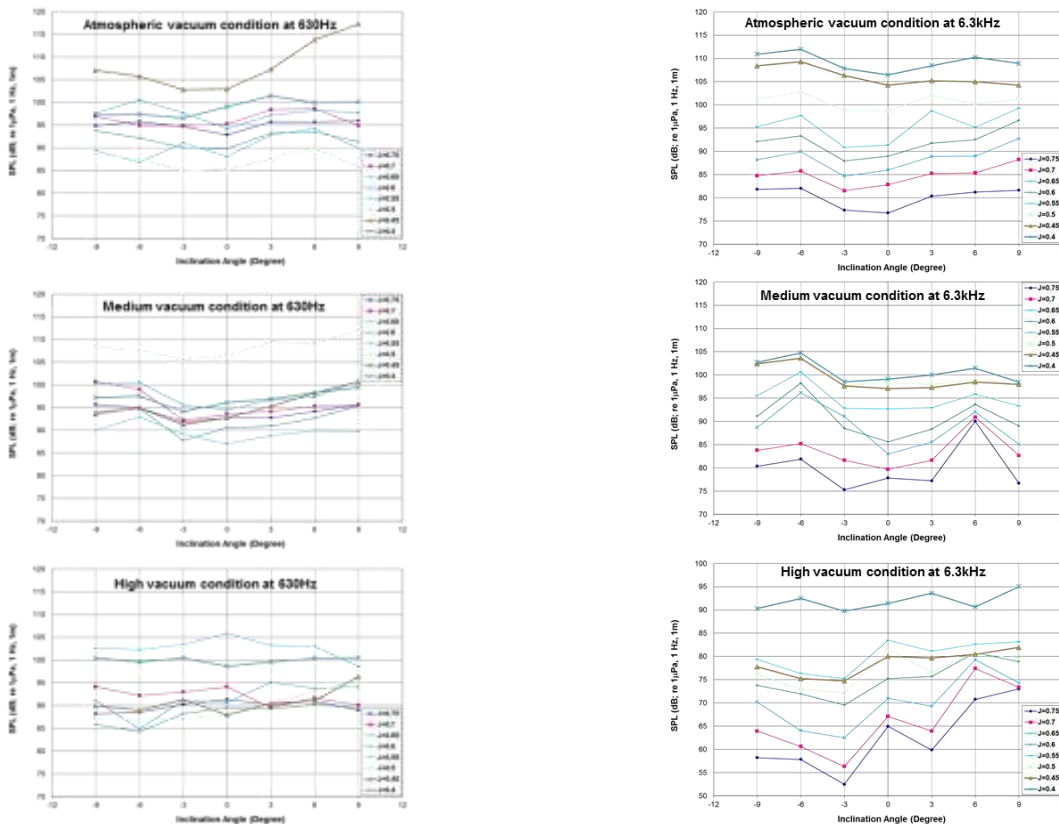


Figure 13 Comparison of noise levels for varying advance coefficients on shaft inclination angles under different cavitation conditions at 630 Hz.

Figure 14 Comparison of noise levels for varying shaft inclination angles on advance coefficients under different cavitation conditions at 6.3 kHz

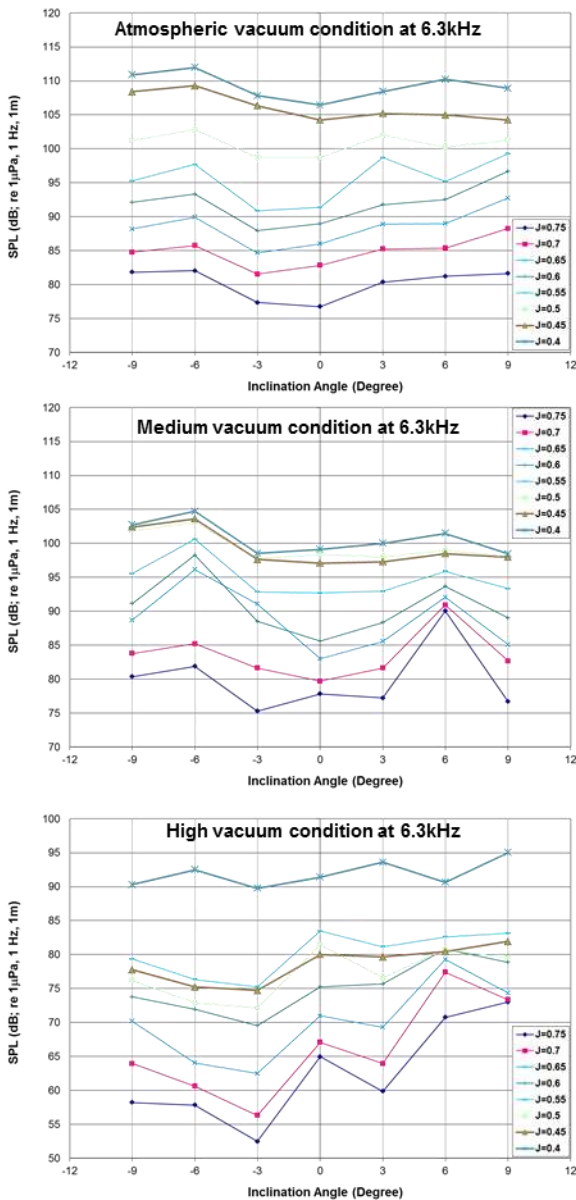


Figure 15 Comparison of noise levels for varying advance coefficients on shaft inclination angles under different cavitation conditions 6.3 kHz

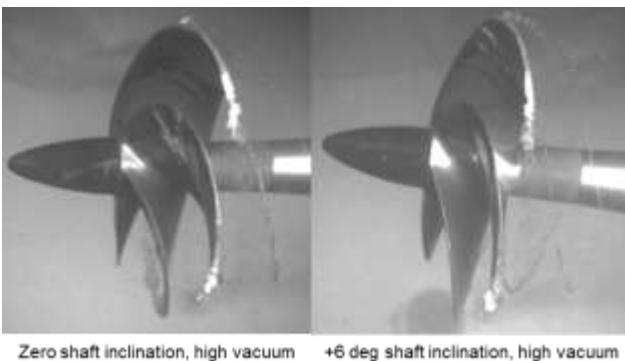


Figure 16 Tip vortex breakdown due to interaction with the sheet cavitation extension at $J=0.4$

7 FURTHER DISCUSSION

7.1 Open Water Efficiency Performance

Effects of the shaft inclination on all test cases are nearly similar for the propeller open water performance curves, namely, showing discernable differences in the torque coefficient (K_Q) at -3° , -6° and -9° inclination angles and hence on the propeller efficiency (η_0) curves. Figure 5 typically shows this trend in the high vacuum condition. As theoretically expected, the inflow velocity is not responsive to the direction of the inclination angle that is in a cosine function. In other words the cosine convention being the same for both minus and plus inclination angles, it sustains the efficiency of the propeller. This can be shown in Figure 17 where no discernable variation in the performance coefficients can be detected with the variations in the inclination angles. The effect of the different vacuum (cavitation) conditions had similar trends in K_T , K_Q and η_0 for the Atmospheric and medium cavitation conditions, hence making difficult to quantify the effect of the inclination under these conditions. It was observed that the increasing vacuum generally reduced the open water efficiency of the propeller at all inclination angles and this effect was also found to be dependent on the J range. For instance comparison of the efficiency of the propeller for 0° and 6° has shown as high as 10% difference at the higher end of the advance coefficient range. But this variance diminishes as the advance coefficient is lowered.

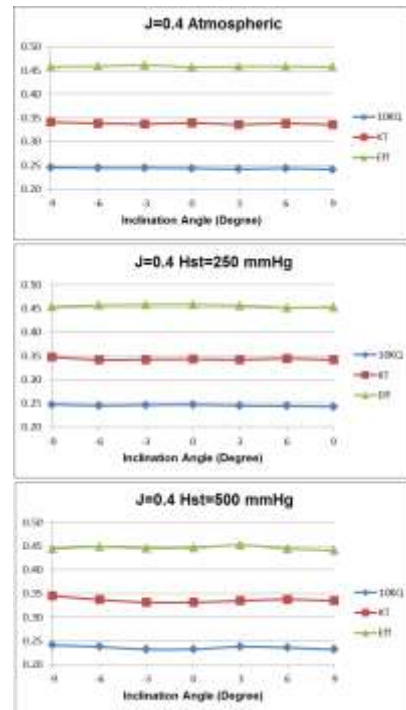


Figure 17 The Non-Dimensional Performance Coefficients at $J=0.4$ for different vacuum conditions

7.2 Cavitation Observations

Cavitation inception observations showed that as the inclination angle was increased the cavitation inception J -value increased for the medium and high vacuum

conditions. However for the Atmospheric condition this trend was different by a smaller range of J - values for the negative inclination angles. Positive shaft inclination stimulated earlier inception on the blades. Overall the inclination angle was observed to initiate an earlier inception for all angles and at all cavitation conditions except Atmospheric condition. The difference observed at the Atmospheric condition can be accounted to the axial flow speed profile of the tunnel and to the lack of nuclei available in the circulating water.

As far as the developed cavitation pattern observations were concerned, these could be discussed under the applied three vacuum (cavitation) conditions as follows:

Atmospheric condition: the propeller model did not cavitate until $J=0.515$ for the top end of the J range without any sensitivity to the shaft inclination. Below this range of J values two distinct types of cavitation patterns, i.e. tip vortex and sheet cavitation, with very slight differences in the extent and strength for the inclined cases relative to the level shaft inclination case, as shown typically in **Figure 18** for zero shaft angle.

Medium vacuum condition: The cavitation-free range was observed above $J=0.55$. Below this range it was observed that the strength of the tip vortices was increased compared to the Atmospheric condition and also displayed distinct nodes in their structures behind the blade trailing edges, as shown typically in **Figure 19**. However, similar to the Atmospheric condition, it was difficult to observe clear differences in the cavitation structures for the same shaft angles in different directions.

High vacuum condition: The cavitation-free range was above $J=0.59$, including variations in the inclination angle. **Figure 16** and **Figure 20** show typical examples for this condition with larger tip vortex structures than observed at the lower vacuum conditions. The cavitation appeared to be similar over the range of shaft inclination range. However, there appeared to be more sheet cavitation at $J=0.4$ and -6 degrees shaft inclination than at the moderate cavitation condition. A wide extent of sheet cavitation was also shown over the blade area combined with severe trailing edge tip vortex collapse.

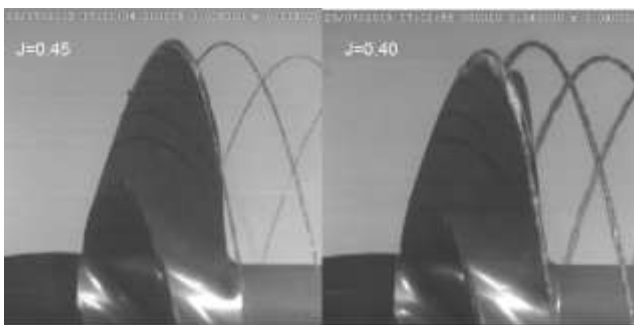


Figure 18 Cavitation patterns at 0° inclination angle under Atmospheric condition

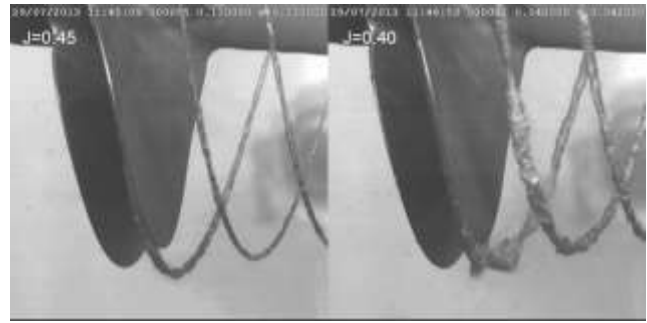


Figure 19 Cavitation patterns at 6° inclination angle under medium vacuum condition

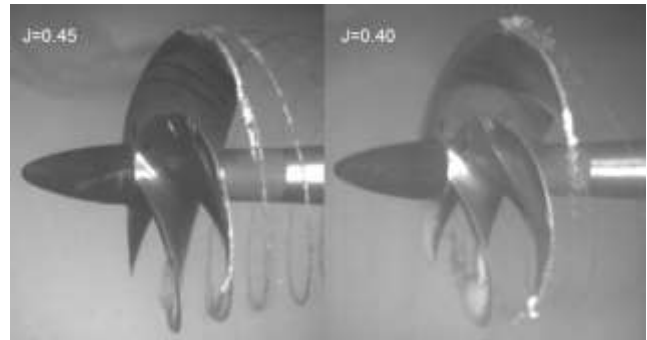


Figure 20 Cavitation patterns at -6° inclination angle under high vacuum condition.

7.3 Noise Measurements

The noise measurements presented here contain the combined propeller and background noise; no correction was made for the background noise of the tunnel. A vibration survey of the tunnel carried earlier showed that the frequencies of the structural vibration generated by the dynamometer and impeller were found to be effective in the frequency region below 100 Hz . Therefore, it is most likely that the noise levels due to the blade rate frequency ranging from 125 Hz to 234 Hz and its harmonics, together with structural vibration, would be affected by these effects in the frequency region up to 1000 Hz . In other words the contribution of the major noise sources during the operation of the tunnel imposed a rather noisy environment for frequencies lower than 1000 Hz .

However the analyzed results for the effect of advance coefficient indicated that the noise levels increased as the advance coefficient, J , reduced in the high frequency range (above 1000 Hz) for $J=0.75$ to 0.55 under the Atmospheric condition. Below $J=0.55$ the noise levels were almost similar. For the medium cavitation condition a similar trend was also observed up to $J=0.50$ in the high frequency range. However at $J=0.45$ and $J=0.40$ the noise level reduced slightly in the high frequency range, demonstrating the fact that the medium and high vacuum conditions may have introduced a cushioning effect in the collapse stage of bubbles which may have reduced the noise levels as conjectured by Ross (Ross, 1987) and discussed in the 18th ITTC (ITTC, 1987).

As far as the effect of the shaft inclination on the noise levels was concerned; at the Atmospheric condition the noise levels in the low frequency range seemed to be similar, regardless of the inclination angle. In the high frequency range the noise levels at the 9° inclination angle case were the noisiest of all the inclination angles tested. This trend changed in the medium cavitation condition as the 6° inclination angle case becoming the noisiest while the 9° case was the quietest.

In order to quantify the effect of cavitation on the noise levels, the analyzed results for the Atmospheric and medium cavitation conditions were compared. At 0° inclination angle in the frequency range less than 100 Hz the noise levels at medium cavitation case were slightly less than those at the Atmospheric condition. For the higher frequency range a similar behaviour was also observed, however at $J=0.45$ and $J=0.40$ the reduction in the noise levels were more pronounced. This also confirmed the effect of the developed cavitation on the noise levels. As the propeller loading increased the effect of more developed cavitation and possible cushioning effects became more obvious. This trend was also observed at 3° inclination angle. However, for the 9° shaft inclination the differences in the comparative noise levels between the Atmospheric and medium vacuum conditions were more prominent than for the 0° and 3° cases. At 6° , -3° , -6° and -9° inclination angles and in the high frequency range, the comparative noise levels displayed 3 different trends depending on J range, namely, for $J=0.75$ to 0.65 the noise levels for the Atmospheric and medium vacuum cases were similar; for $J=0.60$ to 0.55 the medium vacuum case displayed higher noise levels; but for $J=0.50$ to 0.40 the Atmospheric condition displayed higher noise levels. It was again observed that more developed cavitation was an effective noise source at low J number range from 0.50 to 0.40 .

The spectrum levels were observed to disperse for the range of inclination angles until the inception advance coefficients. However following the appearance of the visible cavitation and the development of the stable cavitation, the sound pressure levels were observed to converge. This can be attributed to the earlier inception caused by the inclination and as the differences between the extents of developed cavitation reduced the measured SPL levels at different conditions started to radiate almost exact spectrum levels.

8 CONCLUSIONS

Systematic cavitation tunnel tests were carried out to investigate the open water (efficiency) performance, cavitation and noise characteristics of the model propeller of the UNEW research vessel, *The Princess Royal*, in uniform (open water) and in inclined flow conditions. These tests were part of a round robin test campaign organized by the members of the Noise CoP in the HTF.

The tests reported in this paper are the first experiments in this round robin campaign. Therefore, while some early

conclusions from these tests are given in the paper, the main objectives of the entire test campaign will be achieved when the entire campaign is finalized in 2015 and hence the final conclusions will be drawn based on the whole campaign. The following is therefore the local findings from the UNEW test campaign.

- Effect of shaft inclination on the propeller open water performance was more influential on the torque and hence the propeller efficiency and the effect was asymmetric depending on the direction (up/down) of the inclination and the J range. The thrust was relatively insensitive to the change in the shaft angles. The propeller efficiency was reduced with increasing vacuum over the vacuum range tested.
- Effect of shaft inclination on the cavitation inception (and desinence) of the tip vortices was clear and this effect was asymmetric in general depending on the direction of the inclination. However this asymmetry was gradually replaced with relatively symmetric behaviour with increasing vacuum levels. The asymmetry for the atmospheric and medium cavitation condition can be attributed to the variance of the tunnel velocity profile. The **Figure 3** shows the relatively higher inflow speeds over the top half of the propeller plane than at the bottom half.
- Two distinct types of well-developed cavitation patterns, which are tip vortex and sheet cavitation, were observed as well as their complex interactions at the trailing edges of the blades. The extent and strength of these cavitation phenomena were influenced by the change in the inclination angles.
- Effect of shaft inclination on the extent and strength of the fully developed tip vortex and the sheet cavitation was rather less influenced by upward inclinations than downward inclinations.
- Bearing in mind the fact that the measured noise levels were the total levels including the tunnel background noise, the effect of change in the shaft inclination in the low frequency range seemed not to be influential since all the inclined conditions displayed similar noise levels and trends. However this trend changed in the high frequency range depending on the direction of the inclination as well as the vacuum levels applied.
- The recorded radiated noise levels were found to be highly sensitive to the type and extent of cavitation as well as the frequency range that the particular cavitation contributed into.
- Relative noise levels were mostly reduced in the higher frequency range, propeller loading and vacuum conditions suggesting the physical phenomenon that the developed cavitation may have had a cushioning effect in the collapse stage of bubbles as conjectured by Ross (Ross, 1987) and 18th ITTC (ITTC, 1987)

ACKNOWLEDGEMENTS

This research project is funded by the School of Marine Science and Technology (MAST) of Newcastle University (UNEW). The research is part of the Noise Community of Practice (CoP) activities of the Hydro

Testing Forum (HTF) under their task of the round robin test campaign with the model propeller of *The Princess Royal*. The members of the Noise CoP of HTF include CRN-INSEAN, DGA/H, KIOST/MOERI, MARIN, SSPA and UNEW. The Authors thank to Mr. George Politis, the tunnel manager of the Emerson Cavitation Tunnel, for his collaboration and help during the experiments.

REFERENCES

- Abrahamsen, K. A. (2012). 'The ship as an underwater noise source'. ECUA 2012, 11th European Conference on Underwater Acoustics, Edinburgh, 2-6 July.
- Aktas, B., Korkut, E., Fitzsimmons, P., & Atlar, M. (2014). 'Systematic cavitation tunnel tests with a propeller in uniform and inclined flow conditions as part of a round robin campaign', MAST Report No: MT-2014-001, Newcastle University, September.
- Arveson, P., & Vendittis, D. (2000). 'Radiated noise characteristics of a modern cargo ship. The Journal of the Acoustical Society of America'. 107(1), pp 118–129.
- AMT'11. (2011). 2nd Intl. Conference on Advanced Model Measurement Technology for the EU Maritime Industry, Newcastle University, Newcastle Upon Tyne, 3-5 April
- Atlar, M. (2011). 'Recent upgrading of marine testing facilities at Newcastle University', 2nd Intl. Conference on Advanced Model Measurement Technology for the EU Maritime Industry., Newcastle University, Newcastle upon Tyne, 3-5 April.
- Atlar, M, Baktas, B., Sampson, R., Seo, K-C, Ignazio, M.,V., Fitzsimmons, P. (2013), 'A multi-purpose marine science & technology research vessel for full-scale observations and measurements', 3rd Intl Conference on Advanced Model Measurement Technologies for the Maritime Industry, Gdansk, Poland.17-18 September.
- AMT'13. (2013). 3rd Intl Conference on Advanced Model Measurement Technologies for the Maritime Industry, Gdansk, 17-18 September.
- Bark, G. (1986). 'Development of violent collapses in propeller cavitation'. International Symposium on Cavitation and Multiphase Flow Noise', Proc. ASME Symposium, Anaheim, CA, USA, FED 45, pp 65–75.
- Bark, G. (1988). 'On The mechanisms of propeller cavitation noise'. PhD thesis, School of Mechanical Engineering. Chalmers University, Goteborg, Sweden.
- Carlton, J. (2012). Marine propellers and propulsion. 3rd ed. Butterworth-Heinemann. Oxford,UK.
- Gutsche, F. (1964). 'Untersuchung von Schiffsschrauben in schräger Anströmung' Schiffbanforschung. Translation in DTMB. March
- Hadler, J. B. (1966). 'The Prediction of Power Performance on Planing Craft.' Trans. SNAME, Vol. 74, New York, USA,10-11 November.
- Hildebrand, J. A. (2005). 'Impacts of anthropogenic sound' Marine mammal research: conservation beyond crisis. The Johns Hopkins University Press, Baltimore, Maryland. pp 101-124.
- IMO. (2011). 'Noise from commercial shipping and its adverse impact on marine life development of an international standard for measurement of underwater noise radiated from merchant ships'. MEPC 62nd session agenda item 19. pp. 61–62.
- ITTC (1987). Report of The Cavitation Committee , 18th International Towing Tank Committee. Kobe, Japan.October. pp. 159-220
- ITTC. (2011). Model – Scale Cavitation Test. 26th ITTC – Recommended Procedures and Guidelines. Rio de Janeiro, Brazil.
- ITTC. (2014) Specialist Committee on Hydrodynamic Noise Final Report and Recommendations to the 27th ITTC. Copenhagen, Denmark.
- Konno, A., Wakabayashi, K., Yamguchi, H., Maeda, M., Ishii, N., Soejima, S., & Kimura, K. (2002). 'On the mechanism of the bursting phenomena of propeller tip vortex cavitation'. Journal of Marine Science and Technology6(4) pp 181-192.
- Kozhukharov, P. G., & Sadovnikov, M. Y. (1983). 'Investigation on cavitating screw propellers operating in oblique flow'. 2nd International Conference on Cavitation. Edinburgh, UK
- McKenna, M. F., Ross, D., Wiggins, S., & Hildebrand, J. A. (2012). 'Underwater radiated noise from modern commercial ships'. Journal of Acoustical Society of America, pp 92–103.
- MCR. (2011). 'Cruise report for research projects conducted from R/V Song of the Whale in French and UK waters of the English Channel', The Final Report. Retrieved 14 October 2014, from <http://www.marineconservationresearch.co.uk/download/>
- MEPC (2010) 'Noise From Commercial Shipping and Its Adverse Impacts on Marine Life'. Marine Environment Protection Committee. MEPC 60/18. December.
- Ross, D. (1987). 'Mechanics of Underwater Noise'. Peninsula Publishing. California, USA.
- SONIC. (2012). 'Suppression Of underwater Noise Induced by Cavitation'. EC-FP7, Grant agreement no: 314394.
- Taniguchi, K., Tanibayashi, H., & Chiba, N. (1969). Investigation into the Propeller Flow Cavitation in Oblique'. Mitsubishi Technical Bulletin No. 45, March.

Propeller Acoustic Measurements in Atmospheric Towing Tank

Henri Haimov^{1*}, Vicente Gallego², Enrique Molinelli¹, Borja Trujillo²

¹Canal de Experiencias Hidrodinámicas de El Pardo (CEHIPAR), Madrid 28048, Spain

²Instituto Tecnológico “La Marañosa” (ITM), Madrid, Spain

Abstract: The study describes the implementation of experimental procedure for measuring the hydrodynamic noise generated by model scale marine propellers in atmospheric towing tank. The towing carriage and conditions have not been altered admitting the existence of considerable background noise. The feasibility analysis included experimental and theoretical study of the background noise at the operating conditions. Some considerations about the uncertainty of the results are also presented. The experimental equipment, set up and procedure for measuring the acoustic pressure around model ship propeller and/or hull is also described. Simultaneous measurements with various differently positioned hydrophones at multiple hydrodynamic conditions permitted to evaluate the background and propeller/hull generated acoustic field at a range of frequencies. An appropriate treatment of the recorded time series characterised the background disturbances and permitted to obtain net results with sufficient signal to noise ratio, mostly from narrowband spectral analysis. Results for the impact of the hull presence on propeller acoustic field are presented and discussed. The extrapolated results are compared informatively with full scale measurements. The research presented in this article is a result of the Collaboration agreement on underwater acoustics between CEHIPAR and ITM and is partially funded by the European Commission project AQUO (Achieve Quieter Oceans by Shipping Noise Footprint Reduction), Seventh Framework Programme, Grant number 314227, FP7-SST-2012.1.1-1.

Keywords: Model marine propellers and hulls, model tests, experimental acoustics, noise, towing tank.

1 INTRODUCTION

The modelling and prediction of the noise generated by the ships and marine structures is of increased interest due to the environmental impact consisting of health and comfort problems for the humans and disturbance of serious consequences for the marine life. This latter has been observed worldwide and the former is experienced daily by crew and passengers (See SILENV Project D3.1).

There are few regulations limiting the noise and vibrations for special ships and conditions but the tendency is to introduce rules for commercial vessels and areas. These limitations cannot be expanded widely because of the age of the fleet requiring serious investments to improve and also due to the lack of reliable prediction tools capable to assure the accomplishment of the rules by the new-built vessels.

One of the goals of the research projects co-financed of the European Commission is to promote the development of experimental and numerical tools for reliable prediction of the noise and vibrations during the project stage of the vessel. One of those project is called SILENV completed in 2012 and there are currently going on two such projects named AQUO and SONIC.

There are several sources of noise and vibrations in a contemporary ship, but this study is limited to the hydrodynamic underwater noise generated by the propeller alone and in presence of the hull at standard navigation conditions.

Model scale hydrodynamic tests of marine vehicles were becoming indispensables to guarantee the propulsive, sea-keeping and manoeuvring characteristics of the ships at design stage. Nowadays more requirements begin to be imposed on the ships that should be satisfied before the ship is constructed.

The existing model test facilities and equipment fail to model all the parameters that would assure similarity with the full scale ship conditions. Closer modelling can be achieved in a depressurized towing tank as it permits more complete hydrodynamic similarity, still leaving not satisfied the mechanical and acoustical ones. This kind of facility is a big investment, expensive to maintain and exploit that is why only very few exist worldwide. An example of applying a depressurized tank in ship acoustics is shown in Kooij & De Bruijn (1982), Bosschers et al. (2013).

As the noise contribution of the propellers is more pronounced at cavitating conditions, the Cavitation Tunnels are the most used facilities for such kind of tests. The interaction between the propeller and the hull is crucial for the study of noise, so a better choice are the big size tunnels that permit to locate inside a full hull model and in the same time model correctly the cavitation. An example of such an installation is given in Fréchou et al. (2001). Nevertheless, the small and medium Cavitation Tunnels are also used to carry propeller acoustic tests taking into account the propeller hull interaction only as a non-uniform flow (wake) upstream of the propeller using wake screens or dummy models (Atlas et al. (2001), (Wills 1989), (Bertetta et al.

2011), (Yuasa et al. 1986), (Sevik 1996). A weak points of these facilities is the absence of free surface that is known to contribute, although less than the cavitation, to the whole acoustic field as well the reverberation of tunnel's walls.

There are only a few attempts to measure the propeller noise in atmospheric tank due to the incomplete modelling that leads normally to non-cavitating condition. In addition, the towing carriage is a strong source of background noise. The choice of such facility in the present work is justified by the need to produce non-cavitating acoustic propeller data for CFD validation purpose and can be of interest when the propeller is generally non-cavitating, contributing to distinguish the non-cavitating part of the noise produced by a cavitating propeller. The interaction with the hull is also better modelled in towing tank.

2 EXPERIMENTAL FACILITIES AND EQUIPMENT

2.1 Towing Tank Specifications

Acoustics measurements were performed at CEHIPAR's calm water towing tank (CAT), the main particulars of this facility are shown in the following figure:

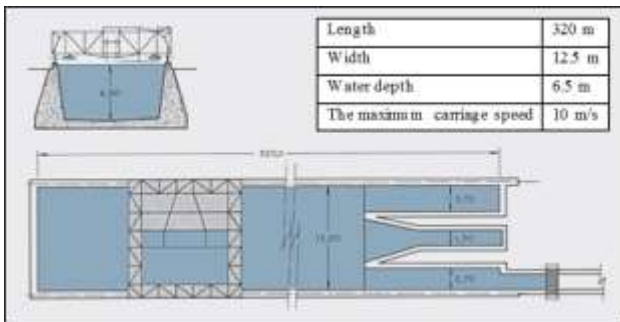


Figure 1 CAT facility

From acoustic point of view, the CAT facility is considered as acoustic channel with free surface opened at its extremes and rectangular cross-section (vertical sides and flat bottom). The structural arrangement is adjacent to a terrain allowing acoustic transmission between water and the ground. This leakage was calculated through the analysis of the experimental results

2.2 Hydrophones Support System

The four hydrophones used to measure the noise, are placed outside of the propeller slipstream in different positions shown in Figure 2 and Figure 3. The non-dimensional distances from each hydrophone to the centre of the propeller are shown in Table 1:

Table 1 Hydrophones positioning

Hydrophone N°	Distance to propeller origin/Diameter
1	0.80
2	1.42
3	1.44
4	5.44

Hydrophone 1 is placed at the propeller disc plane, hydrophones 3 and 4 are located downstream. Their sensitive elements are projecting upstream. Only hydrophone 2, placed upstream has its sensitive element projecting downstream. Further in the text they will be referenced as H1, H2, etc. (see Figure 2).

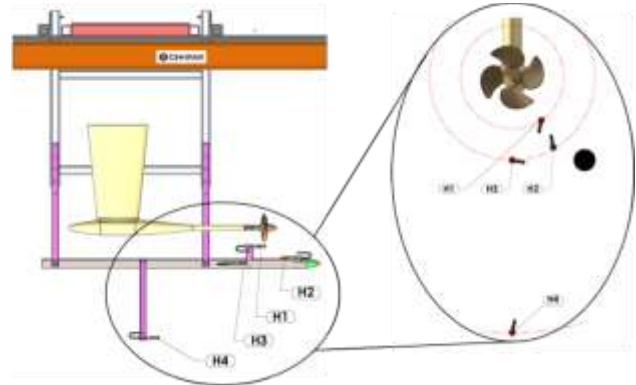


Figure 2 Hydrophones arrangement

For a fix positioning of the hydrophones during the tests a support structure has been designed and constructed. This structure is fixed to the carriage. The propeller dynamometer and the model ship are also fixed making compatible the measurements with both configurations (OW, open water and SP, self-propulsion). Figure 3 shows CAD view of the installation design with both configurations together and the photos in Figure 4 - the structure installed on the carriage.

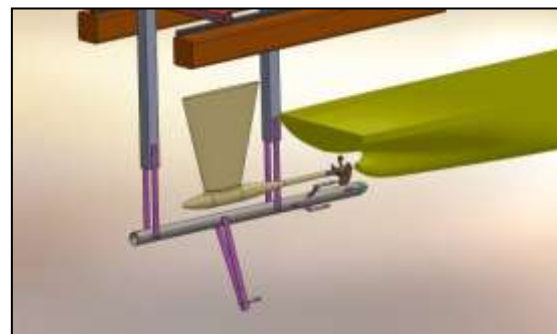


Figure 3 Tests arrangement



Figure 4 Hydrophones support installed in both configurations (left: OW and right: SP)

The support made of steel and the hydrophones were fixed to the structure through steel cylinders coupled with rubber toric joints. The cylinders were fixed to the structure in a way permitting to adjust the positions of the sensors.

A fifth hydrophone was installed fixed on a pole in the tank bottom (not shown). Although the background noise due to the movement and vibrations of the rest of the hydrophones has been avoided in this hydrophone, the

results of measurements using that one are not presented here because of the weakness of the signal.

2.3 Measurement Equipment Specifications

Commercial 21 mm hydrophones and compact-low noise conditioning charge amplifiers were used to measure the underwater signals.

2.2.1 Hydrophones and Conditioning Charge Amplifier Specifications

The hydrophone model used was *RESON TC4040* (Figure 5 left). It was chosen due to the many advantages it offers: Flat frequency receiving response over a wide frequency range (± 2 dB from 1 Hz to 80 kHz). Its ceramic sensor element ensures high stability and performance, resistant to fresh water but also to other liquids like oil. Other core specifications are listed below:

- Receiving voltage Sensitivity: -206 dB re 1 V/ μ Pa (56 μ V/Pa).
- Omnidirectional horizontal directivity (± 2 dB) at 100 kHz.
- Vertical directivity: 270° (± 2 dB) at 50 kHz.

Each hydrophone was connected to individual conditioning charge amplifier, in order to obtain high resolution signal responses at low frequency ranges.

The *RESON EC6067-CCA1000* charge amplifier provides low-noise responses and enables the use of long cables between sensors, without affecting their sensibility. The amplifier has an operating frequency range from 1 Hz to 1 MHz and the output gain can be selected from 0 to 32 dB.

2.2.2 Hydrophone Calibrator

Calibrating pistophone *GRAS 42AC* (Class 1 L and ANSI S1.40-1984), Figure 5 right, was used to generate precise sound pressure (Source Level of 134 dB re 20 μ Pa, at 250 Hz) for the low frequency process of hydrophones calibration in air.



Figure 5 Hydrophone and Calibrating pistophone

2.2.3 Data Acquisition and Analysis System

For registration of each of the acoustic signals, a portable acquisition module *PROSIG P8402* was used. It has 3 card chassis with 4 different configurable inputs each one, up to 12 ADC 16 bit channels with BNC inputs. It is also lightweight and resistant to extreme humidity and temperature conditions and is controlled by the signal acquisition and processing software *DATS 7.0* having a wide range of features. The sampling rate was fixed at 20 kHz and the acoustic parameters were displayed in real time during the tests.

2.4 Acoustic Properties of the Facility

The limitations of facility in comparison with open sea conditions consist in the presence of two vertical walls parallel to the sound source course and the depth of the water column is limited to a few meters. Only the longitudinal dimension allows almost free field condition for the acoustic field to be achieved. Acoustically, this represents a rectangular cross-sectional waveguide (Figure 6) where the transversal eigen modes could be excited with enough source level.

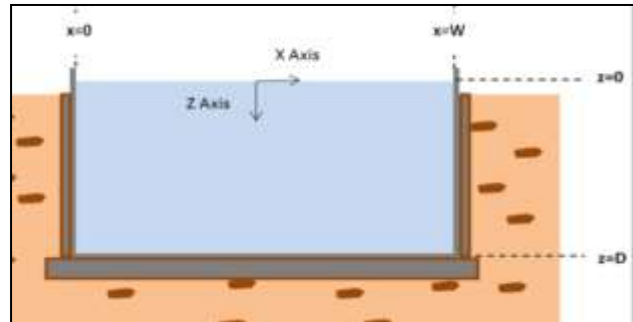


Figure 6 Schematic cross-section of the underwater acoustic waveguide

Fortunately, the acoustic features of the channel boundaries are far from ideal and their acoustic impedance is not infinite related to the acoustic impedance of water. This allows the sound to fly out of the channel to the surrounding ground, especially in the low frequency range (under 200 Hz). Some preventive checks have been made from the temporal files recorded during the experiments, searching for echo traces from the temporal autocorrelation of the signals. The results of this check show that only for very high speeds of the towing carriage echoes are perceptible beyond 150 Hz. In Figure 7 some of these temporal correlation curves are shown.

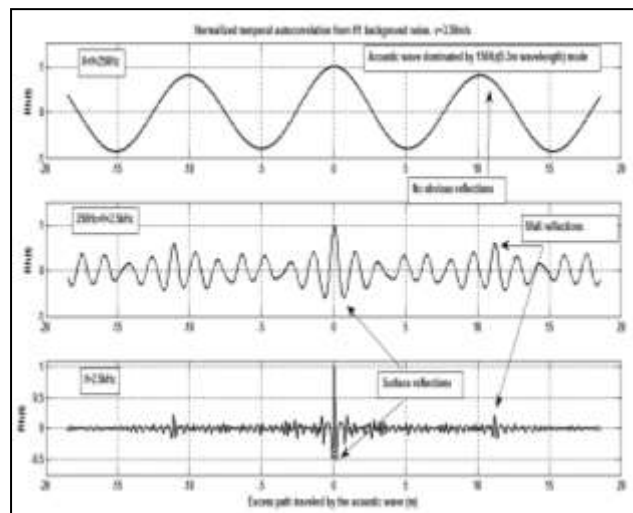


Figure 7 Examples of correlation curves obtained from the recorded time signals

2.5 Background Noise Sources and Characteristics

The first experimental results revealed that the acoustic background of the towing tank under real operation conditions would be the most important problem for achieving a feasible acoustic measurement. The drive

system of the carriage and the sliding of the assembly on the rails mounted on top of the lateral walls generated a high level underwater acoustic background. Additional background noise is generated by the flow around the proper hydrophones. It was reduced by locating the H2 pointing downstream. The most outstanding features of this acoustic background were:

- 1) Spectra with a striking tonal structure;
- 2) Amplitude and frequency dependence of the spectrum discrete components upon the speed of the carriage;
- 3) Significant amplitude and frequency dependence upon the measuring position of the hydrophone.

In view of these, it was considered to obtain first the average narrowband acoustic background for each hydrophone, with the speed factor decoupled from the processed signal. For this, the time signals obtained were normalized with respect to its maximum amplitude. Then, the Cross Spectral Density (CSD) was calculated for all possible combinations of pairs of towing speeds. Eight configurations, which would suppose 64 pairs, minus the autocorrelation cases, not considered, result in 56 pairs to be analysed. Finally, the result for each hydrophone was once more normalized to its maximum value. Accordingly, the average Cross Spectral Density (discrete) for the n^{th} hydrophone is obtained from Equation (1):

$$\langle SPL_{bk}(l) \rangle_n = \left(\sum_{\substack{x=1 \\ x \neq y}}^8 \sum_{y=1}^8 CSD_{xy}(l) \right) / 56, \quad (1)$$

where the discrete spectrum $CSD_{xy}(l)$ is calculated for each pair (x, y) of tested speeds according to Eq. (2):

$$CSD_{xy}(l) = \left(\Delta T \cdot \sum_{m=1}^M X_m(l) \cdot Y_m^*(l) \right) / M \cdot W_f, \quad (2)$$

being $X_m(l) = FFT(x_m(r))$ and $Y_m(l) = FFT(y_m(r))$ the m^{th} FFT periodogram of the corresponding series of data $x_m(r)$ and $y_m(r)$ extracted from the recorded files; M is the total number of series of data used; W_f a correction factor corresponding to the selected time window (Hamming window in our case); and ΔT the sampling time of the signal acquisition process. The final frequency resolution obtained in the signal analysis process is given by the known Equivalent Noise Band Width factor (ENBW). Its resulting value was 0.10322 Hz.

The average background CSD spectrum for H2 is shown in Figure 8. Similar behaviour with more or less tonal lines was observed for the rest of hydrophones. Quite different spectrum was obtained from the signals of H5, shown in Figure 9.

The CSD spectrum shows a noticeable tonal structure. The discrete lines obtained must be discarded when analysing the corresponding noise spectrum of the tested source. Note the presence of spectral components due to the 50 Hz electric hum noise present in the water.

This way, the narrowband analysis allowed us to extract the most prominent features of the acoustic signature from the underwater acoustic emitter, even when the environment is very noisy.

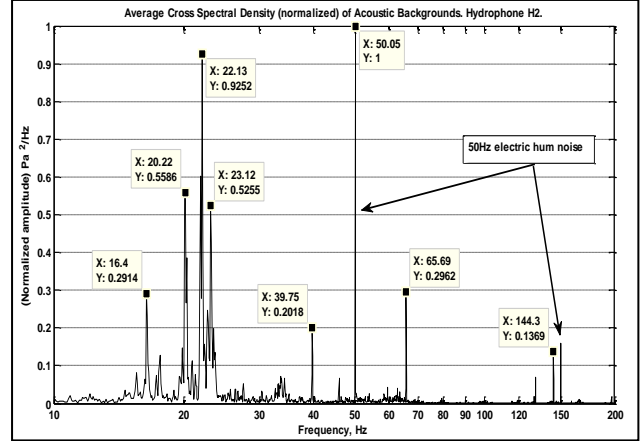


Figure 8 H2 average low frequency acoustic background

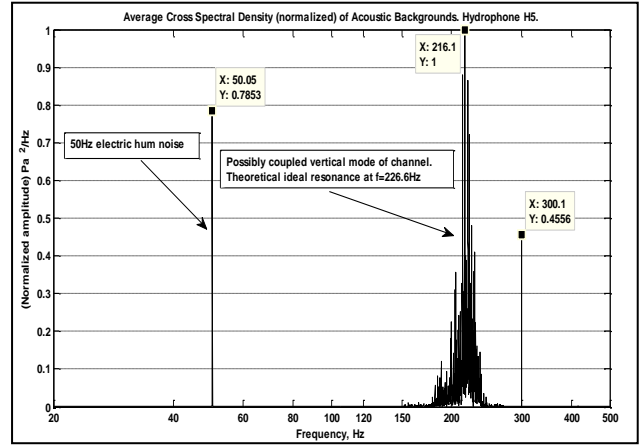


Figure 9 H5 average low frequency acoustic background

As expected H5 presented lower number of background tonals, although a set of strong tonal components was observed in the range of 200 – 240 Hz. This could be due to the excitation of a vertical mode in the underwater acoustic waveguide of the tank. Casually H5 was positioned in a depth where this mode had strong amplitude.

3 TEST CONDITIONS

3.1 Objectives

The objective of the study is to quantify the acoustic field around the propeller alone and in presence of the hull in atmospheric model conditions and to evaluate the contribution of the hull to the whole field at specific hydrodynamic conditions.

3.2 Experimental Setup

The support structure with the hydrophones and the OW dynamometer or the hull, as shown in Figure 3 and Figure 4 are used to measure the noise around the propeller. The majority of the hydrophones are located close to the source, as low signal was expected in the non-cavitating

propeller cases. The structure was adapted for both open water and behind the hull functioning of the propeller.

In the OW case the propeller is mounted on the shaft of the dynamometer, while for the SP, it is mounted on hull shaft. In both cases the background noise is registered without propeller but rotating shaft.

Additionally, vertical and lateral accelerometers were fixed in the stern part of the hull in order to detect possible vibrations as additional source of underwater noise. As expected, only low accelerations were detected thus permitting not to consider the hull vibrations as significant additional noise source.

3.3 Description of the Tested Configuration

The above described equipment and procedure are applied to the propeller and hull of the case selected in AQUO project of a 60 m length training research vessel, propelled by a 2.26 m of diameter 4 bladed controllable pitch propeller. The wooden hull model was manufactured in CEHIPAR and the propeller – provided by CTO – Poland. The scale factor is 10. Photos of both models are shown in Figure 10 below.



Figure 10 Hull & Propeller models

The detailed geometry of the tested configuration is a confidential part of the project.

3.4 Test Conditions

The propeller and the hull models had been tested previously at OW and SP conditions applying Froude similarity to the full scale case. To reproduce the SP of the ship the same combinations of hull speed and revolutions of the propeller have been used during the acoustic tests. The hull was kept fixed to the carriage to assure constant distance of the hydrophones from the acoustic sources. For most of the tests the propeller blades were set to one of the two pitch positions called “high pitch” – HP0 corresponding to the design pitch and “low pitch” – HP1. This choice reflects two possible real conditions as the ship engine is generally working at fixed shaft revolutions.

The conditions and designation of selected sets of tests is given in Table 2 below:

Table 2 Measurement settings

Noise measurement tests			Model data		Ship data	
Setting N ^o	Basic test	Pitch	Speed [m/s]	Hz	Speed [kn]	Hz
12	SP	P0	1.95	11.10	12.00	3.62
17	SP	P1	1.15	10.10	7.10	3.40
8	OW	P0	1.07	11.10		
4	OW	P1	0.58	10.10		
11	SP	P0	0.00	15.00		
6	OW	P0	0.00	15.00		

4 NOISE MEASUREMENTS TECHNIQUE

4.1 Calibration Process

Correct calibration of the transducers is required to get a reliable response from each of the sound sources to study. Using the pistophone, at static ambient pressure of 101.3 kPa, no further correction factors need to be applied.

The operating procedure is straight forward: Each hydrophone was fitted into the coupler of the pistophone and the constant sound pressure level produced was recorded. Since the output level of a pistophone depends on the static ambient pressure, the use of a barometer was needed, showing directly the correction factor in dB. The barometric correction at a given altitude very seldom varies by more than ± 0.2 dB. The calibration of the hydrophones in air is adequate for this work at least in the low frequency range of the acoustic spectrum, where the impedance and response of the hydrophones are equivalent to the underwater case.

4.2 Acoustic Noise Descriptors

As the noise emitting source is continuous the evaluation method chosen for calculating the noise level is by time averaging. In the wideband range one descriptor used is the $SPL_{1/3\text{ octv}}$, that is the acoustic pressure level (in dB re 1 μPa) averaged over 1/3 octaves bands. Moreover, this average level can be further normalized in respect to the bandwidth of each 1/3 octave filter in which case the descriptor is $SPL_{1\text{ Hz}}$, expressed in (dB re 1 $\mu\text{Pa}/\text{Hz}$). The relation between them is given by (ITTC 2013):

$$SPL_{1\text{ Hz}} = SPL_{1/3\text{ octv}} - 10 \cdot \log_{10}(0.23 \cdot f_0), \quad (3)$$

where f_0 is the central frequency of the band.

Both, the background and the acoustic signature of the emitter are expected to include some discrete lines over its general continuous spectrum. This was the reason to perform a very narrow band analysis of the recorded signals in order to distinguish between tonal components of the background and tonal components radiated by the source under study. The acoustic descriptor selected is the Power Spectral Density (PSD) of the acoustic signal, expressed in dB re.1 $\mu\text{Pa}^2/\text{Hz}$ and calculated using the following expression:

$$PSD_{xx}(l) = \left(\Delta T \cdot \sum_{m=1}^M |X_m(l)|^2 \right) / M \cdot W_f \quad (4)$$

The parameters in the Eq. (4) should be interpreted in the same sense that Eq. (2). The PSD curves obtained depend upon the real frequency resolution (ENBW) used for the analysis. The finer the spectral analysis, the higher the amplitude will be, as the product of PSD and ENBW must be constant and equal to the *rms* value of the signal at each frequency. It is recalled that ENBW being 0.10322 Hz defines a quite narrow band analysis.

Another frequently used descriptor is the dimensionless pressure, obtained from the pressure using the expression:

$$K_p = \frac{p}{\rho n^2 D^2}, \quad (5)$$

where \mathbf{p} is the measured pressure in Pa and reduced to 1 m from the propeller centre; ρ is the water density in kg/m^3 ; \mathbf{n} is the rotational velocity of the propeller in *rps* (revolutions per second) and \mathbf{D} is the diameter of the propeller in meters. The corresponding level, in dB, is then:

$$L_{K_p} = 10 \cdot \log_{10} \left(\frac{K_p}{K_{p_{REF}}} \right), \quad (6)$$

where $K_{p_{REF}} = 10^{-6}$.

When K_p is used instead of \mathbf{p} , the acoustic descriptors, SPL and PSD transform, respectively in:

$$SPL_{K_p}, \text{ in dB re. } K_{p_{REF}}/\text{Hz} \quad (7)$$

$$PSD_{K_p}, \text{ in dB re. } K_{p_{REF}}^2/\text{Hz} \quad (8)$$

4.3 Correction for Background Noise

The presence of a significant underwater background prevents the exact measurement of the underwater noise emitted by the source. To limit the error that could be associated with this measurement in a noisy environment it is necessary to apply a correction for background noise. The criterion (ITTC-2013) was used in this work and consists of the following rules. First the level difference ΔL is defined as:

$$\Delta L = SPL_{s+bck} - SPL_{bck} = 10 \cdot \log_{10} \left(\left(\frac{p_{s+bck}}{p_{bck}} \right)^2 \right) \quad (9)$$

Then, depending on the value obtained there are three options, namely

$$\begin{cases} \text{if } \Delta L > 10 \text{ dB, } SPL_{NET} \cong SPL_{s+bck} = 20 \cdot \log_{10}(p_{s+bck}(\mu Pa)) \\ \text{if } 3 \text{ dB} < \Delta L < 10 \text{ dB, } SPL_{NET} = 10 \cdot \log_{10}(10^{SPL_{s+bck}/10} - 10^{SPL_{bck}/10}) \\ \text{if } \Delta L < 3 \text{ dB, } SPL_{NET} \text{ is discarded} \end{cases} \quad (10)$$

The graphic results shown in this article have been all obtained according to this criterion. When the third condition was satisfied, the corresponding point was directly omitted from the respective curve.

4.4 Geometric Reduction Law for the Net Pressure

The results obtained for the net noise pressure from each hydrophone are reduced to a reference point in space. The propagation law applied to the acoustic waves that

propagate from the measurement point to the reference distance (usually 1 m) is a delicate issue to treat. The far field of a sound source is reached at a distance from it which depends on its geometric dimensions and the sound wavelength λ . In this regard, if D is the diameter of a circular source (the rotating propeller, in this case) a criterion commonly accepted considers the range given by $r_0 \sim 2 \cdot D^2 / \lambda$; a reference distance from which it can be assumed that the far field is well developed. For the case presented in this article and if quasi-free field condition is assumed, the positions of all hydrophones fall in the acoustic far field and the spherical propagation law can be applied, at least for low frequencies. There are other criteria that would situate the first three hydrophones in the near field

Further conceptual complications can arise when the complete moving model (hull + propeller) is considered as the real acoustic source. On one hand, the size of the emitter is larger; on the other, the propagating medium is moving and turbulent near the source position. Clearly, these facts can disturb the previous consideration about the acoustic far field. Nevertheless, as this topic is still under discussion, the spherical law of propagation has been adopted.

4.5 Estimation of Uncertainty in the Experimental Results.

The method selected to estimate the measurement error was based on the standard deviation of the spectral curve (PSD) for a representative experimental case. For this, a temporal file recorded during the experimental work was divided into ten sections of equal length. Then, the FFT-PSD spectra of each temporal section were extracted and, from these ten frequency curves, the PSD of the standard deviation was calculated for all the frequencies in the spectral range of interest. Figure 11 and Figure 12 show the confidence interval for the PSD curves of Setting 11 and Setting 12, respectively using the standard deviation for the experimental results.

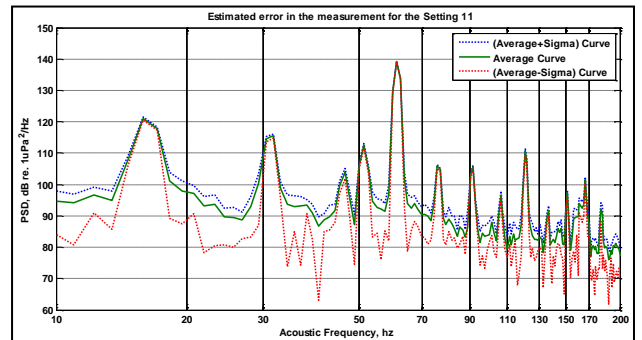


Figure 11 PSD curves for visualization of the measuring confidence interval. Setting 11

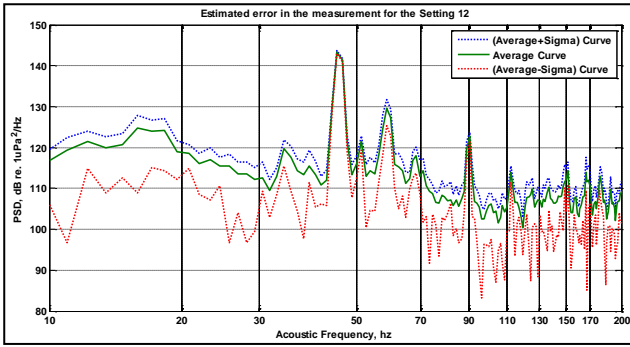


Figure 12 PSD curves for visualization of the measuring confidence interval. Setting 12

The main conclusion that can be extracted from the two previous figures is that the measuring error can be very important in absence of a strong signal, in the general noise field, but just in the tonal lines emitted by the propeller this deviation is less than 1%.

The uncertainty of the results is also evaluated using repeatability tests. The precision tolerance is then estimated in 1dB.

5 RESULTS AND COMMENTS

The results of the measurements for the net sound pressure level and/or its power spectral density at the conditions given in Table 2 for model scale are presented in Figure 13 through Figure 27 for H2. The conditions are marked implicitly through the setting number. In 1/3rd octave presentation, in many cases, as one shown in Figure 14, part of the spectrum is omitted due to high level background, while the narrowband analysis permits to distinguish the contribution of the configuration tested in almost the whole spectrum.

The SP condition for two pitch settings (HP0 and HP1) is presented from Figure 13 to Figure 20.

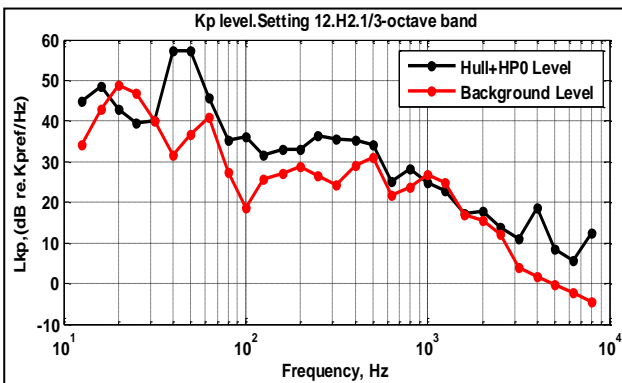


Figure 13 Total and background 1/3 octave Kp SPL level for Setting 12

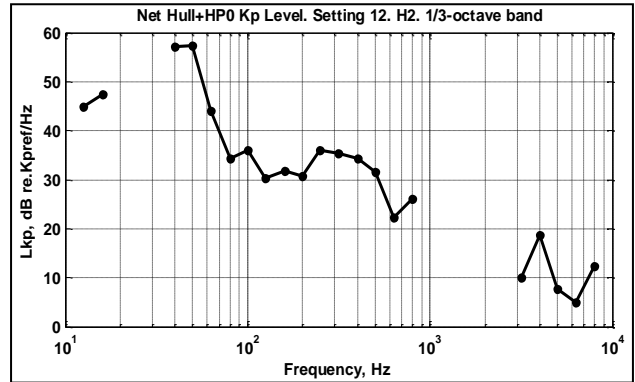


Figure 14 Net 1/3 octave Kp SPL level for Setting 12

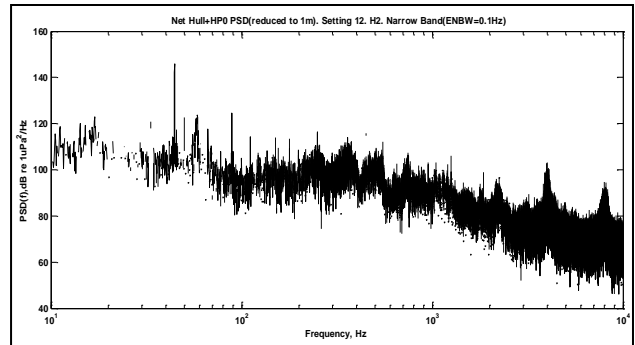


Figure 15 Net narrow band PSD level for Setting 12

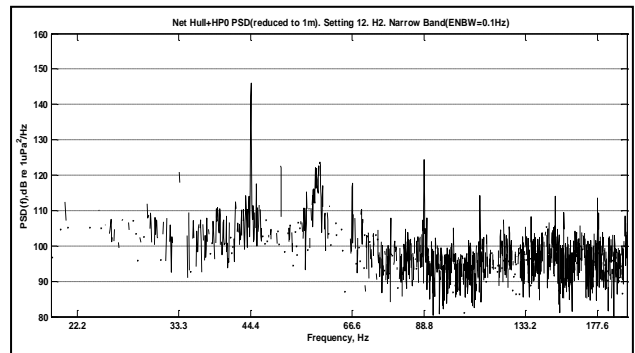


Figure 16 Net narrow band PSD level for Setting 12. Low frequency region

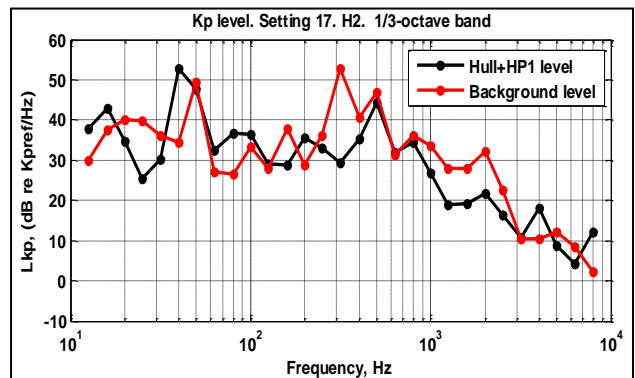


Figure 17 Total and background 1/3 octave Kp SPL level for Setting 17

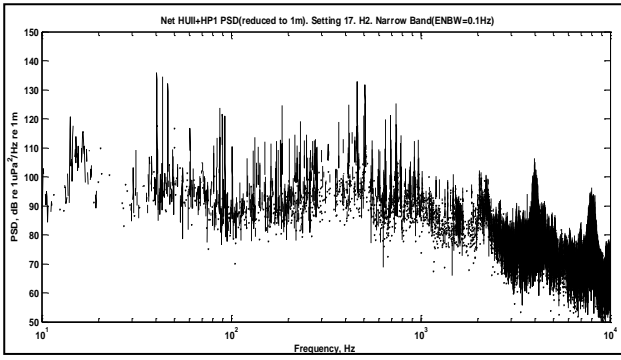


Figure 18 Net narrow band PSD level for Setting 17

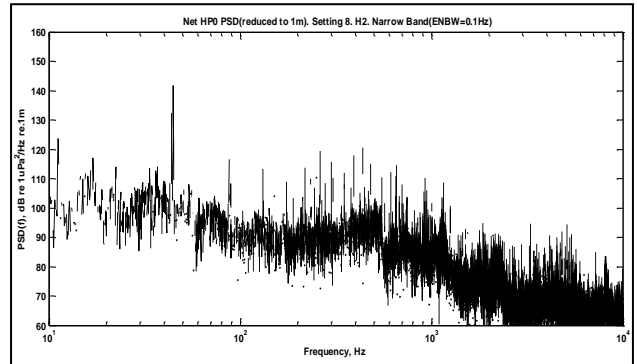


Figure 22 Net narrow band PSD level for Setting 8

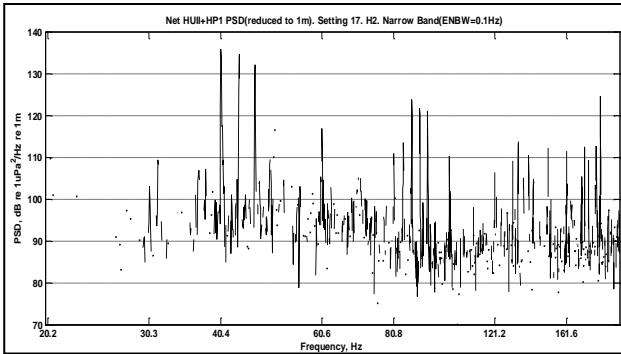


Figure 19 Net narrow band PSD level for Setting 17. Low frequency region

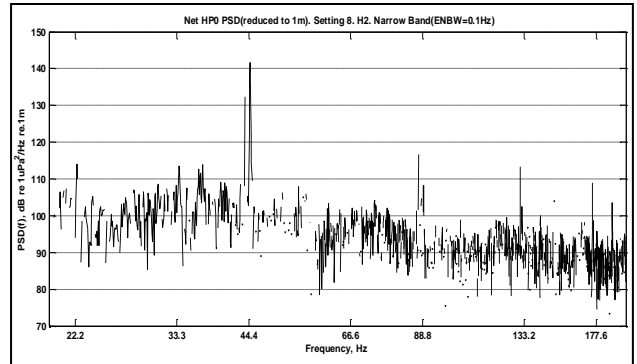


Figure 23 Net narrow band PSD level for Setting 8. Low frequency region

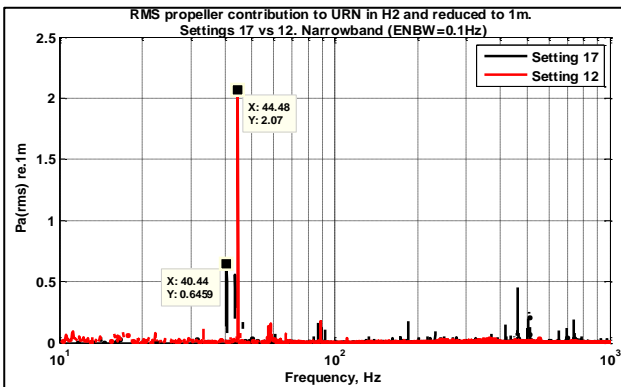


Figure 20 Narrow band pressure amplitude for setting 12 and 17

The following figures show the spectra for the open-water case in both pitch conditions:

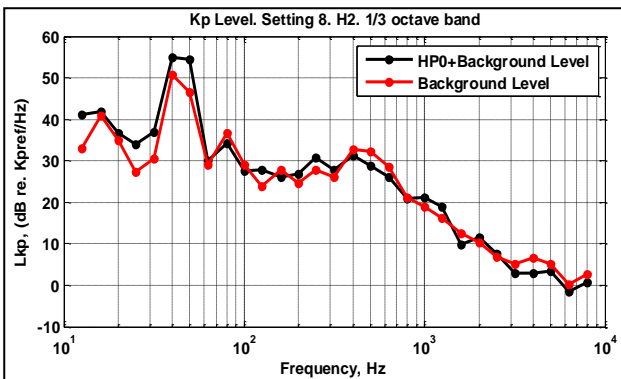


Figure 21 Total and background 1/3 octave Kp SPL level for Setting 8

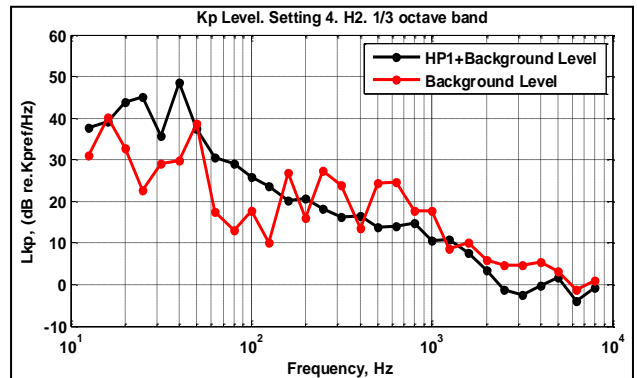


Figure 24 Total and background 1/3 octave Kp SPL level for Setting 4

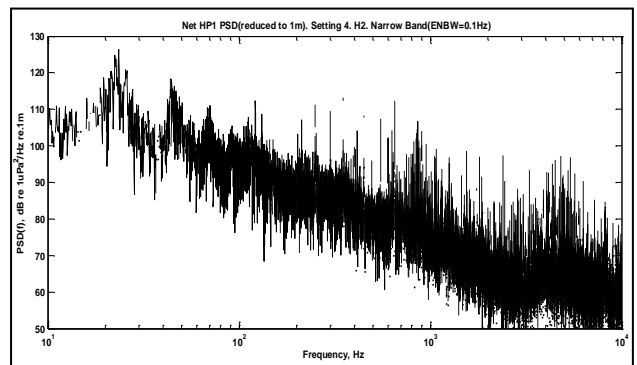


Figure 25 Net narrow band PSD level for Setting 4

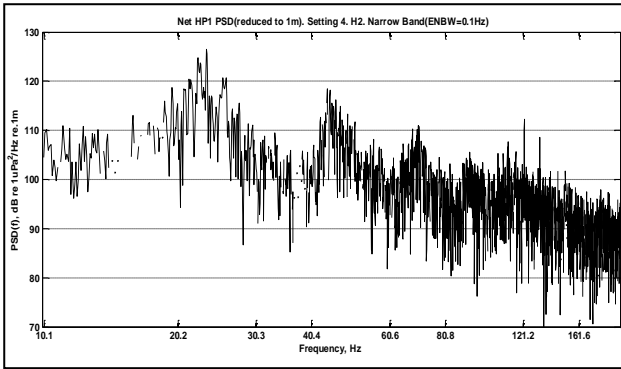


Figure 26 Net narrow band PSD level for Setting 8. Low frequency region

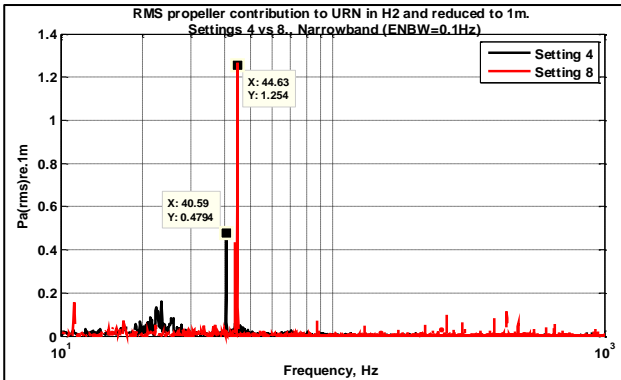


Figure 27 Narrow band pressure amplitude for setting 4 and 8

In the above figures clear tonals are observed corresponding to the blade passing frequencies (BPF), at least until the 4th BPF. At higher frequencies tonal lines of similar order as the BPF's are present. A broadband spectrum is also present for all the cases at frequencies, mostly higher than 10^3 Hz.

As expected in this atmospheric case, the level of the noise is higher for the higher pitch compared to the lower pitch condition (Figure 20 and Figure 27). The higher pitch presents clearer dominance of the BPF's harmonics, while for the lower pitch discrete lines of similar level appear all around the spectrum (Figure 19). As the loading of the blades in both cases is quite similar, a possible cause of this is the significant difference of the pitch of the tip and trailing vortices.

The presence of the hull affects the noise due to the propeller mostly at medium range frequencies (102 - 103 Hz) approximately. This effect is observed for the SP conditions (not shown) as well as in static hull condition, as can be seen in Figure 28. This should be due to the diffraction from the hull and the additional turbulence noise generated by the latter at this range of the spectrum.

There is some difference in the measured pressure level transferred to 1 m depending on the hydrophone position. This is shown in Figure 29 for the case OW setting 11.

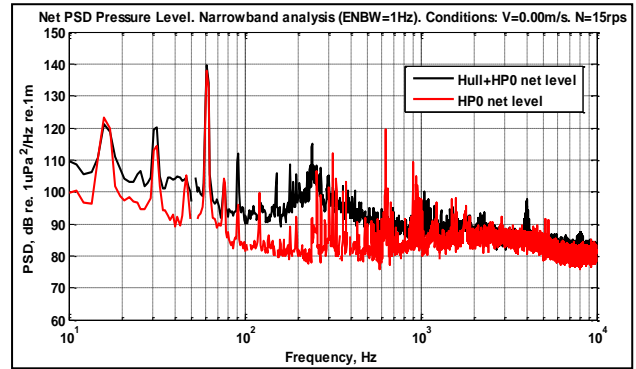


Figure 28 Effect of hull over HP0 net pressure level. Settings 11 & 6. Narrow band analysis.

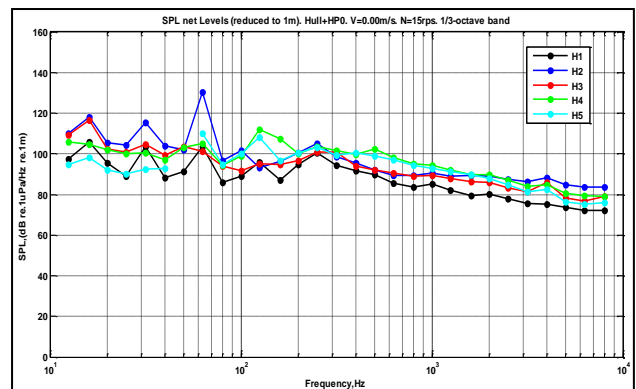


Figure 29 Net SPL Hull+HP0 levels. Hydrophones H1 to H5. Setting 11. 1/3-octave band spectrum

It can be seen that significant difference is observed for H2 mainly at the first blade harmonic. It is concluded that for the rest of the spectrum H2 represents roughly the mean behaviour, thus justifying its choice.

The next Figure 30 and Figure 31 represent an attempt to compare the model scale result extrapolated using the formula adopted by the ITTC-2013 with full scale measurements carried out by CTO-Gdansk and kindly processed for this comparison by UNIGE. This is not a strict validation case because of the lack of full modelling (Euler similarity is not satisfied), but it was an opportunity for comparison and is not meaningless because, as reported, the propeller is only slightly cavitating.

The case of full scale measurements presented in the figures was called WP1 and is the closest but not identical in conditions to setting 12 of the model tests.

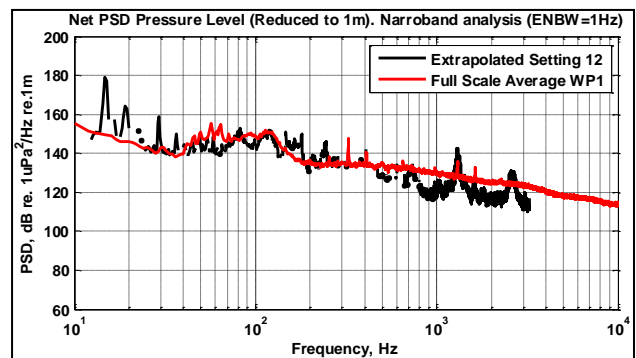


Figure 30 Comparison of net narrow band PSD level

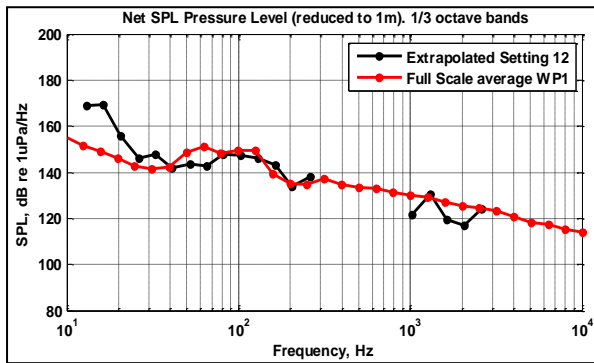


Figure 31 Comparison of net 1/3 octave band PSD level

As shown, general correlation between the prediction and the full-scale measurement exist. It is to be noted that the low frequency tonals are not seen in the full scale spectrum, as well as the peaks just above 1 kHz detected in model test.

Another estimation of the results included in AQUO project is the comparison with the model scale results carried out by UNIGE in their Cavitation Tunnel and although this again is not a strict validation, we expect to obtain some more information about the viability of the results. In an initial comparison (not given) it seems that our results tend to overestimate the SPL in comparison with UNIGE, as is also seen in comparing with the full scale measurement.

6 CONCLUSIONS

Careful acoustic characterization of towing tank facility was carried out permitting to reveal the spectral lines of the background noise due to various sources and the proper characteristics of the tank. It was concluded that the propeller and hull noise can be distinguished from the background mostly using very narrow band analysis. The wide range of conditions tested with a chosen model propeller and hull are partly presented in the previous paragraphs. The typical acoustic results at SP and OW conditions are shown where the expected blade frequency lines appear.

The acoustic fields of the propeller alone and in presence of the hull at different conditions gave interesting information about its influence. Results are also obtained for the impact of the pitch variation on the noise field around the propeller.

As expected, the extrapolated model test results cannot be used for precise quantitative estimation of the full scale far field noise of the ship but can give some qualitative idea about it. Nevertheless the results of the tests can serve for validation purposes of numerical models run at the same physical conditions.

ACKNOWLEDGEMENTS

This work would not be possible without the participation of the Workshops and CAT staff and the support of CEHIPAR and ITM managements. The research presented in this paper is partially generated as part of

European Commission funded project AQUO (Achieve Quieter Oceans by Shipping Noise Footprint Reduction), Seventh Framework Programme, Grant number 314227, FP7-SST-2012.1.1-1.

The authors are also grateful to University of Genoa for the fruitful partnership in the project AQUO and personally to Michele Viviani, Tomaso Gaggero and Giorgio Tani for providing treated full scale acoustic data of the ship.

Acknowledgements are also due to CTO-Gdansk for providing the scale model of the propeller and for measuring ship generated noise in full scale conditions.

REFERENCES

- Atlas, M. et al. (2001). 'Cavitation Tunnel Tests for Propeller Noise of a FRV and Comparison with Full Scale Measurements', CAV2001Conference.
- Bark, G. (1985). 'Prediction of Propeller Cavitation Noise From Model Tests and its Comparison with Full Scale Data', Transactions of the ASME **107**, March 1985, pp.112-120.
- Bertetta, D., Savio, L., Viviani, M. (2011). 'Experimental Characterization of Two CP Propellers at Different Pitch Settings, Considering Cavitating Behaviour and Related Noise Phenomena', SMP'11, Hamburg, Germany.
- Bosschers, J. et al. (2013). 'Underwater Radiated Noise Measurements with a Silent Towing Carriage in the Depressurized Wave Basin', AMT Conference, Gdansk.
- EC FP7 SILENV Project. (2012) D1.3, D3.1
- Fréchou, D. et al. (2001). 'Marine Propulsor Noise Investigations in the Hydroacoustic Water Tunnel <GTH>', 23th Symposium of Naval Hydrodynamics.
- Gaggero, S. et al. (2014). 'Experimental and Numerical Investigations for Modelling Propeller Cavitation Noise', MARTECH'14, Lisbon.
- ITTC (2013) - Recommended Procedures and Guidelines. Model Scale Noise Measurements.
- PROSIG Ltd. (2012) "DATS 7.0 User Manual".
- Sevik, M. (1996). 'Hydroacoustic Considerations in Marine Propulsor Design', 21st Symposium on Naval Hydrodynamics, Trondheim, Norway.
- Van der Kooij, J., De Bruijn, A. (1982). 'Acoustic Measurements in the NSMB Depressurized Towing Tank', NATO Seminar, April, The Hague, The Netherlands.
- Wills, C. B. (1989). 'Development of a Comparative Acoustic Testing Procedure for Model Propellers', RINA, London, UK.
- Yuasa, H., Kamirisa, H., Nojiri, T. (1986). 'Study on the Characteristics of Propeller Cavitation and its Noise', 16th Symposium on Naval Hydrodynamics, Berkeley.

Measurement of Radiated Underwater Noise from a Small Research Vessel in Shallow Water

Alex Brooker^{1*}, Victor Humphrey¹

¹Institute of Sound and Vibration Research, University of Southampton, Southampton, SO17 1BJ, UK

Abstract: The impact of man-made underwater noise on the marine environment has in recent years received increased attention from regulatory authorities, as evidenced by its inclusion in the Marine Strategy Framework Directive (MSFD) of the European Union (EU). Radiated underwater noise from ships, primarily resulting from propeller cavitation, has for many years been understood to be one of the major contributors to ambient ocean noise. Civilian research in this area has to date been relatively limited; standards covering the measurement of radiated noise from ships in deep water and data analysis procedures have only recently been published by national and international standards institutes. Less attention has so far been paid to the measurement of radiated noise from ships in shallow water environments. This is of interest as shallow water areas are more likely to be used by civilian researchers due to the logistical problems involved in undertaking trials in deep water. The issue of shipping noise has been identified as one requiring further research, indicated by the recent funding of several large collaborative projects by the EU (see for example the SILENV, AQUO and SONIC projects). This paper presents ship radiated noise data measured using a three hydrophone array during a recent sea trial undertaken as part of the SONIC project.

(The research leading to these results has received funding from the European Union Seventh Framework Programme (FP7/2007-2013) under grant agreement n°314394)

Keywords: Underwater radiated noise, SONIC project, shipping noise, propeller cavitation

1 INTRODUCTION

Interest in the environmental impact of man-made underwater noise has increased considerably in the last two decades driven by a recognition of the increasing demands placed on the marine environment by, for example, the oil and gas, renewable energy and transport industries as well as an improving understanding of the sensitivity of marine fauna to underwater noise pollution. The inclusion of underwater noise as a key indicator of environmental status in the European Marine Strategy Framework Directive (MSFD) is testament to this interest.

Many studies have identified radiated underwater noise from merchant ships, predominantly resulting from propeller cavitation, as a major contributor to ambient noise levels in the oceans (e.g. Wenz (1962), Urick (1975), Ross (2005)). While more recent studies have presented data indicating that shipping noise levels are increasing (Andrew et al. (2002)). Consequently, any effort to determine the current status of the marine environment should consider shipping noise in detail.

The measurement of radiated noise from ships has historically been undertaken for military purposes using fixed acoustic noise ranges. More recently, researchers from both military (e.g. Wales and Heitmeyer (2002), Scrimger and Heitmeyer (1991)) and civilian (e.g. McKenna et al. (2012), Merchant et al. (2014), Hallett (2004)) backgrounds have used short or long term mobile deployed systems to measure shipping noise. While these have been a valuable contribution to the field, the lack of

a standardised methodology for measurement, data analysis and reporting often hinders the comparison of different datasets.

The recent publication of internationally agreed standards (ANSI/ASA (2009b) and ISO (2012)) is the first step towards rectifying this issue and it is encouraging to see many researchers adopting these methods as closely as possible (Bahtiarian and Fischer (2006), De Robertis et al. (2012), Peña et al. (2011)). The fact that these researchers appear to have found it challenging to meet some of the requirements for the highest measurement precision methodology set out in the standards highlights the difficulty in undertaking these measurements in the real world.

This paper concentrates on the results of full scale trials to measure radiated noise from a vessel following, as closely as possible, the methodology recommended in the standards cited above. As well as presenting some of the results of the trials the methodology used is discussed in detail highlighting any necessary departures from those in the standard and discusses some of the issues encountered when undertaking trials of this type.

2 THE SONIC PROJECT

Funded under the European Union (EU) Seventh Framework Programme (FP7) the SONIC (Suppression Of underwater Noise Induced by Cavitation) project commenced in October 2012 and will run until October

2015. It is a multinational collaborative project involving thirteen organisations from five European countries including universities, classification societies, and naval, marine engineering and technical research institutes.

The aim of the project is to investigate radiated noise from ships, primarily concentrating on underwater noise from propeller cavitation as this is the main source of noise generation when the ship is operating at design conditions. It is the most recent demonstration of the commitment of the EU to reduce the environmental impact of human activities on the seas.

The project involves developing techniques for the accurate prediction of ship radiated noise levels from scale model tests and numerical modelling techniques. A number of approaches to improve the accuracy of these predictions are being explored. These include novel techniques for the measurement of cavitation noise in cavitation tunnels and towing tanks, taking into account the acoustically reverberant nature of these environments and developing tools to separate out cavitation noise from machinery noise.

These predictions will be informed by and validated against measurements of radiated noise from full scale sea trials involving the research vessel Princess Royal operated by the University of Newcastle. The first of these trials was undertaken in September 2013 and aimed to measure radiated noise using a deployed hydrophone array using similar methodology to recently published international standards (Section 2). In addition, multiple on-board sensors including hull pressure pulse sensors, hull and engine mounted accelerometers, microphones, torque and shaft speed gauges and ultrasonic transducers were installed on the vessel.

The third aspect of the project focusses on mitigation. It aims to develop an underwater noise propagation model to estimate the “noise footprint” of an individual vessel and a “noise map” showing the contribution to the overall underwater noise levels in an area of ocean from multiple vessels transiting through the region over a period of time. Other than the noise propagation model itself, the inputs to this final stage include an empirical ship source level model that is based on a database of existing ship radiated noise level data compiled for the SONIC project. In addition, other mitigation measures relating to design and operation of propellers and the reduction of machinery noise are being investigated.

3 ISO PUBLICLY AVAILABLE SPECIFICATION FOR SHIP RADIATED NOISE MEASUREMENTS

The American National Standards Institute (ANSI) standard (and the ISO Publicly Available Specification (PAS) subsequently based upon it) provides recommendations covering environmental conditions, suitable locations, specification and setup of measurement equipment, behaviour of the target vessel, post processing of data and the metrics by which to report the data. It also provides three grades of measurement standard from

Grade A, which provides the most stringent set of conditions, to Grade C which allows for a reduced degree of measurement detail and estimated accuracy. It is, therefore, a very comprehensive guide for researchers undertaking ship radiated noise measurements which takes into account a number of common issues.

Figure 1 shows the recommended hydrophone setup geometry relative to the target vessel for Grade A measurements. The depths of the hydrophones are defined in relation to the distance at Closest Point of Approach (CPA) of the vessel and the elevation angles specified by the standard of 15°, 30° and 45°. Assuming a vessel of less than 100 m in length (as is the case for the present study) the depth of the shallowest hydrophone, d_1 , is recommended as 27 m, $d_2 = 58$ m and $d_3 = 100$ m. This, however, is based on the trials being undertaken at a location that meets the minimum water depth requirements, that is the greater of 300 m or 3 x ship length for Grade A measurements, 150 m or 1.5 x ship length for Grade B measurements and 75 m or 1 x ship length for Grade C measurements.

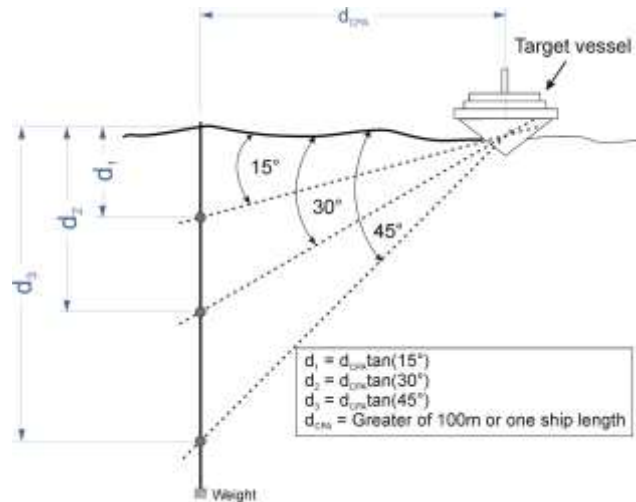


Figure 1 Hydrophone array geometry recommended by the ANSI/ISO Standards

The Standard also covers the manoeuvring of the vessel during the measurements, shown in Figure 2 for the measurement of radiated noise from the starboard side of the vessel. The procedure requires the vessel to run along a track such that it passes the hydrophone array at CPA, perform a Williamson turn and return along the same track so that measurements of radiated noise from both port and starboard sides are made. The Data Window Length (DWL) is the distance between two points along the track either side of the CPA point defined by a $\pm 30^\circ$ angle about the hydrophone array position. The COMEX and FINEX points define the start and end of the run respectively with each point a distance 2DWL either side of the CPA point. Between the COMEX and FINEX points the vessel must maintain constant speed and running conditions with minimal use of rudder to maintain course along the track.

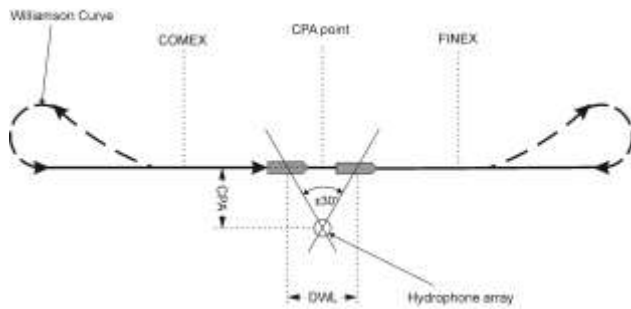


Figure 2 ANSI recommended vessel manoeuvre during trials for starboard side measurements

4 SONIC FULL SCALE TRIALS: MEASUREMENT AND DATA PROCESSING METHODOLOGY

4.1 Measurement system

During the SONIC full scale trials undertaken in September 2013 the University of Southampton deployed a vertical hydrophone array from a moored support vessel. The array consisted of three Reson TC4032 hydrophones and associated Reson cables, input modules and battery supplies. The acquisition system consisted of a National Instruments USB-6251 DAQ device sampling at 240 kHz on each channel and proprietary acquisition software running on a standard laptop PC. A diagram of the basic setup is presented in Figure 3.

The influence of surface wave motion on the array was mitigated by use of a spar buoy to control motion due to the array surface suspension and by using an elastic tether to decouple the array from the movement of the support vessel.

The hydrophones were attached to a central rope using a custom built stainless steel protective cage and mounting setup. As well as preventing damage to the hydrophones during deployment and recovery, this provided a solid mounting on to the central rope to maintain the separation distance between hydrophones. In addition, the mounting fixed the hydrophones away from the central rope and cables, reducing unwanted system self-noise from turbulence around the array. The maximum hydrophone depth of the array was 50 m, a departure from the specifications of the ANSI standard. However, the hydrophone depths within the 50 m maximum were fully adjustable in order to allow the deployment of all three hydrophones even in shallow water areas (the selected location for the trial is discussed below).

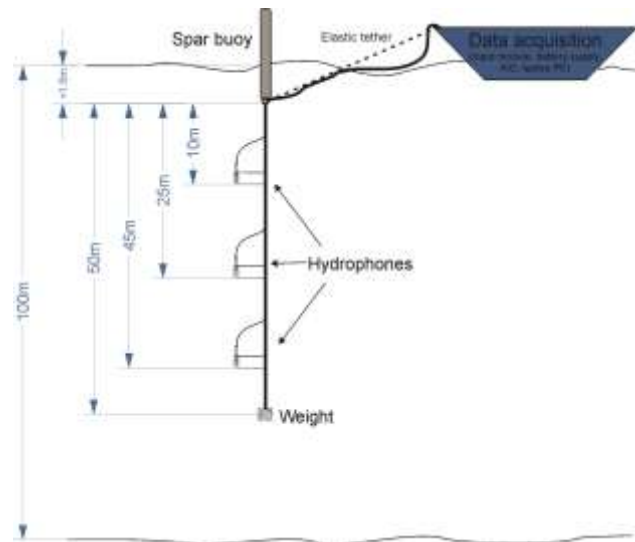


Figure 3 University of Southampton hydrophone array setup

4.2 Additional Measurements

In addition to the hydrophone array a differential GPS system was set up on the target vessel and the support vessel from which the hydrophone array was deployed. This GPS data was subsequently used during data post-processing to define the CPA distances for each run (and therefore the range correction used for “source level” estimation, discussed below) and the data window used for analysis corresponding to the period of the recorded files when the target vessel was transiting through the data window.

In total, thirty transducers were installed on-board the target vessel measuring hull pressure pulses, engine and hull vibration, airborne noise, propeller shaft speed and torque, engine power and a boroscope and several cameras to carry out detailed propeller cavitation observations. As well as providing extremely detailed information for on-board noise and vibration generated by the propeller cavitation and engines this also allowed detailed records of vessel operation during each run to be made in addition to the ships own readouts.

In addition to the above, for each run a record was made of wind speed, wave height, vessel speed over ground (SOG) and speed through water (STW), rudder angle and water depth from observations and the vessels own equipment.

4.3 Target Vessel and Running Conditions

The target vessel used during the trials was the Princess Royal operated by the University of Newcastle pictured in Figure 4. Table 1 provides a specification of the vessel. In terms of access to the vessel, control over its operation during the trials and existing facilities to install on-board sensors, this vessel offered the ideal platform for the trials. The location of the trials could be dictated by the requirements of the measurements rather than the commitments or operating restrictions of the vessel. Additionally, vessel running conditions could be carefully controlled and logged and extensive on-board and off-

board data to validate the scale model and numerical modelling results could be obtained. The disadvantage of the vessel is that in terms of hull design and size it is not particularly representative of the majority of the current merchant shipping fleet. The radiated noise data may therefore not be a good indicator of the typical levels of underwater noise generated by merchant ships.



Figure 4 The target vessel Princess Royal

Table 1 Specification of the target vessel Princess Royal

Classification	MCA Cat 2
Length	18.9 m
Beam	7.3 m
Design draft	At AP: 1.845 m At FP: 1.745 m
Displacement	44 tonnes (approx.)
Payload	5 tonnes
Max speed	20 knots
Cruising speed	15 knots
Engines	2 x 602 BHP
Propulsion	2 x 5-bladed, fixed pitch propellers
Propeller diameter	0.75 m
Approximate source depth	1.15 m
Max operational sea state	4 – 5
Range	400 Nautical Miles
Cavitation inception point (engine rpm/speed)	800 rpm/6.5 kn
Gearbox ratio	1.75

In total, thirty eight vessel runs undertaken broadly in line the ANSI standard guidelines were completed during the 2013 SONIC full scale trial. The vessel running conditions for each run were defined based on nominal

engine revolutions per minute (rpm) values that could easily be controlled by the master of the vessel. During the initial phases of the trial, detailed cavitation observations were undertaken to determine the cavitation inception point for the vessel and also to record the extent of cavitation on the propeller for each running condition. Subsequently, several rpm values were chosen for the remainder of the trial; these were 600, 700, 900, 1200 and 1500 rpm, with additional runs at 2000 rpm as time allowed. Two runs at each rpm value (one port side aspect and one starboard side aspect) have been used for the analysis presented in this paper.

4.4 Trials Location

Three locations were selected for the trials, one preferred location and two backup locations, all off the north east coast of England. The backup locations were chosen to allow options for the measurements to continue in the event of poor weather conditions, albeit at a less ideal location to fulfil the aims of the trial. The preferred location was located approximately 28 km from the coast. The water depth at this location was approximately 100 m and the seabed type consisted of soft mud. The other two locations were in shallower water and closer to shore in slightly more sheltered areas. All of the data presented in this paper are from measurements undertaken in the preferred deep water location.

4.5 Data Analysis Procedures

Typically, data acquisition for each run was started when the target vessel team confirmed to the off-board measurement team via VHF radio that they had reached the COMEX position and stopped when the target vessel reached the FINEX position. The first stage of the analysis procedure was therefore to define the time window in the data corresponding to $\pm 30^\circ$ either side of CPA for each vessel run. This was achieved using GPS data to calculate the speed of the vessel, v (in this case Speed Over Ground, SOG) and defining the data window period, DWP :

$$DWP = DWL/v \quad (1)$$

The measurement system was synchronised to GPS time and hence the analysis window for each run can be defined from the above.

The same analysis procedure was used for recorded data from each of the three hydrophones. The section of data corresponding to the DWP for each run was split into 1 second samples and a Hanning window applied to each sample. The Power Spectral Density (PSD) of each sample was then calculated to obtain the received levels (RL) at the hydrophones in terms of dB re $1\mu\text{Pa}^2/\text{Hz}$. The PSD of the entire acquisition run was then calculated by averaging across all 1s samples (with no overlap of windowed data). One Third Octave (OTO) band levels are then calculated from the narrowband data by integration of the narrowband frequency points across each OTO band in accordance with the ANSI S1.11-2004 (ANSI/ASA (2009a)). Data are presented over the frequency range from 10 Hz to 10 kHz.

In order to determine radiated noise levels (RNL) of the vessel in terms of dB re $1\mu\text{Pa}^2\text{m}^2$ a range correction must be applied. The correction applied to the data in this paper is of the form:

$$RNL = RL + 20 \log_{10} \left(\frac{r}{r_{ref}} \right) \quad (2)$$

where RL is the received level, r is the CPA range and r_{ref} is the reference range (1 m).

The RNL is also referred to as the dipole or “affected” source level. This terminology reflects the fact that this quantity has not been corrected for interference effects caused by the interaction of sound propagating along direct paths between the source and receiver and indirect paths that are reflected from the sea surface and seabed. The series of peaks and troughs in received level resulting from reflections from the sea surface are often referred to as the Lloyd’s Mirror Interference Pattern (LMIP) and may be approximated by the expression: (Ainslie (2010))

$$LMIP = 10 \log_{10} \left(4 \sin^2 \left(\frac{k d_s d_r}{r} \right) \right) \quad (3)$$

where k is the wavenumber, d_s and d_r the source and receiver depths respectively, and r is the source-receiver range. Further discussion on this can be found in Ainslie (2010) and De Jong (2009).

The ANSI standard requires that data are presented as affected source levels and much of the data in the literature is also in this form. To allow comparison with the literature the spectral source level data presented in this paper are presented as “affected” source levels unless otherwise stated. However, as discussed by De Jong (2009), the analysis procedures described in the ANSI standard, in particular averaging across three hydrophones and across the DWP, mitigates to some extent the influence of this interference. This is due to the fact that the locations in the frequency spectrum of the peaks and troughs caused by the interference are highly dependent on the geometry of the measurements such as measurement range, source depth and receiver depth (as well as many other factors related to the environment during the measurements).

Figure 5 presents the results of LMIP predictions using the above expression for the trial geometry shown in Figure 1 and using the given source depth for the Princess Royal target vessel of 1.15 m. The figure demonstrates that while the peaks and troughs associated with the interference pattern are still evident after averaging, they are reduced when compared to those of a single receiver.

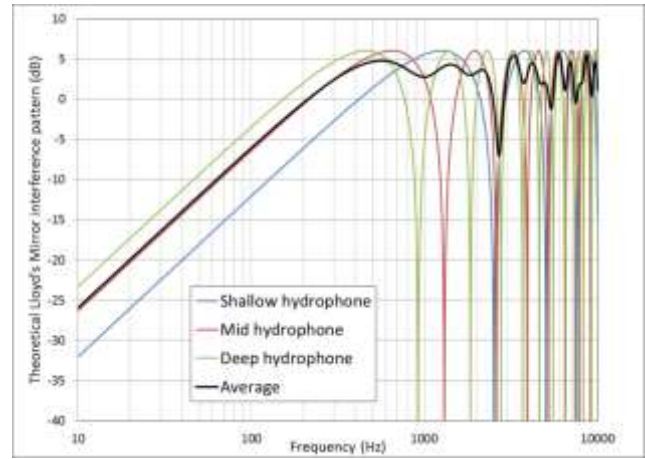


Figure 5 Theoretical Lloyd’s Mirror interference pattern. Horizontal CPA range = 100m, Source depth = 1.15 m, $d_1 = 27\text{m}$, $d_2 = 58\text{m}$ and $d_3 = 100\text{m}$

Analysis of recorded data as the vessel passes a receiver array presented as a spectrogram clearly demonstrates the LMIP effect in practice, as shown in Figure 6. These data are for a single pass of the target vessel at a nominal CPA range of 100 m. The point at which the vessel passes the hydrophone location can clearly be identified by the increase in received underwater noise levels at around 60 seconds into the recording (a smaller section of this file corresponding to the DWP has been used for detailed analysis). The “U-shape” that can be seen in the figure is the result of the LM effect and shows that the location in the frequency spectrum of the peaks and troughs changes as the vessel passes the receiver. In a similar way to averaging across multiple receivers, averaging the data across a vessel transit therefore further reduces the prevalence of the interference pattern in the data.

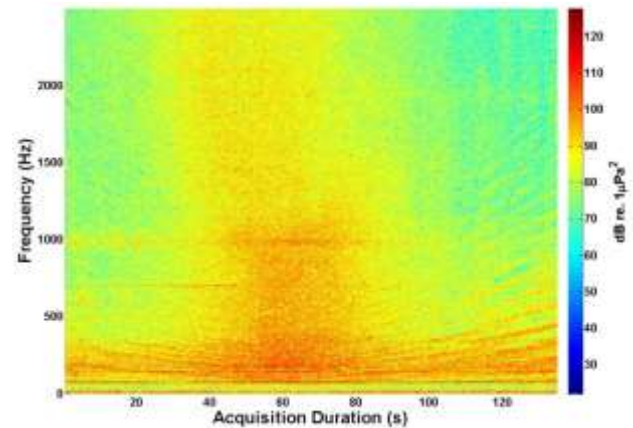


Figure 6 Spectrogram of vessel radiated noise for a pass at 100 m CPA and a speed of 11kn

In addition to multiple receiver and position averaging, the presentation of the measured data in terms of one-third-octave (OTO) bands rather than as narrowband (NB) spectral levels further reduces the prevalence of the interference pattern in the data, but does not reduce the significance of the low frequency fall off evident in Figure 5.

5 RADIATED NOISE DATA

5.1 Variation with Receiver Depth

Figures 7 and 8 present typical examples of the radiated noise levels measured on each of the three hydrophones in the vertical array during the SONIC trials. These data are dipole source levels, corrected for range assuming spherical spreading as in Equation 2, using the slant ranges between the source and each receiver. Figure 7 presents data for a low speed run at 600 rpm (4 kn) and Figure 8 shows data for a run at 1500 rpm (10.5 kn). The comparison indicates a clear increase in underwater noise levels between approximately 80 Hz – 10 kHz. Also evident in the higher speed run data in Figure 8 are the lower measured levels on the shallowest hydrophone which is a consistent feature in the data for all runs above 700 rpm. This is expected as indicated by the LMIP in Figure 5, the propagation losses are greater the closer the receiver is to the sea surface. The fact that this is less evident in the lower speed run data in Figure 7 reflects the fact that at low frequencies (below a few hundred Hz) the radiated ship noise is below the ambient underwater noise levels.

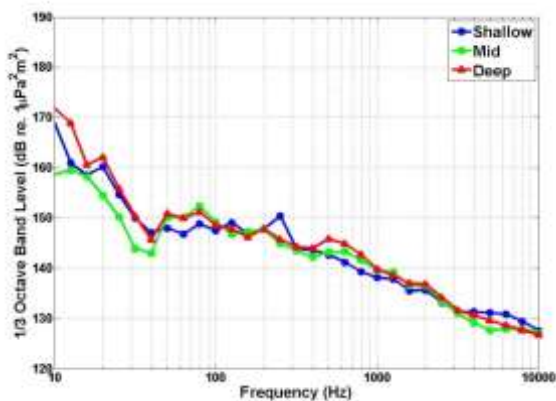


Figure 7 OTO band “affected” (dipole) source levels for target vessel at 600 rpm (5kn) calculated from measured pressures on individual hydrophones

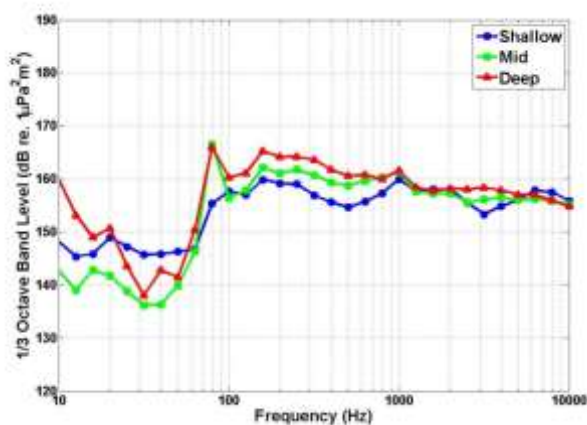


Figure 8 OTO band “affected” (dipole) source levels for target vessel at 1500 rpm (11kn)

Figure 9 presents data from the same acquisition as in Figure 8 but in terms of narrowband Power Spectral Density (PSD) levels.

This plot shows a number of important features of the radiated noise data. Firstly, the spectrum is characterised by a number of high amplitude narrow peaks in the frequency range from approximately 70 Hz – 400 Hz with the highest level peak at approximately 70 Hz. The target vessel has a gearbox ratio of 1.75 giving the propeller Revolutions Per Second (rps) at an engine speed of 1500 rpm as:

$$RPS_{prop} = \frac{1500/1.75}{60} = 14.3. \quad (4)$$

With a 5 bladed propeller this would give a blade passing frequency (BPF) of 71.4 Hz, corresponding to the highest amplitude peak in the narrowband spectrum with lower level peaks indicating harmonics of the ~71 Hz fundamental. The other lower amplitude peaks in the spectrum at frequencies greater than this fundamental occur at approximately 14 Hz intervals and are most likely a combination of higher harmonics relating to BPF, propeller shaft speed and engine firing rate.

Another important feature of the data shown in Figure 9 is the high levels of low frequency noise below about 20 Hz, particularly evident on the data measured on the deepest hydrophone which is consistent across the majority of the acquisitions. It is likely that this is associated with self-noise of the hydrophone array, probably from movement of the hydrophone vertically in the water column due to surface wave motion or laterally due the effects of the current. There may also be contributions from turbulent flow around the rope, protective cage and hydrophone itself. The analysis of spectral data indicates that this does not consistently affect the higher frequencies. While this source of noise in the system does not prevent further analysis of the data in terms of spectral levels it is very likely to influence the overall broadband radiated noise level data and hence further processing is required prior to undertaking this analysis (discussed in Section 4.3 below).

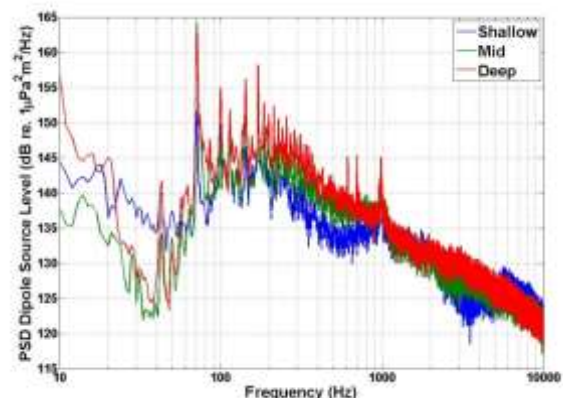


Figure 9 “Affected” (dipole) source level in terms of narrowband Power Spectral Density for target vessel at 1500rpm

5.2 Variation with Engine Speed – Spectral Data

Figure 10 presents RNLs for a number of vessel speeds from starboard aspect. This plot clearly demonstrates the increase in radiated noise as the vessel speed increases. The nature of this increase in RNL is similar to that attributed by other researchers to propeller cavitation noise (e.g. Wittekind (2014)). At lower ship speeds it is first evident in the higher end of the frequency spectrum, in this case above approximately 1 kHz when the speed is increased from 600 – 700 rpm. Clear increases are then seen above about 300 Hz between 700 – 900 rpm, 100 Hz between 900 – 1200 rpm and about 70 Hz from 1200 – 1500 rpm.

Figure 11 presents the corresponding dataset from the port side aspect runs. The measured RNL and spectral characteristics are in general very similar to the starboard side runs. The maximum increase in radiated noise is slightly greater for the port side aspect runs at approximately 33 dB while the corresponding value for the starboard side runs is approximately 28 dB.

In order to provide a comparison with what may be considered typical levels of underwater noise generated by a commercial ship the data may be compared to an adapted average ship source level model based on a large ensemble of measurements reported in Wales and Heitmeyer (2002). The model presented is in terms of the monopole source level for a ship. Therefore, in order to provide a valid comparison the dipole RNL data from the Princess Royal may be converted to an approximate monopole source level using equation 3. These data are presented in Figure 12. The comparison indicates that the radiated noise from the Princess Royal running at higher speeds is similar to typical underwater noise levels from a commercial ship operating at service speed.

The model does appear to overestimate the source level at frequencies below approximately 70 Hz. The Wales and Heitmeyer model is based on measurements of radiated noise from ocean going merchant vessels, likely to be considerably larger than the Princess Royal. Larger merchant ship engines and propellers tend to operate at a lower rpm than the target vessel in this study. Therefore, the peaks in spectrum level shown in Figure 9 associated with the blade passing frequency, engine speed and associated harmonics would be at lower frequencies in the spectrum. This may partly explain why the measured levels of underwater noise for the Princess Royal are lower than the model predictions in this part of the frequency spectrum.

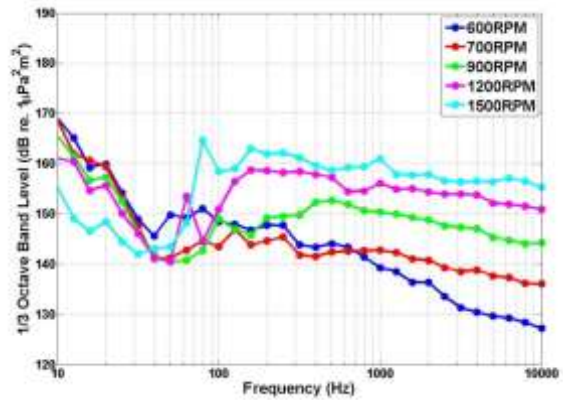


Figure 10 Radiated noise at several engines speeds measured in starboard aspect (averaged over three hydrophones)

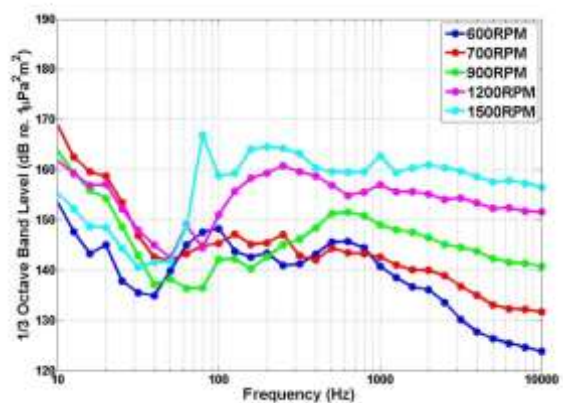


Figure 11 Radiated noise at several engines speeds measured in port aspect (averaged over three hydrophones)

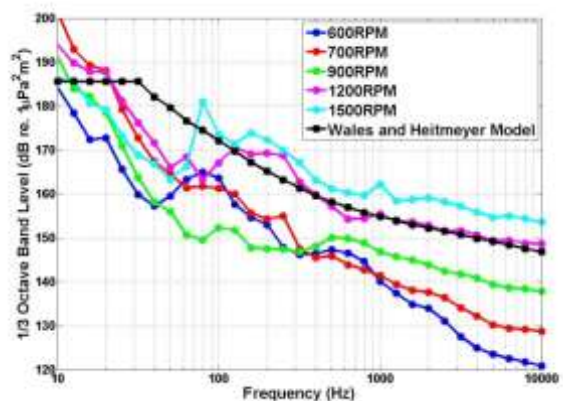


Figure 12 Approximated monopole source levels at several engines speeds measured in port aspect (averaged over three hydrophones)

5.3 Variation in Radiated Noise Level with Ship Speed – Overall Broadband Levels

As discussed above, the spectral data indicates that a considerable amount of low frequency noise, below approximately 20 Hz, is present in the recordings which is likely to be self-noise of the hydrophone array. Analysis of the raw data in terms of overall broadband RMS Sound

Pressure Levels (SPL) does not suggest a clear correlation between vessel speed and radiated noise levels. To investigate whether the low frequency components of the measured data are dominating the broadband analysis the data were reanalysed using a High Pass (HP) filter with a cut-off frequency (-3 dB) at approximately 24 Hz. It is appreciated that components of vessel noise are likely to extend to frequencies below 24 Hz and hence this filtering is not ideal. However, it is applied here to demonstrate the issue of system noise and to present further characteristics of the measured data.

Figure 13 presents the overall broadband RMS Source Levels as a function of ship speed for 16 vessel runs under various running conditions. This plot also includes data for a number of runs during which only the port side engine was running (whereas the preceding data has been for normal running conditions with both engines running).

Also shown in the figure is an historical speed dependence model (black solid line) first proposed by Ross (1976) based on extensive data from radiated noise trials undertaken during World War II. This model is of the form:

$$SL = A + c_v 10 \log_{10} \left(v/v_{ref} \right) \quad (5)$$

where A and c_v are given constants, v is the ship speed and v_{ref} is a ship reference speed.

The purple dashed line shows a least squares fit to the SONIC measured data using the form of the Ross model. This is a fit to the normal running condition (both engines operational) data only, excluding the data from runs where only one engine was operational. The difference between the historical model and the fit to the measured data ranges between approximately 2 – 6 dB over the range of vessel speeds tested indicating that the model may underestimate the radiated noise levels from the target vessel over the range of vessel speeds tested.

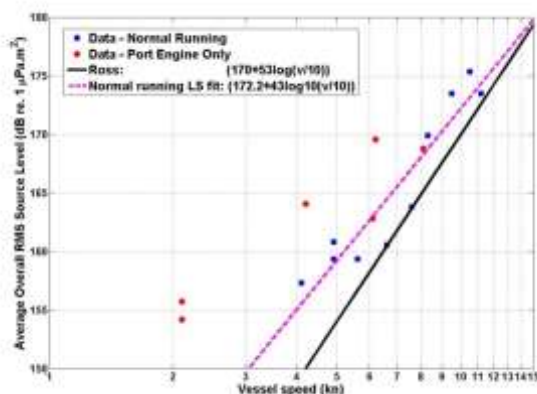


Figure 13 Overall broadband RMS Source Level vs. vessel speed. Also shown is the classical model from Ross (1976) and also a non-linear least squares fit to the measured data

6 DISCUSSION AND CONCLUSIONS

The measurement of radiated noise from ships to meet the recently published international standards is a challenging

undertaking. In the absence of a fixed noise range, a vessel deployed mobile hydrophone array is the most viable alternative. The design and deployment methodology of such an array will inevitably have significant implications on the quality of the measured data due to possible self-noise of the array. The data presented in this paper provide an indication of some of the practical issues encountered with the deployment of a typical array.

Undertaking these measurements in Northern European waters is also particularly demanding due to the relatively shallow water depths and the presence of other vessel traffic (and hence generally high ambient noise levels). However, as a region incorporating some of the busiest shipping lanes in the world it is important to investigate and develop tools and techniques to accurately measure or monitor shipping noise under these conditions. The SONIC project aims to contribute to this understanding using a range of approaches of which these full scale trials are one.

While improvements to array design and deployment would certainly enhance the quality of the measured data, the results presented in this paper show that the radiated noise characteristics of a vessel operating under trials conditions can be ascertained in some detail using a relatively simple hydrophone array. Comparison of radiated noise level data with a widely used ship source level model indicates that the target vessel used in this work is fairly typical in terms of the levels of underwater noise generated by a commercial ship. A further comparison with another widely used model for variation in ship source level with speed has indicated that there is a clear positive correlation between radiated noise level and ship speed, although there is some disagreement between the measured data and model predictions.

(The research leading to these results has received funding from the European Union Seventh Framework Programme (FP7/2007-2013) under grant agreement n°314394).

REFERENCES

- Ainslie, M. (2010). "Principles of Sonar Performance Modelling." Springer.
- Andrew, R. K., Howe, B. M., Mercer, J. A. & Dzieciuch, M. A. (2002). "Ocean ambient sound: Comparing the 1960s with the 1990s for a receiver off the California coast." *Acoustics Research Letters Online*, **3**, 65.
- ANSI/ASA (2009a). ANSI S1.11: Specification for octave-band and fractional-octave-band analog and digital filters. Acoustical Society of America.
- ANSI/ASA (2009b). Quantities and Procedures for Description and Measurement of Underwater Sound from Ships- Part 1: General Requirements. Acoustical Society of America.
- Bahtiarian, M. & Fischer, R. (2006). "Underwater radiated noise of the NOAA ship Oscar Dyson." *Noise Control Engineering Journal*, **54**, 224-235.

- De Jong, C. (2009). "Characterisation of ships as sources of underwater noise". NAG/DAGA International Conference on Acoustics, Rotterdam, The Netherlands
- De Robertis, A., Dorn, M., Ferno, A., Gerlotto, F., Handegard, N. O., Hawkins, A., Jones, E., Josse, E., Parrish, J. K., Simmonds, E. J., Wood, D. & Wooder, B. (2012). "Causes and consequences of fish reaction to fisheries research vessels." Report Prepared for: Report from the Study Group on Fish Avoidance to research Vessels (SGFARV).
- Hallett, M. A. (2004). "Characteristics of merchant ship acoustic signatures during port entry/exit". Annual Conference of the Australian Acoustical Society, Gold Coast, Australia
- ISO (2012). Acoustics. Quantities and procedures for description and measurement of underwater sound from ships. General requirements for measurements in deep water. International Organization for Standardization
- McKenna, M. F., Ross, D., Wiggins, S. M. & Hildebrand, J. A. (2012). "Underwater radiated noise from modern commercial ships." *Journal of the Acoustical Society of America*, **131**, 92-103.
- Merchant, N. D., Pirota, E., Barton, T. R. & Thompson, P. M. (2014). "Monitoring ship noise to assess the impact of coastal developments on marine mammals." *Mar Pollut Bull*, **78**, 85-95.
- Peña, H., Øvredal, J. T., Totland, B., Olav, N. & Handegard, N. O. (2011). "Underwater sound measurements from fishing vessel "Brennholm"." Report Prepared for: Institute of Marine Research, Norway.
- Ross, D. (1976). "Mechanics of Underwater Noise." New York, Pergamon Press.
- Ross, D. (2005). "Ship Sources of Ambient Noise." *IEEE Journal of Oceanic Engineering*, **30**, 257-261.
- Scrimger, P. & Heitmeyer, R. M. (1991). "Acoustic source-level measurements for a variety of merchant ships." *J Acoust Soc Am*, **89**, 691-699.
- Urick, R. J. (1975). "Principles of Underwater Sound." New York, McGraw-Hill.
- Wales, S. C. & Heitmeyer, R. M. (2002). "An ensemble source spectra model for merchant ship-radiated noise." *Journal of the Acoustical Society of America*, **111**, 1211.
- Wenz, G. M. (1962). "Acoustic ambient noise in the ocean: spectra and sources." *Journal of the Acoustical Society of America*, **34**, 1936-1956.
- Wittekind, D. K. (2014). "A Simple Model for the Underwater Noise Source Level of Ships." *Journal of Ship Production and Design*, **30**, 7-14.

Propeller Cavitation Noise and Background Noise in the Sea

Dietrich Wittekind^{1*}, Max Schuster¹

¹DW-ShipConsult GmbH, Schwentinental, Germany

Abstract: Background noise in the sea due to shipping has increased continuously over the past decades and became a concern of environmentalists in particular concerning masking of communication calls of baleen whales. The cause of this low frequency noise is solely attributable to propeller cavitation at frequencies below 300 Hz. The noise spectrum features a characteristic maximum at around 50 Hz with most ships independent of type, size and speed. This spectrum and its cause are widely unexplained. This paper describes the observations made in full scale ships particularly with respect to the broad band part of the low frequency spectrum. A simple acoustic ship model is presented and procedures to investigate into the physics of noise generation by cavitation are suggested and the possible influence on background noise in the sea be estimated.

Keywords: Ship acoustics, cavitation, underwater noise, noise pollution.

1 INTRODUCTION

Background noise in the sea caused by anthropogenic sources became of increasing concern due to its possible negative effect on marine life. One of the last impressions concerning shipping noise came from IMO in early 2014 (IMO 2014).

The most pressing problem can be located in the low frequency regime below around 300 Hz (Andrew et al 2002, McDonald 2006). The background noise spectrum in the deep oceans has some similarity with the radiated noise spectrum of most individual ships. Frequencies below 300 Hz are used in vocalization of large baleen whales. Comparing background noise with and without ships suggests that the range over which the animals could communicate is reduced to a fraction due to the presence of ships. Figure 1 show the contribution for Sea state 2 and distant shipping derived from (Urlick 1983)

The discussion of whether shipping noise has an adverse effect on whales or marine life in general alone or together with other stressors will not be discussed here. Note, that shipping noise contribution has a characteristic shape with a peak at around 50 Hz.

In the following it shall be shown that background noise can be attributed to single ships and the low frequency part solely to the cavitating propeller. Measurements help to quantify this contribution. (Wittekind 2009). Emphasis is on large ocean going ships with fixed pitch propeller as these are the main sources of continuous low frequency noise from shipping.

2 THE NOISE SOURCE AND ITS CHARACTERISTICS

Six contributors to noise from propellers are identified:

1. Noise transferred to the hull from the pure displacement effect of the blades. This will show as multiples of blade rate and is hardly directly observable at distance. The effect comes also with the non-cavitating propeller. The

contribution observed in far field are not from direct radiation but likely rather from hull excitation through thrust variations

2. Tonals at blade rate harmonics caused by cavitation developing during passage of blades through areas with low inflow velocity
3. A broad band contribution in the frequency range where blade rate harmonics are observed
4. A broad band contribution at high frequencies caused by cavitation bubble collapse
5. Radiation of vibratory response of blades caused by turbulent flow over the blades. In case of the cavitating propeller this contribution is comparatively small
6. Tonals caused by vortex induced vibrations know as propeller singing. This phenomenon is understood as to only occur in case of the non-cavitating propeller

In this paper we consider only contribution 3 in connection with 2. While contribution 2 is understood as the main cause of vibration on board, the broad band part does not harm comfort or is in conflict with other criteria. However, low frequency broad band cavitation at low frequency can be seen as the primary cause for background noise in the sea as shown below.

The overall appearance of the resulting spectrum of a ship may look like Figure 2 showing also the relative contribution of machinery. Increasing speed leads to rapidly growing levels at low frequencies with little or no shift in frequencies while the spectrum rises from high frequencies towards low frequencies with increasing speed.

It is this contribution 3 which will be discussed in more detail.

3 MEASUREMENTS

Measurements were made onboard Hansa Europe, a 3,600 TEU container vessel during a voyage across the Atlantic. The ship is operated by Leonhardt & Blumberg. Measurements were made by the China Scientific Ship Research Center, Wuxi, China.

Vessel characteristics are:

Displacement:	63,581 MT
Length between PP	224 m
Breadth	32.2 m
Summer draft	12.5 m
Engine rating	31,710 kW at 104/min
Speed at 96.5 rpm	22 knots over ground
Power at 96.5 rpm	20,660 kW
Prop area ratio	0.732
Prop mean P/D	0.936
Prop diameter	7.75 m
Prop skew angle	37.8°
Prop number of blades	5
Prop designer/maker	Mecklenburger Metallguss

Five pressure transducers were mounted in the hull above the propeller in the propeller plane according to ITTC standard. Cavitation was observed via a borescope in another penetration.

Pressure variation analysis has been made up to a frequency range of 1,200 Hz with a resolution of 0.1 Hz.

Visual observation showed that the propeller develops not unusual sheet cavitation with strong vortex cavitation and vortex bursting. Pressure pulses at blade rate come up to 2.6 kPa at approximately 70% delivered power which is an acceptable result for this ship, Figure 3. Figure 3 suggests that in the normal display with linear scale on both axes that the harmonics of blade rate dominate the picture.

4 EVALUATION

Evaluation concentrates on the broad band, low frequency part of the spectrum but well beyond the range where blade rate harmonics seem to dominate. Figure 4 shows the averaged spectra for the highest and lowest speed measured with the third octave conversion for the higher spectrum. Note that the data in Figure 3 and 4 below 50 Hz is the same for the higher speed. It can be observed:

- Increasing speed leads to a uniform increase in level both for blade rate tonals and the broad band part in most parts of the spectrum. The increase follows a $80\log(\text{velocity})$ law
- The spectrum has a maximum at around 30 Hz for high speed and around 40 Hz at low speed
- At around 40 to 80 Hz the level hardly changes with speed
- At around 300 Hz the level rises more rapidly with speed in a narrow band without shifting

frequency. Under detailed evaluation this is due to a tonal component of around 320 Hz fluctuating heavily by 15 to 20 dB shown in the wave form in Figure 4.

However, the behavior and shape is widely unexplained. There are competing theories of what may cause the high contribution at around 40 Hz. In (Baiter 1992) it is attributed to the stochastic component of the mechanism which creates the high levels at blade rate harmonics. This would be in line with the observation in cavitation tunnels which show obvious fluctuations of cavitation voids in stroboscopic light. It is also supported by (Arveson et al 2000) who could calculate the volume of the void from received levels which fits well with what might be expected from a larger sheet cavitation bubble. A competing view names the tip vortex as the primary source (Raestad 1996). No publication known to the author tried to explain why the broad band spectrum has a maximum at around the same frequency for almost all ships independent of design (Arveson 2000, Heinke 1991) Wittekind 2013).

It is interesting to see what the contribution of the blade rate tonals to the broadband level in 1/3 octave is, see Figure 5. In this display the tonals lines have been manually removed. Their width is about 2 Hz. 1/3 octave summations have then been made for the narrow band spectrum with and without the tonals. It can be seen. That the first two harmonics dominate the 1/3 octave spectrum, the while the higher ones decrease in significance.

In a previous measurement described in (Wittekind 2013) a similar 3,400 TEU ship has been investigated in the same way. Comparison with the present ship is shown in Figure 6. The results can only be compared below 100 Hz. Although different designs from different sources and different propeller designers the spectra show a great degree of similarity.

5 RADIATED NOISE

Levels at pressure transducers are received at about 3 m away from the alleged source of the noise which is the cavitation bubble, however, moving relative to the receivers during its passage and during each measurement of 10 seconds duration. It is therefore not straightforward to estimate noise radiated into the far. Own experience showed that for the moment and if the requirements as to accuracy are not too high it can be assumed that what is measured at the hull is a source level although the distance to the real source (bubble) is about 3 m. It is further deliberately ignored that the level measured in a plate backed by air may be reduced due to the flexibility of the plate described by its mobility. Theoretically this would lead to a relative increase of the measured level with frequency as the mobility decreases with frequency. On top of this, all this can only be reasonable as long as the contribution 2 dominates over 1 (chapter 2) because only this can have a significant fair field effect. This view is facilitated by the assumptions that a bubble with

varying volume acts like a monopole which has a uniform radiation pattern in all directions.

A complexity of radiated noise in low frequencies is the presence of the water surface which can be seen as pressure release boundary with causes a phase shift of 180° on reflected waves. Noise from a source in its vicinity will have 2 propagation paths, one directly to a receiver, the other via reflection on the water surface. At the receiver they superimpose and leave an interference pattern called the Lloyd Mirror Effect (LME) (Urik 1983). At low frequencies the effect reduces to progressing cancellation of the 2 received sound waves with decreasing frequencies. This is illustrated in Figure 7. The LME is generally shown as the anomaly relative to spherical spreading (20log r; shown as dotted line at 0 dB in Figure 7). This anomaly is shown over a normalized distance.

A correct prediction of a received level requires the knowledge of source depth and receiver depth. If these are known the propagation loss from source to the receiver can be calculated from analytical formulas (Urik 1983). For the speed of sound of $c = 1,500$ m/s, a position of source depth at $z_s = 4$ m, receiver depth at $z_r = 50$ m and a distance of $r = 1,000$ m the propagation loss is according to Figure 8. Note, that deviations from the propagation loss according to spherical spreading of 60 dB is very significant. Spherical spreading is demanded by all international standards when calculating source level from received level. Obviously, these deviations become more significant at lower frequencies. In Figure 8 transmission loss above

$$f = \frac{c \cdot r}{8z_s z_r} \quad (1)$$

is 3 dB lower than spherical spreading and can be considered the average level of the interference pattern shown in Figure 7.

6 ACOUSTIC SHIP MODEL

The acoustic ship model is described in (Wittekind 2014). It relates size, the block coefficient, propulsive power, cavitation inception speed and speed of the ship to a radiated noise spectrum. There are 3 components of noise which are low frequency cavitation, machinery noise from 4-stroke diesels and high frequency cavitation noise. This model is continuously compared to most recent data and has been found reasonable. An update has been made which raises levels above 100 Hz for the low frequency cavitation component. The new function is now

$$F_1 = -4 \cdot 10^{-9} \cdot f^4 + 3 \cdot 10^{-6} \cdot f^3 - 0.0007 \cdot f^2 - 0.05 \cdot f + 135 + A + B$$

$$A = 80 \cdot \log\left(\frac{v}{v_{CIS}}\right) \cdot 4 \cdot c_B$$

$$B = 10 \cdot \log\left(\frac{\Delta}{\Delta_{ref}}\right)^{\frac{2}{3}} \quad (2)$$

With

f	frequency in Hz
A	factor modeling speed and block coefficient
B	factor modeling displacement
v	speed through water in knots
v_{CIS}	Cavitation Inception Speed in knots
c_B	block coefficient
Δ	displacement in t
Δ_{ref}	reference displacement in t = 10,000

For the ship in question assuming a cavitation inception speed of 13 knots and a block coefficient of 0.7 the predicted spectra appear as in Figure 9 for speed 21, 18 and 15 knots. The strongest variation with $80\log v$ is observed in the low frequency regime. The model has shortcomings with lightly or non cavitating propellers, at least if the estimated contribution of the non cavitating case (component 5) is considered. The prediction for contribution 5 results from extrapolation of own experience with naval ship propellers. In the frequency range above 300 to about 2000 there is a speed independent contribution from the auxiliary diesel engines, above that high frequency cavitation noise dominates.

7 COMPARISON OF MEASUREMENT AND MODEL

The model and the measurement are now easily combined, Figure 10. Also shown here is the received level assuming the transmission geometry of Figure 8. The model matches the measurement quite favorably, except for the frequency range above 200 Hz. At 300 Hz the unexplained high level which comes from a constant frequency effect the measurement is, naturally, considerably higher. Above 300 Hz the model does not expect any contribution from the low frequency effects from cavitation but rather from machinery noise. The prediction from the complete model therefore shows less deviation.

This measurement is a nice example of individual features of unexplained nature which may raise noise radiation of a ship by considerable levels.

There are verbal reports of ships which are also considerably quieter or noisier than what you might expect. One reason could be particularly good or bad wake field and propeller design, which, possible have a high reduction or augmentation effect on the broad band part.

8 CONCLUSIONS

The noise generated from the propeller of this ship is well within experience. Except for the tonal at 300 Hz and the

broad band part around 60 Hz it roughly changes with speed as assumed in the simple acoustic model.

It cannot be overlooked, however, that some crude purely empirical assumptions have been made to convert the measurement to radiated noise in some distance. More research in the related mechanisms is needed.

Findings cannot safely tell the effect of the main cavitation bubble as cause of the broad band spectral contribution from the one caused by effects from the tip vortex as both features appeared in all conditions measured. Further investigations are planned for clarification.

The acoustic ship model can be used as a bench mark to compare measurements of ships. More measured data is needed together with exact features of the ship such as displacement, block coefficient, draft and speed.

9 FURTHER WORK

It is intended to compare these measurements with cavitation tunnel measurements with the scale model and propeller at CSSRC. The radiated noise measurement under controlled conditions is also intended. The viability of model tests have been shown in few publications (Bark 1985, Heinke 1991). They offer a great chance to investigate broad band cavitation noise in model scale at much lower cost and ultimately systematically clear the picture to devise mitigation measures.

ACKNOWLEDGEMENTS

We are indebted to the technical staff of Leonhardt & Blumberg for the support and patience. We thank the technicians of CSSRC headed by Mme. Lu Fang for their professional work during measurements at sea.

Florian Holz has contributed greatly in post processing and evaluation of measured data.

REFERENCES

- IMO Marine Environment Committee (2014). 66th session Agenda item 17 'Noise from Commercial Shipping and its Adverse Impacts on Marine Life'
- Andrew, R. K., Howe, B. M. & Mercer, J. A. (2002). 'Ocean ambient sound: comparing the 1960s with the 1990s for a receiver off the California coast'. Acoustics Research Letters Online, **3**, 65-70.
- McDonald, M. A., Hildebrand, J. A. & Wiggins, S. M. (2006). 'Increases in deep ocean ambient noise in the Northeast Pacific west of San Nicolas Island, California'. Journal Acoustical Society of America, **120**(2), 711-718.
- Urik, R.J. (1983). Principles of Underwater Sound, 3rd edition Peninsula Publishing
- Wittekind, D. (2009). 'The Increasing Noise Level in the Sea' – a Challenge for Ship Technology Yearbook of the German Society for Maritime Technology

- Baiter, H.-J. (1992). 'Advanced Views of Cavitation Noise'. International Symposium on Propulsors and Cavitation, STG 1992
- Arveson, P. & Vendittis, D. (2000). 'Radiated noise characteristics of a modern cargo ship'. Journal of the Acoustical Society of America, 107(1), 118-129.
- Raestad, A.E. (1996). 'Tip Vortex Index – an Engineering Approach to Propeller Noise Prediction'. The Naval Architect July/August 1996
- Heinke, H.-J. (1991). 'Prognose von propellerinduzierten Schallpegeln aus Modellversuchen im Kavitationstunnel' (Prediction of propeller induced noise levels from model tests in a cavitation tunnel). Rostocker Schiffstechnisches Symposium, Sept. 1991
- Wittekind, D. (2013). 'Underwater noise generation of merchant ships: mechanisms and mitigation'. Internoise 2013, Salzburg, Austria
- Wittekind, D. (2014). 'A simple Model for the Underwater Noise Source Level of Ships'. Journal of Ship Production and Design, Vol. **30**, No. 1, February 2014, pp. 1–8
- Bark, G. (1985). 'Prediction of Propeller Cavitation Noise From Model Test and Its Comparison With Full Scale Data'. Journal of Fluids Engineering, 3/1985, Vol. **107**.

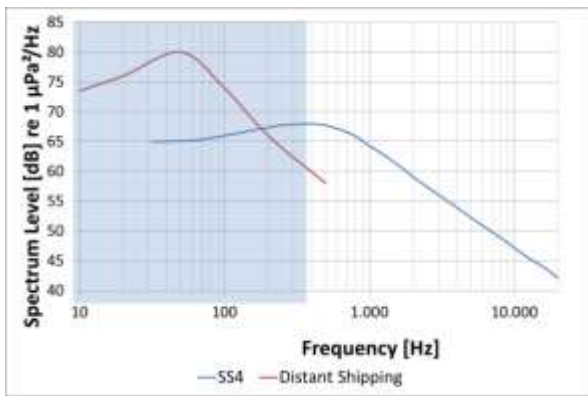


Figure 1 Background noise in the sea due to wind and waves and shipping derived from (Urick)

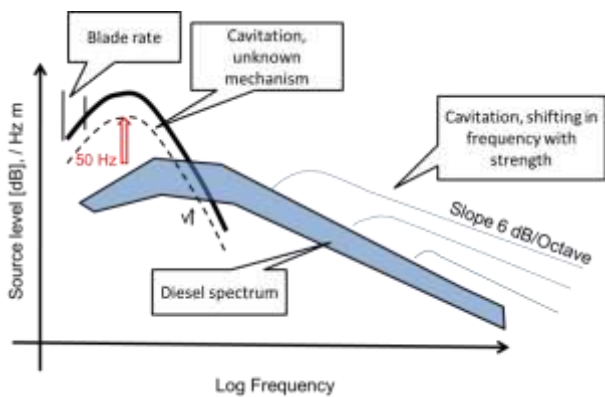


Figure 2 Generic spectrum of a commercial vessel with effects from speed variations

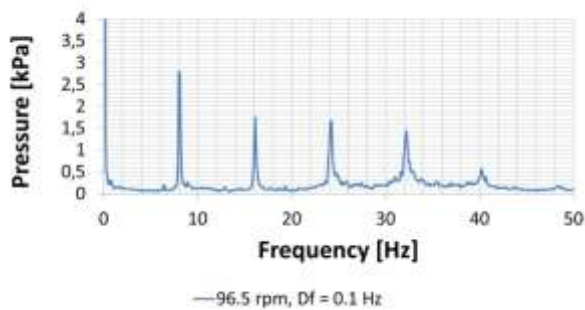


Figure 3 Pressure pulses

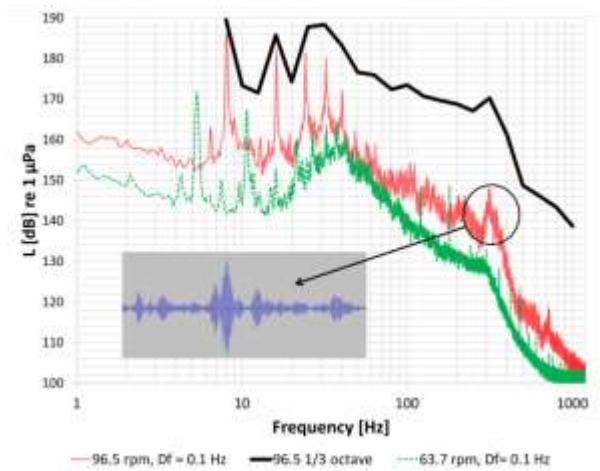


Figure 4 Narrow band spectra for highest and lowest speed measured and third octave display for high speed. Wave form is for band filtered range of 300 to 350 Hz

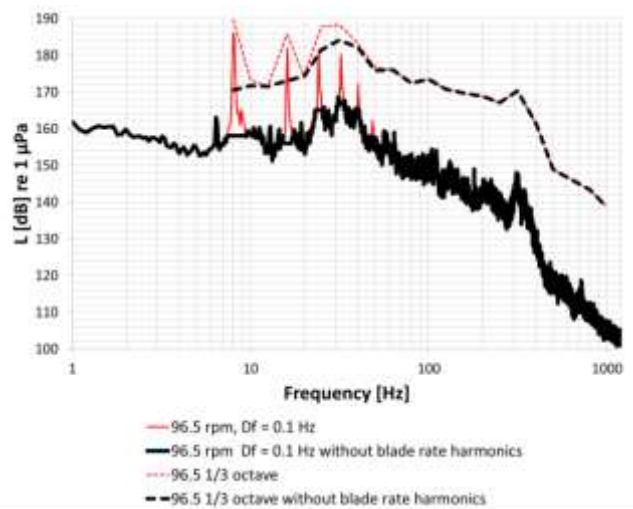


Figure 5 Influence of tonals on third octave spectrum

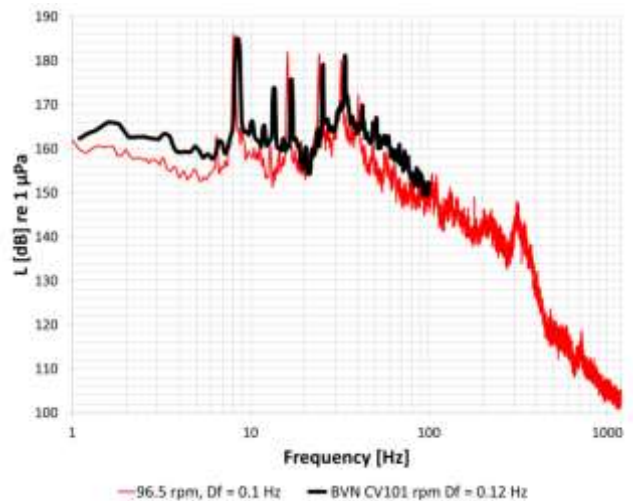


Figure 6 Comparison to results from a similar ship

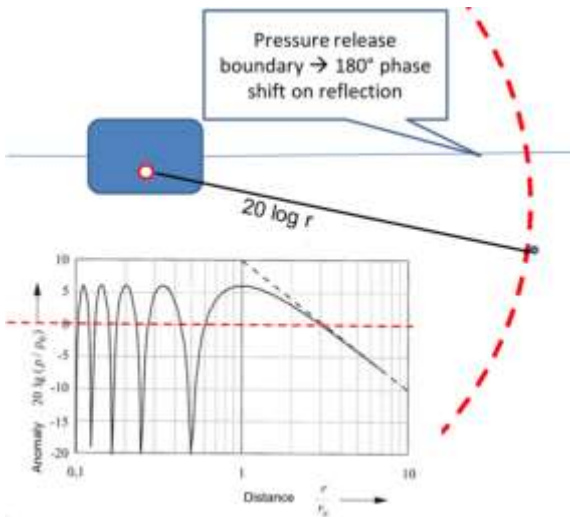


Figure 7 Illustration of the Lloyd Mirror Effect, Anomaly diagram from (Urick 1983)

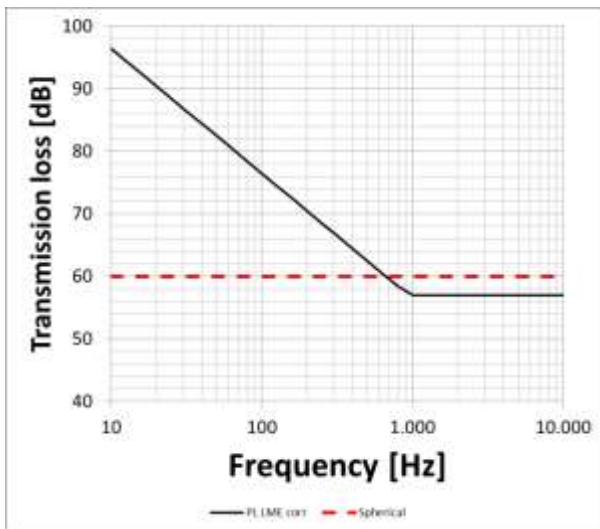


Figure 8 Transmission loss for 1000 m distance, source depth 4 m, receiver depth 50 m

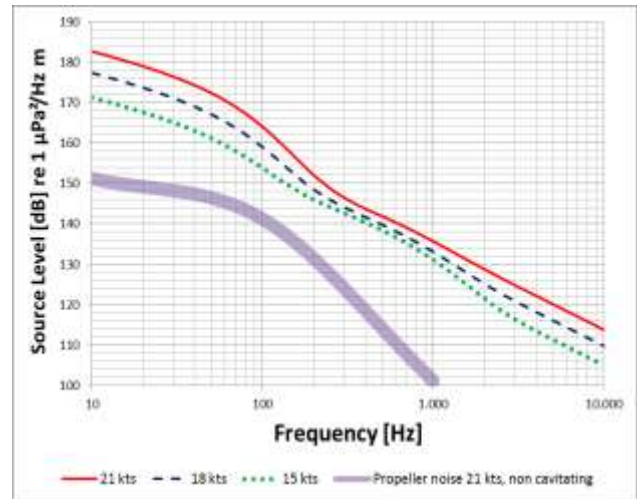


Figure 9 Acoustic ship model

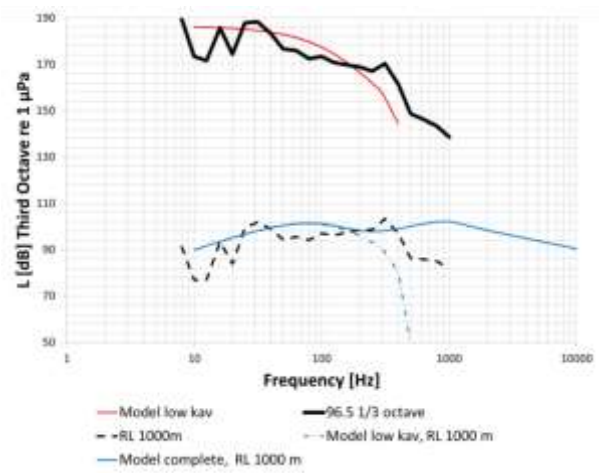


Figure 10 Comparison of measured data to acoustic ship model

Underwater Noise and Marine Wildlife: Current and Future Implication and Assessment

Paula Kellett^{1*}, Osman Turan¹, Atilla Incecik¹

¹Department of Naval Architecture, Ocean and Marine Engineering, University of Strathclyde, Glasgow, Scotland

Abstract: There has been growing concern regarding the potential impact of ship radiated underwater noise, and in particular propeller noise, on marine wildlife. Pressure from the US Government and conservation bodies has led the IMO to establish a committee to further investigate this issue. The EU has also taken steps to further knowledge in this area, through funding of research projects such as the recently completed SILENV Project, and the currently ongoing AQUO and SONIC Projects. Whilst ship radiated underwater noise is not currently formally regulated for the majority of vessels, several bodies have taken steps to propose thresholds and limits for various purposes, including those proposed by the EU research projects. These have been derived in a variety of ways. There are also a number of directives and legal instruments which directly or indirectly address the subject. These have again arisen for a variety of different reasons. This paper explores the existing and potential future requirements placed upon ship designers, owners and also upon flag states, in particular in relation to underwater noise and its impact on marine wildlife. It then explores the need for methods of assessing the potential impact of a particular ship on wildlife within its operational area. Three different types of assessment are discussed, namely biologically-based, rules-based and goals-based approaches. The methods are demonstrated by way of a case study example. Finally, the paper looks at ways in which the proposed methods could be extended or adapted in response to future changes in regulation.

Keywords: Impact assessment, marine wildlife, underwater radiated noise, regulations.

1 INTRODUCTION

The potential impacts of ship radiated underwater noise have been brought to the attention of the marine industry through the IMO.

There are several key potential impacts that are typically associated with the underwater noise radiated by transiting ships: masking, avoidance, behavioral changes and in very extreme cases, physical hearing damage. Masking is where important sounds, either from their own species, other species and predators/prey, or from natural sources are effectively drowned out by other sounds in a very similar frequency range. Avoidance behavior occurs when a sound source causes the animals to swim away from it, or even to stay away from a given area or migration route, usually for the duration of the sound but sometimes a period after the noise has ceased. Behavioral changes can take the form of different feeding, vocalisation, diving, breeding and swimming behaviors in response to a noise source (Nowacek et al. 2007), (Hildebrand 2004). Hearing damage, either temporary or more permanent, can occur when a noise with high sound pressure level (SPL) affects the sensitivity of the animals auditory system so that higher sound pressure above ambient is required before a given sound can be detected.

The potential impacts of ship radiated noise on marine wildlife has been considered by the fisheries research vessel community since the early 1990's however this concern was more driven by the need to improve fish survey results. Although several specialised groups of vessels such as cruise vessels have since started

addressing the acoustic performance (Vie 2013), it has not spread to the wider marine industry and hence it is only fairly recently that interest in the subject of impact on marine wildlife has reached the commercial sector.

Extensive research has been, and continues to be, carried out regarding all aspects of ship underwater acoustics: sources, propagation, prediction, reduction. There is also a very comprehensive body of literature covering research into marine wildlife hearing and vocalisation, sensitivity to and use of underwater sound, and reactions to anthropogenic underwater noise sources. However there has only been limited inter-disciplinary collaboration between these two distinct fields. In order to take both subjects forward towards the common goal of reducing the impact of ship radiated noise on marine wildlife, in a satisfactory way for both fields, this is indispensable.

The currently ongoing EU FP7 Framework Project AQUO (Achieving QUIeter Oceans) (AQUO Consortium 2012) has a dedicated work-package for conducting studies on different marine species representative to European maritime areas, aiming to derive criteria regarding shipping underwater noise acceptable limits and to further knowledge in this area. The project will also proposed noise reduction and mitigation measures, and these will also be assessed specifically on how to reduce the potential impact on marine wildlife. The SONIC Project (SONIC Consortium 2012), which is funded under the same call, also addresses some of these areas with close communication between the projects. It is important that such collaborative work continues, as this

* Corresponding author e-mail: paula.kellett@strath.ac.uk

will greatly assist in the development and furthering of knowledge.

This paper aims bridge the two fields, to further the discussion on this subject.

2 CURRENT REGULATORY LANDSCAPE

At present, only the underwater acoustic performance of fisheries research vessels is formally regulated. There are no formal regulations for any other commercial vessels, and for naval vessels where acoustic performance is considered, this is not carried out with regard to impact on marine wildlife. Several bodies have produced proposed underwater radiated noise limits, and these will be discussed in later.

Notwithstanding the absence of formal regulation, it is important to consider the other requirements which are places upon designers, ship owners, flag states and governments in relation to underwater noise and its potential impacts on marine wildlife. The following section will discuss these existing legal instruments. Comprehensive discussions on these instruments can be found in Simmonds et al. (2004) and Scott (2004).

Listed below are the main legal instruments which have to be considered as they relate, directly or indirectly, to the impact of ship radiated underwater noise on marine wildlife.

National

- The US Marine Mammal Protection Act (MMPA) of 1972, as amended in 2007
- The EU Marine Strategy Framework Directive (MSFD) (2008/56/EC) established in 2008
- 1997 Council Directive 97/11/EC, on the Assessment of the Effects of Certain Public and Private Projects on the Environment
- 1992 Council Directive 92/43/EEC, on the Conservation of Natural Habitats and Wild Flora and Fauna

Regional

- 1992 Agreement on the Conservation of Small Cetaceans of the Baltic and North Seas (ASCOBANS), extended in 2008 to include the North East Atlantic and Irish Seas
- 1996 Agreement on the Conservation of Cetaceans of the Black Sea, Mediterranean Sea and Contiguous Atlantic Area (ACCOBAMS)
- The Helsinki Commission (HELCOM), which is the governing body of the "Convention on the Protection of the Marine Environment of the Baltic Sea Area"
- 1979 Bern Convention on the Conservation of European Wildlife and Natural Habitats
- The Convention for the Protection of the Marine Environment of the North-East Atlantic, also known as the "OSPAR Convention"

- The Joint Nature Conservation Committee (JNCC) which is the statutory adviser to Government on UK and international nature conservation.

International

- 1979 Convention on the Conservation of Migratory Species of Wild Animals (also known as CMS or the Bonn Convention)
- The United Nations Convention on the Law of the Sea (UNCLOS) from 1982 and the United Nations Open-Ended Informal Consultative Process on Oceans and the Law of the Sea (UNICPOLOS) which has been operating since 2004
- International Maritime Organisation's (IMO) Resolution A.927(22) 2001"Guidelines for the Designation of Special Areas Under MARPOL 73/78 and Guidelines for the Identification and Designation of Particularly Sensitive Sea Areas"
- The International Union for the Conservation of Nature (IUCN) Resolution RESWCC3.068 which was the first to deal with underwater noise pollution problem at the global level
- The International Whaling Commission (IWC) Resolution 1998-6
- Work by many conservation groups, such as International Council for the Exploration of the Seas (ICES), the International Fund for Animal Welfare (IFAW), the Whale and Dolphin Conservation Society (WDCS), and the International Ocean Noise Coalition (IONC)

The EU Marine Strategy Framework Directive (MSFD) requires all member states to prepare national strategies to manage their seas in order to establish a good environmental status (GES) by 2020. GES Descriptor 11 specifies that "Introduction of energy (including underwater noise) does not adversely affect the ecosystem" and therefore covers ship noise specifically. Governments will therefore be required to gather evidence and data to support their reporting with relation to this requirement. This is the only instrument to do so, with the remainder placing requirements on either marine wildlife protection or pollution prevention. Several instruments require the parties to ensure that prohibition against intentional taking or killing of any covered species or habitat is covered by national law, where "take" is typically defined to include harassment or activities which would result in the harassment of these species or habitats. In other instruments, the pollution of the seas is discussed, with the input of energy being discussed however it is not clear whether noise is included in this bracket. The lack of clarity regarding the implications of these instruments and directives has meant that they have not been used in the regulation of underwater noise from ships, by both designers and regulatory bodies. It is also felt that trying to adapt these instruments to more specifically cover underwater noise would not be the most

suitable approach for governance, and it may be more appropriate to produce new specific regulations.

Under the United Nations Convention of the Laws of the Sea (UNCLOS) Art. 211, member states have a duty to establish international rules and standards and flag states to adopt laws and regulations. The absence of any international regulations on noise do not change the duty of coastal and flag states to implement their own laws, and in fact gives states an option to introduce unilateral regulations in their own waters. Recently, several flag states have taken steps towards such measures, either by implementing protected areas or by setting their own limits for underwater noise emissions within their own waters. Marine Protected Areas (MPA's) which are being established globally, and it may be that these are also utilised within such regulations, as areas for low noise emissions.

As any formal regulation on a global scale would require global agreement and implementation, this could still be a long way off. Nevertheless, in the meantime, the requirement does exist for regional and national bodies to take steps towards ensuring that they comply with the existing directives and legal instruments. This is already beginning to take place and is likely to continue growing.

3 IMPACT ASSESSMENT OF UNDERWATER RADIATED NOISE ON MARINE WILDLIFE

Taking into consideration the requirements which already exist for considering ship acoustic characteristics as discussed above, and also the potential future obligations, it seems that there is a need for means of assessing both the impact of this noise on marine wildlife and also the general acoustic performance of the vessel. Three different approaches are proposed here for conducting such an assessment. The three approaches are termed Biologically-Based Assessment, Rules-Based Assessment and Goals-Based Assessment.

The following sections will outline the three different approaches which are proposed for use in assessing the impact assessment of ship radiated underwater noise on marine wildlife. The advantages and disadvantages of these approaches are outlined, and the type of information required for each approach is also discussed.

3.1 Biologically-Based Assessment

The biologically-based approach is based on the use of threshold values for different types of impact in different marine wildlife species. In particular, the threshold limits proposed by the US National Marine Fisheries Service (NMFS) have been considered (Southall et al. 2007) in this case. Within this paper, single exposure events for pulsed, multiple pulse and continuous sounds are considered in relation both physical and behavioral effects. The physical effect considered in this case is temporary or permanent damage to hearing, known as Temporary Threshold Shift (TTS) or Permanent Threshold Shift (PTS). The thresholds also vary for different functional hearing groups within the broader

group of marine mammals, i.e. cetaceans and pinnipeds. Table 1 below shows the limits, which are taken as constant for the full frequency range, that are proposed by NMFS in Southall et al. (2007), for continuous sound:

Table 1 NMFS Threshold limits

Threshold Type	Limit (dB re 1µPa)
Behavioral Changes in Pinnipeds and Cetaceans	120
TTS in Cetaceans	224
TTS in Pinnipeds	212
PTS in Cetaceans	230
PTS in Pinnipeds	218

These limits were developed by an expert panel who carried out an extensive review of all the available literature of marine mammal auditory and behavioral responses, and hence comparing a vessels performance against these limits should provide a good indication of how it might impact at least on mammal species in the short term.

The advantages of using this kind of approach, which is based on actual marine wildlife impact is that the benefits of noise reduction are clearer, and there is a clear limits which designers can aim for. This can make it more likely for designers and ship owners to consider these limits when designing a new vessel.

The disadvantages of this approach are that the limits are generalised for large groups of species, where significant variations in habituation to noise, sensitivity and response may exist. The generalisation is also over a full frequency range, and so might prove to be very demanding to achieve in the lower frequencies but easier to abide by at higher frequencies where ship radiated noise tends to have a lower sound energy content. No account is taken of the likely distance of species to a vessel, as the limits quoted are for vessel source level.

The approach here uses only a small number of threshold values however this could easily be expanded to include additional species such as fish, and additional impacts. The limits discussed here only take into account single exposure events for short term impact however the authors of the paper noted that with additional research, these limits could be refined to take account of longer-term impacts on not only individuals but also indirect impacts on population groups.

3.2 Rules-Based Assessment

The rules-based assessment uses ship radiated noise limits which have to date been proposed by various research groups and regulatory bodies. Only one of these limits, the International Council for the Exploration of the Seas (ICES) limit (Mitson 1995), which is a regulatory requirement for fisheries research vessel, is compulsory at present. This limit defines the allowable acoustic performance for fisheries research vessels, with the lower

limits aiming to minimise avoidance behavior in fish species and based on Atlantic Cod and Herring hearing, and the higher frequencies aiming to improve acoustic equipment performance by minimising vessel self-noise. This is also the only limit which takes into account consideration of marine wildlife, as the remaining limits discussed here are only based on what the researchers felt was achievable for current world fleets using available knowledge, techniques and technology.

In 2010, classification Det Norske Veritas (DNV) released the optional "SILENT" class notation (DNV 2010). The notation provides specific limits designed for four different groups of classes in which acoustic performance is important to the main task of the vessel, called Acoustic, Seismic, Fisheries and Research. In addition, an Environmental limit is proposed, for use by any vessel wanting to demonstrate controlled noise emissions. It is this final limit which is considered in this case, as it has a much wider applicability than the more category-specific limits. The limit takes the form of two conditions: a transit limit for vessels at service speed or 85% MCR, and a quiet cruise limits of 11 knots for vessels over 50m in length, and 8 knots for shorter vessels.

One of the major outputs of the EU-funded FP7 Framework Project SILENV (Ships oriented Innovative soLutions to rEduce Noise and Vibrations) which ended in 2012 was a "Green Label" proposal which includes target levels for onboard and emitted noise and vibration (SILENV Consortium 2012). The underwater radiated noise limits proposed here were initially based on the DNV Environmental limit but were refined and made more stringent following comparison of the initial limits against measured in-service vessel spectra. As for the DNV limit, this is proposed initially as an optional notation and addresses two different conditions.

Figure 1 below presents a comparison of the ICES, DNV and SILENV limits. All of these limits are again specified for source level.

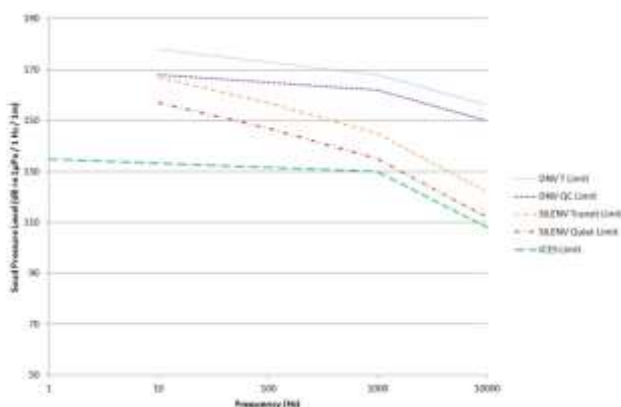


Figure 1 Comparison of underwater noise limits

The advantages of using these limits for assessing the acoustic performance of vessels is that whilst they may be stringent, they should be achievable for the majority of vessels. The limits also take into account variations in

typical spectra between the lower and higher frequency sections. Furthermore, being able to use a recognised Class notation for a vessel may make it more appealing to designers and ship owners.

The disadvantages are that in the case of the ICES limit, it has been designed for a very specific purpose and so has limited applicability for different vessels. It does however take marine wildlife impact into consideration in part. The DNV and SILENV limits are intended to be applied to commercial vessels in general and are less specific however they do not consider marine wildlife impact. It could therefore be difficult to demonstrate whether or not vessels complying with these limits are "better" in terms of minimising impact on wildlife.

3.3 Goals-Based Assessment

The IMO definition of goals-based assessment is *Goal-based regulation does not specify the means of achieving compliance but set goals that allow alternative ways of achieving compliance*". Given the complexity of ship radiated noise and the many potential impacts it could have on a wide variety of species, the authors feel that this problem is remarkably well suited to governance by goals-based standards. Here, a goals-based approach is applied for the assessment of the potential impact of ship radiated underwater noise on marine wildlife.

There is a huge array of information available in the literature regarding the hearing, and where applicable the vocalisation frequency ranges for a significant number of species, along with information regarding their habitats, conservation status and any observed or measured reactions to different noise sources. In this approach, it is proposed that this wealth of information could be used for impact assessment. In order to assist with this assessment, a database was compiled containing the above information, from a wide range of sources. Filtering the database for a given ships operational areas will provide a list of species which have the potential to be affected by the vessel operating in that area. The vessels underwater radiated noise spectra, over the frequency range containing the majority of the sound energy, can be compared with the hearing and vocalisation ranges of these species to identify those which may experience behavioral changes, avoidance and masking impacts. The conservation statuses of the species will help to identify which species may require particular attention. The information regarding previously observed or measured reactions to known underwater noise sources will also provide an indication of the likely response for similar cases.

The advantages of this type of approach is that it specifically takes into account the marine wildlife aspects. In addition, this approach does not apply a general limit for all cases. It allows for appropriate measures to be applied for a given set of conditions and scenarios. This means that excessive time and cost is not incurred in addressing the acoustic performance of a vessel in a case

where only very particular changes at perhaps a given frequency range would be required.

The disadvantages of this approach are that it is not as prescriptive as the other approaches, and therefore requires more effort on the part of the designer and ship owner. There is also likely to be some discrepancy between what a designer or ship owner view as appropriate measures, and what a marine biologist would feel was suitable. For this reason, inter-disciplinary collaboration would be required for the development of a more formalised goals-based approach.

4 CASE STUDY

In order to demonstrate the three approaches for impact assessment discussed above, a case study commercial vessel has been used. The operational area of the vessel is assumed to be within the Mediterranean Sea for the purposes of this case study. Using this operational area, and the marine wildlife database outlined previously, filtered for operational area and conservation status, the following has been observed:

- Not evaluated - 2 species
- Data Deficient - 5 species
- Least Concern - 5 species
- Vulnerable - 2 species
- Endangered - 2 species
- Critically Endangered - 2 species

Taking into account those species which may be considered specifically at risk, i.e. those listed as vulnerable and above, we can obtain Table 2 below:

Table 2 At risk species in operational area

Species	Hearing Range (Hz)	Vocalisation Range (Hz)	Observations
Atlantic Bluefin Tuna	50-1100	N/A	Changes to swimming and schooling behaviors at 135dB in reaction to ferries
Fin Whale	14-1000	10-28000	Behavioral effects at 15-100Hz, dives or faster swimming at around 1km distance, masking effects of social calls at low frequencies
Great White Shark	10-100	N/A	None Published

Green Turtle	Unknown	Unknown	None Published
Mediterranean Monk Seal	2000-40000	Unknown	None Published
Sperm Whale	100-20000	100-20000	Reactions can be variable, and include changing direction, shallower dives, avoidance at up to 2km and changes in breathing patterns

It should be noted that a species should not be disregarded simply because its conservation status is less of a concern. This sample has been taken in this case for the sake of simplicity. This smaller sample will be used in the example impact assessments below.

4.1 Biologically-Based Assessment

Firstly applying the biologically-based assessment, Figure 2 below shows a comparison of the commercial ship noise spectra at source whilst operating at 19 knots, and the NMFS proposed limits which were discussed previously. The frequency range of 0-1000Hz is considered, as this is typically the range where most of the ship noise power is focused:

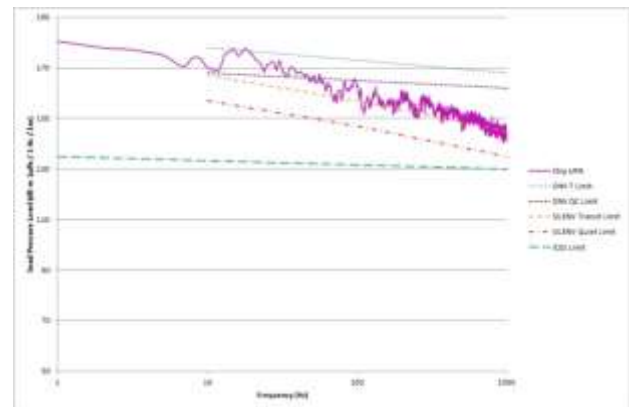


Figure 2 Comparison of ship spectra with biologically-based limits

It can be seen the noise levels are still significantly below the limit for temporary or permanent hearing damage in both cetaceans and pinnipeds, meaning that such impacts are extremely unlikely. However the level is above the limit for behavioral changes and hence it is likely that responses such as changes in breeding, feeding and swimming behavior may be observed.

4.2 Rules-Based Assessment

Now considering the same ship noise spectra in comparison to the ICES, DNV and SILENV Limits

discussed previously, Figure 3 below presents a comparison:

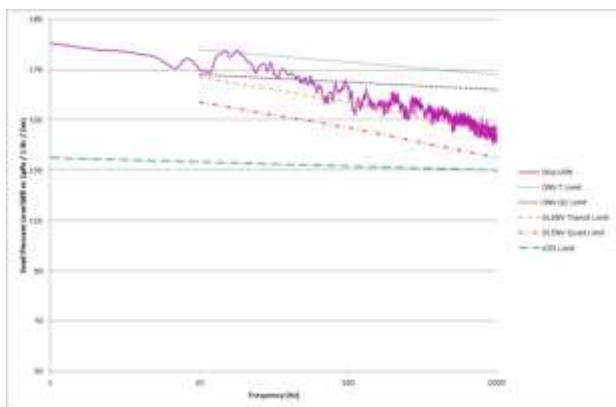


Figure 3 Comparison of ship spectra with rules-based limits

It can be seen that except for a few tonal peaks at around 20Hz, the vessel complies with the DNV Transit limit, and also generally complies with the DNV Quiet Cruise limit. It does not comply with the SILENV limits. The vessel in this case is travelling faster than the requirements for compliance state however there may still be some areas requiring attention to ensure full compliance. The vessel does not comply with the ICES limit, but again, this is intended for vessels travelling at 11 knots, and is also more specific to fisheries research vessels, this is to be expected. However it does give an indication that noticeable impacts on fish species would be expected from the vessel

4.3 Goals-Based Assessment

Now looking at Table 2 with a view of a goals-based approach, it can be seen the exception of the Mediterranean Monk Seal, whose hearing range is above the main noise range for commercial ships of 0-1000Hz, the other species have hearing and vocalisation ranges coinciding with the vessel. This indicates that these species will be able to detect the sound of the vessel, and hence if they are too close, it may cause avoidance and behavioral changes. The two whale species, whose vocalisation ranges also overlap with the vessel spectra, are also likely to experience some masking effects on their own communications. The noted observations provide further indications of what impacts may be expected for the different species. Using such an assessment method, a designer would then be more aware of which frequency ranges may be more problematic and which species' impact should be considered in particular. It should be noted that in some cases, information is not known. This highlights the need for continued research in this area, and does not mean that these species can be neglected.

5 POTENTIAL FUTURE REGULATION

There are several aspects of this subject which are likely to become subject to future regulation and standardisation.

Firstly, ship underwater radiated noise is likely to become more formally regulated, probably through international agreement however this is unlikely to come into force in the very near future. Such regulations would require international agreement on limits and implementation and would hence be very complicated. There are several ways in which the noise may be regulated. Broadband limits, such as those defined by ICES, DNV and SILENV may be applied, either as a general limit or with varying levels in relation to different operational areas or receiver species. Specific zones such as Marine Protected Areas (MPA's) may be utilised as designated "quiet" areas, with ships transiting through or near the areas being subject to requirements on noise emissions or transit speed, or with restrictions being placed on operations at certain times. This could also be implemented in terms of an overall quota for an area, with restrictions being placed based on the number of vessels operating in the area at a given time, with possible links to AIS data to aid in governance. Nevertheless, whichever approach is eventually implemented, methods for impact assessment are likely to be important in allowing for informed decision making. It should be noted that this should not be done with parties in isolation, instead all interested parties from the maritime industry; government and flag state bodies, classification societies, naval architects (designers), owners, operators and marine biologists should all be involved.

Secondly, standardisation of ship noise prediction and measurement procedures and reporting will also be required to allow for comparable results to be achieved. Collation of these results into publically available databases would also be extremely useful to aid in future decision making as the current status will be more clear, however these may arise issues with confidentiality. Within the currently ongoing EU-funded FP7 Project AQUO, a new proposed standard for underwater noise measurement, post-processing and reporting is being created. This will aim to address measurement in both deep and shallow waters, which are more common within European water. It will also define approaches for different levels of measurement accuracy, depending on the time and resources available.

Thirdly, standardisation of data gathering and reporting in relation to the responses of marine wildlife species to anthropogenic underwater noise sources will be required. At present, there is a significant variation in the information provided, meaning that some of it is difficult to use or compare. It is important for designers to know the acoustic details of the anthropogenic noise sources and the propagation properties of the area, while for marine biologists information about the species, the population group and the nature of the response may be more relevant. This information can be expensive and

difficult to gather and it is therefore important that the results can be widely used. Requirements for Governments to gather data and evidence such as that required for reporting on the Marine Strategy Framework Directive (MSRD) within the EU may also aid in furthering such standardisation.

6 DISCUSSION AND CONCLUDING REMARKS

It can be seen from the discussions above that although steps have been taken in the understanding and the control of ship radiated underwater noise and its impact on marine wildlife, there is much more to be done. There is a complex situation arising, as there does appear to be some impact from ship underwater radiated noise on marine wildlife and therefore action should be taken, however the full nature and extent of this impact is not well understood and therefore it will be difficult to develop appropriate and proportional control measures and regulations. There are already some requirements placed on governments and flag states, such as those outlined by the EU MSFD, however they do not clearly state how impacts should be assessed. Designers may also experience similar problems when making changes to their designs, especially prior to the implementation of any formal regulations or limits. Within this paper, several impact assessment methods have been proposed to address this difficulty, and provide several means of assessing the impact which ship radiated noise could be having on marine wildlife species, using publically available data and information. A goals-based approach is proposed as being particularly suitable for this situation, as the very complex and varying nature of ship acoustics and the recipients may make more general and overarching regulation unsuitable. There would however need to be discussions with all interested parties in agreeing what measures may be deemed appropriate, as a designer or ship operator and a marine biologist are likely to have very varying opinions. For this reason, some bodies may prefer to implement either biology- or rules-based assessment measures. Ideally, if limits could be developed which took into account both marine wildlife impact and what is technologically possible for current fleets, these may be more simple to implement and regulate. However having too many different assessment measures for different purposes will cause confusion, therefore a single method should be settled upon and implemented globally.

ACKNOWLEDGEMENT

The work presented in this paper was partially funded by the FP7 AQUO project (Achieve Quieter Oceans by shipping noise footprint reduction. Project Reference: 314227 under FP7-SST-2012-RTD-1)

7 REFERENCES

AQUO Consortium. (2012). Achieve Quieter Oceans by Shipping Noise Footprint Reduction. Available at: <http://www.aquo.eu/> [Accessed August 21, 2014].

DNV. (2010). Rules for Classification of Ship: Part 6, Chapter 24 - Silent Class Notation. , (1322), pp.1–18.

Hildebrand, J.A.. (2004). ‘Impacts of Anthropogenic Sound on Cetaceans’. Sorrento, Italy. Available at: <http://cetuc.ucsd.edu/Publications/Reports/HildebrandIWCSC-56-E13-2004.pdf>.

Mitson, R.B. (1995). ‘Underwater Noise of Research Vessels: Review and Recommendations’. Lowestoft, Suffolk. Available at: http://www.denix.osd.mil/nr/crid/Coral_Reef_Initiative_Database/Underwater_Noise_files/Ritson,1995.pdf.

Nowacek, D.P., Thorne, L.H., Johnston, D.W., Tyack, P.L. (2007). ‘Responses of Cetaceans to Anthropogenic Noise’. *Mammal Review*, **37**(2), pp.81–115. Available at: <http://doi.wiley.com/10.1111/j.1365-2907.2007.00104.x>.

Scott, K.N. (2004). International Regulation of Undersea Noise. *ICLQ*, **53**(April), pp.1–32. Available at: <http://www.mmc.gov/sound/internationalwrkshp/pdf/scott.pdf>.

SILENV Consortium. (2012). Green Label. ‘Noise and Vibration label proposal’. Available at: <http://www.silenv.eu/> [Accessed August 29, 2013].

Simmonds, M.P., Dolman, S. & Weilgart, L.S. (2004). *Oceans of Noise*, Chippenham. Available at: http://www.wdcs.org/submissions_bin/OceansofNoise.pdf.

SONIC Consortium. (2012). ‘Suppression Of underwater Noise Induced by Cavitation’. Available at: <http://www.sonic-project.eu/> [Accessed September 15, 2014].

Southall, B.L., Bowles, A.E., Ellison, T.W., Finneran, J.J., Gentry, R.L., Ketten, D.R., Miller, J.H., Nachtigall, P.E., Richardson, W.J., Thomas, J.A., Tyack, P.L. (2007). ‘Marine Mammal Noise Exposure Criteria: Initial Scientific Recommendations’. *Aquatic Mammals*, **33**(4), pp.411–521. Available at: <http://link.aip.org/link/?JASMAN/125/2517/3>.

Vie, R., 2013. A Ship Designer’s Perspective on Noise and Vibration: A little bit of history. In Carnival Corporate Shipbuilding, ed. 2nd IMarEST Ship Noise and Vibration Conference. London: IMarEST.

Towards Human-Oriented Norms: Investigating the Effects of Noise Exposure on Board Ships

Rafet Emek Kurt¹, Ismail Hakki Helvacioğlu², Osman Turan¹

¹University of Strathclyde, Department of Naval Architecture, Ocean and Marine Engineering, 100 Montrose Street, G4 0LZ
Glasgow, United Kingdom

²Istanbul Technical University, Faculty of Naval Architecture and Ocean Engineering, 34469 Maslak-Istanbul, Turkey

Abstract: With current trends showing a decrease in crew numbers on board ships together with increased operational demands as well as increased paperwork, crew fatigue and comfort has become more critical and recently been given more importance. It is known that environmental factors have an effect on crew comfort and performance. The two outstanding environmental factors which exist in the shipboard environment are ship motions and noise, moreover, in these two areas the findings and lessons learnt from other industrial sectors are considered to be less relevant. Therefore, it was necessary to conduct research to understand the effects of these factors, so that, the lessons learnt can be integrated into design process in order to eliminate the adverse effects of the aforementioned two factors during operation. Due to having more obvious performance outcomes ship motions and motion sickness research attracted more interest where human response to noise have been neglected so far. Therefore, this paper reports the findings of research study which investigated the current levels of crew noise exposure through field studies. Furthermore, developed human response models to noise on board ships and SILENV green label noise standards will also be introduced in comparison with current normative framework.

Keywords: Noise on board ships, SILENV project, shipping noise, noise exposure, seafarers, IMO noise code.

1 INTRODUCTION

Today, together with technological developments, ships are equipped with sophisticated system and automation. Hence the trend to decrease the number of crew members on board ships has been triggered. However, these automated systems still require human intervention, when interpreting the information or when tasks require decision making. Therefore, when compared to the past, even though the physical workload of the crew members on today's vessels decreased, the cognitive load is much higher than it used to be. As a result, maintaining the performance of the crew is becoming more important than before to achieve safe shipping operations. Investigations of the shipping accidents showed that human error is the major contributor of shipping accidents which in turn caused more and more research to be focused on human performance and wellbeing on board ships.

In terms of human factors on-board ships, a naval architect's primary role is to ensure designing ships considering the needs of crew. It is important to mention that the environment on ships which crew members spend their day-to-day life is unique (motions, noise, vibrations, heat, smell etc.) and can be considered as the most extreme when compared with many other industries. Moreover, when it is considered that crew members not only work but also required to live and rest in this same environment for months long, the matter becomes more complex. Therefore, environmental conditions of ships should be designed in a way to ensure not only the health

but also the performance and wellbeing of crew members on board.

One of the most important environmental conditions on ships is motion. Due to having obvious consequences and performance outcomes on crew, 'motion sickness' was studied in-dept, resulting in numerous human response models which can be utilised to estimate the levels of comfort even at the design stage. However, shipping industry failed to develop similar knowledge and even awareness on noise which is one of the most important environmental factors on board ships.

Therefore, in this paper, the research conducted under EU FP7 SILENV Project will be explained which produced a 'Green Label Standard' for noise levels on board ships.

2 LITERATURE REVIEW

The most obvious effect of noise on human is called Temporary Threshold Shift (TTS) which is an auditory fatigue resulting from being exposed to hazardous levels of noise. When TTS becomes repetitive or exposure to very hazardous levels of noise happens Permanent Threshold Shift (PTS) may occur (Alberti 2001) and it would not be wrong to say that current regulatory framework is designed to protect workers from these hazardous noise exposures.

At this point it is important to mention about the two relevant noise standards which are applicable to ships. International Maritime Organization (IMO) recently

updated the old Code on Noise Levels on Board Ships (IMO 1981) with the new one (IMO 2012) which is enforced under the provisions of regulation II-1/3-12 of the SOLAS Convention. The code defines the minimum acceptable noise levels for ship compartments and considers that, when complied with, the equivalent continuous noise exposure of crew members will not exceed 80 dB(A). On the other hand EU Physical Agents Directive for Noise (EC 2003) aims to protect the workers' health from hazardous noise exposures by defining the daily noise exposure limits. This approach considers not only the noise emission levels that a worker is being exposed to, but also takes into account the time spent in that noisy environment. It can be said that the approach of EU Physical Agent Directive is more human focused when compared to the aforementioned IMO Noise Code. However, both regulations are not satisfactory enough when the effect of noise on crew performance and wellbeing is considered, furthermore, in this specific topic there is not enough research conducted in maritime domain. The aforementioned research gap and the need for diverting more research to this important area is also recognised by Martin and Kuo (1995).

Numerous research studies from other industrial sectors were focused on understanding the effect of noise exposure on worker performance and wellbeing. A review of the literature shows that exposure to noise has negative effects on human performance and wellbeing (Weston and Adams 1932, Broadbent 1954, Melamed and Froom 2002, Button, Behm et al. 2004, Melamed, Fried et al. 2004, Kurt, Turan et al. 2010). However, it is also possible to find examples of studies in the literature where researchers found positive relation or no relation between noise exposure and human performance (Jerison 1957, Harcum and Monti 1973, Harrison and Kelly 1989, White, Meeter et al. 2012)

The review of literature demonstrates conflicting findings amongst different studies which shows that the relationship between the noise exposure and human performance/wellbeing may change depending on the duration of noise exposure, type of noise, demography of the subjects, type and complexity of the task. Unfortunately, this situation makes the lessons-learnt from other industrial sectors to be less relevant and therefore less transferrable to the maritime domain. Therefore, effects of on-board noise levels on the human performance and wellbeing needs to be investigated and findings should be taken into account when defining new noise limits for ships.

3 NOISE CRITERIA

3.1 IMO Noise Code

The IMO Code on Noise Levels on Board Ships (resolution A.468 (XII)) has been in use for many years by regulatory bodies, ship owners and designers as

permissible noise limits. Recently some modifications were made to improve on the noise control/allowable exposure levels in the code (IMO 2012) which came into force in January 2013. The new noise limits were compared with the existing ones in Table 1.

Table 1 Noise level limits according to IMO Resolution A468(XII) 1981 and IMO Resolution MSC.337(91) 2012

Locations		IMO 1981 dB(A)	IMO 2012* dB(A)
Work spaces	Machinery spaces (continuously manned)	90	removed
	Machinery spaces (not continuously manned)	110	110
	Machinery control rooms	75	75
	Workshops	85	85
	Non-specified work spaces	90	85
Navigation spaces	Navigation bridge and chartroom	65	65
	Listening post, including navigation bridge wings and windows	70	70
	Radio room (with radio equipment operating but not producing audio signals)	60	60
	Radar rooms	65	65
Accommodation spaces	Cabins and hospitals	60	60/55
	Mess rooms	65	65/60
	Recreation rooms	65	65/60
	Open recreation areas	75	75
	Offices	65	65/60
Service spaces	Galleys, without food processing equipment operating	75	75
	Stores and pantries	75	75
Normally unoccupied spaces	Spaces not specified	90	90

**The limits for ship size greater than 10000 GRT are shown after /.*

As can be seen from this table, a number of noise limits were reduced considering the noise emissions only. Several classification societies and maritime authorities have already imposed more strict standards to control the ship noise (SMA 1973, ABS 2001, DMA 2002, GL 2003, LR 2004, MCA 2007). It is stated in the code that, when ships comply with the noise limits defined in Table 1, the equivalent continuous noise exposure of crew members will not exceed 80 dB(A).

3.2 EU Physical Agents Directive

The European Parliament were followed the same path by issuing physical agent directive to protect workers from risks arising from exposure to noise (EC 2003). The directive covers all workers who are exposed or

potentially to be exposed to risk from noise. The main difference between the IMO resolution and the EU directive is that the EU directive pay more attention to the workers' exposure to the noise emission rather than the source of noise. In a sense, it is a much better approach to regulate the noise limits in a human centred way. The exposure action and limit values defined by EU physical agents directive is shown in Table 2

Table 2 Exposure limit and action values defined by EU physical agents directive

	Daily exposure Levels	Peak levels
Exposure limit values	$L_{EX,8h} = 87 \text{ dB(A)}$	140 dB(C)
Upper exposure action values	$L_{EX,8h} = 85 \text{ dB(A)}$	137 dB(C)
Lower exposure action values	$L_{EX,8h} = 80 \text{ dB(A)}$	135 dB(C)

For both EU Physical Agents Directive and IMO Noise Code, the exposure levels can be calculated by the following equation.

$$L_{EX,T} = 10 \times \log \frac{1}{T} \sum_i^n t_i \times 10^{L_i/10} \quad (1)$$

In the above equation t_i is the duration in a noisy environment while T is 8 when calculating 8 hour equivalent exposure level and 24 when calculating 24 hour equivalent levels.

3.3 Comparative Study

In order to understand the current regulatory compliance, the authors conducted a comparative study on noise exposure on board ships (Turan, Helvacioğlu et al. 2010) which included the following;

- Noise levels of compartments were measured for six different ships during the sea trials.
- A questionnaire was designed and applied to capture the work patterns of the tanker crew.
- Based on the identified work patterns noise exposure levels of all crew ranks were calculated.
- Results were comparatively analysed based on the criteria defined by IMO and EU.

The main particulars of the six Oil/Chemical tanker ships are given in Table 3. It can be seen that all tankers are of similar size apart from the "Oil/Chemical Tanker No: 4" which is a larger vessel.

Table 3 Main particulars of ships used in full scale measurements

Type of Ship	DWT	L _{Overall}	Speed	Engine Power
1.Oil/Chemical Tanker	7915 DWT	121	14 knots	3840 kW
2.Oil/Chemical Tanker	6000 DWT	107	13 knots	2620 kW
3.Oil/Chemical Tanker	8000 DWT	121	14 knots	3840 kW
4.Oil/Chemical Tanker	18000 DWT	148	14 knots	5920 kW
5.Oil/Chemical Tanker	4500 DWT	106	15.5 knots	3250 kW
6.Oil/Chemical Tanker	6100 DWT	123	13 knots	2610 kW

Results showed that although ships are easily fulfilling the requirements set by the IMO for compartment bases, they are failing to comply with the defined noise exposure criteria. Therefore, it is necessary to redesign the noise levels defined by IMO by considering the recent improvements, practical implementation, comfort and performance of crew members. It was also identified that crew members who are working close to machinery spaces are at high health risk because they exceed the safe exposure limits defined to protect health. Exposure levels for each rank was calculated through an exposure assessment tool as reported in Turan, Helvacioğlu et al. (2010).

4 EU FP7 SILENV PROJECT'S GREEN LABEL PROPOSAL

EU FP7 SILENV Project (SILENV 2009) was funded in response to emerging need for reducing ship-generated noise and vibration pollution. SILENV Project dealt with the wide range of issues related to noise and vibration on and from ships. The project a thorough review of the previous literature, conducted field studies and measurements, developed models, and issued guidelines aiming to improve current situation. One of the main outputs of SILENV Project is the 'Green Label Proposal' which defines new innovative noise limits for ships. Following sections will explain the development procedure as well as the final proposed green limits.

4.1 Methodology

In order to define the SILENV Green Label the following methodology was adopted.

- Preliminary target levels for noise has been defined based on the extensive state-of-the-art review conducted in the project.

- Considering the resulting human response (comfort, wellbeing and performance) from the preliminary limits
- Feasibility of these preliminary limits has been assessed based on;
- Finalisation of Green Label Proposal

Proposal’ should use the IMO noise code as a base. Then, through conducting an extensive review on available noise norms, target noise levels were developed. It was thought that SILENV should consider all the limit levels defined by the various existing norms and define the preliminary target noise levels which -if not more stringent- is just as stringent as the existing norms.

4.2 Preliminary Targets and Critical Analysis

The IMO “Code on noise levels on board ships” is fully accepted by the maritime community as a refer-to document when dealing with noise on board ships. Therefore, it was considered that the development of preliminary noise limits for SILENV ‘Green Label

The developed preliminary noise levels are shown in Table 4 and Table 5 in comparison with the existing norms.

Table 4 Proposed preliminary noise limits for crew spaces

		RINA	BV	GL	ABS	DNV	LR	IMO Code	IMO New	PROPOSED
ACCOMMODATION	Crew Cabins	55	52	52	50	50	52	60	55	50
	Day Cabins						55			55
	Officers Cabins	52		50						50
	Hospital	50	55	54	50	55		60	60	50
	Offices	58	57	57	55	60	55	65	65	55
	Open deck recreation	70	70	68	65	70		75	70	65
	Closed Public Spaces	60	57	90		55				55
	Mess room	60	57	57			57	65	60	57
	Recreation			57	60			65	65	57
	Corridors		70	58	60					58
	Dining Spaces				55					55
NAVIC.	Radio room	58	55	55	55	55	60	60	65	55
	Navigation Spaces	58		55				65		55
	Chart Rooms				55					55
	Radar Room				55			65		55
WORK	Engine control room	70	70	67	65	70	75	75	70	65
	Workshops		85	80	80		85	80	80	80
	Open deck working areas	70		75			63			63
	Laundries				75					75
	Continuously Manned Machinery Spaces				85		90	90		85
	Not Continuously Manned Machinery Spaces			110	108		110	110	105	105
	Cargo Handling Spaces/Areas Near Cargo Handling Equipment				80					80
	Fan Rooms				85					85
	Alleyways, changing rooms						70			70
	Listing posts, Bridge wings			65				70	70	65
	Galleys		70	68	70				70	68
	Pantries			66	70		75			66
	Stores			80	70					70
Wheelhouse				55	60	85		65	55	

Table 5 Proposed preliminary noise limits for passengers

	Noise level in dB(A)						
	ABS	BV	DNV	GL	LR	RINA	Proposed
Passenger top level cabins	45	43	44	44	45	45	44
Passenger standard cabins	45	43	43	46	49	50	45
Outside installation (swimming pools, sport decks, promenade decks...)	65	65	65	64	67	63	64
Discotheque, Ballroom	60	65	55	52	55	55	52
Restaurant, lounge	55	55	55	52	55	55	52
Libraries, theatre	55	53	55	52	50	52	50
Shops	55	60	55	52	60	55	52
Gymnasium	65	60	55	52	55	55	52
Corridors, Staircase	60	60	55	54	55	60	54
Hospital	45	55	55	54	52	50	45

4.3 Human Response

It was important to assess the preliminary noise target levels and resulting human response. Hence, innovative human response models were developed in the SILENV Project (Houben, Kurt et al. 2012). In order to achieve this, noise measurements were conducted in various compartments on board of 15 different ships. Together with the noise measurements, questionnaires were also deployed to capture the resulting human response. Then, the human response models were developed describing the relationship between the levels of noise and subjective ratings of crew on performance and passengers on comfort. Various ordinal subjective ratings obtained were reduced through correlation, factor analyses and common sense. The relationship between dependent and independent variables appeared to be non-linear, hence logistic regressions were visited and final models with good fitness were obtained.

In order to represent total human response, 2 comfort and 3 performance models were developed resulting in total of 5 different human response models focusing on different performance or comfort criteria. These models are shown in Table 6.

Table 6 Dependent variable in models

	Variables
Comfort	N2c -Annoyance O1c -Overall feeling of discomfort
Performance	N2p -Annoyance N7p -Quality impairment O1p -Overall feeling of wellbeing

As a result of discussions amongst SILENV partners, for comfort ‘N2c - Noise Annoyance model’ and for performance ‘N7p - Quality impairment model’ were selected to assess the preliminary target levels. These selected models then used to calculate the percentage of

human discomfort and performance impairment. Table 7 shows the limits corresponding to a specific percentage of people annoyed or impaired in their work by the noise.

Table 7 Noise limits per human response

Extra probability relative to base line	Noise Annoyance (dB)	Noise Induced Work Quality Impairment (dB)
5%	48	55
10%	55	64
15%	60	71
20%	65	77
25%	70	82
30%	75	86

In the SILENV Green Label proposal it was aimed to ensure at least 90% of passengers’ and crews’ satisfaction.

4.4 Feasibility of the Preliminary Target Levels

It is important to define realistic noise limits which are achievable for new ships. Therefore, the aim of this analysis is to find an answer to the following question; “what noise criteria should be defined in order to make only 5%, 10%, 20%, 30%, 40%, and 50% of current ships to comply?”. In order to achieve that, only the most recent ships from the SILENV Noise Database was selected considering that the technology in older ships will not be comparable to the new buildings. Total of 64 different vessels were taken into consideration and following table shows the noise limits and corresponding percentage of vessels which can comply with those levels. Table 8 shows the percentages of vessels from SILENV database which comply with the noise levels.

Noise limits which will correspond to 20% of the vessels to comply, was considered reasonable and achievable by the SILENV Consortium.

4.5 Finalisation of Green Label Proposal

The noise requirements defined in previous sections were combined together to obtain the SILENV Green Label Proposal. First, the preliminary noise limits (IMO limits as well as other standards) were taken as a starting point and compared to the human response criteria defined in the previous sections. As a result of this comparison and discussions new noise limits were defined. Then, these noise limits were compared with the noise criteria based on 20% of current vessels compliance. Again after these comparison and discussions within the SILENV Consortium new noise limits were defined. After consolidating all the criteria, through a workshop SILENV partners further discussed and finalised the green label proposal.

Table 8 Percentages of vessels which comply with given noise levels (SILENV 2012)

Space type *	x=50%		x=40%		x=30%		x=20%		x=10%		x=5%	
	Noise limit (dB)	Exact percent. (%)	Noise limit (dB)	Exact percent. (%)	Noise limit (dB)	Exact percent. (%)	Noise limit (dB)	Exact percent. (%)	Noise limit (dB)	Exact percent. (%)	Noise limit (dB)	Exact percent. (%)
Type I	54	46	54	39	51	31	50	27	46	12	44	4
Type II	60	52	59	41	57	33	54	19	51	11	49	7
Type III	59	49	58	42	55	32	52	25	51	14	49	7
Type IV	60	52	59	44	57	32	56	24	55	12	52	4
Type V	66	49	65	42	63	34	60	20	53	10	50	4
Type VI	76	47	76	40	74	27	69	20	59	13	59	13
Type VII	62	54	61	42	58	31	57	23	55	12	54	5
Type VIII	83	53	82	40	79	31	76	18	73	10	69	6
Type IX	70	51	69	40	66	30	62	23	60	11	58	4
Type X	105	46	104	39	102	23	97	15	89	8	79	0
Type XI	108	50	107	40	106	27	105	21	102	10	101	8

*Space types are described in more detail in final green label noise limits (Table9)

The final SILENV Green Label Proposal is shown in Table 9 below. As it can be seen from the table, SILENV introduced its own space groups which are similar to but not identical to IMO.

Table 9 Noise limits in SILENV Green Label

Group number	Group name	Location example	Noise Limits (dB(A))
1	Cabins	Passenger cabins	50
		Crew cabins	
		Hospital	
2	Offices		53
3	Public Space A	Libraries	55
		Calm public spaces	
4	Public Space B	Restaurant	60
		Lounge	
		Mess room	
		Shops	
5	Public Space C	Discotheque, dancefloor	65
		Ballroom	
		Corridor	
		Staircase	
6	Outdoor Areas	Open recreational area	70
		Bridge wings / Open deck working areas	
7	Wheelhouse	Wheelhouse	60
		Radio room	
8	Work space A	Engine control room	65
		Galleys	
9	Work space B	Pantries	75
		Stores	
		Laundries	
		Workshops	
		garage	
10	Work space C	Continuously manned machinery space*	90
11	Work space D	Not continuously manned machinery space*	105

* hearing protection mandatory

5 CONCLUSIONS

In the SILENV Project innovative human response models were developed. Furthermore, these models were utilised for developing the SILENV green label proposal. Therefore, it can be considered that the noise criteria proposed by SILENV is the first example of human oriented noise norm developed for shipping. The

developed green label proposal does not only aim to protect the health of the crew but also aims to maintain a good level of comfort as well as performance on board ships. Analysis of current fleet showed that the new limits are realistic and achievable by the new ships. More information is available in SILENV Green label proposal (SILENV 2012).

Following can be observed from the defined noise limits:

- The difference between crew cabins and passenger cabins were removed.
- Noise levels in cabins were designed to ensure that less than 10% of people will get annoyed.
- Noise levels in wheelhouses were designed to ensure that less than 10% of people will get performance degraded.
- In high noise areas the hearing protection should be worn.
- 'Public Space A' complies with the targeted human annoyance (max. 10 %).
- However the levels defined for 'Public Space B' corresponds to 15% of human annoyance.

ACKNOWLEDGEMENT

Authors gratefully acknowledge that the research presented in this paper is generated as part of European Commission funded project SILENV (Ships Oriented Innovative Solutions to Reduce Noise and Vibrations, Seventh Framework Programme, Project number 234182, FP7-SST-2008-RTD-1).

REFERENCES

- ABS (2001). Guide for Crew Habitability on Ships, American Bureau of Shipping.
- Alberti, P. W. (2001). 'The Pathophysiology of the Ear'. Occupational Exposure To Noise Evaluation, Prevention And Control. H. C. Goelzer B, Sehrndt GA, World Health Organisation (WHO).
- Broadbent, D. E. (1954). 'Some effects of noise on visual performance'. Quarterly Journal of Experimental Psychology **6**(1): 1-5.
- Button, D. C., D. G. Behm, M. Holmes and S. N. Mackinnon (2004). 'Noise and muscle contraction affecting vigilance task performance'. Occupational Ergonomics **4**(3): 157-171.
- DMA (2002). Technical regulation on noise in ships. Technical regulation 4, Danish Maritime Authority.
- EC (2003). 'On the minimum health and safety requirements regarding the exposure of workers to the risks arising from physical agents (noise)'. Official Journal of the European Union. **2003/10/EC**.
- GL (2003). Rules for Classification and Construction, Chapter 16 Harmony Class- Rules on Rating, Germanischer Lloyd
- Harcum, E. R. and P. M. Monti (1973). 'Cognitions and Placebos in Behavioral Research on Ambient Noise' Monograph Supplement 1-V37." Perceptual and motor skills **37**(1): 75-99.
- Harrison, D. W. and P. L. Kelly (1989). 'Age differences in cardiovascular and cognitive performance under noise conditions'. Perceptual and Motor Skills **69**(2): 547-554.
- Houben, M., R. E. Kurt, H. Khalid, P. Zoet, J. Bos and O. Turan (2012). 'Human Response to Noise and Vibration Aboard Ships'. International Conference on Advances and Challenges in Marine Noise and Vibration. 5-7 September, Glasgow UK, University of Strathclyde.
- IMO (1981). Code on Noise Levels on Board Ships. **Resolution A.468(XII)**.
- IMO (2012). Adoption of the Code on Noise Levels on Board Ships, International Maritime Organisation. **RESOLUTION MSC.337(91)**.
- Jerison, H. J. (1957). 'Performance on a simple vigilance task in noise and quiet'. The Journal of the Acoustical Society of America **29**(11): 1163-1165.
- Kurt, R. E., O. Turan, O. Arslan, K. H., D. Clelland and N. Gut (2010). 'An Experimental Study to Investigate Effects of Noise on Human Performance Onboard Ships'. Human Performance at Sea Conference. Glasgow, UK.
- LR (2004). Provisional Rules for Passenger and Crew Accommodation Comfort, Lloyd's Register.
- Martin, A. and C. Kuo (1995). 'The effects of noise and vibration on crew performance'. International Conference on Noise and Vibration in the Maritime Environment. Trinity House, London, UK, The Royal Institution of Naval Architects
- MCA (2007). Codes of Practice For Controlling Risks due to Noise and Vibration on Ships, Maritime and Coastguard Agency
- Melamed, S., Y. Fried and P. Froom (2004). 'The joint effect of noise exposure and job complexity on distress and injury risk among men and women: the cardiovascular occupational risk factors determination in Israel study'. Journal of occupational and environmental medicine **46**(10): 1023-1032.
- Melamed, S. and P. Froom (2002). 'The joint effect of industrial noise exposure and job complexity on all-cause mortality-The CORDIS study'. Noise and Health **4**(16): 23.
- SILENV (2009). Ships oriented innovative solutions to reduce noise and vibrations. Framework Programme 7 Collaborative Project no 234182, European Union.
- SILENV (2012). WP 5: Green Label Proposal - Subtask 5.2: Noise and Vibration label proposal. http://www.silenv.eu/green_label/D5.2_green_label_rev_2.pdf.
- SMA (1973). Sjöfartsverkets meddelanden Serie A, Swedish Maritime Authority. **Nr 27**
- Turan, O., I. H. Helvacioğlu, M. Insel, H. Khalid and R. E. Kurt (2010). 'Crew noise exposure on board ships and comparative study of applicable standards'. Ships and Offshore Structures **6**(4): 323-338.
- Weston, H. C. and S. Adams (1932). 'The effects of noise on the performance of weavers'. Medical Research Council Industrial Health Research Board: 38-62.
- White, K., M. Meeter and A. Bronkhorst (2012). Effects of transportation noise and attitudes on noise annoyance and task performance. INTER-NOISE and NOISE-CON Congress and Conference Proceedings, Institute of Noise Control Engineering.

Proven Benefits from Foul Release Coatings

Trevor Solomon^{1*}

¹International Paint Ltd., Stonegate Lane, Felling, Gateshead, NE10 0JY, UK

Abstract: Most technology providers claim benefits for their products in order to convince their customers to buy them; some are easy to prove (e.g. smaller, lighter, bigger) whilst others are more abstract and not so easy to prove (lasts longer, improved efficiency). Claims that fall into the abstract definition can bring doubt into the customer's mind. Fuel saving claims for the shipping industry clearly fall into the second category. There are many technology providers to the shipping industry who claim that their product or service will improve fuel consumption, save money and reduce CO₂ emissions. These include coatings, propellers, hull modifications, trim optimisation and weather routing to name a few. Why this is the case is very clear; with fuel costs representing over 60% of the operational costs of commercial vessels, even a 1% saving can mean a profitable vessel instead of one that is loss making. In order to tackle this scepticism, technology providers have sought validation of their claims through independent monitoring systems, customer testimonials, Class, industry and academic acknowledged experts. More recently, the carbon credit scheme for ships using energy efficient fouling control technology takes that a step further with UN-sanctioned bodies issuing carbon credits against validated fuel and emission savings using data from the ships themselves.

Keywords: Foul release, fuel, carbon, credit.

1 INTRODUCTION

Foul release coatings have been commercially available for a number of years and give the unambiguous environmental benefit of releasing no biocides into the environment whilst controlling the growth of fouling organisms which can contribute to the poor performance of a vessel in service.

Over recent years, foul release coatings have contributed more to environmental protection through the actual reduction in fuel consumption and the resultant environmental pollutants that come from burning fossil fuels, i.e. carbon dioxide, nitrous oxides and sulphur oxides.

This paper explores the use of foul release coatings, their developments over time and the evidence that exists to prove the fuel and emission saving potential of the technology.

2 FOUL RELEASE COATINGS

Foul release coatings have been commercially available since 1996 when International Paint launched Intersleek[®]425. Based on polydimethyl siloxane chemistry ("silicone"), the coating showed that fouling control was possible without the use of biocides.

The term "foul release" is the name given to this class of coating due to their working mechanism. The coating, when applied to the underwater sides of a vessel, is very smooth and, due to the silicone chemistry, has a very low surface energy. Fouling organisms such as barnacles and tubeworms find it difficult to attach to smooth surfaces and, combined with the low surface energy, any that do manage to settle cannot attach very strongly as their adhesive does not form a strong bond to the surface of the

coating. The result is that the fouling is released through the action of water passing over the hull of a ship when it gets underway.



Picture 1 Easy removal of barnacles from the surface of silicone foul release coating

3 DEVELOPMENTS OF FOUL RELEASE COATINGS

Since the introduction of the first silicone commercial foul release coating in 1996, the product category has expanded to include fluoropolymers, hydrogels and more recently even biocide-containing. To understand the changes that have occurred over the years it is important to understand the limitations of the preceding products which initiated the development of new technology.

Intersleek[®]425 was launched with a limitation of only being used on vessels with operating speeds in excess of 25 knots. This resulted in a small niche market of fast craft for the product.



Picture 2 Fast ferry coated with silicone foul release

Intersleek®700, another pure silicone system was launched in 1999, again by International Paint, specifically for the liner trade; fast and active vessels such as containerships and LNG carriers.

This was followed by a number of other marine coating suppliers releasing silicone foul release systems.

The environmental awareness of shipping was awakened in 2003 when the application of antifouling products containing tributyl tin (TBT) was effectively banned by the International Maritime Organisation. Even though ratification of the ban did not occur until late 2008, most marine paint suppliers stopped supplying what was then the fouling control coating of choice for the majority of shipowners.

A number of shipowners chose at that time to look at products which would be excluded from any potential future legislation and the foul release market started to grow.

From that time onwards, pure silicone foul release systems proved themselves and were shown to work effectively on large ocean-going vessels by controlling macro fouling such as barnacles, tubeworms, oysters, muscles and weed. What also became apparent was that they seemed to show the potential for reducing the fuel consumption of vessels.



Picture 3 Indock condition after 60 months of a Very Large Crude Carrier (VLCC) coated with Intersleek®700

However, pure silicone systems were limited to vessels operating above 15 knots and with relatively high operational activities (>75%). This was due to the fact that the higher speeds were necessary to remove any settled macro fouling.

In the early 2000's, the issue of slime (or micro fouling) became much more prominent; whilst it was clear that the

pure silicones worked well against macro fouling and showed potential for reductions in fuel consumption, they succumbed to slime fouling.

4 EMERGENCE OF NEW TECHNOLOGIES

In response to the limitations for pure silicones, International Paint launched the first fluoropolymer foul release coating Intersleek®900 in 2007 which was designed to work on lower activity, slower vessels as well as reducing the slime build up associated with pure silicones. It is at this time that the first publication of the potential for fuel savings was carried out where Intersleek®900 was predicted to save up to 6% fuel compared to self-polishing copolymer biocidal antifouling.

The fluoropolymer was designed to produce an amphiphilic surface which is described as both water hating and water liking at the same time which essentially “confused” fouling organisms. This reduced the tendency for settlement and reduced the adhesive strength of any organisms that managed to settle even more. Up until that time, foul release coatings were all hydrophobic (hydro = water, phobic = hating).



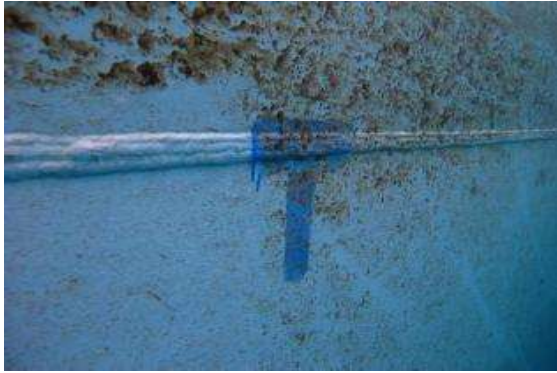
Picture 4. Comparison of slime performance of pure silicone (left) compared to fluoropolymer (right) on a post-panamax containership after 60 months

Fluoropolymers were followed by the launch of the first hydrogel into the foul release market making the surface hydrophilic (water liking) and “nano-spring” technology which were designed to prevent the settlement of organisms.

Slime fouling, though reduced by the new technologies, still remained a concern for foul release coatings.

International Paint launched Intersleek®1100SR in 2013 specifically targeting slime as the fouling challenge, “SR” standing for “slime release”. Again based on fluoropolymer, the coating performance against slime was enhanced through generating a more hydrophilic surface whilst still maintaining the overall amphiphilic surface.

Other coating suppliers took dramatically different routes for the same purpose by introducing biocides to the previously biocide-free foul release systems in an attempt to control the growth of slime.



Picture 5 Comparison of pure silicone Intersleek®700 (top), original fluoropolymer Intersleek®900 (right) and advanced fluoropolymer Intersleek®1100SR (left) after 25 months in service on a conventional LNG carrier trading between Middle East and Japan

5 REDUCTIONS IN FUEL CONSUMPTION

Examples of foul release coatings helping a vessel operator reduce the fuel consumption whilst maintaining the speed are quite widespread.

In 2003, the Spanish ferry operator Buquebus, after converting its whole fleet to Intersleek®425 claimed average speed increases of 1½ to 2 knots combined with fuel savings. During the seatrials of the superfast Patricia Olivia II for Buquebus, the higher than design speeds achieved were attributed to Intersleek®425 (Bonafoux & Higgins 1999)

As the marketing of these coatings has moved more towards the fuel saving potentials, stronger in-service proof has been sought. A number of shipowners have allowed publication of fuel saving numbers by paint companies and others have indeed publicised themselves.

Table 1 Some examples of shipowner testimonies for the benefits of Intersleek®

Vessel	Technology	Owner	Fuel Saving
Ramlah	Silicone	NSCSA	6.4%
Prem Divya	Fluoropolymer	Mercator Lines	9%
Prem Pride	Fluoropolymer	Mercator Lines	6%
Corona Ace	Fluoropolymer	K Line	>8%
Queen Mary II	Fluoropolymer	Cunard	>16%
Álvaro de Bazán	Fluoropolymer	Spanish Navy	+3 knots
Ikuna	Fluoropolymer	Inco Ships	16%
Containership	Silicone	European operator	6%
Containership	Fluoropolymer	Taiwanese operator	5%
LNG carrier	Fluoropolymer	Middle east operator	9%
Ro-Ro	Fluoropolymer	European operator	10%

Study by Corbett et al (2010) from the Environmental & Energy Research Institute showed that foul release

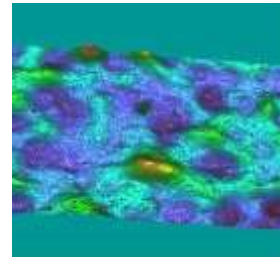
coatings have the potential to reduce fuel consumption by up to 10%.

To understand where these fuel savings came from a series of scientific studies were undertaken.

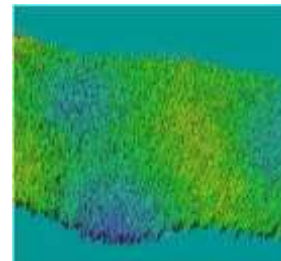
The first indication of the fuel savings possibly is the fact that foul release coatings naturally form the smoothest commercial coatings in the marine industry due to their chemistry.

6 SMOOTH COATINGS

Silicones inherently have low surface energies. The result when they are applied to a surface is that they naturally spread out. This effectively creates a self-smoothing coating. In reality, due to the requirements of applying these coatings on vertical surfaces, the presence of small amounts of organic solvents to allow spraying which evaporate during application plus the fact that they cure on exposure to oxygen, means the surfaces produced on the vertical sides of a vessel in drydock are not laboratory smooth but are the smoothest commercially available.



Picture 6 Surface profile of silicone foul release coating



Picture 7 Surface profile of self-polishing copolymer (SPC) antifouling

Typically, measured using the BSRA Hull Roughness Stylus Gauge, the average hull roughness of a vessel coated with silicone foul release is around 25% smoother than that coated with a conventional biocidal antifouling.

For the newer foul release coatings, that number is even lower with in-field measurements approaching the reliable sensor range of the stylus-type hull roughness gauges which is 50 microns +/- 15 microns.

Exact numbers depend on the quality of application, weather conditions and surface preparation, but foul release coatings will always give the lowest hull roughness of all fouling control coatings.

7 HULL ROUGHNESS

Hull roughness is important in understanding how the coating can influence the performance of a vessel in terms of power and fuel requirements.

Townsin et al (1996) surmised that the increase in power to maintain speed due to changes in hull roughness is around 1% for every 20 microns. As power is roughly proportional to fuel consumption, for every 20 micron difference in hull roughness there would be a 1% difference in fuel oil consumption.

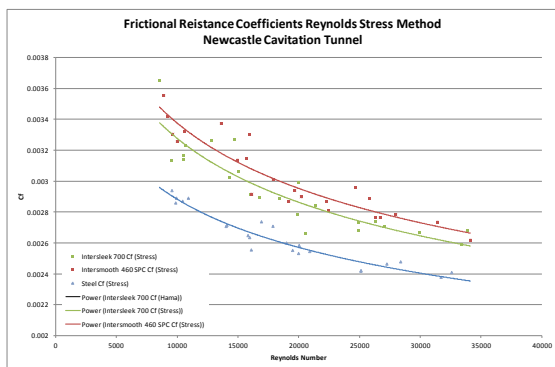
Smoother films would therefore contribute to reducing the fuel consumption of vessels.

However, the difference between in hull roughness of foul release coatings and conventional antifoulings at best would represent 2-3% fuel savings.

8 HYDRODYNAMIC STUDIES

In 2001, Maxim Candries commenced a PhD study to examine the differences between foul release coatings and conventional antifoulings. The coatings used were Intersleek[®]700 pure silicone and Intersmooth[®]360 SPC a copper acrylate-based self-polishing copolymer (SPC).

Using cavitation tunnels and towing tanks at both Newcastle University, England and Madrid University, Spain, Candries showed consistently that the silicone foul release coating contributed less to the frictional resistance of a surface in water than the conventional antifouling. He showed this number to be typically around 5-7% lower (Candries, 2001)



Graph 1 Extract from Candries thesis showing frictional resistance differences between hydraulically smooth surface (blue), Intersleek[®] silicone system (green) and conventional self-polishing copolymer system (red)

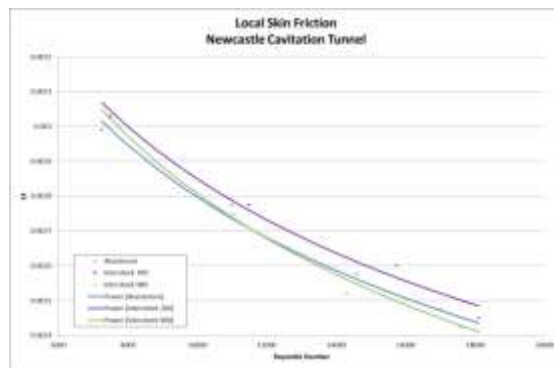
One conclusion from Candries that hasn't yet been either proven or disproven is that the low modulus of the coating also contributes to the improved vessel efficiency and reduced frictional resistance.

Silicone systems have one of the lowest modulus ever measured (Kohl & Singer, 1999). This, combined with the low surface energy is what is needed to create the right balance for foul release. What this means is that the polymer is very soft and flexible; under outside stress such as water pressure, the surface of the coating can be

changed. The speculation is that the silicone systems deform under water flow which influences the frictional resistance beyond that what is simply the hull roughness differences.

Repeat, as yet unpublished hydrodynamic studies carried out since Candries' work, continue to show that foul release coatings have the lowest influence on frictional resistance of all coatings.

Testing as part of the European Union funded project AMBIO (Advanced Nanostructured Surfaces for the Control of Biofouling), George Politis compared silicone and fluoropolymer foul release coatings as the controls within the test programme. The hydrodynamic testing showed that fluoropolymer-based foul release coatings had even lower frictional resistance compared to silicone-based foul release coatings (Atlar et al, 2013)



Graph 2 Extract from Atlar paper showing frictional resistance differences between hydraulically smooth surface (blue), Intersleek[®]700 silicone system (purple) and Intersleek[®]900 fluoropolymer (green)

9 MEASUREMENT OF VESSEL EFFICIENCY

All of the evidence from both scientific studies and vessels in service strongly indicates that foul release coatings have positive impacts on frictional resistance and ultimately vessel efficiency.

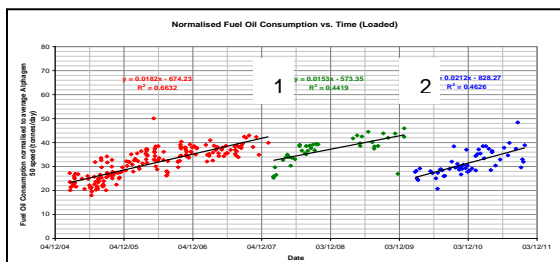
The big question today is how you measure the benefits of the coatings.

Ship operators for many years have been collecting data from their vessels in the form of noon reports recorded in the ships logbook. Indeed, the phrase "logbook" dates back to the early 16th century whereby the speed of a vessel was recorded each day when the sun was at its' highest, i.e. noon, and the distance travelled calculated.

Noon reports consist of data that is collected manually by the crew on board a vessel. The exact level of data collection can vary with ship operator as well as even with individual crews. The methods of measurements can also vary. All of these parameters mean that analysis of data collected from noon reports is usually treated with caution.

However, if the data collected in noon reports is done so in a consistent manner then the relative accuracy of analysis of the data can be improved significantly.

A study by Lucy Aldous of University College London (Aldous et al, 2013) , showed that analysis of data from 40 tankers had a standard deviation of at best +/-1% and at worst +/-8%; the average being around +/-4%. That means that a change in the vessel performance from the “average performance” of +4% or -4% could be within the error of the data. However accurate the absolute definition of performance of a vessel is from noon reports though, they should not be discounted for showing trends over longer time periods. There is a large amount of evidence that noon reports can show the effects of changing something on a vessel. That something could be the underwater hull coating, a hull modification, an in-water propeller polishing etc.



Graph 3 Analysis of noon report data for a product tanker showing effects of changes in fuel oil consumption after underwater cleaning (1) and drydocking (2)

A study carried out by Thijs Hasselaar from 2005 to 2008 concluded that in order to really understand the influence of coatings on vessel performance you required high frequency data collection though he did not conclude any level of accuracy (Hasselaar, 2010).

A number of companies have started to offer automated data collection systems with varying levels of analysis. Those include BMT Smart, Eniram, Marorka and ABS. All of these systems rely on electronic data collection and transfer to a shore-based server via the ships’ broadband connection. Fundamental to those systems working is the availability, reliability and accuracy of sensors on board vessels as well as the use of ship-to-shore communications. However, the advances in those areas over the last few years has made those systems much more viable for vessel operators.

Work is also underway within the International Standards Organisation (ISO) to try and develop a standard method for collecting data manually for the traditional noon reports and automatically. A working group consisting of Ship Operators, Owners, Class Societies, Shipping Organisations, Performance Monitoring Companies, Coating Suppliers and Academics have been developing the standard since June 2013 with an aim for publication by end 2018.

In all of this, the ultimate goal is to be able to consistently and accurately measure the changing performance of a vessel whilst in service in a transparent way in order to remove any uncertainty for all stakeholders. For technology providers, this is a route to prove their performance claims.

10 INDEPENDENT PROOF OF PERFORMANCE

In early 2014, International Paint announced the development of a method for generating carbon credits from emission savings resulting from the use of biocide-free foul release coatings. The methodology was developed with the non-government organisation The Gold Standard Foundation who are the most trusted carbon credit generating organisation. The method is based upon data collected via noon reports though it can use data collected automated if sufficient quantity is available.

What is unique about the methodology is that the emission savings are calculated using the real data from the ship collected over long periods of time. The accuracy of analysis of any set of data including noon reports naturally increases as the deviations in measurements have lower impacts.

Generation of carbon credits adds significant credibility to the claims of fuel and emission savings with one carbon credit representing the saving of one tonne of carbon dioxide being emitted into the environment. Burning of one tonne of fuel oil on board a ship generates just over three tonnes of carbon dioxide.

The first step in this process in order to get the methodology approved required peer reviews prior to approval by the Gold Standard Foundation.

The second step was that the claim for the emission savings was calculated using vessel data and the methodology was audited by an independent UN-approved auditor. The responsibility of the auditor is for assessing the eligibility of the vessel, the quality of the data and the rigour of the analysis.

The last key step is that the claim, the analysis and audit report is assessed by the Gold Standard Foundation and only when everything is acceptable will carbon credits be issued.

Ship operators can therefore be assured that for every three carbon credits issued by the Gold Standard Foundation they have independent third party validation that they have saved one tonne of fuel.

11 CONCLUSIONS

The benefit of foul release coatings delivering performance without the use of biocides is a clear undisputed fact. However, proving a reduction in fuel consumption is much more abstract and as such brings doubt into the minds of ship operators. Attempts over the years to remove that ambiguity have been made with testimonies from ship operators themselves as well as studies by academics and independent authorities.

This paper has highlighted a number of examples of the fuel saving capabilities of foul release coatings showing that on average a 9% saving could be achieved by many ship operators.

The recent carbon credit methodology though brings another level of independence to the discussion with layers of data integrity assessments carried out prior to the issuance of any carbon credits.

REFERENCES

Bonafoux, J. & Higgins, G. (1999). 'Patricia Olivia II, Development of the first 50+ Knot Fast Ferry in North America'. 15th Fast Ferry International Conference, Boston, Massachusetts, USA.

<http://www.international-marine.com/supportadvice/case-studies.aspx>

Energy and GHG Emissions Savings Analysis of Fluoropolymer Foul Release Hull Coating. (2010) Energy & Environmental Research Associates, December, 2010.

Townsin R.L., Bryne, D., Svensen T.E. & Milne A. (1986) 'Fuel Economy Due to Improvements in Ships Hull Surface Condition 1976-1986'. International Shipbuilding Progress, **33** (383), July.

Candries, M. (2001). 'Drag, Boundary-Layer and Roughness Characteristics of Marine Surfaces Coated with Antifouling'. Ph.D. Thesis, University of Newcastle upon Tyne, UK, December.

Kohl J.G. & Singer I.L. (1999). Progress in Organic Coatings, **36**, pp.15-20

Atlar M, Unal B, Unal UO, Politis G, Martinelli E, Galli G, Davies C. & Williams D. (2013). 'An Experimental Investigation of the Frictional Drag Characteristics of Nanostructured and Fluorinated Fouling-Release Coatings Using an Axisymmetric Body'. Biofouling, **29**(1), pp.39-52.

Aldous L., Smith T. & Bucknall R. (2013). 'Noon Report Data Uncertainty'. Low Carbon Shipping Conference.

Hasselaar T. (2010). 'An Investigation into the Development of an Advanced Ship Performance Monitoring and Analysis System'. Ph.D. Thesis, Newcastle University, UK.

Computational Fluid Dynamics Simulation of Cavitating Open Propeller and Azimuth Thruster with Nozzle in Open Water

Tobias Huuva^{1*}, Simon Törnros¹

¹Caterpillar Propulsion Production AB Andvägen 26, SE-475 40 Hönö, Sweden

Abstract: The purpose of this work is to investigate possibilities to study pressure pulses generated from a propeller under cavitation condition. This type of pressure pulses, at least at low order close to the blade rate frequency, can today relatively exactly be modelled using potential flow methods. These type of methods do however have physical limitations, preventing them to develop much further. With Computation Fluid Dynamics (CFD), on the other hands, some development is still needed to come to the same level as well validated potential flow codes. The possibilities to develop more advanced numerical models, also including higher order frequencies, are however much greater using CFD as compared to potential flow. In this work a RANS model cavitation modelling is used to study the cavitating flow on the Potsdam propeller Test Case (PPTC) and a propeller on a ducted Azimuth thruster. The result shows well predicted performance and cavitation extent, comparing with the experiments on the PPTC Propeller. The nozzle propeller shows good cavitation behavior, including the unsteady phenomena arising from the interaction between the propeller and the azimuth gear-house and stem.

Keywords: CFD, cavitation, propeller, unsteady flow.

1 BACKGROUND

Cavitation is the phenomena of phase change, from liquid to vapor, due to a local pressure decrease. It is an important phenomenon for turbo machinery operating in water such as marine propellers, pumps and turbines. Cavitation extent is crucial to control and limit when designing a propeller as it may induce noise, vibrations and erosion as well as performance degradation.

Experiments are useful for predicting pressure pulses and visual estimations of cavitation extent. The downside is that experiments may be expensive, time consuming, yields relatively little flow information and commonly has to be done in model scale. Numerical tools on the other hand can more easily be applied in early design stages for verification and optimization. Numerical methods based on potential flow are commonly used in industry to estimate cavitation extent and pressure pulses but lacks potential of predicting detailed flow phenomena. Complex and viscous flow phenomena such as tip vortex cavitation are responsible for high frequency noise and requires viscous CFD to be resolved. Further benefits of CFD compared to potential flow methods are the possibility to let the propeller operate in a viscous wake field, such as behind a ship or azimuth structure. The inflow to the propeller is significant for the loading and thereby for its cavitating performance.

Viscous CFD utilizing Unsteady Reynolds Averaged Navier Stokes (URANS) is capable of predicting cavitation including flow detail and dynamics (Sipilä, 2011), (Grekula & Li, 2008). Although the level of detail is lower compared to Large Eddy Simulation (Huuva, 2008), (Lu, Bark, & Bensow, 2012) the significant lower

computational cost makes RANS a suitable method for industrial usage.

2 OBJECTIVE

The objective of this study is to simulate cavitating propeller flow using an in-house developed CFD methodology. The methodology is to be applied onto both a well-known open propeller test case as well as a full scale Cat® azimuth thruster.

3 TEST CASES

The well-known Potsdam Propeller Test Case (PPTC) is a five bladed controllable pitch model propeller with high design pitch and moderate skew. The PPTC propeller can be seen in Figure 1.



Figure 1 PPTC in test configuration (Heinke, 2011)

Geometrical data of the propeller can be seen in Table 1.

Table 1 PPTC geometrical properties

D [m]	0.250
$P_{0.7}/D$ [-]	1.635
EAR [-]	0.779
Θ_{EXT} [°]	18.837
d_h/D [-]	0.300
Z [-]	5

The experimentally analyzed test conditions by SVA Potsdam GmbH (Heinke, 2011) are used in this study, at thrust identity, and can be seen in Table 2.

Table 2 Cavitating condition for the PPTC propeller

Case [-]	1	2	3
J [-]	1.019	1.269	1.408
σ_n [-]	2.024	1.424	2.00
n [s ⁻¹]	24.987	24.986	25.014
K_T [-]	0.387	0.245	0.167
ρ [kg/m ³]	997.44	997.44	997.37
ν [m ² /s]	9.337×E-7	9.337×E-7	9.272×E-7

In addition to simulation of the PPTC propeller a Cat® azimuth thruster, Figure 2, will be analyzed as well. The azimuth thruster is a propulsion system which is rotatable around a vertical axis. In this case, the thruster unit is equipped with a nozzle. The nozzle improves performance at low speed and high power, typical for a ship operating in bollard pull or towing mode such as a tug boat or anchor handler.

**Figure 2 Cat® azimuth thruster**

Geometrical properties of the azimuth thruster can be seen in Table 3.

Table 3 Geometrical properties of the azimuth thruster

Diameter	D	[m]	2.3
No. of blades	Z	[-]	4
Sense of rotation		[-]	Left
Nozzle		[-]	Yes
Type		[-]	Azimuth CPP

The full scale thruster is analyzed in open water with regard to cavitating performance in towing condition specified in Table 4.

Table 4 Cavitating condition for the azimuth thruster

Advance ratio	J	[-]	0.24
Inlet velocity	V	[kn]	5×(1-0.12)
Rot. speed	n	[rpm]	250
Cavitation no.	σ_n	[-]	2.6

4 METHODOLOGY

In this study an in-house modified RANS CFD code, based on the finite volume C++ library OpenFOAM, is used for simulating the cavitating flow. The incompressible solver utilizes a volume of fluid (VOF) approach for dealing with the two phases. The cavitation phenomena is modelled by applying the mass transfer model by Kunz (Kunz, o.a., 1999). Turbulence is dealt with using an URANS approach with a modified Renormalization Group Theorem (RNG) k- ϵ model. A damping function of the turbulent viscosity in the mixture region constitutes the modification. The purpose of the damping function is to compensate for the otherwise previously experienced underestimated unsteadiness of cavity dynamics (Reboud, Coutier-Delgosha, & Fortes-Patella, 2002). The damping function, which replaces the density in the expression for turbulent viscosity, equation 1, can be seen in equation 2.

$$\mu_t = f(\rho) C_\mu \frac{k^2}{\epsilon} \quad (1)$$

$$f(\rho) = \rho_v + \frac{(\rho_m - \rho_v)^{10}}{(\rho_l - \rho_v)^9} \quad (2)$$

Wall functions are applied to reduce the necessary discretization resolution near the walls. The computational domains are discretized using the commercial software ANSA by BETA CAE.

The discretization of the PPTC propeller is done for only one fifth of the propeller, taking advantage of the cyclic geometry of the propeller by using cyclic boundary conditions utilizing Arbitrary Mesh Interpolation (AMI). The rotation of the propeller is achieved by rotating the whole domain. The domain can be seen in Figure 3.

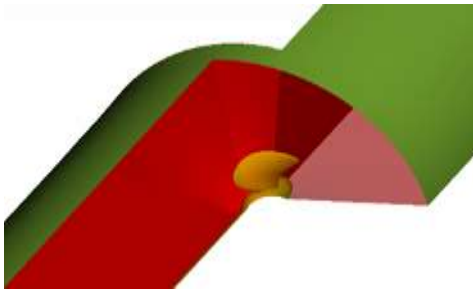


Figure 3 Computational domain for PPTC propeller

The surface mesh is made out of triads and the volume mesh starts from the propeller surface with prism layers followed by a transition zone of pyramids to hexahedrals. The mesh consists of a total amount of 2.3M cells and can be seen near the blade in Figure 4.

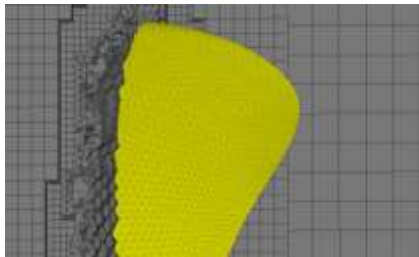


Figure 4 Surface and volume mesh for the PPTC propeller

The azimuth thruster is discretized into 6M polyhedral cells. The gap between the blade tip and nozzle is included and rotation is achieved by rotating a zone containing the hub and propeller blades.

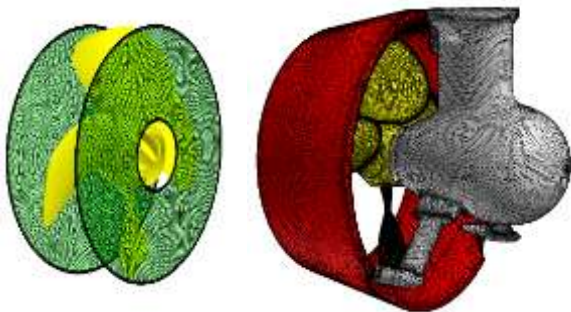


Figure 5 Surface meshed azimuth thruster unit and sliding interface (left)

The interfaces between the rotor (inner volume) and stator (outer volume) are sliding using AMI. The meshed thruster unit can be seen in Figure 5.

The thruster unit is connected to a vertical shaft, which extends upwards all the way to the cylindrical domain boundary. A cut through the domain near the azimuth thruster can be seen in Figure 6.

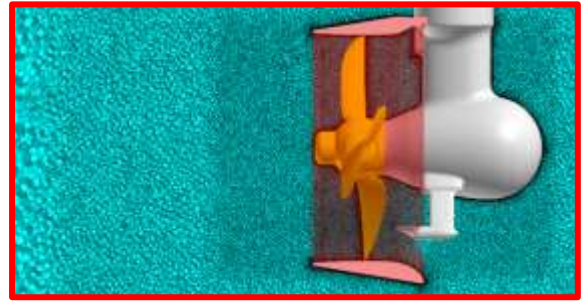


Figure 6 Cut through volume mesh

5 RESULTS

To achieve thrust identity for the PPTC propeller it was necessary to lower the inlet speed in all of the three cases, yielding lower advance ratio as can be shown in Table 5

Table 5 Changed advance ratio to gain thrust identity for the PPTC propeller

Case	ΔJ [%]
1	-1.14
2	-1.03
3	-1.13

Cavitation extent shown by isosurfaces three values of liquid volume fractions (0.2, 0.5, and 0.8) is shown below in Figure 7.

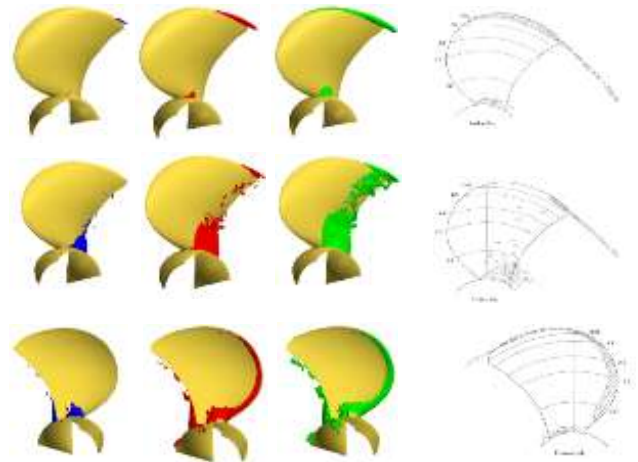


Figure 7 Cavitation extent for the three cases (rows) for three isosurfaces (columns) and experimental results (rightmost column)

The tip vortex and root cavitation in case 1 are both captured, with best resemblance for a volume fraction of 0.5. In case 2, the root cavitation is over predicted for liquid volume fraction 0.5 and 0.8 while the tip vortex cavitation is under predicted for volume fraction 0.2. The (unsteady) bubble cavitation is captured of reasonable extent for volume fraction 0.5. The sheet cavitation on the pressure side in case 3 is captured for liquid volume fraction of 0.5 and 0.8, although the root cavitation is over predicted. The tip vortex cavitation is not present for any of the isosurfaces in case 3.

The thrust from the propeller is decreased in cavitating condition, as seen in Table 6.

Table 6 Cavitation effect on thrust coefficient

	$\frac{K_{T,cavitating}}{K_{T,wetted}} [\%]$	
	Exp.	Sim.
Case 1	96.25	97.96
Case 2	84.25	99.4
Case 3	81.56	88.74

The propeller on the azimuth thruster shows cavitation extent as seen in Figure 8. Note that the pressure distribution on the azimuth thruster is including the effect of gravity. The azimuth thruster is cavitating near the tip at all four blades, the top blade is however experiencing more cavitation than the others. This is expected as the pressure increases with depth due to the presence of gravity as well as the wake due to the azimuth structure ahead of the blades yields higher loading on the top blade.

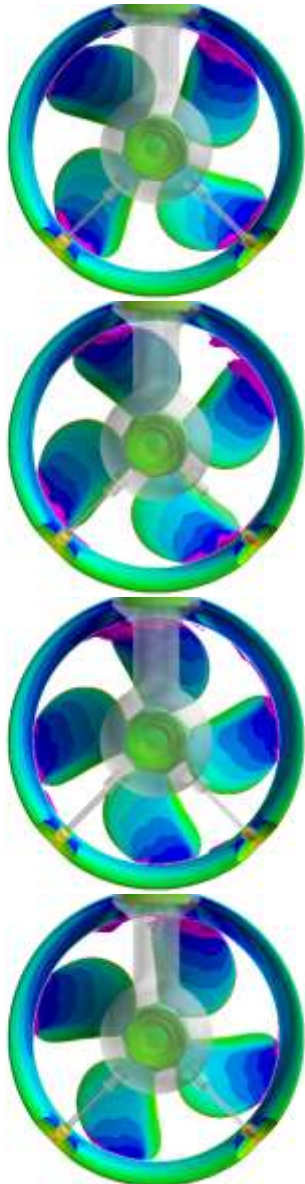


Figure 8 Cavitation isosurface for $\alpha = 0.5$ (magenta) on the azimuth thruster, $\Delta^\circ = 22.5^\circ$

The performance of the azimuth thruster was slightly decreased due to cavitation. The change in thrust, torque and open water efficiency when applying the cavitation model can be seen in Table 7.

Table 7 Change in azimuth thruster performance due to cavitation

$\Delta K_T [\%]$	-1.6
$\Delta K_Q [\%]$	-0.6
$\Delta \eta [\%]$	-1.6

6 DISCUSSION AND CONCLUSIONS

Simulation of cavitation using an in-house modified CFD solver has been performed. The solver is a multiphase solver which models cavitation by using the cavitation model by Kunz (Kunz, o.a., 1999). Furthermore, the solver applies a damping function on the turbulent viscosity in the mixture region, to deal with the otherwise commonly experienced dampening of unsteady effects when simulating cavitation with URANS.

The methodology shows capability of capturing detailed flow phenomena as tip vortex cavitation, bubble cavitation, sheet cavitation and root cavitation are all present in the simulation. These complex flow phenomena are important with regard to noise levels and can as shown be resolved using CFD in contrast to the physically more limited potential flow method. The results shows some inconsistency in best suitable isosurface value to reproduce the visual observed cavitation extent. The under predicted tip vortex cavitation may be due to insufficient spatial resolution. According to the experience of the authors, an improvement of the cavitating results could be achieved by using a polyhedral mesh rather than the currently applied hybrid mesh for the PPTC propeller.

In the second test case the CFD solver was used for simulating cavitation on a Cat® azimuth thruster. CFD is required as the azimuth structure gives rise to a wake field into the propeller. The cavitating azimuth shows reasonable amount of cavitation on the suction side near the tip and in the tip gap volume. The effect of gravity as well as the wake from the azimuth structure can be observed in the increased amount of cavitation on the top blade. It is found that the phenomena of cavitation decreases the performance slightly as expected.

REFERENCES

- Grekula, M., & Li, D. Q. (2008). 'Prediction of dynamic shedding of cloud cavitation on a 3D twisted foil and comparison with experiments'. *27th Symposium on Naval Hydrodynamics*, (pp. 1-17). Seoul.
- Brewer, W. H., Newman, J. C., Burgreen, G. W. & Burg, C. O. E. (2003). 'A Design Method for Investigating Cavitation Delay'. *Proceedings of the 8th*

International Conference on Numerical Ship Hydrodynamics, Busan, Korea.

- Heinke, H. J. (2011). 'Potsdam Propeller Test Case Cavitation Tests with the model propeller VP1304'. SVA Potsdam model basin.
- Huuva, T. (2008). 'Large eddy simulation of cavitating and non-cavitating flows'. PhD thesis. Gothenburg: Chalmers University of Technology.
- Kunz, R. F., Boger, D. A., Chyczewski, T. S., Stinebring, D. R., Gibeling, H. J., Venkateswaran, S., & Govindan, T. R. (1999). 'A Preconditioned Navier Stokes Method for Two-Phase Flows with Application to Cavitation Problems'. Proceedings of 14th AIAA CFD Conference, (pp. 849-875). Norfolk.
- Lu, N., Bark, G., & Bensow, R. (2012). 'Numerical simulations of the cavitating flow on a marine propeller'. Eight Symposium on Cavitation, (pp. 338-343). Singapore.
- Reboud, J. L., Coutier-Delgosha, O., and Fortes-Patella, R. (2002). 'Simulation of unsteady cavitation with a two equation turbulence model including compressibility effects'. Journal of Turbulence.
- Sipilä, T. (2011). 'RANS analyses of cavitating propeller flows'. Espoo: VTT.

Hydroacoustic Simulations Using OpenFOAM

Fatih Ertınaz^{1*}

¹Milper Pervane Teknolojileri A.Ş., Teknopark İstanbul – Sanayi Mahallesi, Teknopark Bulvarı
1/2A Z08 34906 Pendik-Istanbul, Turkey

Abstract: Hydroacoustics is the area that focuses on the study of propagating sound in water. Sound may occur because of a wide variety of reasons. Theoretical basis for the analysis of sound generated by a body moving in a fluid is represented by the Ffowcs Williams-Hawkings (FWH) equation, which can be derived from basic conservation laws of mass and momentum written in terms of generalized functions. In the scope of this project turbulent incompressible flow around cavitated propellers will be investigated to predict the influence of cavitation on the noise waveforms. Therefore we aim to implement a transient multiphase hydroacoustics solver based on the FWH equation to determine the noise generated by ship propellers as well as to compute the influence of cavitation occurring. The nonlinear terms are included in the mathematical model because the results from recent studies show that neglecting the quadrupole terms does not yield sufficient enough results. The software of which this study is based is OpenFOAM, an Open Source object-oriented library for numerical simulations in continuum mechanics written in the C++ programming language. OpenFOAM framework is selected as the basis library for code development because of its flexibility in the development of customized numerical solvers.

Keywords: CFD, Hydroacoustics, Ffowcs Williams-Hawkings equation, OpenFOAM, acoustic perturbation equations.

1 INTRODUCTION

With the increasing capability of computational resources in the past two decades, computational fluid dynamics (CFD) became a crucial tool for analysis in naval hydrodynamics. As a consequence, CFD can be used to tackle the challenging multiphysics applications, as in the topic of hydroacoustics.

Hydroacoustics is the area that focuses on the study of propagating sound in water. Sound may occur because of a wide variety of reasons and the theoretical basis for the analysis of sound generated by a body moving in a fluid is represented by the Ffowcs Williams-Hawkings (FWH) equation, which can be derived from basic conservation laws of mass and momentum written in terms of generalized functions. As it is out of the scope of this study we do not provide the derivation of the FWH equation, however interested reader may refer to the article by Williams & Hawkings (1968).

2 GOVERNING EQUATIONS

FWH equation provides a description of sound generated by a solid body moving in a fluid and it can be written as follows:

$$D^2 p'(x, y) = + \frac{\partial}{\partial t} [\rho_0 v_N + \rho (u_N - v_N) \delta(f)] - \frac{\partial}{\partial x_i} [\Delta P_{ij} n_j + \rho u_i (u_N - v_N) \delta(f)] + \frac{\partial^2}{\partial x_i \partial x_j} [T_{ij} H(f)] \quad (1)$$

where D is the D'Alembert operator:

$$D^2 = \frac{1}{c_0^2} \frac{\partial^2}{\partial t^2} - \nabla^2.$$

Furthermore T_{ij} is the Lighthill stress tensor:

$$T_{ij} = \rho u_i u_j + P_{ij} - c_0^2 (\rho - \rho_0) \delta_{ij}$$

and P_{ij} is compressible stress tensor:

$$P_{ij} = p \delta_{ij} + \mu \left(-\frac{\partial u_i}{\partial x_j} - \frac{\partial u_j}{\partial x_i} + \frac{2}{3} \frac{\partial u_k}{\partial x_k} \right) \delta_{ij}.$$

FWH equation consists of 3 sources because according to Williams & Hawkings (1968) when both the bounding surfaces and the turbulence are compact relative to the radiated length scales, the turbulence is acoustically equivalent to a volume distribution of moving quadrupoles and the surfaces to dipole and monopole distributions.

As Salvatore and Ianniello (2002) states, “The three source terms appearing in FWH equation are known as thickness (monopole), loading (dipole) and quadrupole terms. Thickness contribution is related to the body geometry and kinematics, while the loading noise concerns the load distribution upon the blade; nonlinearities in the flow field are represented by the quadrupole source term and generally become predominant at high speed, when the flow field is characterized by the occurrence of shock waves”.

We can investigate each source term in the equation (1) separately. The monopole term:

$\frac{\partial}{\partial t} [\rho_0 v_N + \rho (u_N - v_N) \delta(f)]$ represents volume displacement effects when the surfaces are moving.

This term is supplemented by surface distributions of acoustic dipoles of strength density $P_{ij} n_j$, which correspond to the second term on the RHS:

$$- \frac{\partial}{\partial x_i} [\Delta P_{ij} n_j + \rho u_i (u_N - v_N) \delta(f)]$$

where $\Delta P_{ij} = P_{ij} - \rho_0 \delta_{ij}$ and u_N is velocity component normal to the surface whereas v_N is the surface velocity component normal to the surface.

The quadrupole term in the equation 1 is the very last term on the RHS and it corresponds to the volume displacement related sound generation as it is aforementioned. In aeroacoustics, it is crucial to consider this nonlinear term only if the flow is in the high transonic or supersonic regime. Even though we are far from being inside these high speed flow regimes for a rotating ship propeller, we still might have to take into account the quadrupole term because of the different nature of underwater physics. A recent study by Salvatore et al. (2012) claims that it is vital to consider the nonlinear term in FWH equation for hydroacoustic applications to capture the sound generation due to the shocks which occur because of the cavity bubbles appearing even for propellers with a relatively low rotational speed.

Since the velocity fields u_N and v_N basically correspond to the same value for incompressible fluids, the monopole and dipole terms are cancelled out for initial stages of this work. Moreover the Lighthill tensor in quadrupole term for incompressible cases reduces to:

$$T_{ij} = \rho u_i u_j \quad (2)$$

An OpenFOAM solver called *acousticsFoam* implemented in this study is based on the D'Alembert operator applied on p' and having equation 2 on the RHS:

$$\frac{1}{c_0^2} \frac{\partial^2 p'}{\partial t^2} - \nabla^2 p' = \frac{\partial^2}{\partial x_i \partial x_j} (\rho u_i u_j) \quad (3)$$

Velocity components on the RHS are computed by the flow solver and pressure fluctuations are resolved using these fields that come from CFD. Adding the acoustic pressure disturbance to the pressure solutions from CFD for each control volume gives us the total pressure in the system.

2.1 Acoustic Perturbation Equations

A different approach derived by Ewert and Schroeder is known as the acoustic perturbation equations (APE):

$$\frac{\partial \rho'}{\partial t} + \nabla \cdot (\rho' \bar{u} + \bar{\rho} u') = 0 \quad (6)$$

$$\frac{\partial u'}{\partial t} + \nabla \bar{u} \cdot u' + \nabla \left(\frac{p'}{\bar{\rho}} \right) = q_m \quad (7)$$

$$\frac{\partial p'}{\partial t} + \frac{1}{c^2} \nabla \cdot (\rho' \bar{u} + \bar{\rho} u') = q_e \quad (8)$$

where q_m and q_e are the source terms determined by LES:

$$q_m = - (\omega \times \bar{u} + \bar{\omega} \times u') + T' \nabla s - s' \nabla T$$

$$q_e = \frac{\gamma \bar{p}}{c_p} \frac{\partial s'}{\partial t}$$

and u is velocity, ω is vorticity, ρ is density, T is temperature, p is pressure, s is entropy and γ is ratio of specific heats:

$$\gamma = \frac{c_p}{c_v}$$

According to Wagner (2007): "These equations describe mean flow convection effects, but unlike other systems for the acoustic field they do not possess instabilities for any nonuniform mean flow field with arbitrary density gradients. The coupling between the LES and the CAA solutions is based on the source terms which are cyclically fed into the acoustic simulation".

Since the computational requirement for an accurate LES case is still too large for multiphase cavity simulations (see Wagner (2007) for grid resolution estimation) we may need to reduce the complexity by using hybrid turbulence models instead of a complete LES. Additionally the timestep needed by acoustics might be larger than the timestep needed by CFD, thus we do not have to call acoustics solver at the end of the each time iteration. Instead we can run acoustic solver after a certain number of CFD loops depending on the ratio between timestep size of acoustics and CFD. Furthermore the author considers only the isothermal cases which allows us to cancel out the terms with T and s from the source terms.

2.2 Acoustic Boundary Conditions

Wagner (2007) states that "Because the radiation boundary condition is based on the asymptotic expansion of the solution, it works best if the nonreflecting boundary is far away from the source of the sound".

This is an appropriate choice for our problem since it avoids an increase in the total energy of the system by using nonreflective condition.

3 IMPLEMENTATION IN OPENFOAM

In this section we provide a short code snippet to show how the OpenFOAM framework is structured for equation mimicking.

Following code block shows a brief implementation of the equation (3):

```
const volTensorField UU("UU", U*U);
fvScalarMatrix pPrimeEqn
(
    1/(sqr(c0))*fvm::d2dt2(pPrime)
    - fvm::laplacian(pPrime)
    ==
    fvc::div(fvc::div(UU))
);
pPrimeEqn.relax();
pPrimeEqn.solve();
```

As it can be seen above correspondence between the implementation and equation is clear. Each term in the partial differential equation is represented by a related function.

4 RESULTS AND DISCUSSION

In the current work-flow of this project, as the initial step one has to run a flow solver to detect the velocity fields and pressure. Once the velocity fields are extracted from a converged CFD case, we can resolve the acoustic pressure fluctuations using acoustics solver.

A more accurate approach is to use LES model for turbulence. In this case one should invoke acoustics solver at the end of each timestep of the transient flow solver.

After determining the pressure fluctuations, one can use a multiphase solver to better predict the cavity bubble locations and then run acoustics solver once more to compute the sound generated by the cavity influence.

4.1 Mesh Generation

Mesh generation is handled using built-in functions that comes with a regular OpenFOAM installation.

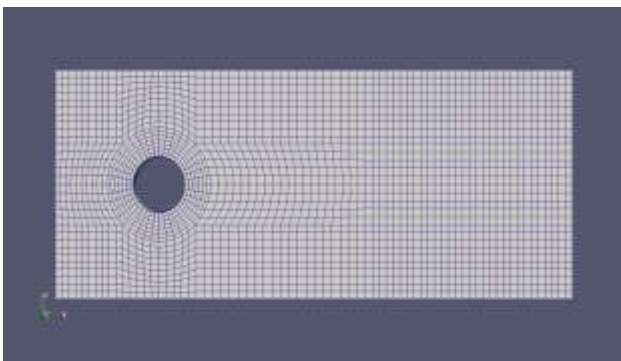


Figure 1 Blockmesh around a cylinder

Above in Figure 1 one can see a simple computational grid around a cylinder. This mesh contains 2280 cells having one cell thickness in z direction. This grid is generated using the *blockMesh* tool of OpenFOAM which is usually used for creating the block structured flow domain as the first step of creating volume meshes.

In order to deal with more complex geometries such as marine propellers, one can use *snappyHexMesh* to create unstructured grids. A sample mesh generated using *snappyHexMesh* can be seen in the figure 2. This mesh has around 525000 elements in the entire domain.

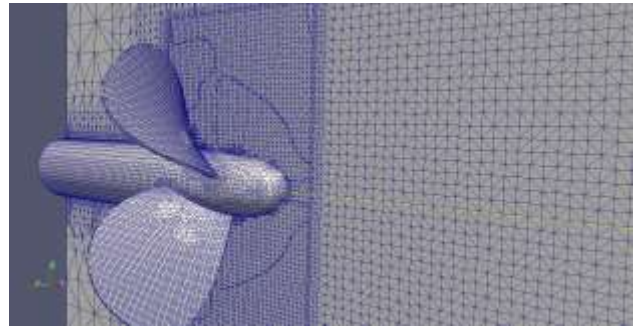


Figure 2 Unstructured mesh around a marine propeller

The *snappyHexMesh* utility generates 3-dimensional meshes containing hexahedra and split-hexahedra automatically from triangulated surface geometries, for further details of mesh generation in OpenFOAM please see the OpenFOAM User Guide (2013).

4.2 Potential Flow Solver

We choose to use the potential flow solver called *potentialFoam* in order to simplify the CFD part of the work-flow. This solver presumes that the flow is steady-state, incompressible, irrotational and inviscid. Usually it is used to generate appropriate initial conditions to achieve smoother convergence.

Figure 3 shows the velocity field in x direction around the cylinder.

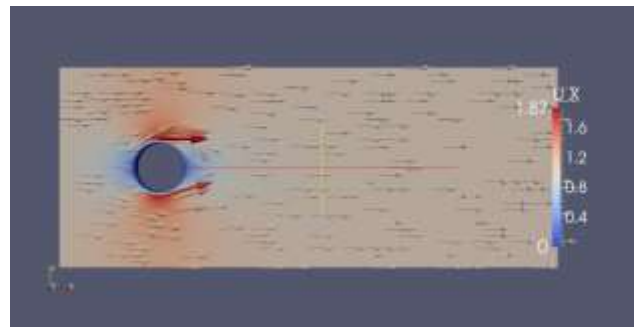


Figure 3 Potential flow solution around a cylinder

Once the flow field is computed we run the acoustic solver to resolve the pressure fluctuations. Even though the physics behind the *potentialFoam* is very restricted, it is a useful solver for test cases.

4.3 Acoustic Solver

As it is stated before, the basis equation for acoustic solver we implemented is given in the equation 3.

This solver reads the velocity fields computed by the potential solver and then applied divergence operator twice. It then applies the D'Alembert operator and finds the new pressure values which are the pressure fluctuations due to the acoustics.

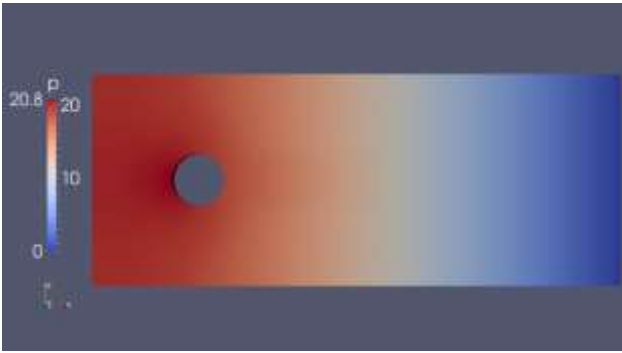


Figure 4 Acoustic pressure distribution around a cylinder

Figure 4 shows us the sample solutions produced using the solver called *acousticsFoam*. Since the physics behind both the *potentialFoam* and *acousticsFoam* is quite limited, the values we have are subject to question. However it is expected to have larger values around the propeller than the values around the far-field.

4.4 Multiphase Cavity Flow Solver

To simulate the cavity influenced flow around a rotating propeller we used the OpenFOAM solver called *interPhaseChangeDyMFoam*. This is a solver for two-phase flow with incompressible, isothermal immiscible fluid. It uses volume of fluid (VoF) method for interface capturing with mesh motion. The momentum is of the mixture and a single momentum equation is solved.

In this test case we used k-ε turbulence model, Schnerr-Sauer for mass transfer model (see Bensow and Bark (2010) for further details), pressure implicit split operator (PISO) based solver with run time adjustable time-steps $1e-05$ and maximum Courant number 2.

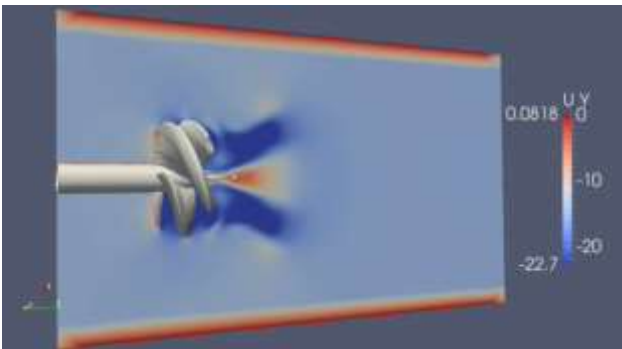


Figure 5 Cavity bubbles around the propeller

In Figure 5 above one can see the cavity bubbles occurring around the propeller. These bubbles should definitely have an impact on the sound propagation in the far-field. This is the reason why we would like to couple the CFD and acoustic solvers.

The bubbles in front of the hub disappear as the simulations continue which can be depicted from Figure 6 given below. This figure is taken at $t=0.18$

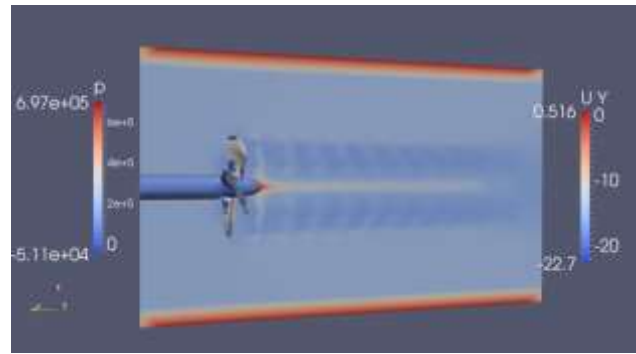


Figure 6 Cavity flow around the propeller

5 CONCLUSIONS AND FUTURE WORK

In this work our purpose is to develop an acoustics solver that is coupled with a flow solver. As the initial step a solver based on the incompressible FWH equation is implemented. Then it is verified by a simple test case which consists of running potential flow around a cylinder and applying the acoustics solver implemented. Tendency of the acoustic pressure distribution seemed physically correct, therefore for further steps we extend the existing solver for compressible equation 1.

The complete project involves development of two different transient compressible acoustic solvers based on APE and FWH respectively coupled with a multiphase cavity solver using LES.

REFERENCES

- Williams, J. E. F., Hawkings, D. L. (1968). 'Sound Generation by Turbulence and Arbitrary Motion'. Philosophical Transactions of the Royal Society, A264: 321-342.
- Salvatore, F., Ianniello, S. (2002). 'Preliminary Results on Acoustic Modeling of Cavitating Propellers', IABEM 2002, International Association for Boundary Element Methods, UT Austin, TX, USA.
- Wagner, C. A. (2007). Large Eddy Simulation for Acoustics. Cambridge University Press.
- Salvatore, F., Muscari, R., Di Mascio A. (2012). 'Hydroacoustic characterization of a marine propeller through the acoustic analogy', Sustainable Maritime Transportation and Exploitation of Sea Resources 2012, CNR-INSEAN, Rome, Italy.
- OpenFOAM Foundation. (2013). 'The Open Source CFD Toolbox – User Guide'.
- Bensow, R.,E., Bark, G. (2010). 'Simulating Cavity Flows with LES in OpenFOAM', European Conference on Computational Fluid Dynamics, ECCOMAS CFD 2010, Lisbon, Portugal.

Propeller Noise Investigations by Means of Middle Size Cavitation Tunnel Measurements

Sebastian Kowalczyk^{1*}, Pawel Hoffmann¹

¹Ship Design and Research Centre (CTO SA), Gdańsk, Poland

Abstract: The hydroacoustic characteristics of propellers under different loading condition have been investigated including both cavitating and non-cavitating conditions. The standard propeller has been investigated in model scale, using the cavitation tunnel. The knowledge of hydroacoustic characteristic allow to design silent propulsion systems with the minimal impact on the marine environment.

Keywords: Propeller, underwater noise, cavitation.

1 INTRODUCTION

Nowadays the ship and offshore structure designers must consider both economical and environmental aspects during design process. The environmental aspects should also relate to the radiated underwater noise. Fortunately the understanding of underwater noise mechanisms increased significantly during last years. Number of research institutes is investigating different aspects of underwater noise mechanisms for both shallow (Kozaczka & Grelowska, 2013) and deep water systems. The Specialist Committee on Hydrodynamic Noise (27th ITTC) define three major classes of underwater noise emissions of vessels:

- machinery noise,
- propeller noise,
- hydrodynamic noise.

The authors of current paper focus their research on underwater noise radiated by operating propeller. Both cavitating and non-cavitating loading conditions are taken into account. The model testing investigations are complemented by the numerical simulations of non-cavitating conditions.

The aim of current work is to check the application of medium size cavitation tunnel for the propeller noise measurements and extrapolation of obtained results to full scale data. Since there is a lack of full scale data there is a need to use validated numerical tools to better understand the full scale effect.

2 MODEL SCALE APPROACH

The best option for every propeller designer is to be able to provide and validate the product by the use of real measurements. It means that the full scale propeller should be delivered and tested. Unfortunately that approach is not justified from the economical point of view. Instead, different modeling approach are used. Interaction of operating propeller with the hull can be investigated with the use of large cavitation tunnels where the entire hull model is employed. The alternative to such

kind of research is the application of medium size cavitation tunnels. In that case it is possible to use the model of the propeller in appropriate scale where the inflow boundary conditions are simulated by the use of "dummy body". Both the time and cost of the tests can be significantly reduced by the application of medium size cavitation tunnels. The point is to use appropriate methodology for the extrapolation of obtained results to full scale.

To be able to carry out correct and accurate model scale tests, three base similarity rules should be employed: geometric, kinematic and dynamic similarities.

Geometric similarity means that both model and real shapes are similar. It is done by application of the scale factor which is defined as a ratio of main dimensions of both geometries.

Kinematic similarity defines the modeling time of investigated phenomena. Keeping the kinematic similarity means to ensure similar time rates of flow motions or flow changes.

Dynamic similarity defines the similarity of all forces acting on model and real geometry, which should be proportional.

According to propeller investigations following non-dimensional parameters should be defined:

- **geometric similarity:**
$$\lambda = \frac{D_S}{D_M} \quad (1)$$

Where λ = scale factor; D_{Sv} = propeller diameter at full scale [m]; and D_M = propeller diameter at model scale [m],

- **kinematic similarity:**
$$J = \frac{V_a}{nD} \quad (2)$$

Where J = advance ratio; D = propeller diameter [m], V_a = advance velocity [m/s], and n = rotational speed [rps];

- dynamic similarity:

$$Fn = \frac{V}{\sqrt{gL}} \quad (3)$$

Where Fn = Froude number; V = ship speed [m/s], g = gravitational acceleration [m^2/s], and L = ship length [m];

$$K_t = \frac{T}{\rho_0 n^2 D^4} \quad (4)$$

Where K_t = thrust coefficient; T = propeller thrust [N], ρ_0 = water density [kg/m^3], D = propeller diameter [m], and n = rotational speed [rps];

$$K_q = \frac{Q}{\rho_0 n^2 D^5} \quad (5)$$

Where K_q = torque coefficient; Q = propeller torque [Nm], ρ_0 = water density [kg/m^3], D = propeller diameter [m], and n = rotational speed [rps];

$$St = \frac{fD}{V} \quad (6)$$

Where St = Strouhal number; f = here frequency [Hz]; D = propeller diameter [m], and V = velocity [m/s];

$$\sigma = \frac{p_{atm} - p_n + \rho_0 g h}{0.5 \rho_0 V^2} \quad (7)$$

Where σ = cavitation number; p_{atm} = hydrostatic pressure [Pa]; p_n = vapor pressure [Pa], g = gravitational acceleration [m^2/s], ρ_0 = water density [kg/m^3], V = velocity [m/s], and h = submergence level [m];

Based on above mentioned rules following parameters for both numerical simulations and model testing were established (m denotes model scale, s denotes full scale):

$$\text{Advance speed: } V_{as} = J n_s D_s ;$$

$$\text{Rotational speed: } n_s = \sqrt{\frac{T_s}{\rho_0 D^4 K_t}} ;$$

$$\text{Thrust: } T_s = T_M \lambda^3 ;$$

Hydrostatic pressure:

$$p_{ams} = \sigma 0.5 \rho_0 (n_s D_s)^2 + p_n + \rho_0 g (h + 0.7 \frac{D_s}{2})$$

3 NUMERICAL APPROACH

Nowadays all research and commercial institutes are using different numerical tools. There is still discussion about what kind of assumption should be applied and how that affect obtained results. One of the option of applying numerical tools is to use Computational Fluid Dynamic (CFD). Since there are many approaches, the authors of current article decided to use commercial tool which base on solution on Reynolds Average Navier Stokes (RANS) equations. During all CFD simulations, StarCCM+ tool was used.

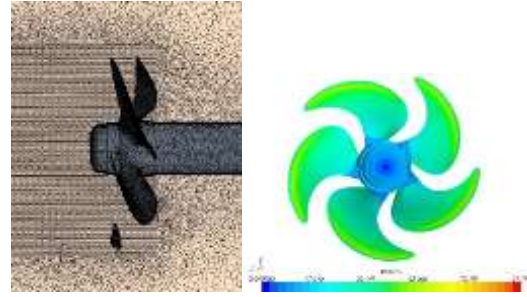


Figure 1 Mesh distribution around propeller (left side), y+ distribution on the propeller (right side)

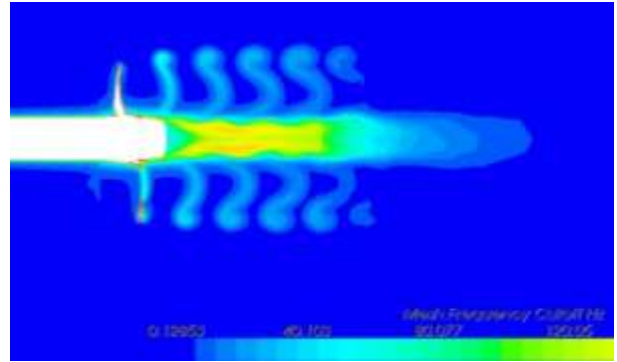


Figure 2 Possible simulated frequency range for the applied mesh



Figure 3 Five blade propeller - geometry of real model (left side), 3D model used during CFD (right side)

The code solves continuity equations in integral form on a polyhedral mesh by means of the finite volume technique. The Reynolds stress is solved by means of k- ω turbulence model which has an advantage over the k- ϵ model by its improved performance for boundary layers under adverse pressure gradients. The movement of the propeller was solved by rotating whole computational mesh around propeller axis.

The flow was computed for full geometry of propeller in the cylindrical domain of the following dimensions: 0.5 D upstream, 2.5D downstream, 2.5D in the radial direction from axis, where D is the diameter of the propeller.

The number of mesh cells was about 2 000 000. The mesh was refined by taking into account 2 aspects:

- proper boundary layer modeling - the boundary layer was assessed by controlling y+ around the propeller surfaces - Figure 1.

- analyzing the frequency that the mesh can resolve, using Cut Mesh option (StarCCM+) - Figure 2.

The details of five blade propeller geometry are depicted in Table 2, as well as in Figure 1 and 3.

The applied loading conditions are depicted in Table 1.

Table 1 Loading conditions

		Model Scale
Advance speed	[m/s]	4.6
Rotational speed	[rps]	15
Advance ratio	[]	1.15
Cavitation number	[]	2.799
Thrust Coefficient	[]	0.211
Scale factor	[]	18.81

The details of propeller geometry are depicted in Table 2. The aim of realized calculations is to validate the numerical calculations for the model scale. As it is mentioned in the (27th ITTC) since there is a lack of full scale data it is important to validate methodology of calculations for the model scale (i.e. by comparison with towing tanks results) and then reuse that methodology for the full scale investigations.

Table 2 Details of propeller geometry

Propeller data		
D [mm]	Blade number	Ae/Ao
0,2657	5	0,774

4 CAVITATION TUNNEL APPROACH

All measurements described in current paper were carried out with the use of one of the test facility of the Ship Design and Research Centre in Poland - cavitation tunnel with a 0.8m×0.8m×3.1m test section with a possibility of wake simulation and maximum flow velocity up to 20m/s, equipped with 2D LDA measuring system. The main technical data are summarized in the Table 3.

Table 3 Cavitation tunnel technical data

	Cavitation tunnel technical data
Max Ø of propeller model [m]	0.3
Max tunnel water speed [m/s]	20
Test section dimensions [m] LxBxH	3.1x0.8x0.8

Existing tunnel with measurement system is very well adopted for cavitation observations as well as for the erosion tests and investigations of the flow around propeller and appendages. Few numerical tools (in-house codes) are validated based on provided experimental analyses the results allow for better understanding of physics of operating propellers at both cavitating and non-cavitating conditions.

Cavitation tunnel was upgraded for the noise measurements with keeping the ability of cavitation observation. The test section was equipped with the acoustic chamber - Figure 4. The acoustic chamber forms a box made of steel plates stiffened by the frames in order to minimize the vibration. Internal walls were covered

with noise damping materials in order to prevent noise reflections. The acoustic chamber can be installed in one of the bottom windows of the test section depending on the size of dummy body and location of the propeller model. The hydrophone, Bruel & Kjaer Type 8100, was installed inside the chamber using the adjustable bracket allowing the precise positioning with reference to propeller model location. The hydrophone was located approximately 1m below the propeller model. The measurements of noise generated by propeller model were complemented by the measurements of the noise background resulting from the cavitation tunnel operation and propeller model drive train. Both the background noise and signal from operating propeller model were processed using the FFT technique and then the signal amplitudes on corresponding frequencies were derived.

Correct and full understanding of hydroacoustic measurements of operating propeller include the complete testing of propeller model with the use of cavitation tunnel i.e. cavitation observation and noise measurements at the same time. Cavitation tests were provided for the simulated inflow conditions affected by the hull shape. In order to obtain a correct wake distribution, a respective dummy body (the aftship part geometrically corresponding to the aftership part of the vessel) was installed in the test section of cavitation tunnel. The propeller model was driven by a shaft passing inside the dummy body. The test conditions were determined from the self-propulsion tests and predictions made for respective draughts and propeller loadings. The inflow to the propeller was corrected by using wire meshes in order to ensure appropriate wake field. The test was performed in accordance with the ITTC (International Towing Tank Conference) recommendations.

The full scale noise prediction was performed based on the recommendations given in 18th ITTC Cavitation Technical Committee Report (1987). The method implies that both the sound pressure level and frequency are transformed according to the following formulas:

$$\Delta L_s = 20 \log \left[\left(\frac{D_s}{D_M} \right)^z \left(\frac{r_M}{r_s} \right)^x \left(\frac{\sigma_s}{\sigma_M} \right)^{y/2} \left(\frac{n_s D_s}{n_M D_M} \right)^y \left(\frac{\rho_s}{\rho_M} \right)^{y/2} \right]$$

$$f_s = f_M \frac{n_s}{n_M} \quad (8)$$

Where r = distance from noise source to the point of interest [m], m - denotes model scale, s -denotes full scale.

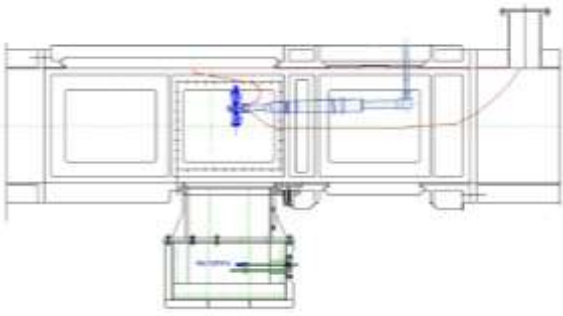


Figure 4 Cavitation tunnel with acoustic chamber cross-section

There are two aims of research with the use of cavitation tunnels. The first aim is to validate numerical simulations. It means that for the comparable geometrical, kinematic and dynamic conditions pressure fluctuations were monitored. For that purpose the test number 1 was started.

The second aim was to check the application of medium size cavitation tunnel for the standard propeller noise measurements. For that purpose test number 2 was started. Details of both tests are listed in the table below.

Table 4 Loading conditions for the cavitation tunnel

		Test #1	Test #2
Cavitation number	[]	2.8	9.3
Thrust Coefficient	[]	0.211	0.099
Advance speed	[m/s]	4.6	5.5

5 RESULTS

Comparison of numerical and experimental results shows very good agreement between monitored non-dimensional parameters. Differences between results are below 1.5%. The accuracy level of modeling, during numerical calculations, cavitation number (difference ~0.8%) and thrust coefficient (difference ~1.4%) is on required level (Table 5). It means that applied CFD methodology can be extrapolated for the use during full scale calculations.

Table 5 Comparison of non-dimensional numbers based on numerical and experimental tests

		CFD	Cavitation Tunnel
Cavitation number	[]	2,776	2,799
Thrust Coefficient	[]	0,208	0,211
$K_{t(CFD)} / K_{t(Tunnel)}$	%	-1,37%	
$\sigma_{(CFD)} / \sigma_{(Tunnel)}$	%	-0,84%	

Based on that results it is possible to compare both the calculated and measured noise generated by operating propeller. Results are depicted in Figure 5. The shape of both curves is comparable. The amplified noise pick values were noticed for the same frequency. Nevertheless the exact value of calculated noise level is significantly different in comparison to the measured one.

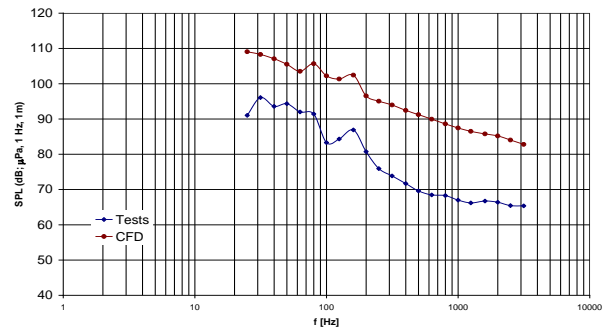


Figure 5 Noise measurements of operating propeller: brown curve - CFD results, blue curve - cavitation tunnel results

The noise measurements were carried out with the use of cavitation tunnel. Noise measurements - both total and background noise of the tunnel were monitored at the reference point. In order to analyze the noise generated by the propeller model the background noise level was subtracted logarithmically from the total noise. As a result the net noise level of operating propeller model was monitored. In Figure 7 the results for the full scale are given. The results of measurements in cavitation tunnel were calculated according to the Equation (8). Both noise levels generated by cavitating and non-cavitating propeller were given. Since neither fully developed cavitation nor hub vortex cavitation was noticed for considered propeller the noise level for both cavitating and non-cavitating propellers was comparable.

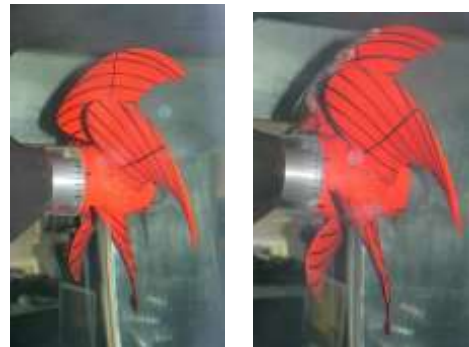


Figure 6 Cavitation observations of operating propeller, Left side - non-cavitating loading - test #2, Right side -cavitating loading - test #1

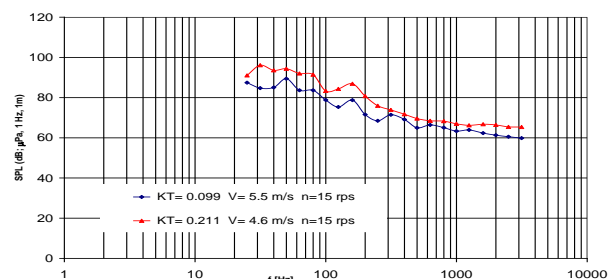


Figure 7 Noise measurements of operating propeller

6 CONCLUSIONS

The provided tests present positive feedback from application of medium-size cavitation tunnel for the propeller induced noise investigations. It is possible to investigate the influence of cavitation on the noise level

of operating propeller model with the use of medium size cavitation tunnel.

The applied methodology of CFD calculations for the model scale gives accurate results according to the prediction of propeller performance. The quality of noise characteristic of operating propeller is comparable to the measured one. Nevertheless more work is requested to obtain better convergence between calculated and measured values of noise level. The further step of CFD investigations is also to reuse this methodology for the full scale calculations.

REFERENCES

<http://www.itc2014.dk/>

Kowalczyk S., Kaiser M. (2013). 'Propeller Noise Investigations by Means of Cavitation Tunnel Measurements'. Proceedings of 1st Underwater Acoustics, Corfu Island, Greece

Kozaczka, E., Grelowska, G., (2013). Hydroacoustics of shallow water, Warsaw, Poland

Miller W., Szantyr J.A. (2010), Practical Design of Marine Propellers, Centrum Techniki Okrętowej S.A., Poland.

Star-CCM+ User Guide.

Outlook on Marine Propeller Noise and Cavitation Modelling

Artur K. Lidtke^{1*}, Stephen R. Turnock¹, Victor F. Humphrey²

¹Fluid Structure Interactions Research Group, University of Southampton, Southampton, SO17 2BJ, UK

²Institute of Sound and Vibration Research, University of Southampton, Southampton, SO17 2BJ, UK

Abstract: Two computational studies are presented in this paper. First, the Potsdam Propeller Test Case which is used to demonstrate the capabilities of mass transfer cavitation models, more precisely the model by Sauer and Schnerr, in tackling the problem of marine propeller cavitation. It is shown that the extents of the predicted cavitation regions agree well with the experiment but suffer from the fact that the tip vortices and the associated low pressure regions are under-resolved when URANS is utilised. Next, preliminary results from the study of cavitation noise modelling attempt are presented for a NACA 0009 section, used as a simplified representation of a propeller blade. Large Eddy Simulation and Ffowcs Williams-Hawkings porous acoustic analogy are used in order to estimate the cavitation-induced noise. Results indicate that the discussed approach provides the means for identifying low-frequency noise generation mechanisms in the flow, yielding sound pressure levels of the order of 40 dB re 20 mPa, but does not allow for fine-scale bubble dynamics to be resolved. One may conclude that the discussed approach is a viable option to predict large parts of marine propeller noise spectra but further work is needed in order to account for the high frequency components.

Keywords: Cavitation, noise, large eddy simulation, propeller, acoustic analogy.

1 INTRODUCTION

Concerns about limiting the input of noise into the Oceans have been increasingly more pronounced in recent years. One may associate the anthropogenic noise with multiple mechanisms, shipping being one of the larger contributors (Hildebrand 2009) (Urlick 1984). The significance of this is even greater given that a large part of the energy of the ship-related noise falls within the 10-1000 Hz regime and thus has a high potential to affect marine wildlife (Lloyd 2013). Hence, several initiatives have been established in order to investigate how to mitigate the impact of shipping on the marine environment (Van der Graaf et al. 2012) (Tasker et al. 2010).

Apart from the noise due to turbulence, associated, for instance, with local changes of the angle of attack of a propeller blade or shedding of vortices, the noise signature of a marine propeller is significantly affected by cavitation. There are several sources of noise typically induced by this phenomenon. The oscillations of the cavity volume, which may also be seen as an effective change of the blade thickness, typically generate monopole-like. The second major source of cavitation noise may be associated with the collapse and oscillation of individual bubbles (Kirsteins et al. 2011) (Park et al. 2009) (Seol et al. 2005) (Salvatore & Ianniello 2002). The last prominent noise source is the impinging of large scale cavity interfaces upon each other or against solid surfaces (Bensow, R. E., & Bark, G. 2010) Turbulence itself will also contribute to the noise signature of a propeller blade and will interfere with the remaining noise mechanisms (Kirsteins et al. 2011).

It becomes apparent that unsteadiness of the flow will play a crucial role in determining the noise signature of a

hydrofoil. Thus, while useful insights may be gained into the cavitation phenomena using approaches such as unsteady RANS or boundary element methods, one should consider using Large Eddy Simulation (LES) to develop a deeper understanding of the underlying flow.

This is of particular importance to the project discussed herein, whose main aim is to enable the assessment of the environmental impact of a ship on marine ecosystems by supplying the information about the propeller-induced noise levels. Therefore, the current focus is put on assessing the potential benefits and disadvantages of turbulence and cavitation modelling techniques from the numerical propeller noise modelling perspective.

In order to allow more detailed analysis to be undertaken a basic understanding of the limitations of the modelling methods constituting the current state of the art must be developed. This is done on the example of the Potsdam Propeller Test Case (PPTC). This has seen a significant amount of both experimental and theoretical attention (Abdel-Maksoud 2011), thus becoming one of the more established validation problems. The presented results were obtained using the Schnerr-Sauer mass transfer cavitation model for the flow being solved using unsteady RANS with the $k - \omega$ turbulence model.

The flow over a propeller may be regarded as complex and is thus not very well suitable for preliminary simulations aimed at assessing the cavitation noise. Hence, a simpler test case of a NACA 0009 hydrofoil is also considered, where LES is used instead of RANS to solve the equations of motion of the flow. The far-field sound pressure level is computed using porous Ffowcs-Williams Hawking acoustic analogy implemented in

* Corresponding author e-mail: akl1g09@soton.ac.uk

OpenFOAM. The presented analysis focuses on correlating the relationships between the predicted flow features and the corresponding noise signals, allowing for preliminary conclusions to be drawn with respect to the aptness of the presented approach to the modelling of noise of a complete propeller.

2 NUMERICAL MODELLING

2.1 Cavitation Modelling

Cavitation may be described as the transition of liquid into vapour in regions of low pressure. This is caused by the presence of small gas nuclei in the liquid (Plesset & Prosperetti 1977). When subject to tensile stress, these nuclei expand and lead to different types of cavitation, such as sheet or bubble cavitation, depending on the flow conditions (Vallier 2013).

It is possible to simulate the behaviour of individual cavitation bubbles, as described, for instance, by Jamaluddin et al. (2011) and Hsiao & Chahine (2004). However, because of the small size of the cavitation nuclei, ranging between 2 and 50 μm for standard sea water (Woo Shin 2010), it would not be feasible to compute the behavior of every individual bubble in full detail for a flow over a full-scale propeller or a hydrofoil.

For this reason a range of modelling approaches has been introduced in the where one avoids resolving the physics of the bubbles and instead considers the large-scale cavities. One of the alternatives is to model the cavities in the form of a vapour fraction with both the liquid and vapour phases occupying the same physical space and being governed by the same set of equations.

Schnerr-Sauer cavitation model has been used here in order to account for the pressure-induced phase change of liquid into vapour and *vice versa* (Sauer & Schnerr 2001). This is done based on solving the transport equation for a volume fraction, α , with an additional source term introduced on the right-hand side to account for the evaporation and condensation:

$$\frac{\partial \alpha}{\partial t} + \nabla \cdot (\alpha \mathbf{U}) = -\frac{\dot{m}}{\rho}. \quad (1)$$

In Equation (1) \dot{m} denotes the rate of change of mass of the liquid-vapour mixture, ρ is the density of the mixture and \mathbf{U} is the fluid velocity. The presence of the additional source term also modifies the continuity equation which now becomes

$$\nabla \cdot \bar{\mathbf{U}} = \left(\frac{1}{\rho_v} - \frac{1}{\rho_l} \right) \dot{m}, \quad (2)$$

where subscripts v and l refer to vapour and liquid phases, respectively. One may also define the density and viscosity of the liquid-vapour mixture as

$$\begin{aligned} \rho &= \alpha \rho_v + (1 - \alpha) \rho_l, \\ \mu &= \alpha \mu_v + (1 - \alpha) \mu_l, \end{aligned} \quad (3)$$

respectively.

In order to close the system of equations, an expression for the rate of mass transfer between the liquid and the

vapour has to be introduced. In the approach proposed by Sauer and Schnerr this is done by considering the equation of motion of a single bubble of radius R and rearranging it to the following form:

$$\dot{m} = \frac{\rho_l \rho_v}{\rho} (1 - \alpha) \frac{3}{R} \sqrt{\frac{2}{3} \frac{(p - p_v)}{\rho_l}}. \quad (4)$$

2.2 Large Eddy Simulation

In the discussed hydrofoil study Large Eddy Simulation (LES) was used in order to model the fluid flow. This approach is based on resolving the most prominent turbulent structures and modelling the remainder of the turbulent kinetic energy spectrum. This is achieved by filtering the momentum equation yielding

$$\frac{\partial \bar{\mathbf{U}}}{\partial t} + \nabla \cdot (\bar{\mathbf{U}} \otimes \bar{\mathbf{U}}) = -\frac{1}{\rho} \nabla \bar{p} + \nu \nabla^2 \bar{\mathbf{U}} - \nabla \cdot \boldsymbol{\tau}, \quad (5)$$

where the overbar notation denotes the filtering operation, p is the fluid pressure, and ν is the kinematic viscosity. Similarly, the continuity equation becomes

$$\nabla \cdot \bar{\mathbf{U}} = 0. \quad (6)$$

The non-linear subgrid stress tensor, $\boldsymbol{\tau}$, used to describe the effect of the filtered eddies on the flow in Equation (6), may be expressed as

$$\boldsymbol{\tau} = \bar{\mathbf{U}} \otimes \bar{\mathbf{U}} - \bar{\mathbf{U}} \otimes \bar{\mathbf{U}}. \quad (7)$$

In order to model this quantity one may consider the Boussinesq hypothesis, whereby the stress tensor is assumed proportional to the fluid strain-rate and an assumed subgrid viscosity, ν_{SGS} , yielding

$$\boldsymbol{\tau} - \frac{1}{3} \boldsymbol{\tau} \cdot \mathbf{I} = 2\nu_{SGS} \mathbf{S}. \quad (8)$$

In the above \mathbf{I} is the identity matrix, and the strain rate may be computed as

$$\mathbf{S} = \frac{1}{2} (\nabla \bar{\mathbf{U}} + \nabla \bar{\mathbf{U}}^T). \quad (9)$$

An expression provided by the Smagorinsky model assumes the subgrid scale viscosity to be dependent on a constant coefficient, C_S , and the filter width, Δ , dictated by the mesh density. These yield and expression:

$$\nu_{SGS} = (C_S \bar{\Delta})^2 |\mathbf{S}|. \quad (10)$$

2.2 Ffowcs Williams-Hawkings Acoustic Analogy

Ffowcs-Williams Hawkings (FWH) acoustic analogy uses the extended Lighthills equation to predict noise originating from the presence of a turbulent flow (Ffowcs Williams & Hawkings 1969). Based on rearranging the mass and momentum conservation equations of the fluids the acoustic analogy introduces a solution to the inhomogeneous wave equation of the form

$$p'(\mathbf{x}, t) = p'_T(\mathbf{x}, t) + p'_L(\mathbf{x}, t) + p'_Q(\mathbf{x}, t), \quad (11)$$

where \mathbf{x} and t are the receiver position and time, respectively, p' is the acoustic pressure disturbance, and subscripts T, L and Q refer to the thickness (monopole), loading (dipole) and quadrupole (non-linear) contributions (Lyrintzis 2002) (Ianniello et al. 2012). Each of the terms on the right-hand-side of Equation (11) is computed by evaluating a surface integral of quantities

dependent on the state of the flow. Note that when a porous formulation is used, as is the case in the presented work, the non-linear term for sources located within the control surface are accounted for via the thickness and loading contributions. This also implies that for such a formulation the monopole and dipole contributions lose their physical meaning (Ianniello et al. 2012).

FWH analogy makes use of two intermediate variables, U_i and L_i . For incompressible flow one may, by definition, neglect the density disturbance. Moreover, when the control surface is stationary the expressions for the acoustic variables may be simplified even further, yielding

$$\begin{aligned} U_i &= u_i, \\ L_i &= (p - p_0)\hat{n}_i + \rho_0 u_i(u_i \cdot \hat{n}_i). \end{aligned} \quad (12)$$

In Equations (12) u_i is the fluid velocity at a point, \hat{n} is a unit vector normal to the control surface, p is the local fluid pressure, p_0 is the reference pressure level, and ρ_0 is the reference fluid density.

For a low Mach number, as is typically the case for a marine propeller blade, the FWH Formulation 2 thickness and loading terms may be computed for a control surface S as

$$4\pi p'_T(\mathbf{x}, t) = \int_S \left[\frac{\rho_0 \dot{U}_n}{r} \right]_\tau dS \quad (13)$$

and

$$4\pi p'_L(\mathbf{x}, t) = \frac{1}{c_0} \int_S \left[\frac{\dot{L}_r}{r} \right]_\tau dS + \int_S \left[\frac{L_r}{r^2} \right]_\tau dS. \quad (14)$$

Here c_0 denotes the speed of sound in the medium, r is the radiation direction, dot defines a source time derivative, and subscripts r and n refer to the dot product of the quantity in question with a unit vector in either radiation or normal directions, respectively.

In order to account for the fact that the sound contribution of an infinitesimal control surface element will take a finite amount of time to travel between the source and the receiver all of the quantities in Equations (13) and (14) must be evaluated at an appropriate emission time, τ , given by

$$t = \tau + \frac{\mathbf{x} - \mathbf{y}}{c_0}, \quad (15)$$

where \mathbf{y} is the location of the source (integration surface element). In the current implementation of the FWH, developed for the purpose of the discussed project, the control surface is defined by a set cell faces. This provides less control over the density and shape of the control surface than if the flow field was interpolated onto an independent discrete surface. On the other hand, the used approach introduces no additional errors and avoids local pressure and velocity perturbations from being lost.

3 POTSDAM PROPELLER TEST CASE

3.1 Simulation Setup

The discussed controllable pitch propeller has parameters as described in Table 1. The presented work focuses on replicating the conditions from the experimental test case 2.3.1, where cavitation measurements were made for the propeller at the advance coefficient of 1.019, rps-based cavitation number of 2.024 and operating at 24.987 revolutions per second.

The propeller and shaft were treated as no-slip walls with wall-functions applied, velocity inlet and pressure outlet boundary conditions were used to impose the axial flow, with the outer extends of the domain assumed to be slip walls. To match the experimental conditions the water and vapour were taken to have densities of 997.44 and 0.023 kg m⁻³, respectively, and kinematic viscosities of 9.337·10⁻⁷ and 4.273·10⁻⁶ kg m⁻², respectively. The saturation pressure was taken to be 2818 Pa.

Table 1 Parameters of the Potsdam Propeller.

Radius [m]	0.125	Eff. Area ratio	0.779
P/D	1.567	c at 70% R [mm]	106.35
No. blades	5	m at 70% R [mm]	3.09

Unstructured hexahedral mesh was created using the OpenFOAM snappyHexMesh utility and consisted of 8.8 million cells. Additional refinement was applied around the propeller tips and roots in order to refine the relevant geometry details. Care was taken to ensure that the y^+ falls within the logarithmic boundary layer region in order for the wall function models to be valid. A cylindrical domain was considered as it was deemed that modelling the cavitation tunnel walls as present in the experiment would be too expensive computationally. In order to account for the rotation of the propeller a sliding mesh interface was used. An overview of the mesh and domain arrangement is presented in Figure 1.

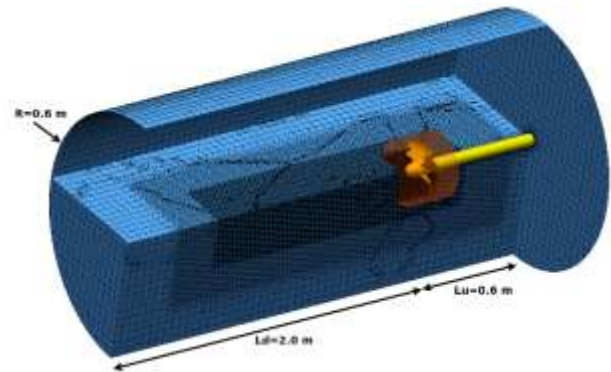


Figure 1 Overview of the domain setup for the PPTC simulation (rotating zone highlighted in orange).

First order time discretisation was used, with the convection term of the RANS equation being resolved using first-second order scheme. First order schemes were used to model the turbulent quantities and van Leer scheme with interface compression was applied to the volume fraction field.

3.2 Results and Discussion

One of the primary considerations for this part of the study was analyzing how well the selected cavitation model predicts the extents of cavitation for a marine propeller operating close to its maximum efficiency point. As shown in Figure 2, a relatively good agreement may be observed between the predicted and measured location of the cavitation regions. One of the immediately apparent drawbacks, however, is the lack of the tip vortex extending downstream of the propeller. This is caused by lack of appropriate refinement of the mesh away from the propeller blade and by the fact that RANS methods in general tend to introduce too much dissipation and thus cause the vortices to disappear much sooner than they would in reality.

Despite the mesh being relatively coarse an accurate prediction of the thrust coefficient was achieved in non-cavitating conditions, yielding 0.3740 against the experimental value of 0.3870, i.e. 3.36% relative error. This indicates that the presented method is well suited to provide information useful throughout the propeller design cycle. Unfortunately, unsteady RANS has been recognized as not being able to predict the unsteady behaviour of the cavities particularly well (Bensow, & Liefvendahl 2008) (Lidtke et al. 2014), nor is it capable of resolving the tip vortex regions accurately. Both of these phenomena may be expected to play a significant role in the noise generation mechanisms of a marine propeller (Salvatore 2009). It is therefore desirable to use Large Eddy Simulation, or similar high-fidelity turbulence modelling techniques, for the purpose of noise prediction.

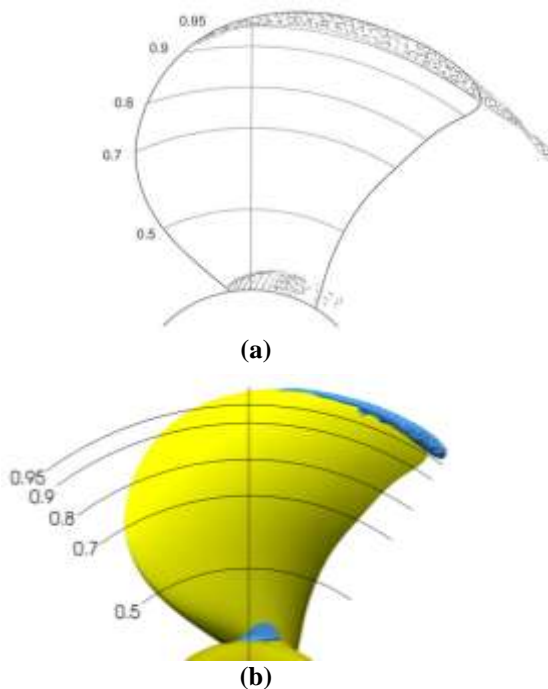


Figure 2 Comparison of the experimental (a) and computed (b) cavitation extents (experimental data from Abdel-Maksoud (2011)). The predicted interface was assumed at volume fraction value of 0.95.

4 NACA 0009 CAVITATION NOISE MODELLING

4.1 Case Setup

Numerical simulations aimed at providing initial noise estimates of a cavitating hydrofoil have been focused on a wing with a NACA 0009 section profile. This was done in order to replicate the conditions used for the Delft Twist 11 foil first presented by Foeth et al. (2006). In said study a wing with a span-wise angle of attack variation symmetric about the mid-span was considered. Here, however, the geometry has been simplified to a fixed span-wise pitch distribution in order to allow a more in-depth study of the sheet cavity behaviour without the added complexity dictated by the complex three-dimensional flow features reported in the original experiments.

The foil with chord of 0.15m, angle of attack of 9° and span of 0.05m was placed in the centre of a domain which was to resemble the working section of the cavitation tunnel used by Foeth et al. The domain was chosen to extend 2.5 chord lengths upstream, 4.5c downstream, and was 2.5c wide. The densities of both fluids were taken to be 998 kg m^{-3} and 0.023 kg m^{-3} for water and vapour, respectively, and their corresponding kinematic viscosities were assumed to be $10^{-6} \text{ kg m}^{-2}$ and $4.273 \cdot 10^{-6} \text{ kg m}^{-2}$. The mean nucleation radius was assumed to be 50 m with the corresponding distribution of 10^8 m^{-3} . Finally, the saturated vapour pressure of the mixture was taken to be 2970 Pa. Speed of sound in water was assumed to be 1500 m s^{-1} .

The control surface used to perform the integration of Equations (14) and (15) has been constructed by expanding the wing section offsets by 0.065m. This distance was chosen so as to avoid any cavities impinging directly onto the surface. Similarly, the downstream extent of the integration surface was chosen to be 0.182m downstream of the trailing edge. The exact placement of the control surface with respect to the wing is depicted in Figure 3.

The inlet was prescribed a fixed velocity of 6.97 m s^{-1} and the simulation was carried out at the cavitation number of 1.07 which was achieved by using a fixed value of pressure at the outlet of 29 kPa (Foeth et al. 2006). Top and bottom of the numerical cavitation tunnel were treated as slip walls and cyclic boundary condition was prescribed to the span-wise boundaries. Convective outlet velocity condition was used in order to limit the amount of reflections being propagated into the domain for the LES simulations. The wing was treated as a no-slip surface and wall functions were used in order to limit the cell count required in the boundary layer region, following the approach outlined by Lu et al. (2010). In order to promote convergence from the early stages of the simulations the runs were initialized from a steady-state, non-cavitating flow solution.

Temporal discretisation has been achieved by the use of a second-order implicit scheme which implied the maximum Courant number limit of 0.5 needed to

maintain stability for LES simulations. The volume fraction was discretised using the van Leer scheme with interface compression and a hybrid convection scheme was adopted in which upwinding is applied when required to maintain stability (Lloyd 2013).

The domain was spatially discretised using a 480x284x40 grid with 5.4 million elements, most of which were concentrated in and near the boundary layer of the foil and between the wing and the FWH integration surface. Special care was taken to ensure that the cavities present would not experience rapid changes in mesh density as they are formed, shed and convected downstream of the foil. Similarly, it was ensured that any flow disturbance moving towards the FWH control surface would not be affected by dissipation errors associated with large changes in mesh topology. The mesh was created using a set of in-house Python libraries combined with the OpenFOAM blockMesh utility. The first wall-normal cell height was ensured to fall within $y^+ < 30$, and, to achieve appropriate span- and chord-wise resolution of the flow, the mesh was designed to be characterised by $x^+ < 200$ and $z^+ < 350$. The grid had been subject to a convergence study whereby the relative change in the predicted steady-state, non-cavitating force coefficients was investigated and found to be less than 2% when compared to a mesh with 9.0 million cells.

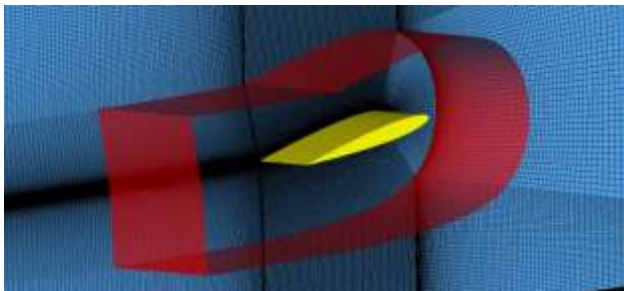


Figure 3 Mesh structure close to the wing (yellow) and the placement of the FWH integration surface (red).

4.2 Results and Discussion

Several receivers were placed around the airfoil in order to record the predicted noise pressure levels. These were located approximately 50 m from the foil and their detailed locations are described in Table 2.

Table 2 Receiver locations

Receiver	x [m]	y [m]	z [m]
0	-c/2	50	s/2
1	0	50	s/2
2	c/2	50	s/2
3	50	0	s/2
4	0	-50	s/2

In order to allow correlation between the recorded noise levels and the predicted flow features the total volume of the cavity was also recorded, together with its extents.

By comparing the chosen parts of the cavity volume and predicted sound pressure levels, Figures 4 and 5, respectively, one may immediately notice that no immediate correlation may be discerned. However, a more in depth analysis of the flow reveals that a new

cavity sheet starts to form before a shed cloud becomes disintegrated, as shown in Figure 6. This implies that the maximum volume of the cavity is reached while a cloud is still present in the vicinity of the foil. It thus becomes apparent that, unless the total cavity volume may be broken down into the contribution of the sheet and the clouds, no reliable conclusions may be drawn by comparing the presented data.

It should be mentioned that when compared to a non-cavitating simulation, conducted at cavitation number of 5.0, the presented noise levels are nearly 20 dB re 20 μ Pa higher. This allows one to deduce that it is the cavitation behaviour and, in particular, that of the cavity sheet that contributes significantly to the noise signature of the presented case. Analysis of the sound pressure levels shown in Figure 5 reveals that there is no significant difference between the sound experienced by receivers spaced radially around the foil. One may thus argue that the noise predicted in this case is of monopole nature, which is expected for a cavity sheet-dominated noise spectrum (Seol et al. 2005).

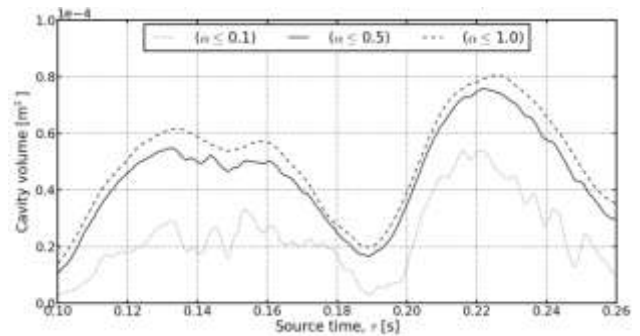


Figure 4 Selected part of the total cavity volume time trace for different volume fraction (α) thresholds.

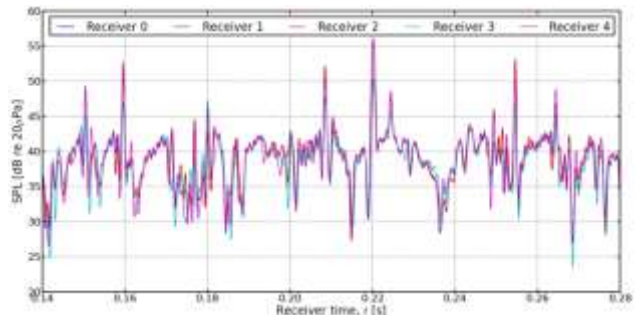


Figure 5 Recorded sound pressure levels for 5 receivers placed in a circumferential manner around the airfoil.

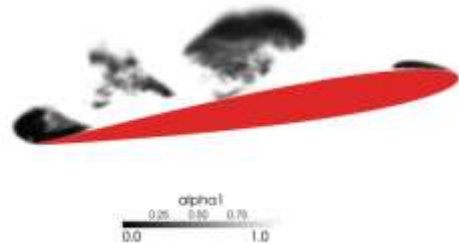


Figure 6 Snapshot of the flow showing formation of a new cavity sheet and the presence of a shed cloud (volume fraction, $\alpha < 1$) downstream of the leading edge.

One may also identify clear peaks in the sound pressure levels in Figure 5. When compared to the state of the flow

at the corresponding emission times, shifted by $\delta t = R_{rec}/c_0 = 0.033$ s into the past, these allow several interesting observations to be made. For the peak at $t = 0.16$ s a large cloud may be seen to shear off from the downstream edge of the cavity sheet, as shown in Figure 7 (a) and (b). As this takes place the cavity interfaces impact upon each other and generate a localised region of high pressure. As already stated, the presented approach utilises the incompressible flow assumption and, as such, is not well suited to capture this type of flow features but still their impact on the computed sound pressure level may be clearly seen.

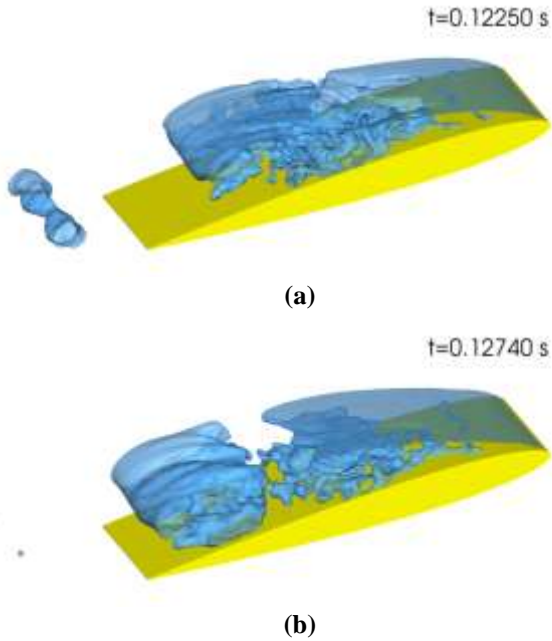


Figure 7 Shedding of a cavity cloud from the downstream end of the sheet responsible for one of the peaks in the noise signal (receiver time $t = 0.16$ s).

Next, for receiver time $t = 0.207$ s a re-entrant jet may be seen to impact upon the upstream end of the cavity and cause a cloud to be shed, as depicted in Figure 8 (a) and (b). This is a typical mechanism by which sheet cavitation experiences instability and transient behaviour (Lu et al. 2010). One may also see a secondary peak in the noise level just after the primary event, likely associated with the interaction of the turbulence and the shed clouds, causing further interface-interface contact.

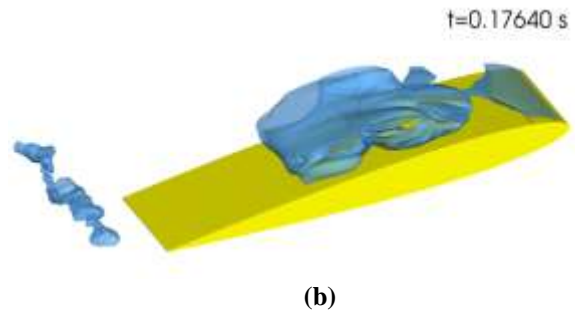
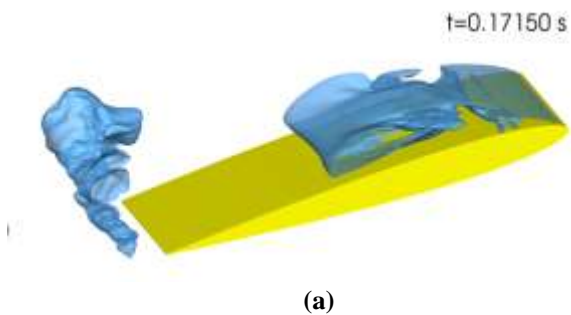


Figure 8 Necking of the cavity sheet close to the leading edge leading to the shedding of a cloud and the generation of a significant noise peak (receiver time $t = 0.207$ s).

Finally, for the listener time of $t = 0.22$ s one may observe the collapse of a shed cloud following the formation of a re-entrant jet; shown in Figure 9 (a) and (b). While similar to the already discussed behaviour this event shows a significant amount of three-dimensional nature. It is also interesting to note the visible wake of the jet around the mid-span of the wing and how it causes the cavity to fold over the foil from the sides. The later of the associated snapshots also reveals a complicated cavity structure that this event gives rise to.

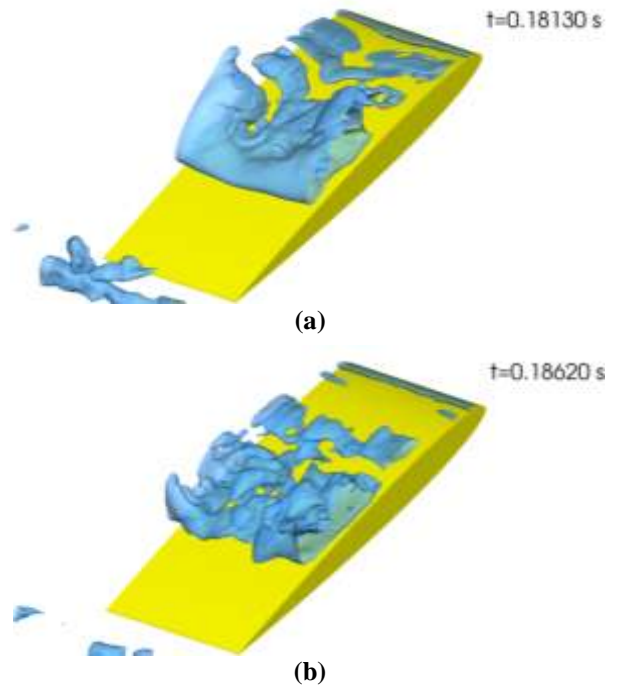


Figure 9 Complex three-dimensional cavity cloud collapse event following the passing of the re-entrant jet and creating a noticeable noise peak (receiver time $t = 0.22$ s).

Results presented in Figure 5 also indicate that there is a significant amount of noise present around the foil whose source may not immediately be correlated with particularly obvious significant flow events. One may speculate that this originates from the small-scale oscillations of the cavity interface which induce a local disturbance to the flow. Note should also be taken of the fact that the presence of a cavity sheet effectively modifies the shape of the hydrofoil, leading to highly

turbulent wake, as shown in Figure 10. This is also likely to affect the noise signature.

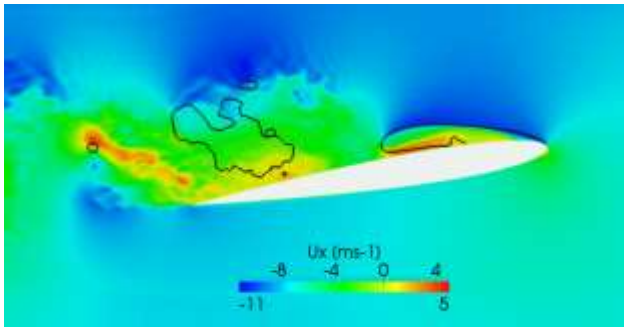


Figure 10 Span-normal cut showing instantaneous axial velocity and volume fraction field iso-contour, $\alpha = 0.9$ (black), at $z/s = 0.5$ and simulation time $t = 0.16s$.

5 CONCLUSIONS

It has been shown that appreciably accurate prediction of the cavitation extents may be made for a propeller at a typical loading condition using unsteady RANS combined with a mass transfer cavitation model. This is of particular importance to the designers, who may utilise such cost-effective computational methods in order to support their decision making process. Drawbacks of this method are, however, the inability to resolve the vortical and other turbulent structures accurately. Thus, while it may still be possible to gain substantial insight into the nature of the noise generation mechanisms with said approach, one may be tempted to suffer the increase in computational costs associated with methods such as LES. These offer the potential benefit of substantially increasing the accuracy of the unsteady flow predictions.

The second of the presented studies, focused on the noise analysis of a hydrofoil, has indicated the vast amount of insight that may be gained into the nature of the noise generation mechanisms when high-fidelity turbulence modelling is employed. In particular, the analysis of the presented data has showed that, despite the incompressible treatment of the flow, the noise signature of events such as cloud shedding and re-entrant jet formation may be captured. These have been shown to be the primary noise sources, followed by the noise due to small-scale oscillations of the cavity interface and the noise due to turbulence.

It may thus be concluded that the proposed numerical approach based on a mass transfer cavitation model and acoustic analogy is capable of predicting the low frequency components of the cavitation noise. It suffers, however, from not being able to predict the effect of small bubbles, either shed from the larger cavities or created in the process of bubble cavitation. Moreover, because the fluid is considered to be incompressible, some noise components are expected to be lost from the analysis. In particular, this may be the case for noise associated with formation of shockwaves due to impact of the cavity interfaces against other surfaces.

The above indicate that the discussed method provides a useful tool allowing greater insight into the nature of cavitation noise but requires further refinement in order to be more reliable.

ACKNOWLEDGMENTS

The authors would like to acknowledge the use of OpenFOAM® libraries and the Iridis 4 supercomputer of the University of Southampton for all of the presented simulations.

REFERENCES

- Abdel-Maksoud, M. (ed) (2011), 'Proceedings of the Workshop on Cavitation and Propeller Performance', Second International Symposium on Marine Propulsors - SMP'11, 17 – 18 June, Hamburg, Germany
- Bensow, R., & Liefvendahl, M. (2008), 'Implicit and explicit subgrid modeling in les applied to a marine propeller', 38th Fluid Dynamics Conference and Exhibit, pp. 1–12
- Bensow, R. E., & Bark, G. (2010). 'Simulating cavitating flows with LES in OpenFOAM', European Conference on Computational Fluid Dynamics, pp. 14–17, Lisbon, Portugal.
- Ffowes Williams, J. & Hawkings, D. L. (1969), 'Sound generation by turbulence and surfaces in arbitrary Motion', Philosophical Transactions of the Royal Society of London Series A, Mathematical and Physical Sciences, vol. 264, no. 1151, pp. 321–342
- Foeth, E. J., Doorne, C. W. H., van Terwisga, T., Wieneke, B. (2006), 'Time resolved PIV and flow visualization of 3D sheet cavitation', Experiments in Fluids, vol. 40, pp. 503–513
- Hildebrand, J. (2009), 'Anthropogenic and natural sources of ambient noise in the ocean', Marine Ecology Progress Series, vol. 395, pp. 5–20
- Hsiao, C.-T., & Chahine, G. (2004), 'Prediction of tip vortex cavitation inception using coupled spherical and nonspherical bubble models and Navier-Stokes computations', Journal of Marine Science and Technology, vol. 8(3), pp. 99–108
- Ianniello, S., Muscari, R., and Mascio, A. D. (2012), 'Hydroacoustic characterization of a marine propeller through the acoustic analogy', Sustainable Maritime Transportation and Exploitation of Sea Resources, pp. 991–1000
- Jamaluddin, A. R., Ball, G. J., Turangan, C. K., Leighton, T. G. (2011), 'The collapse of single bubbles and approximation of the far-field acoustic emissions for cavitation induced by shock wave lithotripsy', Journal of Fluid Mechanics, vol. 677, pp. 305–341
- Kirsteins, I., Clark, P., Atlas, L. (2011), 'Maximum-likelihood estimation of propeller noise modulation

- characteristics', Underwater Acoustic Measurements: Technologies and Results
- Lidtke, A. K., Turnock, S. R., & Humphrey, V. F. (2014), 'The influence of turbulence modelling techniques on the predicted cavitation behaviour on a NACA0009 foil', Numerical Towing Tank Symposium (NuTTS), Marstrand, Sweden.
- Lloyd, T. P. (2013), 'Large eddy simulations of inflow turbulence noise: application to tidal turbines', PhD Thesis, University of Southampton
- Lu, N., Bensow, R. E., Bark, G. (2010), 'LES of unsteady cavitation on the delft twisted foil', Journal of Hydrodynamics, Ser. B, vo. 22(5), pp. 784–791
- Lyrantzis, A. S. (2002), 'Surface Integral Methods in Computational Aeroacoustics - From the CFD Near-Field to the Acoustic Far-Field', CEAS Workshop "From CFD to CAA", (Athens, Greece), pp. 1–53
- Park, C., Seol, H., Kim, K., Seong, W. (2009), 'A study on propeller noise source localization in a cavitation tunnel', Ocean Engineering, vol. 36, pp. 754–762
- Plesset, M. S. & Prosperetti, A. (1977), 'Bubble dynamics and cavitation', Annual Review of Fluid Mechanics
- Salvatore, F. & Ianniello, S. (2002), 'Preliminary results on acoustic modelling of cavitating propellers', IABEM 2002, International Association for Boundary Element Methods, UT Austin, TX, USA
- Salvatore, F. (2009), 'Propeller cavitation modelling by CFD-Results from the VIRTUE 2008 Rome workshop', Proc. Of 1st international Symposium on Marine Propulsors, (Trondheim, Norway)
- Sauer, J. & Schnerr, G. H. (2001), 'Development of a new cavitation model based on bubble dynamics', Zeitschrift für Angewandte Mathematik und Mechanik, vol. 81, pp. 561–562
- Seol, H., Suh, J.-C., Lee, S. (2005), 'Development of hybrid method for the prediction of underwater propeller noise', Journal of Sound and Vibration, vol. 288, pp. 345–360
- Tasker, M. L., Amundin, M. et al. (2010), 'Marine Strategy Framework, Task Group 11 Report: Underwater noise and other forms of energy', European Commission Joint Research Centre, Institute for Environment and Sustainability
- Urick, R. J. (1984), 'Ambient Noise in the Sea', Undersea Warfare Technology Office, Naval Sea Systems Command, Dept. of the Navy, Washington D.C.
- Vallier, A. (2013), 'Simulations of cavitation-from the large vapour structures to the small bubble dynamics', PhD thesis, Lund University
- Van der Graaf, A., Ainslie, M. et al. (2012), 'European Marine Strategy Framework Directive: Good Environmental Status (MSFD-GES)', Tech. Rep.
- Woo Shin, K. (2010), 'Cavitation simulation on marine propellers', PhD thesis, Technical University of Denmark

The Usage of Propeller Tunnels for Higher Efficiency and Lower Vibration

M. Burak Şamşul^{1*}, Naz Görener¹

¹Milper Pervane Teknolojileri A.Ş., Teknopark İstanbul – Sanayi Mahallesi Teknopark Bulvarı –
1/2A Z08 34906 Pendik – İstanbul, Turkey

Abstract: Most of the vessels have their propellers and shaft equipment below the keel. Propellers in tunnel are an alternative to conventional systems; hereby reducing the draft of the craft is the main objective of the tunnels. Moreover designers forced to use small diameter propellers in order to reduce vessel draft but these solutions bring other inefficiencies such as cavitation and poor propulsive efficiency. Tunnel design provides reducing in shaft angle and decreasing in draft, at the same time propellers which have large diameters become available by using propeller tunnels. In order to get advantages of the propeller tunnels, propeller and tunnel geometry must be designed together. According to the experimental results, propeller tunnels does not bring a negative effect on propeller efficiency. Moreover, an optimum tunnel-propeller design may increase efficiency. Small tip clearance, for an optimum tunnel-propeller design, generates higher efficiency than open-water. Reduced clearance provides the propeller to operate with increased efficiency by the help of reduced tip losses. But higher efficiency and lower draft are not the only advantages of the propeller tunnels. By the usage of the propeller pockets which are shallow tunnels, propeller induced vibrations become lower. On conventional installations without tunnels, minimum clearance should be minimum 15 percent of the propeller diameter between the propeller tip and the hull; otherwise excessive vibration will occur. But tunnel usage gives flexibility to reduce the clearance to 5 percent and with an optimum design nearly zero clearance is possible without vibration. This allows a larger propeller diameter, higher efficiency, lower cavitation without vibration. In this study; a specified motor yacht hull and a propeller is analyzed without tunnel and with tunnel geometry by using CFD solver. Propeller induced vibrations and efficiencies are compared for each conditions in order to determine the advantages of the propeller tunnels.

Keywords: Propeller tunnels, Computational Fluid Dynamics, motor yacht, vibration.

1 INTRODUCTION

Most of the vessels have appendages below the hull as propeller, shaft, and brackets. These appendages increases the total draft of the vessel so increased draft creates operational disadvantages for the vessel. In some cases propeller diameter reduction is a solution in order to reduce total draft of the boat. But this method leads to lower propulsive efficiency and limitations cause non optimum conditions.

Propeller tunnel usage causes buoyancy loss for the hull therefore total draft increases. On the other hand, propeller tunnel brings flexibility to reduce the shaft angle. In short, shallow draft may be provided even though hull draft increases.

Propeller tunnel usage provides efficiency increase for most of the cases due to the shrouding effect of the propeller tunnels. Especially shallow partial tunnels lead to reduction in propeller induced vibrations. In order to reduce propeller induced vibrations for conventional propeller installations, propeller tip – hull clearance should be increased; however increased clearance brings increment in total draft.

2 TUNNEL GEOMETRY

In conventional layout, hull form directly effects the nominal wake coming through the propeller zone. But boats which have propeller tunnels, nominal wake is mostly specified by the tunnel geometry. Propeller tunnel geometry has significant influence not only on suction side of the propeller. Tunnel length at the aft side of the propeller affects the wake of the vessel.

According to the experiments and researches, there are some limits for the tunnel entrance zone angles, exit region characteristics, location of the propeller.

Tunnel entrance region should not be longer than required dimensions. This condition causes loss in buoyancy and also increase in draft. Most critical condition is the angle of the entrance zone. Angle between the tunnel entrance the hull buttock at that section should not be more than 15 degrees. Also, diameter of the entrance zone should not have larger diameter than the propeller zone.

Tunnel center and propeller center must be concentric in order to provide a constant clearance between hull and propeller blade tips. Also tunnel longitudinal axis should be parallel to the waterline.

For higher propulsion efficiency, one of the main point is tunnel geometry around propeller zone. Location of the propeller and entrance of the tunnel become critical for hydrodynamic characteristics. Tunnel geometry accelerates the flow and lowers the pressure. Therefore tunnel entrance zone should be close to the propeller zone.

Tunnel hull forms which have a very low propeller – hull clearance may have higher propulsive efficiency than open water efficiency. Because this configuration reduces the propeller tip losses and provides a proper wake.

For the vessels which have propeller tunnels, propeller rate pressures have more uniform distribution.

It is possible to make an arrangement that propeller tip and hull clearance have a dimension close to zero. Avoiding mechanical interaction, propellers which have 5% d/D clearance provides higher efficiency.

Tunnel exit zone mostly affects the hydrodynamic characteristics of the vessel. Especially at semi planning and planning speeds, tunnel exit geometry and lost volume affects the planning angle at that speeds. For $F_{nv} > 2.8$, shorter tunnels bring significant increases in propulsive efficiency.

3 PROPELLER FACTORS

Propeller tunnels lead to reduction in shaft angle and total draft. Tunnel geometry and propeller location in the tunnel depend on the design and there are important points such as inflow velocity, pressure and angle.

Propeller blade tip – hull clearance brings both hydrostatic and hydrodynamic advantages. Lower clearance brings possibility to reduce the tunnel diameter and increases propulsive efficiency. Smaller tunnel diameter increases the shrouding effect and leads to top speed increment.

4 DYNAMIC FACTORS

Number of propeller blades also an important selection for the vessels that have propeller tunnels. In order to minimize the torsional resonance, determining the number of blades of the propeller regarding the engine RPM range is one of the main points of this selection. For reducing the vertical blade rate forces, if one blade enter the tunnel than another blade should not leave the tunnel at the same time.

5 CFD BACKGROUND

In many areas computational fluid dynamics is a very important and useful method to solve complex problems as well as marine applications. It is mostly used for determining hull resistance, propeller performance, pressure and velocity distribution of flow around hull. By using this tool, it is possible to find out effects of any appendage on hull or any change on hull form. Moreover all of these calculations can be solved for steady or

transient conditions. It is possible to make different assumptions or simplifications for various conditions.

According to the problem characteristics, different turbulence models can be useful in order to reach the minimum error margin.

In short, computational fluid dynamics equations satisfy:

- Conservation of fluid mass
- Rate of change in momentum of the fluid particles are equal to the sum of the forces acting on
- The change in energy input to the particles is equal to the heat or work.

6 GEOMETRY INFORMATIONS

Fluid analysis is carried out for hull and propeller geometry together. Design parameters of hull and propeller geometries are shown in Table 1.

In this study, two different hull geometries are analyzed and influence of hull shape on propeller efficiency are evaluated. One of the hull geometry includes shaft, propeller and P bracket, second hull configuration involved a tunnel inside hull geometry, shaft and propeller without P bracket. Thus effect of tunnel geometry is examined.

Table 1 Propeller and hull design parameters

Propeller		Hull	
Blade Number (Z)	4	L _{OA}	24 m
Propeller Diameter (D)	720 mm	L _{WL}	19 m
EAR	0.85	B	5.16 m
Average Pitch Ratio (P/D)	1.05	T	1.05 m
Revolution (n)	900 RPM	D	3.65 m
Rake	0	Design Speed (V _s)	22 Knots
Skewness	0	Displacement	45000 kgs

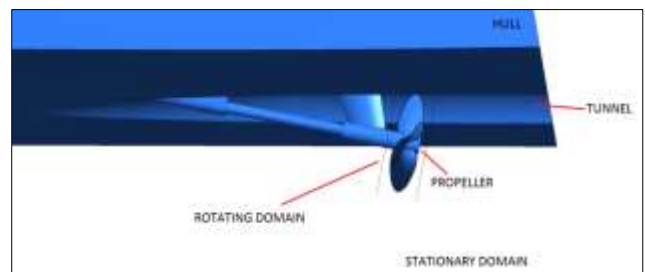


Figure 1 Geometries and domains

7 MESH GENERATION

Unstructured mesh (tetra mesh) is preferred as a grid generation for this study and mesh quality criteria values are provided. Skewness, aspect ratio and orthogonal

quality are examined and these values are shown in Table 2.

Skewness is one of the most important quality measures. It determines how close to ideal a face or cell is. There are two methods for measuring skewness:

- Based on the equilateral volume (applies only to tetrahedral cells).
- Based on the deviation from a normalized equilateral angle. This method applies to all cell and face shapes, e.g., pyramids and prisms.

ANSYS scaled this property to an interval between 0 and 1. In this scale 0 refers to the best possible value. However it is hard to make skewness lower than 0.9 for complex geometries such as propellers. According to our experiences 0.95 is a suitable value to make the simulations run properly.

Orthogonality has an influence on numerical errors, convergence rate and stability. This is also in the range 0 to 1 and higher values correspond to better orthogonal quality.

Table 2 Mesh quality values

	With Tunnel	Without Tunnel
Number of Elements	7523045	7612893
Number of Nodes	2697003	2585022
Skewness	0.90	0.93
Orthogonal Quality	0.10	0.11
Aspect Ratio	149.7	66.291

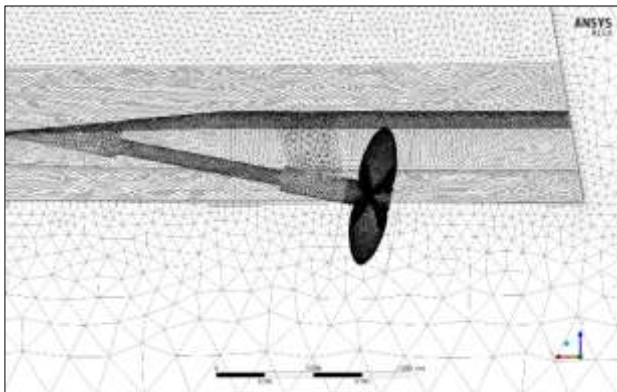


Figure 2 Grid generation (without tunnel)

8 SOLVER SETUP

After mesh generation, setup and boundary conditions are defined in pre-processing. In this study, type of fluid is defined as water with 1025 [kg/m³] density value and turbulence model is selected as k- ω SST.

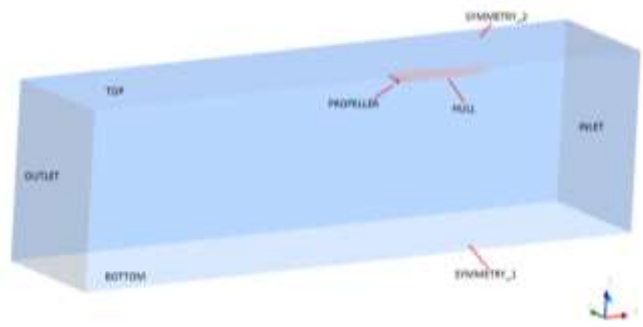


Figure 3 Boundary conditions

Table 3 CFD analysis setup & boundary conditions

Turbulence Model	K- ω , SST
Type of Fluid	Water, 1025 [kg/m ³]
Revolution	900 [rpm]
Inlet	22 [knot]
Outlet	Pressure value is 0 [Pa]
Blade (Wall)	Propeller blade is described no slip wall and rotating velocity is 0 [rpm]
Hull (Wall)	Hull is described no slip wall
Symmetry	Exterior surface of domain is described symmetry.

9 SOLUTION AND RESULTS

At the end of the analysis thrust and torque values of the propeller are evaluated and pressure distribution on blade and hull surface is examined. The pressure distribution on propeller and hull is evinced in Figure 4.

Table 4 Solution results

Propeller		Without Tunnel	With Tunnel
Diameter	[m]	0,72	0,72
Speed	[m/s]	11,300	11,300
Rotation	[rpm]	900	900
Rotation	[s ⁻¹]	15	15
J	[-]	1,046	1,046
Thrust	[N]	40700	50842
Torque	[Nm]	13612	15923
K _T	[-]	0.65731	0.81963
K _Q	[-]	0.30478	0.35652
10K _Q	[-]	3.048	3.565
Efficiency	[-]	36%	38%

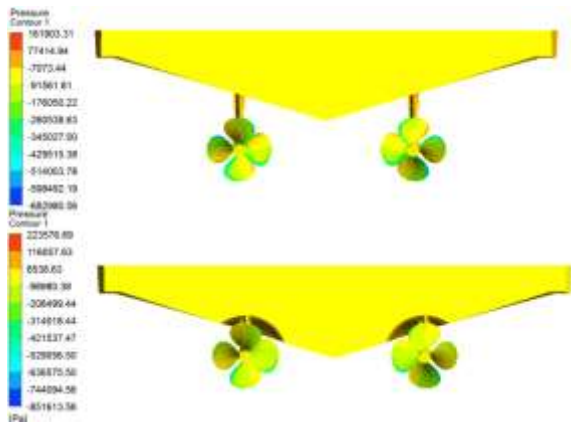


Figure 4 Pressure Plots

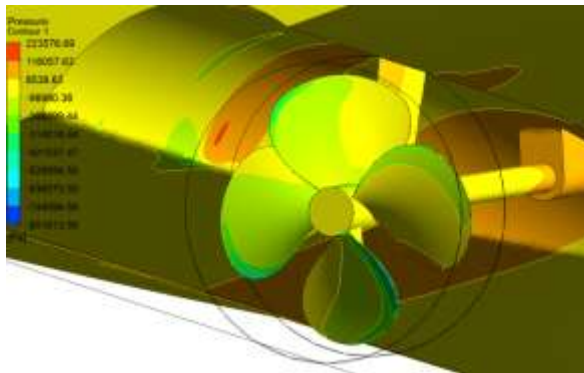


Figure 5 Tunnel Geometry Pressure Plot

10 CONCLUSION

Computational fluid dynamics solutions that examine propeller – hull interactions indicate that propeller induced pressure effects on hull have significant influence on vibration. If two calculations are compared, the differences in the propeller induced pressure distribution can be observed.

The uniform pressure distribution in the axis of the tunnel provides lower vibrational effects on the vessel (Figure 5). On the other hand, on the conventional hull form, every blade pass near the hull creates pressure drop. Every pressure drop effect increases vibrational effects on the non-tunnel hull geometries.

Advantages of the tunnel applications and decreased propeller – hull tip clearance are:

Reduced circumferential blade load vibration, reduced blade-rate hull pressures, increased propulsive efficiency and reduced shaft torsional loads, but on the other hand more critical relationship occurs between blade number and tunnel shape.

REFERENCES

Donald L. Blount (2004). ‘Design of Propeller Tunnels For High Speed Craft’. School of Marine Science and Technology, University of Newcastle, UK.

Sing Kwan Lee, Min Liao, and Suqiu Wang (2006). ‘Propeller Induced Hull Vibration’. Proceedings of the 2nd International Ship Noise and Vibration Conference, London, UK.

Sing Kwan Lee, Hamn Ching Chen (2005). ‘The Influence of Propeller/Hull Interaction on Propeller Induced Cavitating Pressure’. Presented at the ISOPE 2005 Conference, Held in Seoul, Korea.

Hamn Ching Chen, Sing Kwan Lee (2003). ‘Time-Domain Simulation of Propeller-Ship Interactions Under Turning Conditions’. 16th ASCE Engineering Mechanics Conference, University of Washington, Seattle.

Hamn Ching Chen, Sing Kwan Lee (2003). ‘Chimera RANS Simulation of Propeller-Ship Interactions Including Crash-Astern Conditions’. American Bureau of Shipping ABS Plaza, 16855 Northchase Drive Houston, USA.

Shin Hyung Rhee, Shitalkumar Joshi (2003). ‘CFD Validation For a Marine Propeller Using An Unstructured Mesh Based RANS Method’. 4th ASME JSME Joint Fluids Engineering Conference, Honolulu, Hawaii, USA.

John Carlton, *Marine Propellers and Propulsion* Second Edition (2007), Propeller Ship Interaction.

LI Da-Qing, ‘Validation of RANS Predictions of Open Water Performance of a Highly Skewed Propeller With Experiments’, Conference of Global Scholars on Hydrodynamics.

HydroComp Technical Report, Definition of Propeller Tunnels for PropExpert.

S. Brizzolara, D. Villa, S. Gaggero, A. (2008). ‘Systematic Comparison Between RANS And Panel Methods For Propeller Analysis’, University of Genova Department of Naval Architecture and Marine Engineering, Genova, Italy.

Underwater Radiated Noise Prediction for a Submarine Propeller in Different Flow Conditions

M. Cansın Özden^{1*}, Ahmet Y. Gürkan¹, Yasemin Arıkan Özden², Talat G. Canyurt¹, Emin Korkut¹

¹Istanbul Technical University, Faculty of Naval Architecture and Ocean Engineering, 34469 Maslak-Istanbul, Turkey

²Faculty of Naval Architecture and Maritime, Yıldız Technical University, 34349 Beşiktaş-Istanbul, Turkey

Abstract: International Maritime Organisation (IMO) and other bodies have been trying to set-up regulations to reduce/limit noise levels at sea which influence marine environment particularly marine mammals and fish varieties. Ships with low noise characteristics will be a must in the near future for almost all ship types, however for special ships, such as naval surface vessels, fisheries, submarines, etc. this has already been an issue for their missions. Propeller is one of the main sources of underwater noise generated by ships and it is important to predict and control the underwater noise characteristics of propellers. Within this respect, the main objective of this study is to calculate numerically the propeller radiated noise. Therefore, propeller noise is investigated numerically for the INSEAN E1619 submarine propeller in open water and behind a generic DARPA suboff submarine at non-cavitating conditions due to their deeply submerged operations. Flow around the propeller is solved with a commercial CFD software using Reynolds Averaged Navier-Stokes (URANS), while hydro-acoustic analysis is performed using a model based on Ffowcs Williams-Hawking equation. This paper reports on preliminary results of the study. The paper includes the details of the bodies and study, and discusses further improvement of the methodology.

Keywords: Propeller noise, RANS, non-cavitating, DARPA Suboff submarine, INSEAN E1619 submarine propeller, Ffowcs Williams-Hawkings (FWH) model.

1 INTRODUCTION

Ship underwater radiated noise has recently been concerned by international bodies, such as International Maritime Organisation (IMO), classification societies as well as by conservation groups and governmental departments due to negative effects of shipping on marine environment. Increasing shipping activities also increases ambient noise levels at seas around the world and this has a potential impact on marine wildlife, particularly on marine mammals and fish varieties.

Ships with low noise characteristics has always been an important issue for some ship types, naval vessels, fisheries, research vessels and also for submarines due to their missions and operations. Propeller is one of the most dominant sources of noise on ships. Propeller noise becomes the only traceable signal with sonars particularly for naval surface ships and submarines since all other sources can be eliminated by appropriate insulation methods. Nevertheless, it determines the detectability, operability and even survivability of the ship. Therefore, noise predictions for propellers in cavitating and non-cavitating states have become a momentous subject of naval architecture for a long time.

Empirical, semi-empirical methods and Bernoulli-based methods have been investigated by many researchers (Testa 200). However, generation of a method by aero-acousticians Ffowcs Williams-Hawkings (FWH) for calculation of noise of an arbitrary body moving in a fluid can be considered a mile stone in acoustic predictions (Ffowcs et. Al. 1969). With the development in

computing power and numerical practice, this method became available also for hydro-acoustic predictions. Seol et. al. (2002) investigated the non-cavitating propeller noise employing Boundary Element Methods (BEM) for the calculation of flow around propeller in time-domain and used FWH method to predict the far-field acoustics. Seol et. al. (2005) extended their work to cavitating noise stage. They predicted cavity extent by the sheet cavity volume model and used the sheet cavity volume data and time dependent pressure as the input for the FWH equation to predict far-field acoustics (Seol et. al. 2005).

Salvatore and Ianniello (2003) published the preliminary results for cavitating propeller noise predictions. A hydrodynamic model for transient sheet cavitation on propellers in non-uniform inviscid flow was coupled with a hydroacoustic model based on the Ffowcs Williams-Hawkings equation. They split the noise signature into thickness and loading term contributions. They demonstrated that noise predictions by the FWH equation were in satisfactorily agreement with those obtained by using the Bernoulli equation model (Salvatore and Ianniello 2003).

Barbarino and Casalino (2012) studied and validated noise predictions for a NACA-0012 airfoil. Then they applied the same method to compute the broadband noise spectrum of an aircraft. Gao et al. (2012) simulated numerically the unsteady viscous flow around AUV with propellers by using the Reynolds-averaged Navier-Stokes (RANS) equations, shear-stress transport (SST) $k-\omega$ model and pressure with splitting of operators (PISO)

* Corresponding author e-mail: ozden@itu.edu.tr

algorithm based on sliding mesh. The hydrodynamic parameters of AUV with propellers such as resistance, pressure and velocity reflected well the real ambient flow field of AUV with propellers. Then, the semi-implicit method for pressure-linked equations (SIMPLE) algorithm is used to compute the steady viscous flow field of AUV hull and propellers, respectively. The computational results agree well with the experimental data, which shows that the numerical method has good accuracy in the prediction of hydrodynamic performance (Gao et al. 2012). On the other hand, after the 22nd ITTC Workshop on Propeller RANS/Panel Methods, a number of studies have been published (ITTC 2008). In 2004, Kawamura et al. (2004) comparatively analysed different turbulence models for the prediction of open water performance for a conventional propeller. Later Li published his results of estimating open water characteristics of a highly skewed model propeller employing $k-\omega$ turbulence model and validation study with experimental data (Li 2006). The detailed literature review on the prediction of open water performance of propellers can be found in 26th ITTC (2011).

In the above context a study has been carried out to investigate the prediction of propeller noise for submarines and underwater vehicles. The main objective of the study is to obtain accurate propeller noise prediction and to use this information to control noise on submarines. This paper presents the results of the study following the previous research project (Ozden et. al. 2012 & Korkut et. al. 2013). Firstly a validation study has been carried out for the prediction of DARPA Suboff generic submarine model's hydrodynamic drag force and wake properties in comparison with the experimental results given in Liu and Huang (1998) and Chase (2012), respectively. Calculations were continued with the validation of open water hydrodynamic characteristics of E1619 generic submarine propeller in comparison with the experimental results published by Di Felici et al. (2009). Simulations were performed for DARPA Suboff fitted with E1619 propeller under self-propelled condition. Results were compared with the ones carried out by Chase and Carrica (2013). Acoustic calculations were performed for E1619 propeller in open water condition, inlet induced DARPA Suboff wake condition and self-propulsion condition.

The method used for the noise prediction is given in Methodology Section. Results of the study are included. Finally some conclusions withdrawn from the study are also given.

2 METHODOLOGY

Flow around a propeller is solved using a RANS solver with the SST $k-\omega$ turbulence model. Then, transient solution is performed with second order implicit pressure based solver. Velocity and pressure coupled via SIMPLE algorithm Numerical Methods and Flow Solver. Time

dependent pressure data is used as the input for the FWH equation to predict far-field acoustics.

2.1 Numerical Methods and Flow Solver

For the numerical calculations ANSYS 13 Fluent is used to satisfy the following governing equation for continuity Alin et. al. (2010);

$$\frac{\partial \rho}{\partial t} + \frac{\partial}{\partial x_i} (\rho v_i) = 0 \quad (1)$$

where x_i and v_i are the tensor form of axial coordinates and velocities, respectively. Then the momentum equation becomes;

$$\frac{\partial(\rho v_i)}{\partial t} + \frac{\partial(\rho u_i u_j)}{\partial x_j} = -\frac{\partial p}{\partial x_i} + \frac{\partial}{\partial x_j} \left[\mu \left(\frac{\partial u_i}{\partial x_j} + \frac{\partial u_j}{\partial x_i} - \frac{2}{3} \delta_{ij} \frac{\partial u_l}{\partial x_l} \right) \right] + \frac{\partial}{\partial x_j} (-\rho \overline{u'_i u'_j}) \quad (2)$$

where δ_{ij} is Kronecker Delta and $-\rho \overline{u'_i u'_j}$ are the unknown Reynolds stresses.

For the turbulence modelling, SST $k-\omega$ turbulence model is employed due to its good performance on wall bounded boundary layer flows (Li 2006).

FLUENT employs cell-centered finite volume method. RANS formulation is used with absolute velocity selection. Transient solution is performed with second order implicit pressure based solver. Velocity and pressure coupled via SIMPLE algorithm. Green Gauss Node Based is used for gradient and PRESTO for pressure discretizations. For Momentum, Turbulent Kinetic Energy and Specific Dissipation Rate calculations, QUICK scheme is selected.

2.2 Noise Predictions

Ffowcs Williams – Hawkings Method

Ffowcs Williams Hawkings (FWH) equation is an inhomogeneous wave equation derived from the continuity and Navier-Stokes equations (ANSYS 2009).

$$\frac{1}{a_0^2} \frac{\partial^2 p'}{\partial t^2} - \nabla^2 p' = \frac{\partial^2}{\partial x_i \partial x_j} \{T_{ij} H(f)\} - \frac{\partial}{\partial t} \{ [P_{ij} n_j + \rho u_i (u_n - v_n)] \delta(f) \} + \frac{\partial}{\partial t} \{ [\rho_0 v_n + \rho (u_n - v_n)] \delta(f) \} \quad (3)$$

where

u_i : flow velocity in x_i direction

u_n : flow velocity normal to the surface ($f = 0$)

v_i : surface velocity component in x_i direction

v_n : surface velocity component normal to the surface

$\delta(f)$: Dirac delta function

$H(f)$: Heaviside function

P' , is the far-field sound pressure ($p' = p - p_0$). $f = 0$ is a mathematical surface used to facilitate the application of the generalised function theory and the free-space Green function to the unbounded space exterior flow problem

($f > 0$) to reach the solution. This surface ($f = 0$) represents a source (emission) surface and can be used as a surface overlapping with the body (impermeable) or as a permeable surface far from the body. n_i is the unit normal vector indicating the exterior region ($f = 0$). a_0 is the sound velocity in the far field and T_{ij} is the Lighthill tensor defined as below (ANSYS 2009);

$$T_{ij} = \rho u_i u_j + P_{ij} - a_0^2 (\rho - \rho_0) \delta_{ij} \quad (4)$$

P_{ij} is the compressive stress tensor. For a Stokesian fluid it is defined as follows;

$$P_{ij} = p \delta_{ij} - \mu \left[\frac{\partial u_i}{\partial x_j} + \frac{\partial u_j}{\partial x_i} + \frac{2}{3} \frac{\partial u_k}{\partial x_k} \delta_{ij} \right] \quad (5)$$

The free-stream quantities are denoted by the subscript 0.

The solution of Eq. (4) is obtained by the use of the free-space Green function ($\delta(g)/4\pi r$). The complete solution includes the surface and volume integrals. While the surface integrals include the effects of monopole, dipole and partially quadrupole effects the volume integrals include only the quadrupole sources except the regions of the source surface. In cases where the flow is in low subsonic region the value of the volume integral value diminishes and the source surface encloses the source region. Thus the volume integrals are not included to the calculations and the equations below are obtained;

$$p'(\vec{x}, t) = p'_T(\vec{x}, t) + p'_L(\vec{x}, t) \quad (6)$$

where;

$$4\pi p'_T(\vec{x}, t) = \int_{f=0} \left[\frac{\rho_0 (\dot{U}_n + U_n \dot{n})}{r(1-M_r)^2} \right] dS + \int_{f=0} \left[\frac{\rho_0 U_n \{rM_r + a_0(M_r - M^2)\}}{r^2(1-M_r)^3} \right] dS \quad (7)$$

$$4\pi p'_L(\vec{x}, t) = \frac{1}{a_0} \int_{f=0} \left[\frac{\dot{L}_r}{r(1-M_r)^2} \right] dS + \int_{f=0} \left[\frac{L_r - L_M}{r^2(1-M_r)^2} \right] dS + \frac{1}{a_0} \int_{f=0} \left[\frac{L_r \{rM_r + a_0(M_r - M^2)\}}{r^2(1-M_r)^3} \right] dS \quad (8)$$

where;

$$U_i = v_i + \frac{\rho}{\rho_0} (u_i - v_i) \quad (9)$$

$$L_i = P_{ij} \hat{n}_j + \rho u_i (u_n - v_n) \quad (10)$$

When the integration surface is overlapping with a closed wall (impenetrable wall) the expressions $p'_T(\vec{x}, t)$ and $p'_L(\vec{x}, t)$ from Equations (7) and (8) are referred as the thickness noise term and the loading noise term (ANSYS 2009). The thickness noise term express the noise generated by the displacement of the flow and the loading noise term express the noise generated by the thrust generated by the rotation of the blade (Test 2008). The terms in brackets in Equations (7) and (8) express that the kernels of the integrals are solved for the retarded time steps (τ) expressed as in Equation (11) where t is time and r is the observer distance;

$$\tau = t - \frac{r}{a_0} \quad (11)$$

The expressions in the equations denoted by a subscript are elements of vectors and unit vectors. For example \hat{r} and \vec{n} denote the unit vectors in radiation and wall-normal directions in $L_r = \vec{L} \cdot \hat{r} = L_i r_i$ and $U_n = \vec{U} \cdot \vec{n} = U_i n_i$. The dot over a variable denotes source-time differentiation of that variable (ANSYS 2009).

3 VERIFICATION AND VALIDATION

The methodology and the software used have been tested for a fisheries research vessel propeller (Korkut et. al. 2013). Atlar et.al (2001) presented the results of cavitation tunnel tests carried out with model propeller of a Sumitomo Heavy Industries Fisheries Research Vessel (FRV) and those of noise measurements with its full-scale propeller to validate the low-noise performance of this propeller. The tests involve the simulation of a target wake using a wake screen and the determination of the noise behind the simulated wake.



Figure 1 Fisheries Research Vessel propeller model

A 4-bladed fisheries research vessel propeller was investigated where cavitation tunnel hydrodynamic performance and hydro-acoustics tests were conducted in Emerson Cavitation Tunnel in University of Newcastle upon Tyne, UK. During the tests, the target wake velocity ratios (V_a/V_s) were simulated using different size of meshes attached to a square frame and the wake velocities were measured using a pitot static tube comb and “scanivalve” assembly. Main particulars of the propeller is given in Table 1

Table 1 Main particulars of propeller

Number of Blades, Z	4
Propeller Diameter, D	0.30 m
Pitch Ratio at 0.7R, P/D	0.8464
Expanded Blade Area Ratio, A_E/A_0	0.55
Boss Ratio, r_b/R	0.276
Rake	0 Degrees
Skew	40 Degrees
Direction of rotation	Right handed

To take into account the influence of the wake characteristics, velocity profile of the wake was

implemented to velocity inlet of the calculation domain to simulate the non-uniformity. Figure 2 shows the measured wake and adaptation of the velocity inlet.

Both cavitation tunnel tests and CFD calculations were conducted for the 0.3m diameter propeller turning with 978 RPM at an advanced speed of 3m/s and the density of the water in the tunnel was 1002 kg/m³.

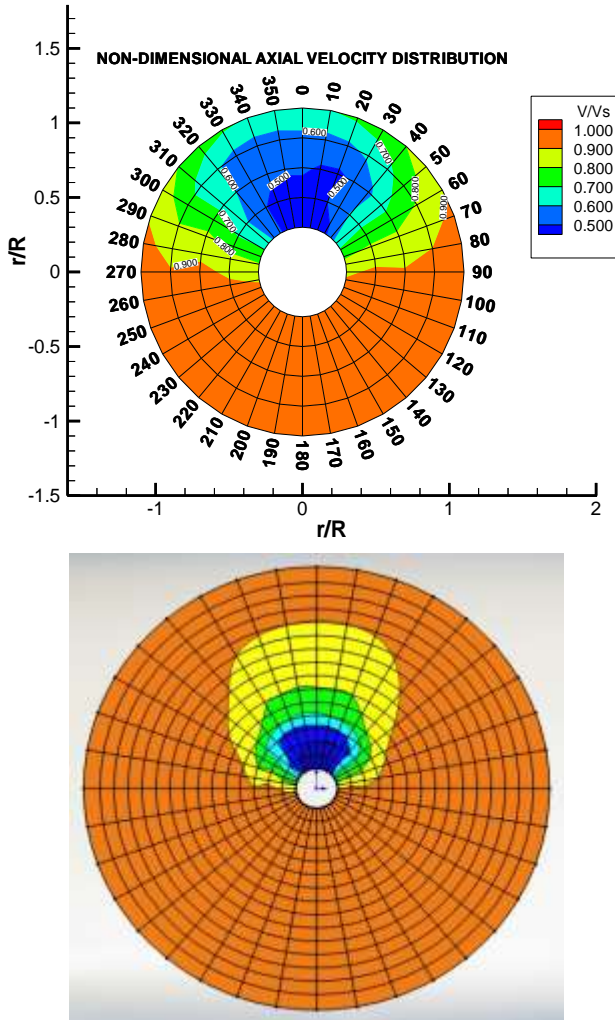


Figure 2 Measured wake (top) and adapted wake (bottom)

Calculation was performed for the J value 0.61. Unsteady flow solver was employed for the prediction of performances of the propeller in wake condition. Results of K_T , K_Q and η_0 values are given in the Table 2 in comparison to the experimental values.

Table 2 Comparison of CFD results with experiment

	J	K_T	$10K_Q$	η_0
Experiment	0.61	0.12	0.17	0.66
CFD	0.61	0.11	0.19	0.59
% Error		1.12	8.93	11.69

K_T values were predicted with a better accuracy than K_Q values. η_0 values were also affected by the prediction of K_Q values as expected.

Concerning the noise prediction there is a good agreement between predicted results with the experiments for the frequency range of 200 Hz to 5000Hz. For lower and higher ranges RANS over predicted the flow noise.

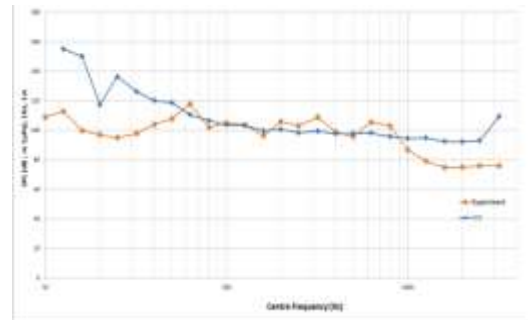


Figure 3 Comparison of CFD results with the experiment at J=0.61

4 GEOMETRIES OF BODIES

4.1 DARPA Suboff

The DARPA Suboff AFF8 is a generic submarine model geometry with a length of 4.36m sum of a forebody of 1.02m, a midbody of 2.23m and an aftbody of 1.11m. It has cylindrical cross-section with a maximum diameter of 0.508m. AFF8 has a sail which is located at the top dead center of the hull starting at $x=0.92m$ from the bow and ends at $x=1.29m$. It has cross shaped rudder design where rudders and hydroplanes are located at $x=4m$. The hull and appendage arrangement of DARPA Suboff AFF8 is given in Figure 4 and main particulars are given in Table 3. Views of the calculation domain and DARPA suboff are shown in Figure 5 and Figure 6, respectively.



Figure 4 Geometry of DARPA Suboff AFF8

Table 3 Main particulars of DARPA Suboff AFF8

Generic Submarine Type	DARPA Suboff AFF8	
	Symbol	Magnitude
Description		
Length overall	L_{oa}	4.356 m
Length between perpendiculars	L_{dp}	4.261m
Maximum hull radius	R_{max}	0.254 m
Centre of buoyancy (aft of nose)	FB	0.4621 L_{oa}
Volume of displacement	∇	0.718
Wetted Surface	S_{wa}	6.338

DARPA Suboff AFF8 hull was investigated experimentally by Li & Huang (1998) for $Re=12 \times 10^6$.

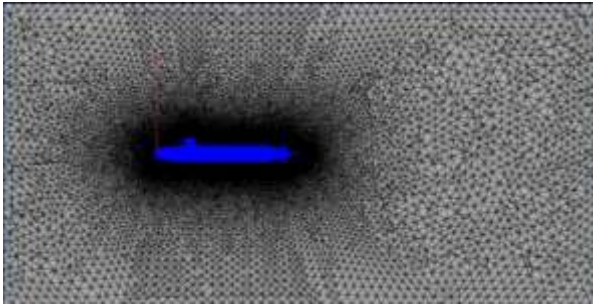


Figure 5 Calculation domain of DARPA Suboff

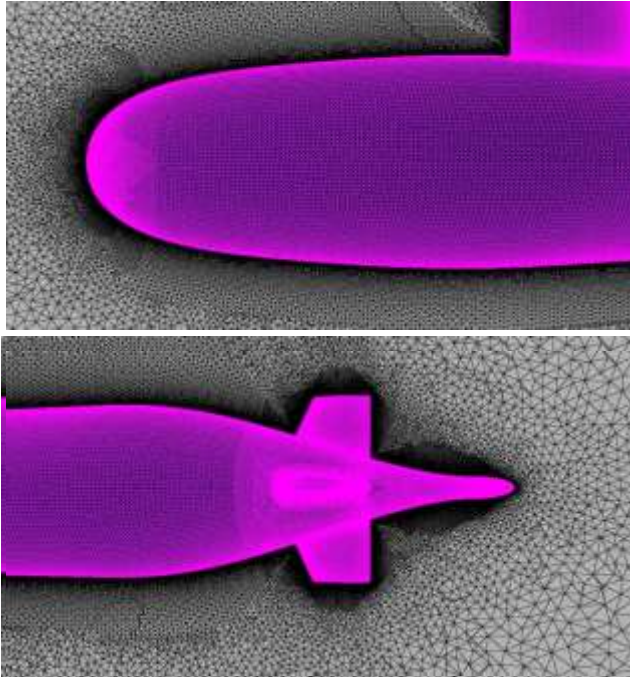


Figure 6 Cut away views of DARPA Suboff

Table 4 Main particulars of INSEAN E1619 submarine propeller

Propeller Type	INSEAN E1619
Advanced Speed	1.68 m/s
RPM	280 RPM
Diameter	0.485 m
Number of Blades	7
A_E/A_0	0.608
Hub/Diameter Ratio	0.226
Pitch to Diameter ratio, P/D at 0.7R	1.15

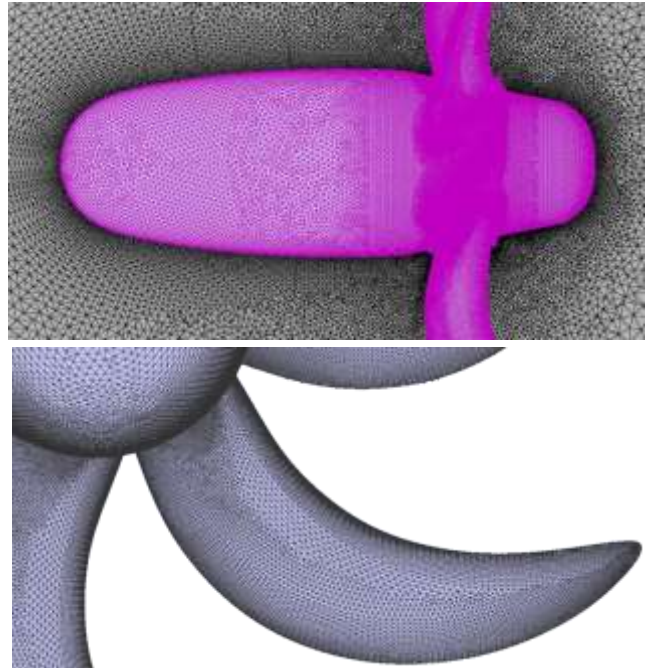


Figure 8 Detailed fine mesh for INSEAN E1619

4.2 INSEAN E1619 Submarine Propeller

The INSEAN E1619 generic submarine propeller has been analysed in open water, within artificial wake and propelling DARPA Suboff AFF8 conditions. The propeller was a seven-bladed highly skewed submarine propeller with an unloaded tip blade design. Open water experiments were performed in the INSEAN towing tank, and wake velocity measurements were made, using LDV in the large circulating water channel of INSEAN. Results were presented by Di Felice (2009). 3-D views and the main particulars of the E1619 submarine propeller are given in Figure 7 and in Table 4, respectively. In Figure 8 the detailed fine mesh used for the study is presented.



Figure 7 3-D views of INSEAN E1619 propeller

5 VALIDATION OF THE METHODOLOGY IN UNIFORM FLOW

5.1 Performance Prediction

Open water performance calculations of E1619 propeller was carried out at $J=0.74$ and $J=0.85$. A computation domain has been generated with a 1.5m diameter where 1.5m region left prior and 3m after the propeller geometry. A mesh independence study was performed from coarse to fine meshes, using 6,386,638, 8,065,679 and 10,513,205 cells, respectively with non-dimensional wall distance value of $y^+ \approx 50$.

The convergence of grid study can be seen in Figure 9 with above grid properties in comparison with the experimental values at $J=0.74$.

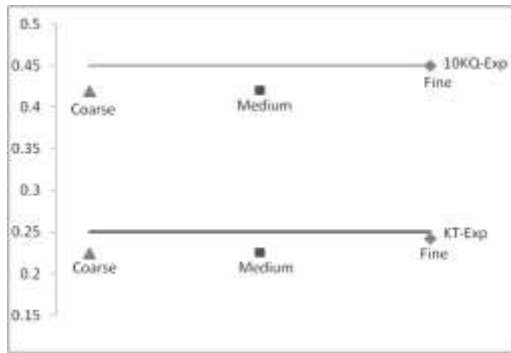


Figure 9 Comparison of convergence of CFD values and experiment results from coarse to fine mesh

Results of the fine mesh are presented in Figure 10. It can be seen that RANS calculations very well captured the thrust and torque values at given advanced ratios.

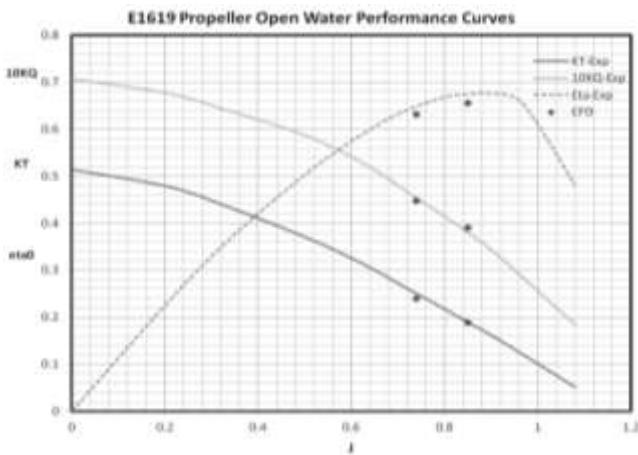


Figure 10 Comparison of open water characteristics calculation for E1619 with experimental results by Di Felice et al. (2009)

5.2 Noise Prediction in Open Water

After the steady computations which were performed for the performance predictions of E1619 generic submarine propeller, calculations were carried out transiently to predict the noise characteristics.

The domain which contains the propeller body was selected as the source of noise and a number of receiver locations was defined for the calculation. For the calculations performed for E1619 propeller in open water condition acoustic predictions were made for a total of 6 receivers located 1m away from the propeller reference point (0,0,0) and 0°, 45° and 90° angles from the shaft axis (x,0,0). Position of receivers can be seen in Figure 11. Figure 12 shows the noise predictions for different receivers at J=0.74.

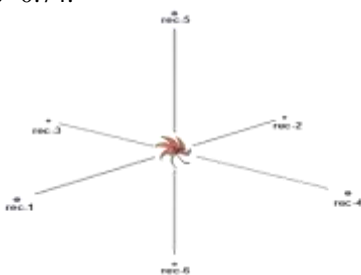


Figure 11 Receiver locations for E1619 propeller

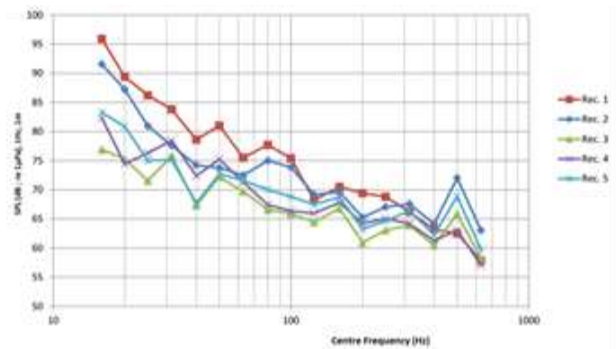


Figure 12 Comparisons of noise predictions for different receiver positions at J=0.74

6 FLOW CALCULATIONS FOR DARPA SUBOFF

Post processes of the solution are also performed by ANSYS 15 FLUENT by using Fast Fourier Transform properties. Hanning filter was used and results are presented for Sound Pressure Level (dB) form for 1/3 Octave band.

Before computing self-propulsion a set of computations were performed for DARPA Suboff towed in fully appended configuration without propeller, and results were shown in Figure 13 in comparison with the experiment results (Liu and Huang 1998). Computations were carried out in a cylindrical domain with a diameter of 9m and a region of 4.5m prior to model geometry and a 9m of after the model. Two different grids were generated with 7,812,122 and 11,511,137 cells where $y^+ \approx 50$.

Results indicated that the resistance predicted by RANS computations was in a good agreement with the experiments.

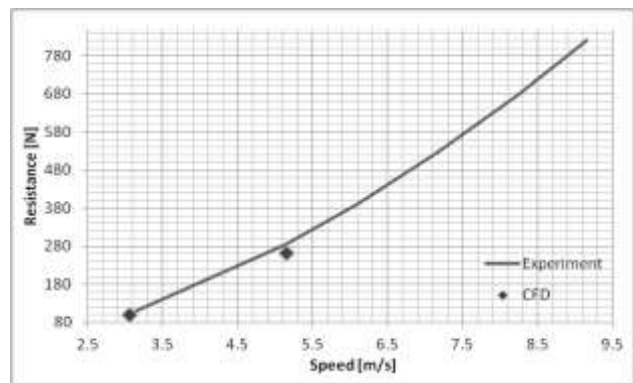


Figure 13 Comparison of resistance predicted by CFD method with experiment (Liu and Huang (1998))

7 NOISE PREDICTIONS

Noise predictions were performed in simulated (induced) wake condition and behind DARPA Suboff condition.

7.1 Propeller in Simulated (Induced) Wake

RANS calculations were conducted in order to simulate the submarine moving straight ahead. The computationally predicted wake at the location $x/L=0.978$ was compared to the wake measured by Crook (1990).

The hole at the middle of each figure is due to the body of the submarine. As can be seen from the figures overall pattern of the wake is very similar. Reduced flow velocity can be traced downstream of the rudders and hydroplanes, higher wake field which can be observed at the top is due the wake of the sail.

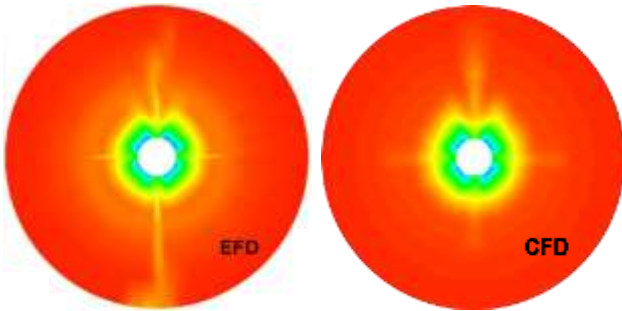


Figure 14 Measured and computed wake of DARPA Suboff AFF8 configuration

The “V” shaped higher velocity field on the top side which differs from sides and bottom is because of the horseshoe vortices which deplete the boundary layer at the center and send low momentum flow to the sides. In the experimental wake data, the low velocity field between lower rudder and bottom is due to presence of struts which were used during the wind tunnel tests.

For the computations a grid with 8.5m region prior and 9m after the propeller geometry was left and 9,834,381 cells used where $y^+ \approx 50$.

7.2 Propeller behind DARPA SUB OFF

DARPA Suboff AFF8 propelled by the E1619 propeller has been studied by several authors for self-propulsion (Chase 2012, Chase and Carrica 2013), cycle-to-cycle blade loading (Liefvendahl and Töerng 2011) and hull interactions (Alin. et al. 2011). Similar to the listed studies, the geometry of DARPA Suboff was kept constant and E1619 propeller diameter was scaled to 0.262m.

Simulation of the DARPA Suboff AFF8 fitted with the E1619 propeller under self-propelled conditions was performed using RANS. Geometric details are similar to those listed in Table 3.

Computations were carried out in a cylindrical domain with a diameter of 9m and a region of 4.5m prior and a 9m after the model geometry. The grid was with 19,777,345 cells where $y^+ \approx 50$. Figure 15 shows the DARPA Suboff with E1619 propeller fitted and Figure 16 shows the calculation domain and cut away views. Figure 17 also shows the perspective view from the stern where contour plots of the axial velocities are shown on transverse and longitudinal cross-sections along the hull.



Figure 15 3-D view of DARPA Suboff with E1619 propeller fitted

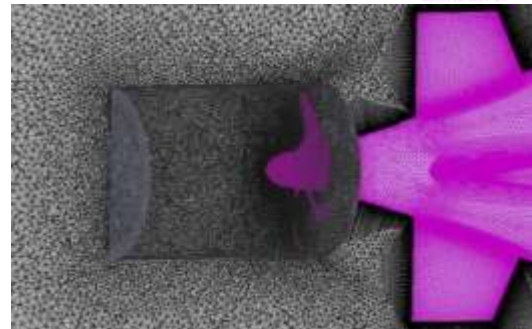
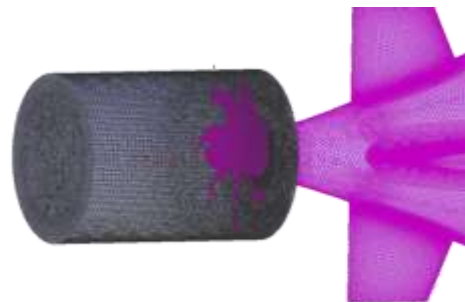
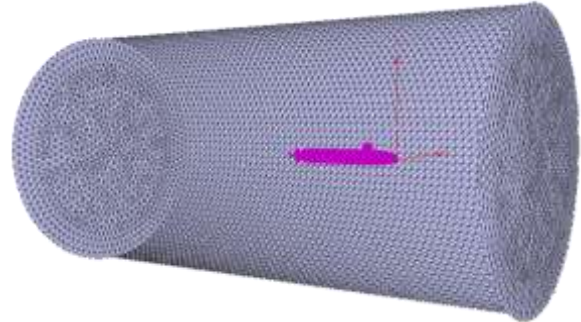


Figure 16 Calculation domain and cut away views of the bodies

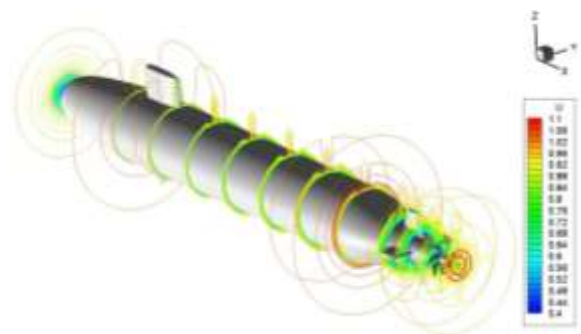


Figure 17 Axial velocity cross-sections around DARPA Suboff with E1619

8 PRESENTATIONS AND DISCUSSIONS OF RESULTS

In Figure 18 longitudinal cross-section views of both self-propelled and within induced wake conditions of DARPA Suboff and INSEAN E1619 propeller were presented. The

main difference between two cross-sections is velocity profiles after the hub region which is due to the blunt hub geometry at the absence of the submarine body. This affects the region about two diameters long behind the propeller hub with a wide boundary layer. This can also be traced on the transverse cross-section views of the behind propeller region which can be seen from Figure 19 to Figure 22 with 0.005 x/L intervals.

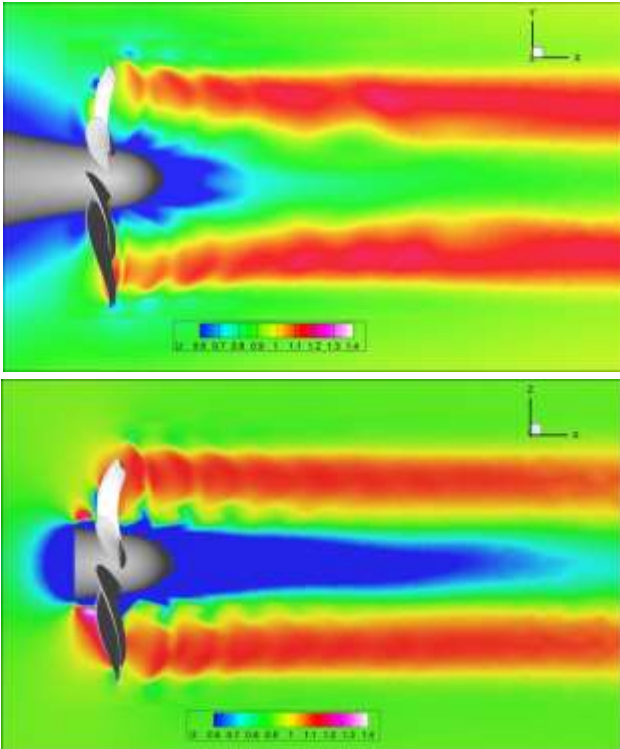


Figure 18 Cross section plan view of the wake for self-propelled and induced wake conditions

The results of the analysed conditions are presented in Figures 23 through 25. In each graph: the logarithmic-scaled x-axis represents the centre frequencies in Hz, while the linear-scaled y-axis represents the sound pressure levels in dB re 1 μPa (standard reference pressure for water), 1 Hz, 1m.

Although the characters of the SPL curves of both conditions are almost similar, there is a difference in values of receivers located behind the propeller. This is not identical for the second receiver which is located in the front of the propeller plane. Computations predict almost the same SPL spectra in the vortically undisturbed region (in front of the propeller) but predicting shifting values on dB scale for the receivers located behind the propeller. This difference between the receivers in two computations is probably also due to the blunt hub shape.

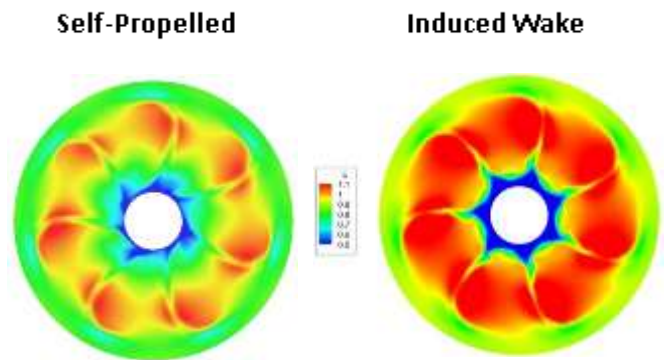


Figure 19 Wake at $x/L=1.005$

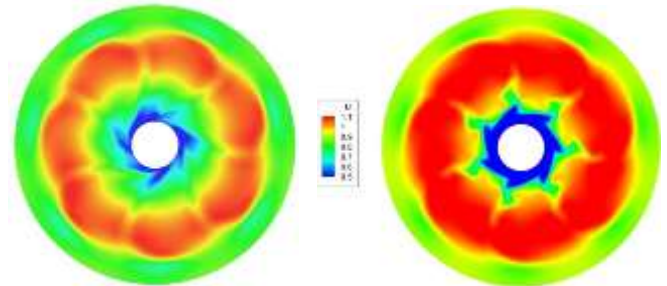


Figure 20 Wake at $x/L=1.010$

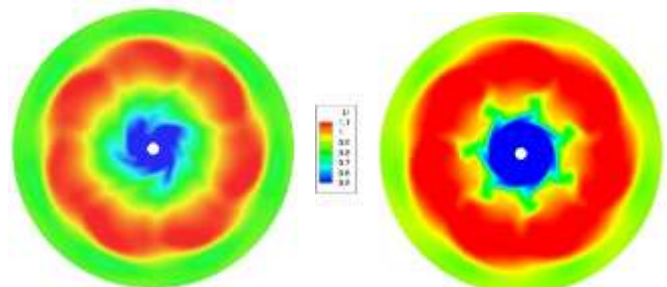


Figure 21 Wake at $x/L=1.015$

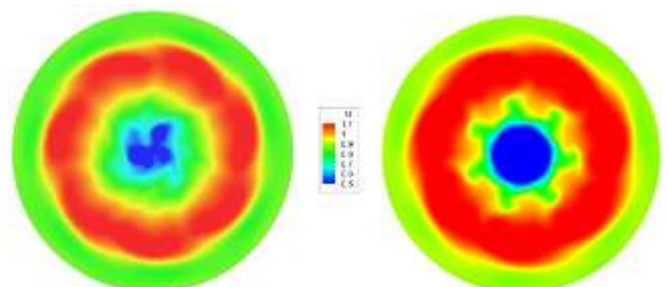


Figure 22 Wake at $x/L=1.020$

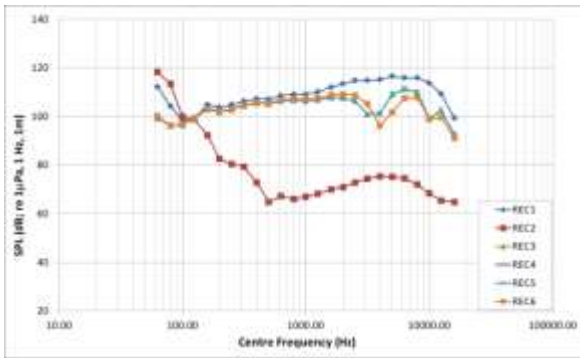


Figure 23 Underwater noise predictions for varying receiver positions in the case of self-propelled DARPA Suboff by E1619 propeller

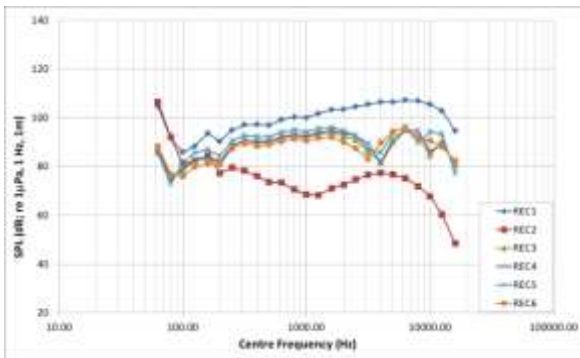


Figure 24 Underwater noise predictions for varying receiver positions in the case of DARPA Suboff with induced wake

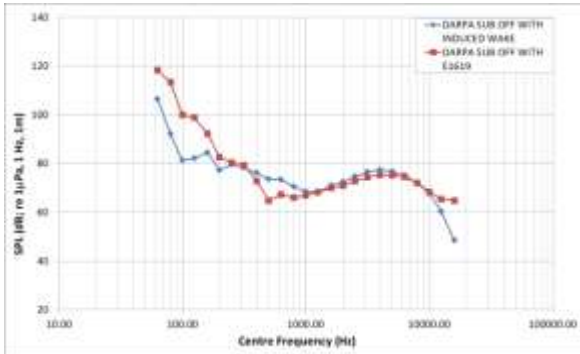


Figure 25 Comparison of underwater noise predictions for self-propelled DARPA Suboff by E1619 propeller with those by induced wake at receiver2

9 CONCLUSIONS

A validation study was conducted in a model scale for highly skewed fisheries research vessel propeller. The predicted noise, using RANS and employing Ffowcs Williams-Hawkings method, was compared to the experimental data which was measured in Emerson Cavitation Tunnel of Newcastle University. Calculations were extended to predict the noise characteristics for a submarine propeller.

DARPA Suboff AFF8 fully appended body was chosen as a model scale submarine geometry and INSEAN E1619 highly skewed 7-bladed generic model scale submarine

propeller was also selected for the study. A number of validation studies and mesh independence studies were performed to verify the predictions of experimentally measured drag & wake data of submarine and thrust & torque data of the propeller. Noise calculations were performed for two cases; in the first case, calculated wake profile was induced at the inlet of the domain where propeller was rotated and, in the second case computations performed for the propeller rotating behind the submarine model in self-propelled condition. Some conclusions drawn from the study are as follows:

- In the validation case, experimental and computational noise data showed good agreement between 200Hz to 5000Hz. For lower and higher frequencies, CFD over-predicted the noise.
- Steady computations of drag and wake over DARPA Suboff AFF8 fully appended body showed a good agreement with experimental measurements.
- Open water performance of the INSEAN E1619 propeller was well predicted, which was a preparatory study prior to noise calculations.
- During the induced wake computations, the blunt hub shape at the absence of submarine body caused a wider boundary layer behind the propeller comparing the self-propelled condition. A more streamlined hub geometry could terminate this difference.
- Similar to the validation case where a highly skewed four-bladed surface ship propeller was used, the two computations on INSEAN E1619 showed good agreement between 200Hz to 5000Hz while using almost half the mesh elements for induced wake condition which changed the computation time significantly.
- Experimental noise data is publicly published for neither DARPA Suboff submarine body, nor INSEAN E1619 submarine propeller. Future studies may include the experimental measurements of noise characteristics for hull only, propeller in open water conditions, propeller within wake and self-propelled conditions.

Studies focused on predicting the flow details around the model scale submarine and propeller. This is due to the published experimental data regarding the Suboff models and E1619 propeller. Community seeks high quality experimental data for full scale submarines which can be used for validation of computational noise predicting methods.

ACKNOWLEDGEMENTS

Authors would like to thank Prof M. Atlar of Newcastle University for sharing the geometry, wake and noise data of Sumitomo Fisheries Research Vessel. We would also

like to thank M. Felli and F. Salvatore of INSEAN for sharing the 3D geometry of INSEAN E1619 submarine propeller for use in our academic studies. The authors are grateful to Assist. Prof. O. Unal and Prof. O. Goren of ITU for useful discussions and use of the high speed computer at Numerical Hydrodynamics Laboratory. Authors also wish to acknowledge Mr. B. Can of Wichita State University for his invaluable help and E. Demir from DATUM Ltd for preparation of 3D geometries.

REFERENCES

- Atlar, M., Takinaci, A.C., Korkut, E., Sasaki, N. & Aono, T., (2001). 'Cavitation Tunnel Tests for Propeller Noise of a FRV and Comparisons with Full-Scale Measurements', 4th International Symposium on Cavitation CAV2001, Pasadena, California, USA
- Alin, N., Chapuis, M., Fureby, C., Liefvendahl, M., Svennberg, U. & Troeng, C. (2010). 'A Numerical Study of Submarine Propeller-Hull Interaction'. Proceedings of the 28th Symposium on Naval Hydrodynamics, Pasadena, California.
- ANSYS (2009) ANSYS 12 FLUENT Theory Guide.
- Barbarino, M. & Casalino, D. (2012) 'Hybrid Analytical/Numerical Prediction of Propeller Broadband Noise in Time Domain'. Int. Jour. of Aeronautics, **11**(2), pp.157–175.
- Bull, P., (1996). 'The Validation of CFD Predictions of Nominal Wake for the SUBOFF Fully Appended Geometry'. 21st Symposium on Naval Hydrodynamics, June, pp.1061– 1076.
- Chase, N., (2012) 'Simulations of the DARPA Suboff Submarine Including Self-propulsion with the E1619 Propeller'. M.Sc. Thesis, University of Iowa, USA.
- Chase, N. & Carrica, P. M. (2013). 'Submarine Propeller Computations and Application to Self-propulsion of DARPA Suboff'. Ocean Engineering, **60** pp.68-80.
- Crook B. (1990) 'Resistance for DARPA Suboff as Represented by Model 5470'. David Taylor Research Center Report, Report No: DTRC/SHD-1298-07.
- Di Felice, F., Felli, M., Liefvendahl, M. & Svennberg, U. (2009) 'Numerical and Experimental Analysis of the Wake Behavior of a Generic Submarine Propeller'. Proceedings of the 1st International Symposium on Marine Propulsors, Trondheim, Norway.
- Ffowcs Williams JE, Hawkings DL (1969) 'Sound Generation by Turbulence and Surfaces in Arbitrary Motion'. Philosophical Transactions of the Royal Society A264: 321–342.
- Gao, FD., Pan, CY. & Han, YY. (2012) 'Numerical Computation and Analysis of Unsteady Viscous Flow Around Autonomous Underwater Vehicle with Propellers Based on Sliding Mesh'. J. of Central South University of Technology. **19**(4),pp.944–952.
- Groves, N., Huang, T. & Chang, M. (1998) 'Geometric Characteristics of DARPA SUBOFF Models (DTRC Model Nos. 5470 and 5471'. David Taylor Research Center Report, Report No. DTRC/SHD-1298-01, March.
- ITTC. (2008) 'Propulsion Committee Report'. Proceedings of the 25th ITTC, 25th International Towing Tank Conference, Fukuako, Japan, , Vol. I, pp. 83-141.
- ITTC. (2011) 'Specialist Committee on Computational Fluid Dynamics Report'. Proceedings of the 26th International Towing Tank Conference. Rio de Janeiro, Brazil, pp. 337-375.
- Kawamura, T., Watanabe, T., Takekoshi, Y., Maeda, M., Yamaguchi, H. Numerical (2004) 'Simulation of Cavitating Flow around a Propeller' JSNA. **195**.
- Korkut, E., Ozden, M.C., Avci, G.A, Goren, O., Takinaci, A.C. & Danisman, D.B. (2013) 'Numerical Calculations of Noise Characteristics of Surface and Underwater Navy Ships Generated by Propeller'. Turkish Scientific and Research Council (TUBITAK) Project, Project No: 110M327.
- Li, D.-Q. (2006) 'Validation of RANS Predictions of Open Water Performance of a Highly Skewed Propeller with Experiments'. Conference of Global Chinese Scholars on Hydrodynamics, Journal of Hydrodynamics, **18**(3), Supplement, pp.520-528.
- Liefvendahl, M., Toerng, C. (2011) 'Computation of Cycle-to-Cycle Variation in Blade Load for a Submarine Propeller, using LES'. 2nd International Symposium on Marine Propulsors, SMP11, Hamburg, Germany.
- Liu, H.-L. & Huang, T. (1998). 'Summary of DARPA SUBOFF Experimental Program Data'. Report No. CRDKNSWC/HD-1298-11, June.
- Ozden, M.C., Avci, G.A. & Korkut, E. (2012). 'A Numerical Study on Prediction of Noise Characteristics Generated By a Propeller'. 10th International Conference on Hydrodynamics – ICHD2012, St. Petersburg, Russia.
- Salvatore, F. & Ianniello, S. (2003) 'Preliminary Results on Acoustic Modelling of Cavitating Propellers'. Comp. Mechanics, **32**, pp.291–300.
- Seol, H., Suh, JC, & Lee, S. (2002) 'Prediction of Non-Cavitating Underwater Propeller Noise'. J. Sound and Vibration, **257**(1), pp.131-156.
- Seol, H., Suh, JC. & Lee, S. (2005) 'Development of Hybrid Method for the Prediction of Underwater Propeller Noise'. J. Sound and Vibration, **288**(1), pp.345-360.
- Testa, C. (2008). 'Acoustic Formulations for Aeronautical and Rotorcraft Noise Prediction Based on the Ffowcs Williams and Hawkings Equation'. Ph.D. Thesis, Universita degli Studi di ROMA TRE, Italy.